Biofilm Reduction of Oxidized Contaminants

By

Youneng Tang

A Dissertation Presented in Partial Fulfillment
of the Requirements for the Degree
Doctor of Philosophy

Approved January 2012 by the
Graduate Supervisory Committee:

Bruce E. Rittmann, Chair
Paul Westerhoff
Rosa Krajmalnik-Brown
Rolf Halden

ARIZONA STATE UNIVERSITY

May 2012

ABSTRACT

The overall goal of this dissertation is to advance understanding of biofilm reduction of oxidized contaminants in water and wastewater. Chapter 1 introduces the fundamentals of biological reduction of three oxidized contaminants (nitrate, perchlorate, and trichloriethene (TCE)) using two biofilm processes (H_2-based membrane biofilm reactors (MBfR) and packed-bed heterotrophic reactors (PBHR)), and it identifies the research objectives. Chapters 2 through 6 focus on nitrate removal using the MBfR and PBHR, while chapters 7 through 10 investigate simultaneous reduction of nitrate and another oxidized compound (perchlorate, sulfate, or TCE) in the MBfR. Chapter 11 summarizes the major findings of this research.

Chapters 2 and 3 demonstrate nitrate removal in a groundwater and identify the maximum nitrate loadings using a pilot-scale MBfR and a pilot-scale PBHR, respectively. Chapter 4 compares the MBfR and the PBHR for denitrification of the same nitrate-contaminated groundwater. The comparison includes the maximum nitrate loading, the effluent water quality of the denitrification reactors, and the impact of post-treatment on water quality. Chapter 5 theoretically and experimentally demonstrates that the nitrate biomass-carrier surface loading, rather than the traditionally used empty bed contact time or nitrate volumetric loading, is the primary design parameter for heterotrophic denitrification. Chapter 6 constructs a pH-control model to predict pH, alkalinity, and precipitation potential in heterotrophic or H_2-based autotrophic denitrification reactors.

Chapter 7 develops and uses steady-state permeation tests and a mathematical model to determine the H_2-permeation coefficients of three fibers commonly used in the MBfR. The coefficients are then used as inputs for the three models in Chapters 8-10. Chapter 8 develops a multispecies biofilm model for simultaneous reduction of nitrate and perchlorate in the MBfR. The model quantitatively and systematically explains how operating conditions affect nitrate and perchlorate reduction and biomass distribution via four mechanisms. Chapter 9 modifies the nitrate and perchlorate model into a nitrate and sulfate model and uses it to identify operating conditions corresponding to onset of sulfate reduction. Chapter 10 modifies the nitrate and perchlorate model into a nitrate and TCE model and uses it to investigate how operating conditions affect TCE reduction and accumulation of TCE reduction intermediates.

ACKNOWLEDGMENTS

First, I express my deepest gratitude to my supervisor, Bruce E. Rittmann, for his excellent guidance and great help. I appreciate all his contributions of time, ideas, and funding during my Ph.D. experience. I thank him for having taught me, both consciously and unconsciously, how to write reports and manuscripts, present work, manage time, and behave professionally. I also thank him for always responding to my questions and requests quickly and effectively. As a successful and enthusiastic professor, he has set me an excellent example. It is an honor to be one of his Ph.D. students.

Second, I thank the members of my graduate committee, Paul Westerhoff, Rosa Krajmalnik-Brown, and Rolf Halden for their time and advice. I especially thank them for their questions and suggestions to my dissertation proposal, which significantly improved my dissertation. I am thankful to Rosa Krajmalnik-Brown for also providing me guidance to construct and evaluate my biofilm models.

Third, I thank all co-workers during my Ph.D. study. I gratefully acknowledge Kerry J. Meyer, Paul D. Swaim, Daniel Candelaria, and William D. Bellamy from CH2M HILL, and Rick Scott from City of Glendale for managing the pilot-scale denitrification project. I also gratefully acknowledge Chen Zhou, Michal Ziv-El, Jung Hun Shin, and Chang Hong Ahn from Arizona State University and David Friese and Ryan Overstreet from APTwater for assisting daily operation of the pilot-scale denitrification project. I owe thanks to Chen

Zhou, Andrew Marcus, and Steven W. Van-Ginkel for discussing with me when I constructed the pH-control model, the H_2-permeation model, and the biofilm models. I also owe thanks to Aura Ontiveros-Valencia and Heping Zhao for conducting experiments to evaluate my biofilm models. I am grateful to members in the Swette Center for Environmental Biotechnology for a good source of friendships, advice, and collaborations, and to Diane Hagner, Dana Aguilar, and Saunia Calloway for their administrative assistance.

Four, I gratefully recognize the funding sources that made my Ph.D. work possible. I was supported by the Water Research Foundation Project # 4131, which was funded by the Water Research Foundation and the City of Glendale. I was also supported by the grant number ER-200541 from the Environmental Security 314 Technology Certification Program (ESTCP), United States Department of Defense, via a sub315 contract with CDM.

Finally, I thank my Mom Yixian Zhao, my Dad Weiping Tang, and my brother Youzhi Tang, for their endless love and faithful support.

Youneng Tang

Arizona State University

January 2012

TABLE OF CONTENTS

Page

LIST OF TABLES

Table Page

LIST OF FIGURES

Figure Page

Figure Page

Figure Page

LIST OF ABBREVIATIONS AND ACRONYMS

ADB	autotrophic denitrifying bactria
BAP	biomass-associated products
BDOC	biodegradable dissolved organic carbon
CFU	colony-forming unit
CMBR	completely mixed biofilm reactor
COD	chemical oxygen demand
DB	denitrifying bacteria
DCE	dichloriethene
DH	*Dehalococcoides*
DO	dissolved oxygen
DOC	dissolved organic carbon
EBCT	empty bed contact time
EPS	extracellular polymeric substances
FISH	fluorescence in situ hybridization
GAC	granular activated carbon
HB	heterotrophic bacteria
HDB	heterotrophic denitrifying bacteria
HPC	heterotrophic plate count
IB	inert biomass
IRIS	Integrated Risk Information System
LSI	Langlier Saturation Index

MBfR	membrane biofilm reactor
MCL	maximum contaminant level
PBHR	packed-bed heterotrophic reactor
PLC	programmable logic controller
PRB	autotrophic perchlorate-reducing bacteria
qPCR	real-time quantitative polymerase chain reaction
SL	carrier-surface loading
SM	*Standard Methods for the Examination of Water and Wastewater*
SMP	soluble microbial products
SRB	sulfate-reducing bacteria
TCE	trichlorethene
TDS	total dissolved solids
UAP	substrate-utilization-associated products
USEPA	United States Environmental Protection Agency
VC	vinyl chloride
VL	volumetric loading

Chapter 1

INTRODUCTION AND BACKGROUND

This chapter has three sections. In the first section, I introduce reduction of three oxidized contaminants, nitrate, perchlorate, and trichloroethene, by two biofilm reactors, the H_2-based membrane biofilm reactor and the packed-bed heterotrophic reactor. Also, I introduce the first objective of the dissertation here. In the second section, I review fundamentals of biofilm reduction of oxidized contaminants, including inoculation, electron donor supply, nutrients supply, biofilm management, the most fundamental design parameters, pH control, and simultaneous reduction of two oxidized compounds. I identify six research objectives after reviewing these fundamentals. In the third section, I compile the seven objectives and introduce how the dissertation addresses them.

This chapter is adapted from a book chapter (Rittmann, Tang, Meyer, Bellamy, and Nerenberg, 2011) and a final report (Meyer, Swaim, Bellamy, Rittmann, Tang, and Scott, 2010). I am the primary author of the adapted contents.

1. Overview of Biofilm Reduction of Oxidized Contaminants

Biological water and wastewater treatment depends partly or wholly on biological mechanisms to achieve treatment objectives. Like all living organisms, bacteria live by oxidizing and reducing chemicals in their environment. Bacteria are able to oxidize and reduce an enormous range of different chemicals, some of which are contaminants in water and wastewater. When the bacteria oxidize or

reduce these contaminants, the contaminants typically are transformed into harmless products, eliminating water-quality problems. Thus, biological treatment of water and wastewater is based on finding ways to take advantage of the unsurpassed ability of bacteria to oxidize or reduce contaminants. In this dissertation, I focus on three oxidized contaminants: nitrate (NO_3^-), perchlorate (ClO_4^-), and trichloroethene (TCE, C_2Cl_3H).

Nitrate (NO_3^-) can cause eutrophication in an aquatic system and is a pervasive drinking water contaminant. Nitrate contamination is mainly due to use of agricultural fertilizers and wastewater discharges. The primary health concern regarding nitrate is methaemoglobinaemia, so-called "blue-baby syndrome" (Kapoor and Viraraghavan 1997). The current maximum contaminant levels (MCL) for nitrate of the United States, Europe, and World Health Organization are 10, 11, and 11 mg N/L, respectively (Soares 2000). Closely related to nitrate is nitrite (NO_2^-), which is an even more serious cause of methemoglobinemia; its MCL is 1 mg N/L (Soares 2000).

Perchlorate (ClO_4^-) is an emerging water contaminant that affects over 20 million people across the United States (USEPA, 2002). Perchlorate in water is believed to come mainly from improper disposal of solid rocket fuel. While no federal standard for perchlorate exists yet, several states have established standards ranging from 1 to 18 μg/L for portable water (Srinivasan and Sorial, 2009).

Trichloroethene (TCE) is a contaminant frequently found at Superfund sites across the States. USEPA released the final health assessment for TCE to

the Integrated Risk Information System (IRIS) database and characterized the chemical as carcinogenic to humans and as a human noncancer health hazard (USEPA, 2011). TCE has been widely used as a cleaning agent and solvent for many military, commercial, and industrial applications (McCarty, 1997; Bradley, 2000). Its current MCL is 5 μg/L (USEPA, 2009).

The three oxidized contaminants can be removed using either suspended-growth or biofilm (also called attached-growth or fixed-film) reactors. In this dissertation, I study two types of biofilm reactors: the H_2-based membrane biofilm reactor (MBfR) and the packed-bed heterotrophic reactor (PBHR).

In an MBfR, H_2 gas, an electron donor, is delivered by diffusion through the walls of gas-transfer membranes (Lee and Rittmann, 2002). Autotrophic bacteria develop naturally as a biofilm on the outside of the bubbleless (*i.e.*, no pores) gas-transfer membranes. As the bacteria oxidize H_2 to reduce nitrate or other oxidized contaminants, the concentration gradient pulls more H_2 across the membrane wall. This allows self-regulation of the H_2-delivery rate and eliminates the off-gassing problems encountered in a traditional reactor, in which biofilm attaches to media and H_2 is delivered through sparging (Gros et al., 1998; Rittmann, 2006). The H_2 concentration in the liquid of the MBfR is low (e.g., 9 μg/L) (Lee and Rittmann, 2002; Ziv-El and Rittmann, 2009a), suggesting a high H_2-utilization efficiency (Rittmann, 2006). In the recent decade, MBfR has been tested at bench- and/or pilot-scale for removal of nitrate, perchlorate, and TCE in groundwater and/or wastewater.

A PBHR is packed with biomass carriers consisting of either plastic modules that are systematically stacked or granular media (*e.g.*, sand, granular activated carbon, expanded clay) that are dumped in the reactor vessel. Packed-bed reactors can be operated in either down-flow or up-flow modes. Up-flow systems are more common as the possibility of plugging is reduced and the bacterial biomass is constantly submerged. An external organic substance should be added for tertiary wastewater treatment or drinking water treatment. Methanol is the most common electron donor for wastewater treatment, and ethanol and acetic acid are the most common electron donors for drinking water treatment (Rittmann and Huck, 1989; Richard, 1989; Rogalla et al., 1990a; 1990b). PBHR has been widely used for advanced nitrate removal worldwide. It is also the most widely used reactor for nitrate removal in drinking water treatment in Europe (Richard et al., 1980; Janda et al., 1988; Gayle et al., 1989; Rittmann and Huck, 1989; Richard, 1989; Rogalla et al., 1990a; Rittmann and McCarty, 2001). While the U.S. has only one full-scale precedent for drinking water denitrification for potable use (Silverstein and Carlson, 1999), several new full-scale processes are currently being developed for this purpose. Perchlorate and TCE can also be reduced by PBHR at bench- and/or pilot-scale (Logan, 1998; van Ginkel et al., 1998; Coates et al., 1999; Brown et al., 2003; 2005; 2009).

The first objective of this dissertation is to demonstrate denitrification of a nitrate-contaminated groundwater in the City of Glendale, AZ using two pilot-scale reactors: MBfR and PBHR; the results directly compare the performance of the two pilot-scale reactors in two ways. The first is to compare the maximum

surface loading able to simultaneously meet the maximum contaminant levels for nitrate (10 mgN/L) and nitrite (1 mgN/L). The second is to compare effluent water quality directly from the two denitrification reactors and after post-treatment with ozone and filtration with GAC and sand.

2. Fundamentals of Biofilm Reduction of Oxidized Contaminants

2.1 Inoculation

In almost all applications of biological water and wastewater treatment, the reactor is inoculated simply by feeding it with the water to be treated. This approach normally works well because the bacteria that carry out the oxidation or reduction reactions are naturally occurring and common. The accumulation of enough biomass to provide treatment requires a few days to a few weeks, depending on the number of bacteria in the feed water and the growth rate of the relevant bacteria.

In some cases, the bioreactor is inoculated with a special culture of bacteria, often obtained from another bioreactor of the same type and achieving the same treatment goal. Per California Department of Public Health (CDPH) requirements (for nitrate/perchlorate systems), any special inoculation used for a biological drinking water treatment system must be "identified and characterized as not containing human pathogens" (Brown et al. 2009). Special inoculation is used to lower the startup time, to ensure that specialized bacteria are present, or both. Whether or not special inoculation is used, the conditions in the bioreactor must be maintained in the optimal range for the metabolism, proliferation, and

accumulation of the desired microorganisms. This includes providing the correct type and amount of electron donor, electron acceptor, nutrients, and pH control (as described below).

2.2 Electron donor supply

The key to any biological process is accumulating a sufficiently large mass of microorganisms that bring about desired reactions. Growing and maintaining active microorganisms require that the microorganisms have available to them three basic materials: an electron donor, an electron acceptor, and nutrients (Rittmann and Huck, 1989; Rittmann and McCarty, 2001). Because biological processes used for drinking-water preparation and other aspects of environmental control must operate continuously for extended periods of time, these basic materials must be supplied on a regular basis.

In biological treatment of nitrate, perchlorate, and TCE, the contaminants to be removed serve as the electron acceptors. The addition of an external electron donor is always required in drinking water treatment or tertiary wastewater treatment. Depending on the biological approach in use, the donor could be an organic compound (*e.g.*, acetate, ethanol, or methanol), H_2, or a reduced sulfur compound (*e.g.*, S^{2-}, HS^-, H_2S, S, $S_2O_3^{2-}$, SO_3^{2-}, or $S_4O_6^{2-}$) (Lampe and Zhang, 1996).

The required dose of the electron donor is stoichiometrically related to the loading of the contaminant(s). The stoichiometric reactions can be obtained using the method established in Rittmann and McCarty (2001). Eq. 1.1(a & b)

gives example stoichiometric reactions in which ethanol is the electron donor and nitrate and oxygen are the electron acceptors. The ethanol dose can be estimated using Eq. 1.2, which is derived from Eq. 1.1(a & b)

$$NO_3^- + 0.659CH_3CH_2OH + H^+ = 0.437N_2 + 0.127C_5H_7O_2N + 2.033H_2O + 0.684CO_2 \quad \text{(Eq. 1.1(a))}$$

$$O_2 + 0.617CH_3CH_2OH + 0.122NO_3^- + 0.122H^+ = 0.122C_5H_7O_2N + 0.626CO_2 + 1.487H_2O \quad \text{(Eq. 1.1(b))}$$

$$C_{CH_3CH_2OH} = 1.13\ N_{NO_3^-} + 0.46\ DO_{in} \quad \text{(Eq. 1.2)}$$

where:

$C_{CH_3CH_2OH}$ = CH_3CH_2OH requirement (mg C/L)

$N_{NO_3^-}$ = target NO_3^- removal (mg N/L)

DO_{in} = dissolved O_2 in the influent (mg O_2/L)

Electron donors should be supplied according to stoichiometry. Under-dosing causes insufficient contaminant removal efficiency and/or the accumulation of intermediates, since the donor is depleted before the reduction reactions can be driven to completion. Over-dosing results in the leakage of biodegradable donor to the effluent, making the water biologically unstable and increasing the load on downstream biofiltration (Rittmann and Snoeyink, 1984; Rittmann and Huck, 1989). In severe cases of over dosing, sulfate reduction may occur. This results in the formation of sulfides, which have a strong rotten-egg odor and can also cause serious color and corrosion problems.

2.3 Nutrients supply

Nutrients are the precursors to the building blocks of cell mass. Although many micronutrients are required in trace amounts, the major nutrients are C, N, P, and S (Rittmann and Huck, 1989; Rittmann and McCarty, 2001). The nutrient requirements can be estimated using the stoichiometric reactions and the ratios among the major nutrients in the biomass. For example, the stoichiometric phosphate requirement (Eq. 1.3) in heterotrophic denitrification is estimated using Eq. 1.1(a & b) to obtain the N incorporated into biomass and then assuming N:P = 5:1 (g:g) for P in biomass (Rittmann and McCarty, 2001).

$$P_{CH_3CH_2OH} = 0.025\, N_{Rem} + 0.011 DO_{in} \qquad \text{(Eq. 1.3)}$$

where:

$P_{CH_3CH_2OH}$ = phosphate requirement (mg P/L in the influent)

If the nutrient concentration in the water to be treated is lower than the estimated stoichiometric requirement, then external nutrient addition is required.

In most heterotrophic reactors, the organic electron donor also is the carbon source. The dose of the organic electron donor estimated in "Electron donor supply" includes its usage as the carbon source (*e.g.*, Eq. 1.1(a & b) and Eq. 1.2). In autotrophic reactors, the carbon source is the inorganic carbon (CO_2, HCO_3^-, and CO_3^{2-}), and its concentration in natural waters usually is sufficient to supply the small demand for carbon.

2.4 Biofilm management

Maintaining enough microorganisms to carry out the biological processes is essential to successful treatment; excessive biofilm, however, can lead to the plugging of media, which reduces the effective biofilm area, exacerbates short-circuiting, and increases mass-transport resistance and head loss (Adham et al., 2004; Lee and Rittmann, 2003). Each of these can result in decreased performance of the system.

To prevent the problems of excess biomass in biological reactors, it is possible to adapt the most effective backwashing strategy established for non-biological reactors -- simultaneous use of air (or N_2) and water at sub-fluidization velocities to achieve collapse pulsing conditions (Amirtharajah, 1993; Urfer et al., 1997). Research supports that backwashing does not lead to an excessive loss of biofilm during backwashing or to an impairment of contaminant-removal performance (Urfer et al., 1997; Hozalski and Bouwer, 1998; Choi et al. 2007).

Most treatment plants use nonchlorinated backwash water for their biological reactors; others are operated with chlorinated backwash water, often intermittently (Urfer et al., 1997). Although disagreement exists on the effects of using chlorinated backwash water (Miltner et al., 1995; Miltner, 1996), the general understanding is that using chlorinated backwash water leads to more removal of biomass, but no major loss of contaminant-removal performance. However, the duration of the backwashing procedure, *i.e.*, the period of Cl_2 exposure (similar to the contact time concept for disinfection), and Cl_2 concentration in the backwash water are the relevant factors. Thus, vigorous

backwashing for a short period of time might be preferable to a longer, less powerful backwashing procedure if the backwash water contains Cl_2 (Urfer et al., 1997).

2.5 The most fundamental design parameter

While the fiber-surface loading is the most fundamental design parameter for the MBfR, the literature is inconsistent in the most fundamental design parameter for heterotrophic reactors. In the previous studies and applications, empty-bed contact time (*EBCT*) and volumetric loading (*VL*) are the most widely used design criteria for heterotrophic reactors. However, several researchers have used the carrier-surface loading (*SL*) as the design criterion (Ergas and Rheinheimer, 2004; Welander and Mattiasson, 2003; Rittmann and McCarty, 2001; Silverstein and Carlson, 1999; Mohseni-Bandpi et al., 1999; Rusten et al., 1995; Vrtovšek and Roš, 2006).

The second objective of this dissertation is to evaluate which parameter is most fundamental in design of heterotrophic reactors; this is especially interesting in drinking-water denitrification, since the criterion of limiting nitrate loading is usually the concentration of effluent nitrite, an intermediate of nitrate reduction.

2.6 pH control

pH control is of great importance due to three factors. First, some biological processes change the pH of the water by adding or consuming

alkalinity. Denitrification adds one equivalent of strong base per mole of NO_3^- that is reduced to N_2. TCE reduction adds three equivalent of strong acid per mole of TCE that is reduced to ethene. Second, an optimal pH range exists for biological activity; a pH outside the optimal range will slow the biological reactions and can lead to process failure in extreme cases. Third, high pH is associated with precipitation. Precipitates generally have a negative impact on the biological processes, since the build-up of mineral solids inside the biofilm can lead to increases in mass-transport resistance, medium clogging, and poor flow distribution (Lee and Rittmann, 2003).

When problems associated with pH change are significant, pH control is necessary. In denitrification reactors, the pH can be controlled using either of two methods: One is to add acid (*e.g.*, HCl) in the influent at a concentration that balances excessive base production from denitrification (method 1); the other is to sparge CO_2 into the reactor to control the pH in the reactor at a set point using a pH-control loop (method 2) (Adham et al. 2004).

Though the significance of pH control has been well established in the literature and the two pH-control methods have been proposed (Kurt et al. 1987; Janda et al. 1988; Lee and Rittmann 2003; Adham et al. 2004; Baeseman et al. 2006; Sengupata and Ergas 2006; Ziv-El and Rittmann 2009b), pH-control models for denitrification have not been reported previously. A reliable pH-control model should be able to predict the alkalinity, pH, and precipitation risk within the denitrification reactor. Furthermore, the model should have the ability to estimate the acid concentration in the influent in method 1 and the pH set point

in method 2. Therefore, the third objective of this dissertation is to construct and experimentally test such a model. The method for constructing the pH-control model for denitrification can also be used to construct a model for TCE reduction, but this is not studied in this dissertation.

2.7 Simultaneous reduction of two oxidized compounds.

Co-occurrence of two or more oxidized compounds such as nitrate, perchlorate, TCE, oxygen, and sulfate are common. Since they are all respiratory electron acceptors, they may affect the reduction of each other. Therefore, I investigate simultaneous reduction of the following three combinations of oxidized compounds in the MBfR: nitrate and perchlorate, nitrate and sulfate, and nitrate and TCE.

2.7.1 Nitrate and perchlorate

Simultaneous removal of nitrate and perchlorate, two commonly co-occurring contaminants, can occur in an MBfR by growing autotrophic H_2-utilizing bacteria as a biofilm in the MBfR (Nerenberg et al., 2002; Rittmann et al., 2007). Two key types of autotrophs in the MBfR are denitrifying bacteria (DB), which only reduce nitrate, and perchlorate-reducing bacteria (PRB), which can reduce nitrate and perchlorate. The distinction between DB and PRB reflects the fact that, while some bacteria capable of reducing nitrate cannot reduce perchlorate, most bacteria capable of reducing perchlorate can reduce nitrate

(Shanmugam et al, 1992; Kengen et al., 1999; Giblin and Frankenberger, 2001; Okeke et al., 2001; Chaudhuri et al., 2002; Nerenberg et al., 2002; Xu et al., 2004).

In an MBfR, three operating conditions -- H_2 pressure, nitrate loading, and perchlorate loading -- control the nitrate and perchlorate removals either by directly affecting the reduction kinetics or by influencing the distribution of DB and PRB in the biofilm (Nerenberg et al., 2002; Rittmann et al., 2007). The control can occur through the action of four competition and promotion mechanisms.

Mechanism 1 is competition for H_2. The H_2 pressure controls the availability of H_2, which drives denitrification and perchlorate reduction for PRB; this creates competition for H_2 within PRB and between denitrifiers and PRB. Competition for H_2 occurs only when the H_2 delivered is less than the H_2 required to reduce all nitrate and perchlorate.

Mechanism 2 is promotion of the growth of PRB through their utilization of nitrate. Simultaneous nitrate and perchlorate reductions benefit PRB, because PRB synthesize more biomass by simultaneously using two electron acceptors (nitrate and perchlorate) (Nerenberg et al., 2006).

Mechanism 3 is competition between nitrate and perchlorate for the same resources within PRB: electrons and possibly reductase enzymes (Hochstein and Tomlinson, 1988; Shanmugam et al, 1992; Kengen et al., 1999).

Mechanisms 4 is competition for space in the biofilm. H_2 pressure and the nitrate and perchlorate loadings collectively control the biofilm thickness, which affects the competition of DB and PRB for space in a biofilm. For example,

locations near the H_2-delivering substratum are advantageous for H_2-oxidizing bacteria.

Due to multiple bacterial species, substrates, and mechanisms, the links between the operating conditions and nitrate and perchlorate removal are not straightforward. Therefore, multi-species biofilm modeling is advantageous for quantitatively integrating the microbiological and physical phenomena that control competition and promotion in biofilms in which nitrate and perchlorate reductions must occur simultaneously. Because MBfRs often operate consistently for months to years, their steady-state performance is of particular interest.

Hence, the fourth objective of this dissertation is to develop a biofilm model that represents how the three important operating conditions affect nitrate and perchlorate reductions in the steady-state biofilm of an MBfR via the four mechanisms. While the model is founded on well-accepted principles, I expand on previous biofilm models by explicitly considering how three important operating conditions control nitrate and perchlorate removal via the four mechanisms, by improving previous simulation of gas delivery through the membrane substratum, and by setting up boundary conditions to allow solving the model directly for steady-state (Eberl et al., 2006; Wanner and Gujer, 1985, 1986; Rittmann and Manem, 1992; Laspidou and Rittmann, 2002a, 2002b, 2004a, 2004b).

A few researchers modeled gas delivery in membrane biofilm reactors (Debus and Wanner, 1992; Matsumoto et al., 2007; Merkey, 2008; Kumar et al., 2010). Debus and Wanner (1992) and Merkey (2008) described gas transfer

through the membrane using Fick's first law. Merkey (2008) employed the gas-diffusion coefficient (L^2T^{-1}, in which, L is length and T is time) and assumed that the gas concentration in the bulk liquid is zero and that the gas concentration in the fiber's inner surface equals its concentration in the fiber lumen. While the first assumption underestimates the gas concentration in the biofilm, since the gas can possibly penetrate the biofilm, the second assumption overestimates the gas concentration in the biofilm, since the gas dissolution from the bulk gas into the fiber is neglected. Debus and Wanner (1992) employed the membrane mass-transfer coefficient ($L^4T^{-1}L^{-2}P^{-1}$, in which, P is pressure), but did not report the detailed modeling approach for gas-transfer. Matsumoto et al. (2007) and Kumar et al. (2010) used an overall gas-transfer coefficient (LT^{-1}), which depends on the operating conditions and should be measured *in situ*. Here, I use the H_2-permeation coefficient. The two assumptions in Merkey (2008) are not needed, and the H_2-permeation coefficient only depends on the fiber type.

2.7.2 Nitrate and sulfate

Sulfate is a common oxidized compound in water and wastewater. Its reduction normally should be prevented, since sulfate reduction produces an odorous and potentially toxic gas, hydrogen sulfide. Also, sulfate reduction consumes externally added electron donors. When sulfate and nitrate are present in the same water, it is important to operate the reactors to favor nitrate reduction while eliminating sulfate reduction. A few experiments were conducted to investigate the onset of sulfate reduction in an MBfR for dentrification (e.g., Ziv-

El and Rittmann, 2009a; Tang et al, 2010). While these case studies concluded that sulfate reduction occurs when nitrate is almost completely reduced, no framework is available to systematically and quantitatively evaluate what operating conditions correspond to onset of sulfate reduction. Thus, the fifth objective of this dissertation is to modify the nitrate and perchlorate model to a nitrate and sulfate model to generalize experimental results and to expand beyond the operating conditions in the limited numbers of experiments.

The nitrate and sulfate model is adapted from the nitrate and perchlorate model by replacing perchlorate with sulfate and replacing perchlorate-reducing bacteria with sulfate-reducing bacteria. Since denitrifying bacteria cannot reduce sulfate and sulfate-reducing bacteria cannot reduce nitrate, Mechanisms 2 and 3 in the nitrate and perchlorate model are not relevant in the nitrate and sulfate model.

2.7.3 Nitrate and TCE

TCE sometimes is present in the nitrate-contaminated water. Reductive TCE degradation occurs via the following pathway:

TCE → dichloroethene (DCE) → vinyl chloride (VC) → ethene

DCE can be produced in different forms but *cis*-DCE form constitutes the main part (95%) of DCE produced by anaerobic reductive dechlorination (Chambon et al., 2009). *Dehalococcoides* are the only bacteria known to allow total reduction to ethene (Duhamel et al., 2002; Krajmalnik-Brown et al., 2004). Chung et al. (2008) demonstrated that a denitrifying MBfR can reduce TCE all the way to ethene.

The sixth objective of this dissertation is to study how the operating conditions in an MBfR, including nitrate loading, TCE loading, and H_2 pressure, affect TCE reduction and accumulation of TCE reduction intermediates using a multispecies biofilm model. The nitrate and TCE model is adapted from the nitrate and perchlorate model by replacing perchlorate with TCE, by replacing perchlorate-reducing bacteria with *Dehalococcoides*, and by adding two new dissolved components: DCE and VC. Since denitrifying bacteria cannot reduce TCE and *Dehalococcoides* cannot reduce nitrate, Mechanisms 2 and 3 in the nitrate and perchlorate model are not relevant in the nitrate and TCE model. However, the three chlorinated ethenes compete for electrons from the common electron donor (Garant and Lynd, 1998; Chu et al., 2004; Cupples et al., 2004a; Cupples et al., 2004b; Lee et al., 2004; Yu and Semprini, 2004; Yu et al., 2005; Christ and Abriola, 2007; Popat and Deshusses, 2011). Kinetics tests suggest that the more-chlorinated ethenes inhibit the degradation of the less-chlorinated ethenes, although the less-chlorinated ethenes inhibit the dechlorination of the more chlorinated ethenes only very weakly (Yu and Semprini, 2004; 2005; Popat and Deshusses, 2011). Therefore, I do not consider the weak inhibition in this model. Thus, in the model, TCE inhibits DCE and VC reductions, DCE inhibits only VC reduction, and VC does not inhibit any reductions.

2.7.4 H_2-permeation coefficients in the membrane

The above three multispecies biofilm models have a common and important model input: the H_2-permeation coefficient through the fibers in an MBfR. Because this value is unknown, the seventh objective is to determine the H_2-permeation coefficients of three commonly used MBfR fibers: composite, polyester, and polypropylene. Besides providing model inputs, the results also provide direct guidance to the design and operation of MBfRs, since H_2-permeation coefficients directly control the H_2 fluxes, which determine the maximum loadings of oxidized contaminants.

Gas permeation through polymer membranes is primarily a diffusion-controlled process and can be described using the Fick's first law at a steady state (Christopher et al., 2003; Sethuraman et al., 2009; Kumar et al., 2010):

$$J_m = \frac{D_m}{z_m}(k_m C_{high} - k_m C_{low}) = \frac{k_m D_m}{z_m}(\frac{P_{high}}{RT} - \frac{P_{low}}{RT}) = \frac{K_m}{z_m}(\frac{P_{high}}{RT} - \frac{P_{low}}{RT}) \quad \text{(Eq. 1.4)}$$

in which

J_m	= gas flux through the membrane	g/m^2-d
D_m	= gas diffusion coefficient in the membrane	m^2/d
z_m	= membrane thickness	m
k_m	= gas solubility coefficient in membrane	dimensionless
C_{high}	= gas concentration on the membrane surface (higher pressure side)	g/m^3
C_{low}	= gas concentration on the membrane surface (lower pressure side)	g/m^3
P_{high}	= gas pressure on the higher pressure side	atm

P_{low}	= gas pressure on the lower pressure side	atm
T	= temperature	K
R	= universal gas constant	8.31×10^{-5} m^3-atm /K-mol (Crittenden et al., 2005)
K_m	= gas permeation coefficient	m^2/d

The permeation coefficient in Eq. 1.4 (K_m) can be determined once the operating conditions (P_{high}, P_{low}, T, z_m) are known and the gas flux (J_m) is measured. The gas flux (J_m) can be calculated by measuring the gas flow rate using a flow meter in the time-lag method (Heilman et al., 1956; Christopher et al., 2003; Kumar et al., 2010) or by measuring the current density in the electrochemical method (Ogumi et al., 1984; Parthasarathy et al., 1991; Sethuraman et al., 2009).

In this work, I determined the H_2-permeation coefficient by conducting steady-state permeation experiments and analyzing the results with a mathematical model. My method differs from the time-lag method in that the gas flow rate measurement is not required in our experiment; this increases the accuracy, since the gas flow rate is too small to be measured accurately. My method differs from the electrochemical method in that our experimental set up is simpler, because it avoids using a fuel cell test station.

3. Research Objectives

In sections 1 and 2, I introduced biofilm reduction of oxidized contaminants, reviewed the fundamentals, and identified seven objectives of this dissertation. In Table 1.1, I summarize the objectives, the chapters that address each of them, and my first-author journal articles from which the chapters are adapted.

Table 1.1 Summary of objectives, chapters, and publications

Objective	Chapter	Publication
1	2	Tang et al., 2010
1	3	Tang et al., 2011a
1	4	Tang et al., 2012a
2	5	Tang et al., 2011a
3	6	Tang et al., 2011b
4	8	Tang et al., 2012c,d
5	9	Tang et al., 2012d
6	10	
7	7	Tang et al., 2012e

The first objective is to demonstrate denitrification of a nitrate-contaminated groundwater in the City of Glendale, AZ using two pilot-scale reactors: MBfR and HPBR. I directly compare the performance of two pilot-scale reactors. Chapter 2 (Bioreduction of nitrate in groundwater using a pilot-scale H_2-based membrane biofilm reactor) discusses the methods and results of the MBfR test. Chapter 3 (Bioreduction of nitrate in groundwater using a pilot-scale packed-bed heterotrophic reactor) discusses the methods and results of the PBHR test. The performance of the two pilot-scale reactors is compared in Chapter 4 (Comparison of heterotrophic and H_2-based autotrophic denitrification

of groundwater). Chapters 2, 3, and 4 are adapted from Tang et al. (2010, 2011a, and 2012a), respectively.

The second objective is to evaluate which parameter (EBCT, VL, or SL) is most fundamental in design of heterotrophic denitrification reactors. This objective is achieved in Chapter 5 (Using carrier-surface loading to design heterotrophic denitrification reactors), which is adapted from Tang et al. (2011a).

The third objective is to construct and experimentally test a model to predict pH change in denitrification reactors; this is discussed in Chapter 6 (A pH-control model for heterotrophic and H_2-based autotrophic denitrification), which is adapted from Tang et al. (2011b).

The fourth objective is to develop a biofilm model that represents how the three important operating conditions affect nitrate and perchlorate reductions in the steady-state biofilm of an MBfR via four mechanisms. This is discussed in Chapter 8 (A multispecies biofilm model for simultaneous reduction of nitrate and perchlorate). This chapter is adapted from Tang et al. (2012b,c).

The fifth objective is to modify the nitrate and perchlorate model into a nitrate and sulfate model and use it to systematically study how operating conditions affect the onset of sulfate reduction in a denitrifying MBfR. This is discussed in Chapter 9 (A multispecies biofilm model for simultaneous reduction of nitrate and sulfate), which is adapted from Tang et al. (2012d).

The sixth objective is to modify the nitrate and perchlorate model into a nitrate and TCE model and use it to investigate how operating conditions affect TCE reduction and accumulation of TCE reduction intermediates. This is

discussed in Chapter 10 (A multispecies biofilm model for simultaneous reduction of nitrate and TCE).

The seventh objective is to test the H_2-permeation coefficients of three fibers commonly used in the MBfR and use them as inputs for the three multispecies biofilm models. This is discussed in Chapter 7 (H_2-permeation coefficients of the fibers used in H_2-based membrane biofilm reactors), which is adapted from Tang et al. (2012e).

Because Chapter 1 provides the background information for each objective, I begin Chapters 2 – 10 directly with the methods I used to achieve the objectives.

Chapter 2

BIOREDUCION OF NITRATE IN GROUNDWATER USING A PILOT-SCALE H_2-BASED MEMBRANE BIOFILM REACTOR

The main goal of this chapter is to demonstrate denitrification of of a nitrate-contaminated groundwater in the city of Glendale, AZ using a pilot-scale H_2-based membrane biofilm reactor (MBfR). Relevant background information was presented in pages 1-4 in Chapter 1. This chapter (Chapter 2) presents the materials, methods, results, and discussion. The main results include groundwater characteristics, maximum nitrate surface loading of the MBfR, and H_2-utilization efficiency in the MBfR.

This work was published in Tang et al. (2010). I led the effort in reactor operation and maintenance, sampling and analysis, and prepraring technical documents such as literature review, experimental plan, weekly reports, and final report for the pilot test. Michal Ziv-El, Chen Zhou, Junghun Shin, and Changhoon Ahn (all at Arizona State University), Daniel Candelaria (CH2M Hill), and David Friese and Ryan Overstreet (APTwater) mainly contributed to reactor operation and maintenance, sampling, and analysis. Bruce E. Rittmann (Arizona State University), Kerry Meyer (CH2M Hill), and Rick Scott (City of Glendale) administered and supervised the pilot study.

1. Materials and Methods

1.1 MBfR configuration and operation

The pilot-scale MBfR was leased from Applied Process Technology, Inc. and operated from May 2008. The pilot-scale MBfR (Figs. 2.1 and 2.2) consisted of two cylindrical modules connected in series, each housing approximately 40,000 hollow polyester fibers (Applied Process Technology, Inc., Pleasant Hill, California) pressurized with H_2 between 0.68 and 2.72 atm; the H_2 diffused through the membrane walls, and water flowed radially outward from a perforated core tube, perpendicularly past the collection of fibers (Fig. 2.2). A biofilm inoculated with bacteria solely from the raw groundwater developed on the surface of the fibers using H_2 as the electron donor and the primary oxidized compounds in the groundwater, O_2 and NO_3^-, as electron acceptors. Because the natural groundwater did not have enough phosphate to support the nutrient requirements of the autotrophic bacteria responsible for denitrification, phosphoric acid was dosed to the influent just above the stoichiometric requirement; the acid was added using a peristaltic pump and an inline static mixer. The influent water flow was 1.1 - 4.2 L/min, and the water was recirculated through each module at 19 -38 L/min in order to increase mass transport to the biofilm and aid in formation of a dense, thin biofilm necessary for optimal operation.

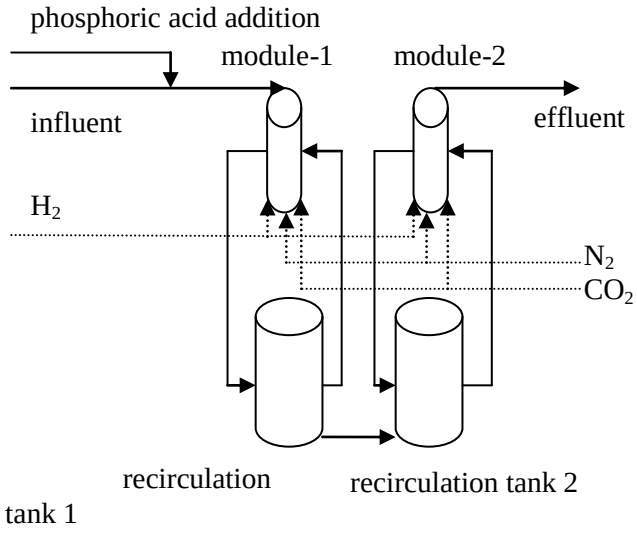

Fig. 2.1 Schematic of the pilot-MBfR system

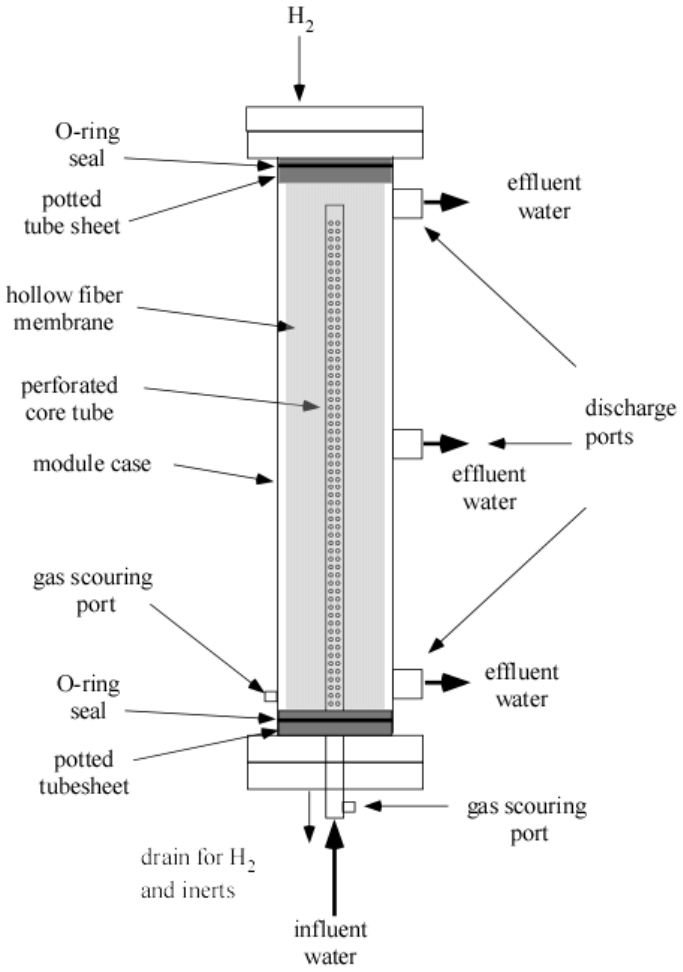

Fig. 2.2 Schematic of a pilot-MBfR module

To dislodge and remove excess biomass, every 1 - 2 h the modules were sparged with N_2 gas for approximately two seconds with the N_2 gas flowing in the forward flow direction and then reverse flow direction. This was followed by an increased recirculation rate of 114 L/min for 5 - 10 min.

The second step of denitrification, reducing NO_2^- (nitrite) to N_2 gas, adds alkalinity. In a system that is not well buffered, this can result in accumulation of calcium precipitates on the fibers and cause fouling. To off-set the alkalinity addition, the pH in the reactor was monitored and maintained at 7.0

by controlled addition of carbon dioxide gas (CO_2). Except for the phosphoric-acid addition, reactor operation was controlled by a programmable logic controller (PLC) with an attached touch-screen operator interface terminal. The PLC included a data-logging system that collected and stored various operational and water quality parameters, e.g., pH and H_2 flow rate.

A summary of the key operating conditions throughout the pilot testing are in Table 2.1. The MBfR was inoculated on May 2, 2008 at a feed rate of 1.1 L/min and at a H_2 pressure of 1.7 atm (beginning of phase 1). Denitrification was insignificant until August 1, when phosphoric acid was first added to the influent water (beginning of phase 2). Then, complete nitrate and nitrite reduction occurred within 7 d. Then, the raw-water feed rate was incrementally increased from 1.9 to 4.2 L/min between September 11 and November 18.

Table 2.1 MBfR operations summary

	Phase 1: Phosphate Limitation (5/2–8/1)	Phase 2: Feed-Rate Increase (8/1–11/18)
raw water flow rate (L/min)	1.1	1.1-4.2
equivalent nitrate demand (mg N/L)	13.4	13.4
reactor diameter (cm)	15.2	15.2
reactor height (cm)	76.2	76.2
reactor volume (m^3)	0.014	0.014
number of stages (reactors)	2	2
fiber specific surface area (m^2/m^3)	1310	1310
total fiber surface area (m^2)	36.4	36.4
nitrate[a] surface area loading rate (g N/m^2-d)	0.6	0.6-2.2
nitrate[a] volume loading rate (kg N/m^3-d)	0.8	0.8-2.9
hydrogen pressure (atm)	Fig. 2.4	Fig. 2.4
phosphoric acid concentration after dosing (mg P/L)	< 0.01	0.15 ± 0.05

Notes:
a) Reflects demand of both nitrate (11.8 mg N/L, from Table 2.2) and oxygen (4.5 mg O_2/L, from Table 2.2). Note that mg O_2/L/2.86 = mg NO_3^--N/L.

As in most biofilm processes, the critical description of MBfR performance is the surface loading of the contaminating oxidized compound, in this case nitrate. Surface loading is defined as $QS°/A_m$, where Q = the influent flow rate, S ° = the influent equivalent oxidized compound demand (Table 2.2), and A_m = the fiber surface area. Since almost all the denitrification occurred in Module-1, only loading to this module was considered. The nitrate surface area loadings corresponding to the above flow rates (1.1 - 4.2 L/min) were 0.6 to 2.2 g N/m^2-d. Prior to increasing the flow rate to 4.2 L/min, the fibers in Module-1 required fiber repair, resulting in a 25% reduction in fiber surface area; this

surface area reduction resulted in increase of nitrate surface loading rate from 2.2 to 2.9 g N/m^2-d for the entire system and 4.4 to 5.9 g N/m^2-d based on Module-1, where most denitrification occurred.

1.2 Sampling and analysis

The raw water, Module-1 effluent, and Module-2 effluent were assayed three times per week for nitrate, nitrite, and phosphate and once per week for dissolved oxygen (DO) and sulfate. The methods followed standard procedures listed in Table 2.2. For dissolved H_2, four water samples were taken from each reactor. 2 mL of effluent sample was injected into a 20-mL serum bottle with a N_2 headspace and the headspace H_2 was analyzed with a Reduced Gas Analyzer (Ametek ta3000). The raw water, Module-1 effluent, and Module-2 effluent were assayed for pH, temperature, total dissolved solids (TDS), hardness, alkalinity, and turbidity on a daily basis. The analytical methods for these tests are listed in Table 2.2.

Table 2.2 Raw water characteristics

parameter	mean ± standard deviation	range	units	data points	method
temperature	27.7 ± 1.9	21.5–31.4	°C	101	SM[a] 2550 B
pH	7.6 ± 0.1	7.1–7.9	s.u.	115	SM 4500 H B
TDS	723 ± 53	613–790	mg/L	102	SM 2510 B
turbidity	0.18 ± 0.21	0.03–1.1	NTU	56	SM 2130 B
alkalinity	84 ± 5	72–102	mg/L as $CaCO_3$	115	SM 2320 B
hardness	356 ± 6	337–377	mg/L as $CaCO_3$	115	SM 2340 C
nitrate	11.8 ± 0.9	9.1–14.7	mg N/L	108	EPA[b] 300.1
nitrite	< 0.01	< 0.01	mg N/L	110	EPA 300.1
sulfate	107.6 ± 2.1	104.1–114.6	mg/L	46	EPA 300.1
phosphate	< 0.01	< 0.01	mg P/L	84	EPA 300.1
DO	4.5 ± 0.9	2.7–6.7	mg/L	54	SM 4500 O G
BDOC	< 0.1	< 0.1	mg C/L	5	SM 5310 C

Notes:
a) SM = *Standard Methods for the Examination of Water and Wastewater*, 20th ed.
b) EPA = U.S. Environmental Protection Agency

2. Results and Discussion

2.1 Raw water characterization

Table 2.2 summarizes the raw water characteristics. The raw groundwater nitrate concentration was 11.8 ± 0.9 (mean ± standard deviation) mg N/L, which is higher than the MCL. The nitrite concentration was < 0.01 mg N/L, which is well below the MCL (1 mg N/L). Phosphate and total phosphorus were

below the detection limits (< 0.01 mg PO_4^{3-}-P/L, < 0.02 mg P/L). Since phosphorus is required as a nutrient by the denitrifying bacteria, phosphoric acid was added to the influent water in Phase 2. The stoichiometric requirement, 0.12 mg P/L, was estimated using Eqs. 2.1-2.3 (assuming N:P = 5:1 (mass:mass)) (Rittmann and McCarty, 2001). To ensure that phosphate was not a limiting factor, it was added just above the stoichiometric requirement so that the influent concentration was 0.15 ± 0.05 mg P/L.

$$NO_3^- + 3.03H_2 + 0.229\ CO_2 + H^+ = 0.477N_2 + 0.0458C_5H_7O_2N + 3.37H_2O \quad \text{Eq. 2.1}$$

$$O_2 + 2.39H_2 + 0.0282NO_3^- + 0.141CO_{2(g)} + 0.0282H^+ = 0.0282C_5H_7O_2N + 2.31H_2O \quad \text{Eq. 2.2}$$

$$P_{H_2}\ (\text{mg P/L}) = 0.0092\, N_{Rem} + 0.0025\, O_{Con} \quad \text{Eq. 2.3}$$

where:

P_{H2} = phosphate requirement (mg P/L)

N_{Rem} = target NO_3^- Removal (mg N/L)

O_{Con} = O_2 consumed (mg O_2/L)

The temperature of the raw water ranged between 21.5 and 31.4 ℃. The raw water pH was between 7.1 and 7.9, close to the previously determined optimum range for autotrophic denitrification in the MBfR of 7.7 - 8.6 (Lee and

Rittmann, 2003). Using the average pH (7.6), alkalinity (84 mg/L as $CaCO_3$), calcium (65.7 mg/L as $CaCO_3$), and total dissolved solids (TDS) (723 mg/L), the Langelier Saturation Index (LSI) in the raw water was calculated as 0.27 (Snoeyink and Jekins, 1980). Since the raw water LSI was less than zero, the raw water was slightly under-saturated with $CaCO_3$. Since pH and the LSI increase from base production in hydrogen-based denitrification (Eq. 2.1), CO_2 was sparged in each reactor to maintain a pH of 7.0 in each module to prevent precipitation on the fibers.

2.2 Maximum nitrate surface loading

Denitrification was insignificant until phosphoric acid was added to the influent water, but complete nitrate and nitrite reduction occurred within seven days of P addition. To determine the maximum nitrate surface area loading rates, the feed rate was incrementally increased between September 11 and November 18 from 1.9 to 4.2 L/min (phase 2). The maximum nitrate surface loading was defined as the maximum H_2 pressure that did not cause H_2 bubbling and at which the effluent nitrate or nitrite concentrations just reach their MCLs. The maximum nitrate surface area loading can be estimated using Fig. 2.3, for which the H_2 pressure was 1.7 atm. The influent refers to the raw water, and the effluent refers to Module-1. Since the effluent nitrite concentration approached the MCL (1 mg N/L) at a nitrate surface area loading of 5.9 g N/m^2-d, this was the approximate maximum for 1.7 atm. The bubbleless H_2 pressure recommended by the

manufacture (2.4 atm) is higher than 1.7 atm; thus the loading limit is likely > 5.9 g N/m^2-d, corresponding to a nitrate volume loading rate > 7.7 kg N/m^3-d.

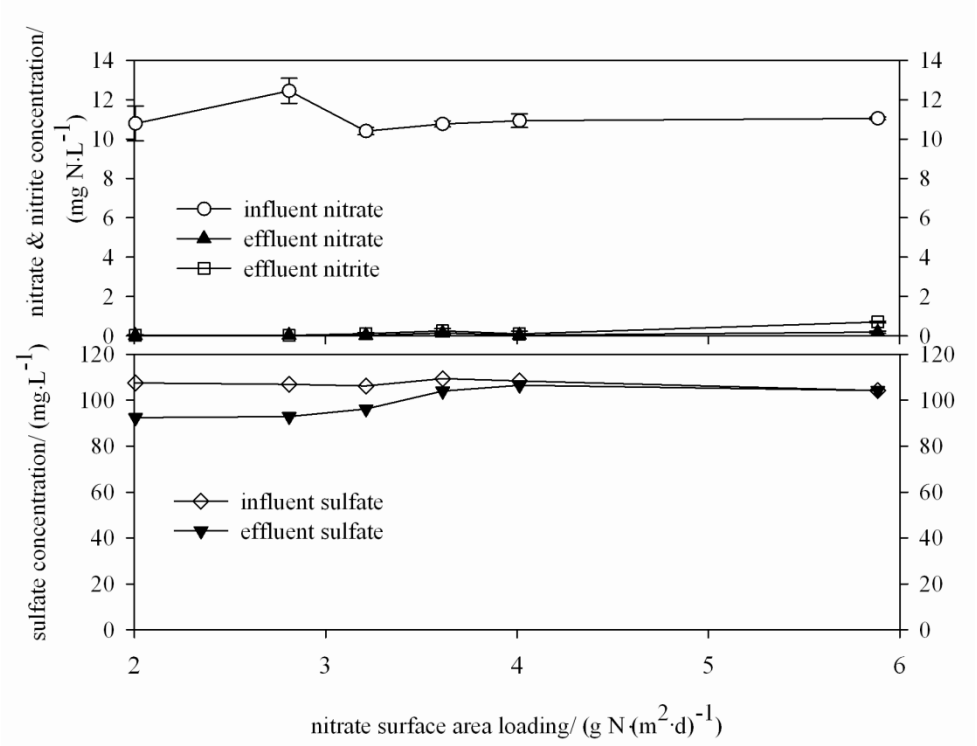

Fig. 2.3 Nitrate, nitrite, and sulfate performance data for the incremental loading increase test. Nitrate and nitrite are on the top plot and sulfate on the bottom (H_2 pressure = 1.7 atm). Note: DO was completely removed at all loadings.

The maximum nitrate surface loading of > 5.9 g N/m^2-d is higher than the highest nitrate surface loading reported in the first-generation MBfRs using composite membranes (2.6 g N/m^2-d in Ziv-El and Rittmann (2009a)). The higher loading associated with the polyester fibers was associated with a higher H_2 pressure inside the fibers, and this is due to the fact that the non-porous layer in the polyester membrane (thickness: 70 μm) is much thicker than the non-porous layer in the composite membrane (thickness: 1 μm). Thus, the H_2 pressure

in this study (1.7 atm) was higher than that in Ziv-El and Rittmann (2009a) (up to 0.65 atm).

2.3 Hydrogen supply and consumption

The H_2 consumption in the reactors was computed using the stoichiometric H_2 requirements from the reductions of nitrate to N_2, O_2 to H_2O, and sulfate to H_2S (Eqs. 2.4 - 2.7).

$$NO_3^- + H_2 = NO_2^- + H_2O \qquad \text{Eq. 2.4}$$

$$NO_2^- + 1.5H_2 \; ^+ H^+ = 0.5N_2 + 2H_2O \qquad \text{Eq. 2.5}$$

$$O_2 + 2H_2 = 2H_2O \qquad \text{Eq. 2.6}$$

$$SO_4^{2-} + 4H_2 + 2H^+ = H_2S + 4H_2O \qquad \text{Eq. 2.7}$$

The actual H_2 supply rate was computed using the measured H_2 flow rate, recorded by the data-logging system, combined with the ideal gas law.

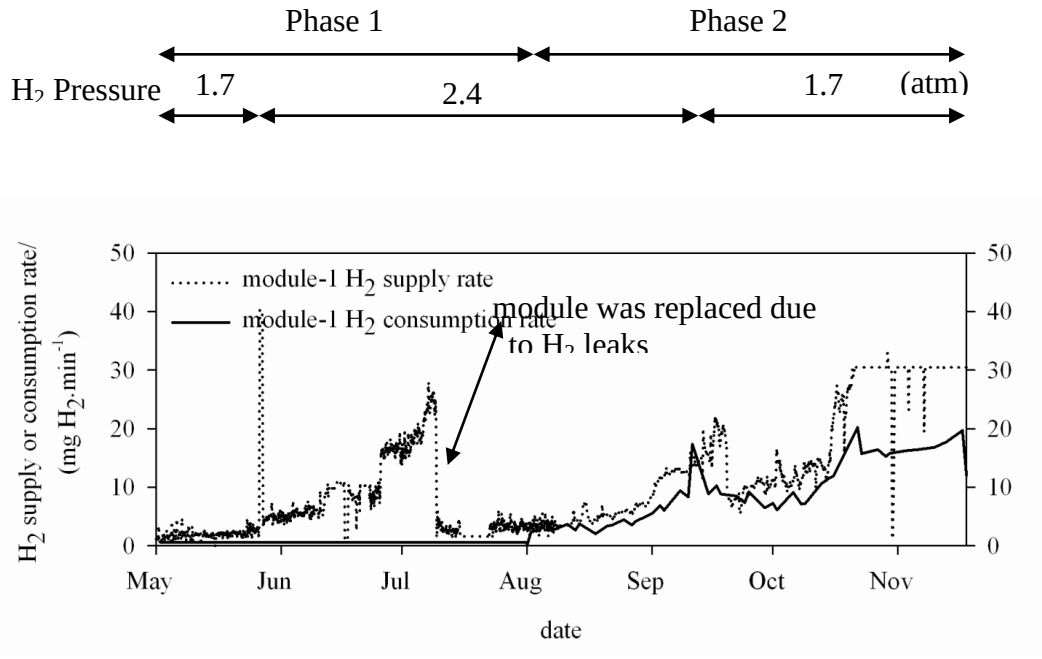

Fig. 2.4 H_2 supply and consumption rates during the entire pilot test for Module-1. (2.4 atm was the bubbleless H_2 pressure. Considering a safety factor of 0.7, the MBfR was operated at a H_2 pressure of 1.7 atm from September.)

Fig 2.4 compares the H_2 supply and consumption rates for Module-1, in which most of the nitrate reduction occurred. For much of the operating time, the supply and consumption lines are nearly coincident. The steady and small deviations can be attributed to two different factors that consume added H_2: (1) Biomass synthesis required reduction of the autotrophs' inorganic carbon source. (2) Oxygen may have intruded into the modules through the recirculation tanks, as the lids of the recirculation tanks were not air-tight. During Phase 1 and again in October and November, the H_2 supply rate was much higher than the consumption rate, eventually reaching the maximum supply rate set by the PLC; this was evidence of broken fibers in the modules, which caused advective, non-

stoichiometric flow of H_2 into the reactor. As long as biofilm was well accumulated on the fibers and H_2 delivery was by diffusion (no bubbling), the actual H_2 utilization rate was close to the stoichiometric rate, or nearly 100% efficient. This was confirmed by the very low effluent H_2 concentration (1-16 μg/L).

3. Conclusions

Once severe phosphate limitation was overcome, the MBfR systems rapidly (within seven days) achieved complete denitrification of NO_3^- to N_2. The steady-state maximum nitrate surface area loadings (> 5.9 g N/m^2-d) was higher than the highest nitrate surface loading reported in the first-generation MBfRs using composite fibers (2.6 g N/m^2-d). The measured H_2 supply rate was only slightly higher than the stoichiometric H_2-utilization rate unless the fibers developed leaks. Thus, H_2 utilization was close to 100% efficient, and H_2 delivery was controlled by diffusion once biofilm accumulated on the polyester-fiber surface and the fibers had no leaks.

Chapter 3

BIOREDUCTION OF NITRATE IN GROUNDWATER USING A PILOT-SCALE PACKED-BED HETEROTROPHIC REACTOR

The main goal of this chapter is to demonstrate denitrification of a nitrate-contaminated groundwater in the city of Glendale, AZ using a pilot-scale packed-bed heterotrophic reactor (PBHR). Relevant background information was presented in pages 1-4 in Chapter 1. This chapter (Chapter 3) presents the materials, methods, results, and discussion. The main results are the nitrate carrier-surface loading limits obtained from two load-increase tests: flow rate increase and influent nitrate concentration increase.

This work was published in Tang et al. (2011a). I led the effort in reactor operation and maintenance, sampling and analysis, and prepraring technical documents such as literature review, experimental plan, weekly reports, and final report for the pilot test. Michal Ziv-El, Chen Zhou, Junghun Shin, and Changhoon Ahn (all of Arizona State University), and Daniel Candelaria (CH2M Hill) mainly contributed to reactor operation and maintenance, and sampling and analysis. Bruce E. Rittmann (Arizona State University), Kerry Meyer, Paul Swaim, and James McQuarrie (CH2M Hill), and Rick Scott (City of Glendale) administered and supervised the pilot study.

1. Materials and Methods

1.1 System configuration and operation

Fig. 3.1 is a schematic of the pilot-scale heterotrophic denitrification reactor, which consisted of two columns (7.6 cm in diameter and 500 cm length) connected in series, each housing buoyant plastic biomass carriers (Siemens ABC 5) with an effective size of 14 mm, a reported effective specific surface area of 660 m^2/m^3, and a bed depth of 3 m. The biomass carriers are made of high-density polyethylene, which has a density of 950 kg/m^3. The total bed volume and biomass-carrier surface area were 0.028 m^3 and 18.3 m^2, respectively. The biofilm colonizing the carriers came solely from bacteria in the feed groundwater, which is the same groundwater as for the MBfR. Because the groundwater did not have enough phosphate to support the nutrient requirements, phosphoric acid was added using a peristaltic pump and an in-line static mixer after day 58. The phosphate addition rate was larger than the stoichiometric dose in order to guarantee that the surface loading loading (*SL*), not phosphate limitation, controlled denitrification performance. The bioreactor influent water flow rate was 1.9 to 7.6 L/min. In order to dislodge and remove excess biomass, the reactors were sparged with N_2 gas every 24 hours at a rate of 20 m^3/m^2-hr for approximately one minute, followed by an upward influent-water flow rate of 80 m/hr for 5 to10 minutes to clear the dislodged solids. Longer backwash times were used for higher loadings. The 24-hour interval was selected based on the experimental observation that delaying more than 24 hours led to head loss that caused malfunctioning of the pump.

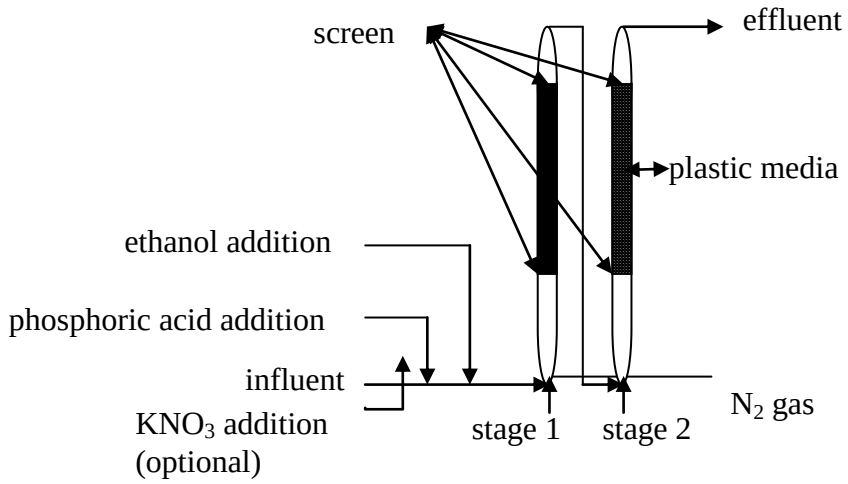

Fig. 3.1 Schematic of the two-stage pilot reactor for heterotrophic denitrification. Note: the KNO_3 addition line was used only in the loading-increase tests, which involved an increased nitrate concentration.

The key operating conditions throughout the pilot testing are summarized in Table 3.1. The reactor was inoculated at a feed rate of 1.9 L/min. Denitrification was insignificant until Day 58, when ethanol and phosphoric acid were dosed above the stoichiometric requirements (from Day 58). The cause for minimal denitrification up to Day 58 was phosphate limitation, as the phosphate concentration in the groundwater was less than 0.01 mg P/L, while ethanol had been supplemented from the start of the run. Complete NO_3^- and NO_2^- reductions occurred by Day 78 and were consistent until Day 94, the end of Phase 1. The flow rate was increased incrementally from 1.9 to 7.6 L/min (between Day 95 and 235, Phase 2), corresponding to an increase in *SL* from 2.0 to 7.9 g N/m^2-d (Table 3.1). During phase 2, ethanol was supplied at the stoichiometric requirement and phosphoric acid was supplied at > 2 times the stoichiometric requirement to make

sure that phosphate was not a limiting factor. In Phase 3 the NO_3^- concentration in the influent was increased from 11.8 mg N/L to 19.6 and 32.1 mg N/L from Day 236 to 257 and the flow rate was 3.8 L/min. The corresponding *SLs* were 4.0, 6.3, and 10.0 g N/m^2-d (Table 3.1). Ethanol and phosphate were supplied above the stoichiometric requirements since the target nitrate concentrations were 25 and 40 mg N/L, but the actual nitrate concentrations were lower than the target concentrations due to inaccurate pumping.

Table 3.1 Operations summary

	Phase 1: start-up (days 1 to 94)	Phase 2: flow rate increase (days95 to 235)	Phase 3: nitrate concentration increase (days 236 to 257)
flow rate (L/min)	1.9	1.9-7.6	3.8
equivalent influent nitrate concentration[a] (mg N/L)	13.4	13.4	21.2-33.7
nitrate[a] *SL* (g N/m^2-d)	2.0	2.0-7.9	6.3-10.0
nitrate[a] *VL* (kg N/m^3-d)	1.3	1.3-5.2	4.2-6.6
EBCT(hour)	0.24	0.06-0.24	0.12
stoichiometric ethanol requirement (mg C/L)	15.4	15.4	24.2-38.3
delivered ethanol (mg C/L)	4.8-20	15.4	30.3-47.3
stoichiometric phosphate requirement (mg P/L)	0.35	0.35	0.68-1.06
phosphate concentration after deliver (mg P/L)	0.17-1.50	0.75-1.50	2.0-3.0

[a]Reflects nitrate (11.8 mg-N/L, from Table 3.2, 19.6, and 32.1 mg-N/L after nitrate increase) and oxygen (4.5 mg O_2/L, from Table 3.2). Note that (mg O_2/L)/2.86 = mg NO_3^--N/L.

1.2 Sampling and analysis

The influent, Stage1 effluent, and Stage2 effluent were assayed daily for pH, temperature, total dissolved solids (TDS), hardness, alkalinity, and turbidity. The same samples were assayed three times per week for NO_3^-, NO_2^-, NH_4^+, and PO_4^{3-}, and once per week for DO, DOC, COD, biodegradable organic carbon (BDOC), and SO_4^{2-}. The methods followed the standard procedures listed in the right column of Table 3.2.

Table 3.2 Groundwater characteristics

parameter	mean ± standard deviation	range	units	No. data points	method
temperature	27.7 ± 1.9	21.5-31.4	^{o}C	101	SM[a] 2550 B
pH	7.6 ± 0.1	7.1-7.9	s.u.	115	SM 4500 H B
TDS	723 ± 53	613-790	mg/L	102	SM 2510 B
turbidity	0.18 ± 0.21	0.03-1.1	NTU	56	SM 2130 B
alkalinity	84 ± 5	72-102	mg/L as $CaCO_3$	115	SM 2320 B
hardness	356 ± 6	337-377	mg/L as $CaCO_3$	115	SM 2340 C
nitrate	11.8 ± 0.9	9.1-14.7	mg N/L	108	EPA[b] 300.1
nitrite	< 0.01	< 0.01	mg N/L	110	EPA 300.1
ammonium	< 0.01	< 0.01	mg N/L	38	EPA 300.7
sulfate	107.6 ± 2.1	104.1-114.6	mg /L	46	EPA 300.1
phosphate	< 0.01	< 0.01	mg P/L	84	EPA 300.1
DO	4.5 ± 0.9	2.7-6.7	mg/L	54	SM 4500 O G
DOC	0.2 ± 0.2	< 0.1-0.5	mg C/L	15	SM 5310 C
COD	3.0 ± 2.0	0.4-4.5	mg/L	10	SM 5220 C
BDOC	< 0.1	< 0.1	mg C/L	5	SM 5310 C

[a]SM = *Standard Methods for the Examination of Water and Wastewater*, 20th ed.
[b]EPA = U.S. Environmental Protection Agency

2. Results and Discussion

2.1 Groundwater characterization

Table 3.2 summarizes the groundwater characteristics. The groundwater was pumped from a well and stored in a tank upstream of the denitrification reactors. The influent NO_3^- concentration was 11.8 ± 0.9 (mean $\pm$ standard deviation) mg-N/L, which is higher than the MCL. The NO_2^- concentration was < 0.01 mg N/L. Ammonium, phosphate, and total phosphorus were below the detection limits (< 0.01 mg N/L, < 0.01 mg PO_4^{3-}-P/L, < 0.02 mg P/L). Since phosphorus is required as a nutrient, phosphoric acid was added to the influent water from Day 58 (within Phase 1). To ensure that phosphate did not limit denitrification kinetics, it was added at > 2 times the stoichiometric requirement during Phases 2 and 3. BDOC in the influent was below the detection limit (0.1 mg C/L). Ethanol was added to the raw water at or greater than the stoichiometric requirement during Phases 2 and 3. The temperature of the raw water ranged from 21.5 to 31.4 ^oC. The raw-water pH was between 7.1 and 7.9 within the previously determined optimum range (7.0-9.0) for denitrification (Rittmann and McCarty, 2001; Janda et al., 1988).

2.2 Nitrate loading limit

Two load-increase tests were conducted by increasing either the flow rate or the influent nitrate concentration. The results are plotted in Figs. 3.2 and 3.3. In the tests increasing the flow rate incrementally from 1.9 to 7.6 L/min, the *SL* increased from 2.0 to 7.9 g N/m^2-d. Ethanol was supplied at the stoichiometric

requirement based on the average influent NO_3^- and DO concentrations over Phase 1. Fig. 3.2 shows that, when the *SL* was less than 6.0 g N/m^2-d, the effluent NO_3^- and NO_2^- concentrations were < 1 mg N/L. However, when the *SL* was increased to 7.9 g N/m^2-d, the effluent NO_3^- concentration increased to approximately 3.3 mg N/L, and the effluent NO_2^- concentration increased to approximately 2.6 mg N/L. Since the effluent NO_2^- was below the MCL (1 mg N/L) when the *SL* was < 6.0 g N/m^2-d and above the MCL when the *SL* was 7.9 g N/m^2-d, the loading limit was between 6.0 and 7.9 g N/m^2-d based on the tests using flow-rate increases.

In the tests increasing the influent nitrate concentration from 11.8, to 19.6, and then to 32.1 mg N/L, the *SL* increased from 4.0, to 6.3, and then to 10.0 g N/m^2-d. Ethanol was supplied at the stoichiometric requirement based on the target influent NO_3^- concentrations (25 and 40 mg N/L), which caused high DOC in the effluent: approximately 5 mg C/L in the 19.6 mg N/L test and approximately 13 mg C/L in the 32.1 mg N/L test. When the *SL* was less than 6.3 g N/m^2-d, the effluent NO_3^- and NO_2^- concentrations were < 1 mg N/L. When the *SL* was increased to 10 g N/m^2-d, the effluent NO_3^- concentration increased to approximately 1.0 mg N/L, and the effluent NO_2^- concentration increased to approximately 2.5 mg N/L. Therefore, the loading limit was between 6.3 and 10.0 g N/m^2-d based on the nitrate concentration increase test. Incomplete denitrification at the highest loading (10.0 g N/m^2-d) also contributed to the high effluent DOC (13 mg C/L), but most (9 mg C/L according to Table 3.1) was a result of over-supplying ethanol.

The loading limits obtained from increases to the flow-rate (between 6.0 and 7.9 g N/m^2-d) and the nitrate concentration (between 6.3 and 10.0 g N/m^2-d) were similar. This loading limit is in the range of the values in literature (1.3 - 10 g N/m^2-d, Chapter 5).

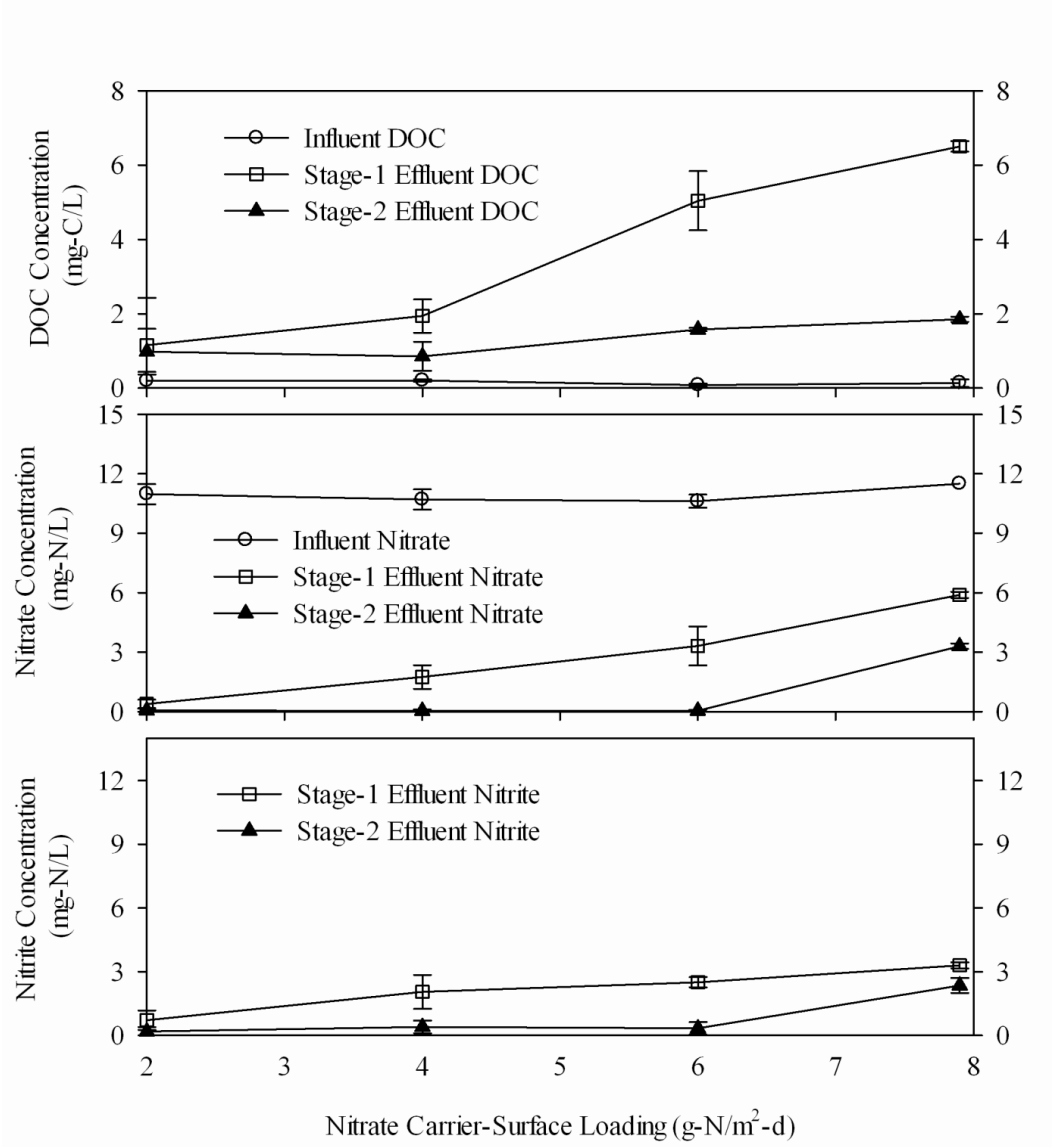

Fig. 3.2 DOC, NO_3^-, and NO_2^- performance data in the test in which the flow rate was increased. Notes:

1) The NO_2^- concentration was negligible in the influent.
2) The DO concentrations were relatively stable around 4.5 mg/L in the influent and close to zero in the effluents.
3) The flow rate was increased from 1.9 to 7.6 L/min.

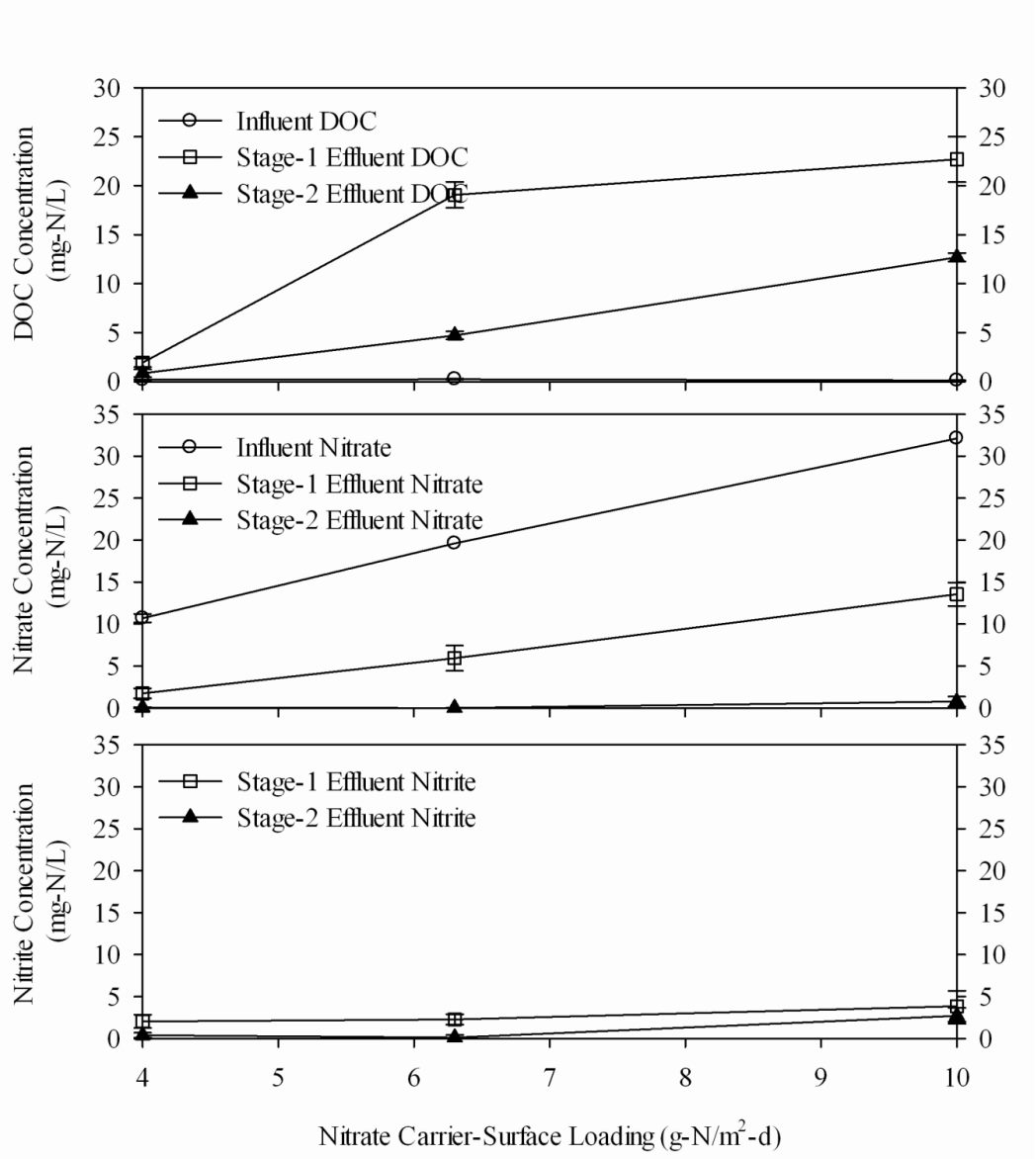

Fig. 3.3 DOC, NO_3^-, and NO_2^- performance data in the test in which the influent nitrate concentration was increased. Notes:

1) The NO_2^- concentration was negligible in the influent.
2) The DO concentrations were relatively stable around 4.5 mg/L in the influent and close to zero in the effluents.
3) The flow rate was 3.8 L/min.

3. Conclusions

Two load-increase tests were conducted to determine the maximum nitrate carrier-surface loading (*SL*) at which the effluent NO_2^- concentration was around the Maximum Contaminant Level. The loading limits obtained using these two means were around 6 g N/m^2-d, which is in the range of 1.3 to 10 g N/m^2-d based on literature reports.

Chapter 4

COMPARISON OF HETEROTROPHIC AND H_2-BASED AUTOTROPHIC DENITRIFICATION OF GROUNDWATER

The main goal of this chapter is to compare the two pilot-scale denitrification reactors (MBfR and PBHR) for maximum loadings, effluent water quality, and the impact of post-treatment on water quality. Relevant background information was presented in pages 1-4 in Chapter 1. This chapter (Chapter 4) presents the materials, methods, results, and discussion. The maximum loadings compared are nitrate volumetric loading and nitrate carrier-surface loading. The water quality parameters compared are nitrate, nitrite, DO, sulfte, DOC, BDOC, HPC, turbidity, ammonium, and pH. The post-treatment train consisted of an ozone-contact tank and a post filter.

This work was published in Tang et al. (2012a). I led the effort in reactor operation and maintenance, sampling and analysis, and prepraring technical documents such as literature review, experimental plan, weekly reports, and final report for the pilot test. Michal Ziv-El, Chen Zhou, Junghun Shin, and Changhoon Ahn (all at Arizona State University), and Daniel Candelaria (CH2M Hill) mainly contributed to reactor operation and maintenance, and sampling and analysis. Bruce E. Rittmann (Arizona State University), Kerry Meyer, Paul Swaim, and James McQuarrie (CH2M Hill), and Rick Scott (City of Glendale) administered and supervised the pilot study.

1. Materials and Methods

1.1 Configuration and operation

Fig. 4.1 is a line diagram of the reactor system. Groundwater containing nitrate at ~12 mg N/L was pumped from a well at the Cholla Water Treatment Plant of the City of Glendale, Arizona, and stored in a raw water storage tank (8 m^3). Downstream of the raw water tank, the piping split to provide influent to the MBfR and PBHR. The MBfR (0.028 m^3) was a two-stage reactor that had polyester fibers for H_2 delivery and biofilm attachment. The PBHR (0.028 m^3) was a two-stage reactor filled with plastic media for biofilm attachment and supplemented with ethanol as the organic electron donor. Effluent from one denitrification reactor at a time was routed to a single post-treatment train, which included an ozone-contact tank (0.01 m^3) followed by a post-filter (0.01 m^3).

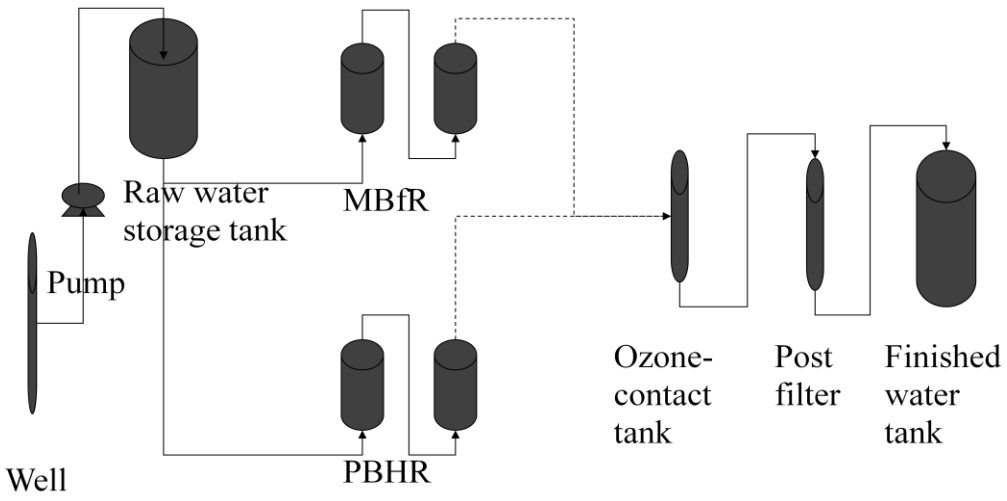

Fig. 4.1 Line diagram of the reactor system.

The groundwater characteristics and denitrification reactor configurations and operations were described in detail in Chapters 2 and 3. Here, I provide the detailed configurations of the post-treatment and operating conditions that correspond to comparison of water quality in the effluents of the two denitrification reactors, the ozone-contact tank, and the post-filter.

The MBfR was operated at a flow rate of 3.8 L/min, corresponding to a nitrate biomass-carrier surface loading of 2.0 g N/m^2-d. The PBHR was operated at a flow rate of 1.9 L/min, corresponding to the same biomass-carrier surface loading of 2.0 g N/m^2-d. This loading was selected because it was the highest value for which both denitrification reactors achieved nearly complete denitrification (Chapters 2 and 3).

Ozone was generated on site and dosed at ~ 2 mg/L for oxygenation and disinfection. The ozone-contact tank was a 10-cm diameter, 120-cm height column and operated at 1.9 L/min, corresponding to an empty bed contact time (EBCT) of 5 minutes. The ozone-contact tank effluent was routed to a 7.5-cm diameter post-filter, which included 180 cm of exhausted granular actived carbon (Filtrasorb F820; effective size of approximately 1.1 mm) over 30.5 cm of coarse sand (effective size of approximately 0.7 mm). The exhausted granular activated carbon (GAC) was from a filter in the Cholla Water Treatment Plant (Glendale, Arizona). The filter had been operated for about 12 months, and the GAC was exhausted when the total organic carbon in the filter effluent reached 2.8 mg C/L; thus. the role of adsorption (but not biodegradation) was minimized. The post-filter was operated at a flow rate of 0.55 L/min, corresponding to an EBCT of 17

minutes and a hydraulic loading of 7.5 m^3/m^2-hr. Water from the ozone-contact that did not go through the post filter was wasted. The objective of post-filtration was to remove biodegradable organic matter and to decrease the turbidity and heterotrophic plate counts prior to final disinfection, although final disinfection was not studied.

1.2 Sampling and analysis for water quality

The methods followed the standard procedures listed in Chapters 2 and 3. For each reactor, the influent, stage-1 effluent, stage-2 effluent, ozone-contact tank effluent, and post-filter effluent were assayed daily for pH, temperature, total dissolved solids (TDS), hardness, alkalinity, and turbidity. The samples were also assayed three times per week for NO_3^-, NO_2^-, NH_4^+, and PO_4^{3-}, and once per week for dissolved oxygen (DO), SO_4^{2-}, heterotrophic plate count (HPC), dissolved organic carbon (DOC), and biodegradable organic carbon (BDOC). To understand the composition of DOC and BDOC, the samples were assayed thirteen times over the course of the study using HPLC (high-performance liquid chromatography) for ethanol and short-chain organic acids, including formate, acetate, butyrate, iso-butyrate, valerate, iso-valerate, caproate, and lactate.

2. Results and Discussion

2.1 Maximum nitrate loadings

The loading limits were documented separately in Chapter 2 for the MBfR and Chapter 3 for the PBHR. Table 4.1 compares the surface and

volumentric loading limits for the two denitrification reactors. In both cases, the loading limit was set by the nitrite MCL of 1 mg N/L. While the PBHR had a higher biomass-carrier surface loading, the MBfR had the higher volumetric loading. The loadings were similar, however, for both systems.

Table 4.1 Maximum NO_3^- loadings[a] to achieve effluent NO_3^- and NO_2^- concentrations below the MCLs[b]

	Biomass-carrier surface loading[c] (g N/m^2-d)	Volumetric loading[d] (kg N/m^3-d)	Influent NO_3^- (mg N/L)	Effluent NO_3^- (mg N/L)	Influent NO_2^- (mg N/L)	Effluent NO_2^- (mg-N/L)
MBfR	5.4	6.9	12.0	< 1.0	< 0.1	1.0
PBHR	6.3	4.0	12.0	< 1.0	< 0.1	1.0

Notes:

a: The maximum loadings were interpolated from the flow-rate-increase tests described in Figs. 2.3 and 3.3. These values correspond to the influent nitrate biomass-carrier surface loading for which the effluent nitrite concentration was the MCL.

b: nitrate MCL = 10 mg N/L; nitrite MCL = 1 mg N/L

c: nitrate biomass-carrier surface loading = QC °/A, where Q is the influent flow rate [L/d], C °is the influent nitrate concentration [g-N/L], and A is the biofilm-carrier surface [m^2].

d: nitrate volumetric loading = QC °/V, where V is the reactor volume [m^3].

2.2 Effluent water quality from the denitrification reactors and impact of post treatment

All of the comparisons of the effluent water quality are for a nitrate biomass-carrier surface loading of 2 g N/m^2-d. This surface loading was selected because it was the highest value for which both denitrification reactors achieved nearly complete denitrification. For this scenario, the influent NO_3^--N and NO_2^--N concentrations were 11.8 $\pm$ 0.4 and < 0.1 mg N/L, respectively, while all effluent NO_3^--N and NO_2^--N concentrations were < 0.1 mg N/L (41 samples).

2.2.1 NO_3^- and NO_2^-

Fig. 4.2 contains the NO_3^- and NO_2^- concentrations in the effluents from the denitrification reactors, ozone tank, and post-filter. The general trend for the NO_3^- concentration was that it was lowest in the denitrification reactors, and then it increased in the ozone contact tank and further in the post-filter. The increase in NO_3^- during post-treatment can be attributed to the release of NH_4^+ from biomass oxidization in the ozone contact tank, its oxidation to NO_3^- during ozonation, and additional biological oxidation in the post-filter. Compared to the autotrophic train, the heterotrophic train had higher NO_3^- concentrations in the ozone-contact tank and post-filter, a result of the higher biomass yield of heterotrophic denitrification (Rittmann and McCarty, 2001), which led to higher turbidity in the PBHR effluent (shown below). For NO_2^- concentrations, all values were below 0.2 mg N/L (The method detection limit is 0.001 mg NO_2^--N/L).

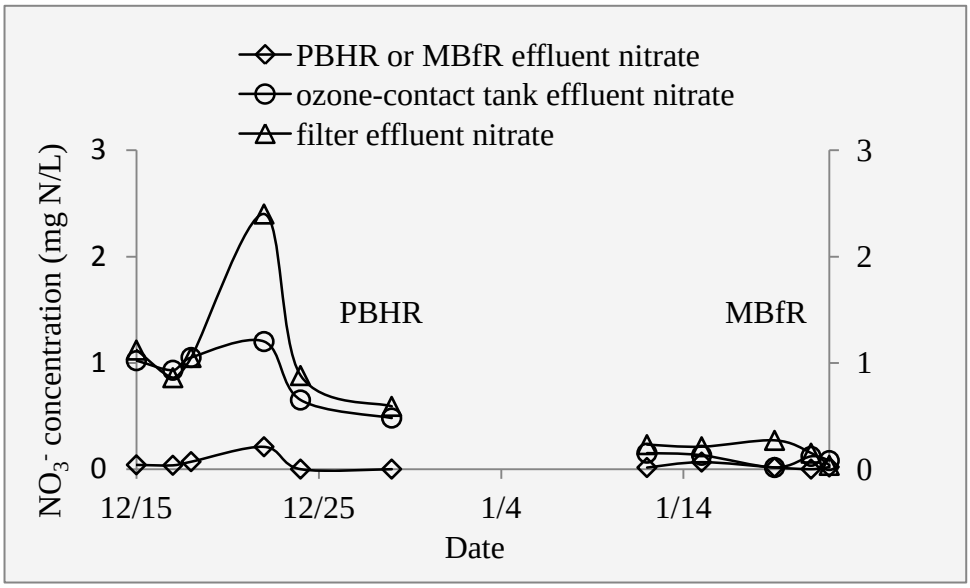

a.

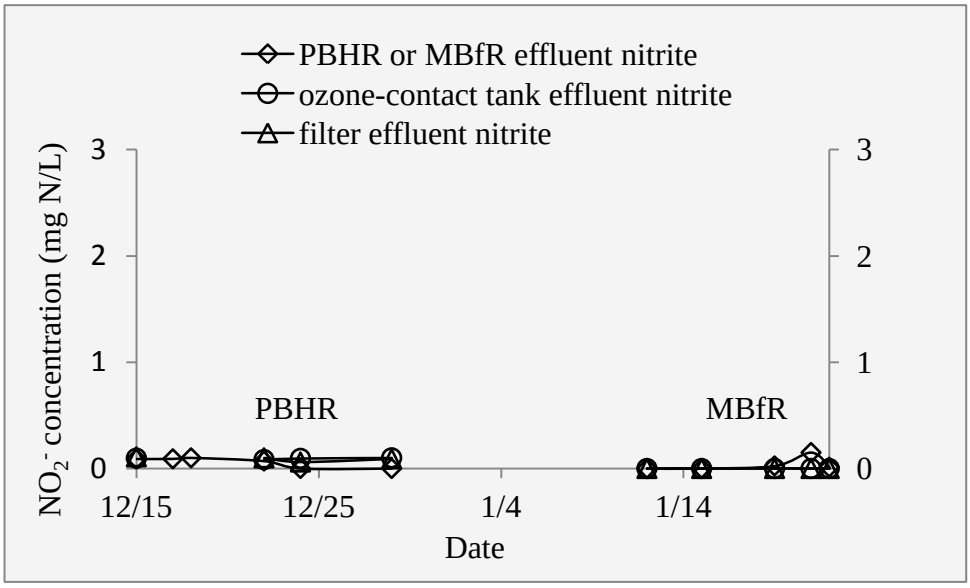

b.

Fig. 4.2 Nitrate and nitrite concentrations in the effluents of the PBHR, MBfR, ozone tank, and post-filter for a nitrate surface loading of 2 g N/m^2-d: a. nitrite, b. nitrate.

2.2.2 DO and sulfate

DO was reduced from 4.5 ± 0.8 to below the method detection limit (0.1 mg/L) in both denitrificaiton reactors (18 samples), and it then increased to ~6 mg/L in the ozone-tank effluent. Since the dose of ozone was < 2 mg/L, most of the DO increase was attributed to oxygen intrusion into the storage tank located between the denitrification reactors and the ozone-contact tank. The sulfate concentration was 108 ± 2 mg/L in the influent and 107 ± 2 mg/L (41 samples) in the effluent of both denitrification systems, indicating negligible sulfate reduction, a result of successfully limiting the electron-donors (H_2 and ethanol) to just enough for complete DO and nitrate reduction.

2.2.3 DOC

Fig. 4.3a shows that the DOC concentration in the influent was approximately 0.2 mg-C/L, increased to approximately 0.4 mg-C/L in the MBfR and to around 1.0 mg-C/L in the PBHR, and after the post-filter decreased to 0.3-0.4 mg-C for both reactors. The DOC increase in the MBfR was from soluble microbial products (SMP) generated by the autotrophic denitrifiers (Rittmann and McCarty 2001). When the MBfR effluent was assayed for short-chain organic acids, only iso-valerate was detected and only in one sample and at a low concentration (< 0.2 mg-C/L). The DOC was substantially higher in the PBHR compared to the MBfR. However, measurements of short-chain organic acids and ethanol indicated that the DOC in the PBHR effluent did not include either organic acids or ethanol. Thus, the DOC in the PBHR effluent was probably SMP

from the heterotrophic denitrifiers. This trend is consistent with the understanding that heterotrophs produce more SMP than do autotrophs (Merkey et al., 2008; de Silva and Rittmann, 2000)

2.2.4 BDOC

The influent contained no BDOC, as seen in Fig. 4.3b. BDOC increased in the MBfR to around 0.2 mg C/L due to SMP production, and its concentration did not change downstream. The BDOC increased to 0.7 mg C/L in the PBHR effluent and decreased to about 0.2 mg C/L through post-treatment. Though BDOC, like DOC, is not regulated, it associated with biomass growth in distribution systems (Rittmann and Snoeyink, 1984; Rittmann and Huck, 1989), and the acceptable concentration of BDOC or DOC depends on the concentrations of chlorine residual in the distribution systems (Woolschlager et al., 2002). While a BDOC concentration of 0.16 mg/L may promote excessive growth of heterotrophs with no chlorine residual, 0.32 mg/L may be tolerable if a chlorine residual of 2 mg/L is maintained throughout the system (Woolschlager et al., 2002). 2 mg Cl_2/L is half of the Maximum Residual Disinfectant Level in the distribution system regulated by U.S. EPA and four times the minimum chlorine residual that utilities must maintain at all points along the distribution network (U.S. EPA, 2009). Thus, the BDOC concentrations in the post-treatment effluents of the post-filter reported here should be acceptable when a chlorine residual of 2 mg/L is maintained. An increase in BDOC and DOC likely increases the

formation potential for disinfection products, which are regulated (Escobar and Randall, 2001).

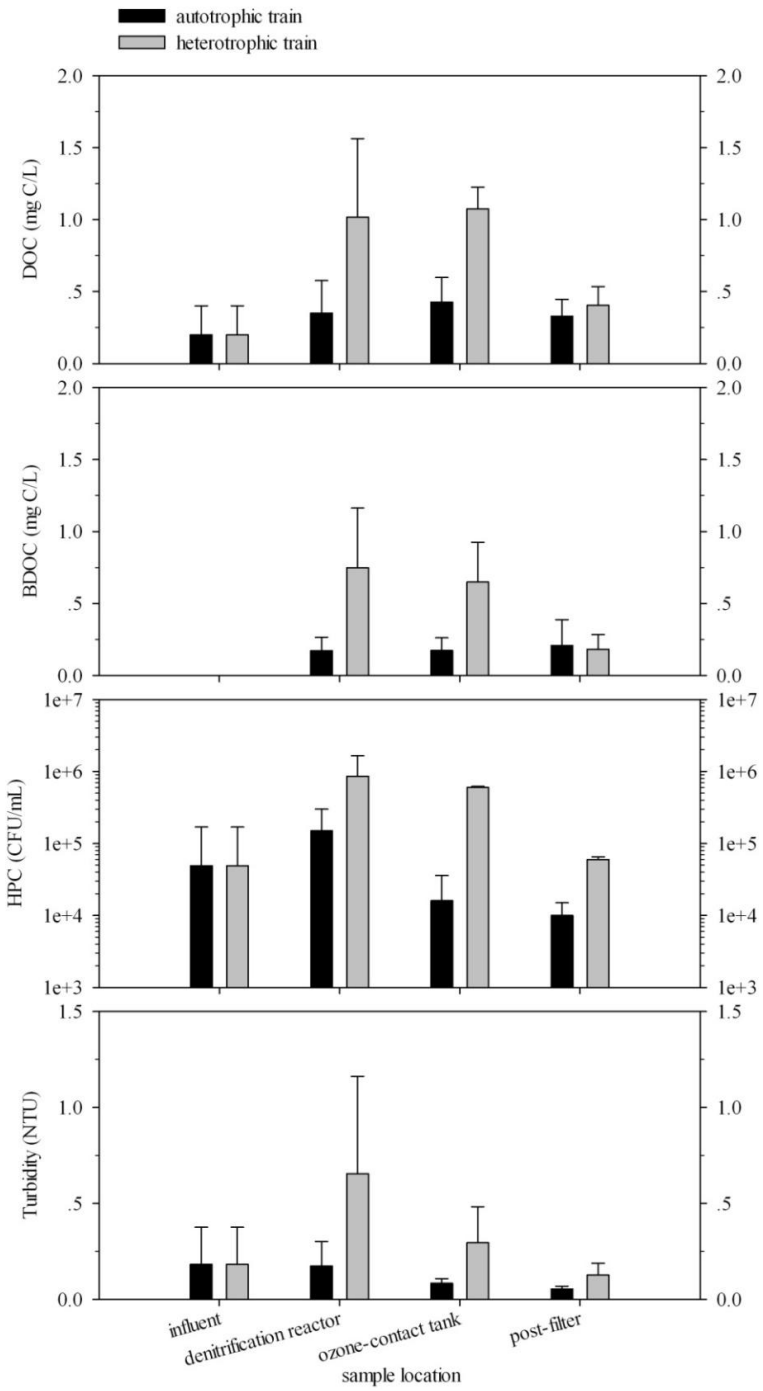

Fig. 4.3 Average and standard deviations of DOC (a), BDOC (b), HPC (c), and turbidity (d) in the influent and the effluents from the denitrification reactors, the ozone-contact tank, and the post-filter for a nitrate biomass-carrier surface loading of 2.0 g N/m^2-d. 4 to 20 samples were taken from each sampling location during the 4-week steady-state operation. The numbers of samples depend on the sampling frequency summarized in the section of Materials and Methods.

2.2.5 HPC

Demonstrated in Fig. 4.3c, the HPC levels in the influent water were approximately $5.0x10^4$ CFU/mL, and they increased to around $2.0x10^5$ CFU/mL in the MBfR and $9.0x10^5$ CFU/mL in the PBHR. Although no external organic substance was added to the MBfR, the HPC increase in the MBfR effluent was possible because heterotrophic bacteria grew by oxidizing SMP released by the autotrophic bacteria. Heterotrophic bacteria can oxidize BDOC while reducing nitrate in the MBfR; thus, their presence is generally associated with improved effluent water quality. The HPC increase in the PBHR was higher than that in the MBfR, an expected result, since all of the denitrifiers in the PBHR were heterotrophic.

The HPC concentrations decreased in the ozone contact tank and post-filter. The HPC concentrations in the effluents of the post-filter were approximately $1.0x10^4$ CFU/mL for the MBfR system and $6.0x10^4$ CFU/mL for the PBHR system. Thus, HPC declined across the autotrophic train and the values were only slightly larger for the heterotrophic train. Since the U.S. EPA requires HPC in drinking water lower than 500 CFU/mL (U.S. EPA, 2009), further disinfection would be required for both trains.

2.2.6 Turbidity

Turbidity (Fig. 4.3d) was about 0.2 NTU in the influent and effluent of the MBfR, and it was about 0.7 NTU in the effluent from the PBHR. Turbidity increased more in the PBHR mainly due to higher biomass production rates for

heterotrophic bacteria compared to autotrophic bacteria (Rittmann and McCarty, 2001). Through ozonation and filtration, the turbidity was reduced to < 0.1 NTU in the autotrophic system effluent and < 0.2 NTU in the heterotrophic system effluent, meeting the U.S. EPA's requirement for filtered water turbidity: ≤ 1 NTU at all times for systems that use conventional or direct filtration, and < 0.3 NTU in at least 95 percent of the samples in any month (U.S. EPA, 2009).

2.2.7 Ammonium

Ammonium, generated from biomass decay, was monitored throughout the study and was detected only in the effluents from the denitrification reactors and only when electron donors were suddenly cut off due to an empty H_2 tank or when the ethanol-supply tubing became clogged. The maximum concentrations detected were 0.3 mg N/L in the MBfR and 1.0 mg N/L in the PBHR, but ammonium was completely removed in the post-filter by nitrification. The ammonium spikes appeared within two days after the electron donors were cut off, and they disappeared within two days after the electron-donor supply was re-instated. (Samples were taken every two days for ammonium analysis.) The ammonium spikes were coincident with the nitrate and nitrite spikes.

2.2.8 pH

The effect of denitrification on pH in the two reactors and the pH-control measures were discussed in Chapter 6. In brief, pH increased more in the

MBfR than in the PBHR. Acid (*e.g.*, HCl) addition is the preferred pH-control method for the PBHR, and CO_2 addition is the preferred method for the MBfR.

3. Conclusions

The maximum nitrate loadings of the MBfR and PBHR to achieve effluent NO_3^- and NO_2^- concentrations below the MCLs were similar: The MBfR had a maximum volumetric loading of 6.9 kg N/m^3-d and a biomass-carrier surface loading of 5.4 g N/m^2-d, while he PBHR had a maximum volumetric loading of 4.0 kg N/m^3-d and a biomass-carrier surface loading of 6.3 g N/m^2-d.

The effluent concentrations of DOC, BDOC, HPC, and turbidity were higher in the PBHR effluent than in the MBfR effluent. However, post-treatment that included an ozone-contact tank and a post-filter brought them to the same level; the finished water met drinking water standards except for HPC, which would require further disinfection. Ammonium was only detected in the denitrification reactor effluents during a sudden cut-off of electron donors, resulting in biomass decay, but ammonium was completely removed by the post-filter.

Chapter 5

USING CARRIER-SURFACE LOADING TO DESIGN HETEROTROPHIC DENITRIFICATION REACTORS

The main goal of this chapter is to evaluate which parameter (EBCT, VL, or SL) is most fundamental in design of heterotrophic denitrification reactors. Relevant background information was presented in pages 9-10 in Chapter 1. This chapter (Chapter 5) first presents the theoretical base for the evaluation and then uses the experimental data from literature and the pilot-scale denitrification plant to support it. This work was published in Tang et al. (2011a). I led the effort in forming the theoretical base, reviewing the literature, and conducting the pilot test. Bruce E. Rittmann mainly contributed to the theoretical base, along with reviewing and revising the manuscript.

1. Theoretical Base

In a completely mixed biofilm reactor (*CMBR*), the steady-state-biofilm model (Rittmann and McCarty, 2001) identifies that the flux into the biofilm (J) of the rate-limiting substrate depends on its concentration in the bulk (S):

$$J = f(S) \qquad \text{Eq. 5.1}$$

The relationship is reciprocal, so that S also can be viewed as a function of J:

$$S = f'(J) \qquad \text{Eq. 5.2}$$

The *f'* relationship makes it possible to relate the effluent substrate concentration, the usual measure of performance success, to a loading factor (*J*) that can be controlled by process design and operation.

The rate-limiting substrate can be identified using the method in Rittmann and Dovantzis (1983) and Williamson and McCarty (1976). The electron acceptor is rate limiting when the following two equations are true, the electron donor is rate limiting when the two equations are false, and dual limitation occurs if one is true and the other is false.

$$\frac{S_A}{S_D} < \frac{\hat{q}_A D_{f,D}}{\hat{q}_D D_{f,A}} \qquad \text{Eq. 5.3}$$

$$\frac{S_{s,A}}{S_{s,D}} < \frac{K_A}{K_D} \qquad \text{Eq. 5.4}$$

where

S_A, S_D = concentrations of the electron acceptor and donor in the bulk liquid ($M_s L^{-3}$)

$S_{s,A}, S_{s,D}$ = concentrations of the electron acceptor and donor at the biofilm/water interface ($M_s L^{-3}$)

$D_{f,A}, D_{f,D}$ = molecular diffusion coefficients of the electron acceptor and donor within the biofilm ($L^2 T^{-1}$)

$\hat{q}_A, \hat{q}_D$ = maximum specific rates of the electron acceptor and donor utilization ($M_s M_x^{-1} T^{-1}$)

K_A, K_D = half-maximum-rate concentrations for the electron acceptor and donor ($M_s L^{-3}$)

Using Eqs. 5.3 and 5.4, as well as the kinetics parameters for NO_3^- and electron donor (as COD) in Table 5.1, we identified the conditions for NO_3^- versus donor limitation and calculated the corresponding effluent NO_3^- and COD concentrations (shown in Table 5.2). The effluent concentration of the non-rate-limiting substrate (in Table 5.2) then can be calculated using stoichiometry. For example, when NO_3^- is rate-limiting, the effluent COD concentration is

$$S_D = S_D^{in} - \frac{A \times f(S_{NO3-})}{coefficient\ 1 \times Q} \qquad \text{Eq. 5.5}$$

Eq. 5.5 was obtained by combining Eqs. 5.6 to 5.8:

$$J_D = \frac{(S_D^{in} - S_D) \times Q}{A} \qquad \text{Eq. 5.6}$$

$$\frac{J_{NO3-}}{J_D} = coefficient\ 1 \qquad \text{Eq. 5.7}$$

$$J_{NO3-} = f(S_{NO3-}) \qquad \text{Eq. 5.8}$$

where,

S_{NO3-}^{in}, S_D^{in} = concentrations of NO_3- and COD in the influent ($M_s L^{-3}$)

A = total biofilm surface (L^2)

Q = flow rate ($L^3 T^{-1}$)

Nitrite (NO_2^-) is the immediate product from NO_3^- reduction, and it also is reduced as an electron acceptor in denitrification. We also identified the conditions of the NO_2^- versus donor limitation and calculated the corresponding effluent concentrations. The results also are summarized in Table 5.2.

Table 5.1 Parameters for identifying the rate-limiting substrate in denitrification

$\hat{q}$	K	D_f
0.5 g N/g VSS-d (Rezania et al., 2005)	0.2 mg N/L (Gujer et al., 1999)	1.0 (Williamson and McCarty, 1976)
0.9 g N/g VSS-d (Rezania et al., 2005)	0.3 mg N/L (Gujer et al., 1999)	0.9 (Nogueira and Melo, 2006)
3.0 g COD/g VSS-d[a]	2 mg/L (Gujer et al., 1999)	1.0 (Rittmann and Dovantzis, 1983)

Notes:

a. Based on the maximum specific rates, f_s (the fraction of the electron donor used for synthesis) for NO_3^- and NO_2^- reduction is about 0.5 (Rittmann and McCarty, 2001).

Table 5.2 Conditions for NO_3^-, NO_2^-, or COD limitation and the corresponding effluent substrate concentrations

		condition[a]	effluent NO_3^-, NO_2^-, and COD concentrations
NO_3^- to NO_2^-	NO_3^- limitation	$\frac{S_{NO3-}}{S_D} < \frac{1\ mg\ N/L}{10\ mg\ COD/L}$	$S_{NO3-} = f'(J_{NO3-})$ $S_D = S_D^{in} - \frac{A \times f(S_{NO3-})}{coefficient\ 1 \times Q}$
	COD limitation	$\frac{S_{NO3-}}{S_D} > \frac{1\ mg\ N/L}{6\ mg\ COD/L}$	$S_D = f'(J_D)$ $S_{NO3-} = S_{NO3-}^{in} - \frac{coefficient\ 1 \times A \times f(S_D)}{Q}$
NO_2^- to N_2	NO_2^- limitation	$\frac{S_{NO2-}}{S_D} < \frac{1\ mg\ N/L}{7\ mg\ COD/L}$	$S_{NO2-} = f''(J_{NO2-})$ $S_D = S_D^{in} - \frac{A \times f(S_{NO2-})}{coefficient\ 2 \times Q}$
	COD limitation	$\frac{S_{NO2-}}{S_D} > \frac{1\ mg\ N/L}{3\ mg\ COD/L}$	$S_D = f''(J_D)$ $S_{NO2-} = S_{NO2-}^{in} - \frac{coefficient\ 2 \times A \times f(S_D)}{Q}$

Notes:

a. For simplification, $\frac{S_{s,A}}{S_{s,D}} \approx \frac{S_A}{S_D}$.

With the substrate-limitation information in Table 5.2, we can identify three typical cases in denitrification. In all of the three cases, we assume that the

influent NO_2^- concentration is zero, since this is very common in groundwater. Case 1 occurs when nitrate and nitrite limit. Case 1 normally comes about when the electron donor is supplied well above the stoichiometric requirement so that the effluent COD is high (*e.g.*, S_D > 10 mg COD/L when S_{NO3-} = 1 mg N/L and S_D >7 mg COD/L when S_{NO2-} = 1 mg N/L). In this case,

$$S_{NO3-} = f'(J_{NO3-}) \qquad \text{Eq. 5.9}$$

$$S_{NO2-} = f''(J_{NO2-}) \qquad \text{Eq. 5.10}$$

Because NO_2^- is generated inside the biofilm, J_{NO2-} represents a virtual NO_2^- flux into the biofilm and can be calculated as:

$$J_{NO2-} = NO_2^- \text{ production rate } - NO_2^- \text{ Flux out} = J_{NO3-} - fJ_{NO3-} \qquad \text{Eq. 5.11}$$

The NO_2^- production rate equals the NO_3^- flux into the biofilm (J_{NO3-}) in this case, since all NO_3^--N entering the biofilm is reduced to NO_2^--N if the small amount of N uptake for synthesis is neglected. A portion of the NO_2^- produced in the biofilm may diffuse out of the biofilm, and this is denoted as $-fJ_{NO3-}$. The value of f depends on the intrinsic kinetics of NO_2^- versus NO_3^- reduction and lies in the range of 0 to 1, which represent the following two extreme cases:

1) f = 0: If the NO_2^- kinetics are substantially faster than the NO_3^- kinetics, then all NO_2^- is consumed inside the biofilm, S_{NO2-} is negligible, the out-transport of NO_2^- is zero, and $J_{NO2-} = J_{NO3-} - fJ_{NO3-} = J_{NO3-}$.

2) f = 1: If the NO_2^- kinetics are substantially slower than the NO_3^- kinetics, then all NO_2^- produced in the biofilm transports out, $S_{NO2-} = S_{NO3-}$, the

out-transport of NO_2^- is equal to the in-transport of NO_3^-, and

$J_{NO2-} = J_{NO3-} - fJ_{NO3-} = 0$.

Rezania et al. (2005) evaluated the kinetics of NO_2^- and NO_3^- at different pHs and temperatures and found that the maximum reduction rate of NO_2^- always was faster than that of NO_3^-. For example, at a pH of 8.0 and temperature of 25°C, the reduction rates of NO_2^- and NO_3^- were 0.9 and 0.5 g N/ g VSS-d. Therefore, *f* should be close to zero.

Rearranging Eq. 5-11 gives

$$J_{NO2-} = J_{NO3-} - fJ_{NO3-} = (1-f) \times J_{NO3-} \approx J_{NO3-} \quad \text{Eq. 5.12}$$

when *f* is near zero. Combining Eqs. 5.10 and 5.12 leads to:

$$S_{NO2-} \approx f''(J_{NO3-}) \quad \text{Eq. 5.13}$$

When the effluent NO_3^- approaches zero, the flux of NO_3^- (J_{NO3-}) approaches the *SL* of NO_3^- (SL_{NO3-}). Then, Eqs. 5.9 and 5.13 are transformed to Eqs. 5.14 and 5.15.

$$S_{NO3-} \approx f'(SL_{NO3-}) \quad \text{Eq. 5.14}$$

$$S_{NO2-} \approx f'(SL_{NO3-}) \quad \text{Eq. 5.15}$$

In case 1, the effluent NO_3^- and NO_2^- concentrations increase simultaneously with the increase of the NO_3^- loading. Compared to the effluent NO_3^- and NO_2^- concentrations, the effluent COD concentration is very high. This case should be avoided in practice.

In case 2, the electron donor is supplied close to the stoichiometric requirement, and the effluent N/COD ratio (1 g N/ 10 g COD – 1 g N/ 3 g COD)

is close to the stoichiometric ratio. Dual substrate limitation (N and COD limitation) occurs in this case. COD limitation more strongly affects the second step of denitrification (NO_2^- to N_2) and can cause a high effluent NO_2^- concentration, since the first step of denitrification (NO_3^- to NO_2^-) must take the electrons first. Therefore, the effluent N is mainly in the form of NO_2^-. As the loading increases, the effluent NO_2^- and COD concentrations simultaneously increase, but the effluent NO_3^- is relatively low. This explains why the NO_2^- concentration in the effluent is high even if the kinetics for NO_2^- reduction is faster than the kinetics of NO_3^- reduction. In this case, we can achieve low concentrations of nitrate, nitrite, and COD at the same time; thus, dosing electron donors according to stoichiometry should be the optimal operating criterion.

When the electron donor supply in case 1 is reduced to just enough to start limiting the kinetics, case 1 turns to case 2. In this sense, case 2 is the boundary of case 1. Therefore, Eqs. 5.14 and 5.15, obtained from case 1, can be used for design in case 2; however, at the same NO_3^- loading, the effluent nitrite concentrations in case 2 should be slightly higher than that in case 1, since some donor limitation is in effect.

Case 3 is full donor (COD) limitation, in which the electron donor is supplied below the stoichiometric requirement; then, the effluent COD concentration is low (*e.g.*, S_D < 6 mg COD/L when S_{NO3-} = 1 mg N/L and S_D < 3 mg COD/L when S_{NO2-} = 1 mg N/L). When COD limits the reduction of NO_3^- and NO_2^-, effluent N concentration can be high, even if the NO_3^- loading is low; thus, case 3 also should be avoided in practice.

Clearly, case 2 is the desirable design condition, since neither the N nor the COD concentration is high. Eqs. 5.14 and 5.15 can be used for design. NO_2^- -- an intermediate of reduction of NO_3^- to N_2 -- has a much lower MCL (1 mg N/L) than does NO_3^- (10 mg N/L). Therefore, NO_2^- is more likely to control process performance. For this reason, we use a NO_2^- concentration just below its MCL as the criterion of performance success, and Eq. 5.15 becomes the controlling design criterion.

In practice, fluctuations in the influent water quality (influent nitrate and DO concentrations) can lead to variation of the stoichiometric dose. On-line instrumentation can help achieve close to the stoichiometric dose. For instance, nitrate and DO concentration can be monitored in the bioreactor's influent. Combined with the flow rate, the concentrations produce the stoichiometric electron-donor dose. On-line measurement of nitrate, nitrite, and DOC in the effluent of the denitrification process can be used to fine tune the dose.

Eqs. 5.16-5.18 show the relationships between *J* and the *EBCT*, *VL*, and *SL*.

$$J = \frac{Q(S^{in} - S)}{aV} \approx \frac{S^{in}}{a}\frac{1}{EBCT} \qquad \text{Eq. 5.16}$$

$$J = \frac{Q(S^{in} - S)}{aV} \approx \frac{QS^{in}}{aV} = \frac{VL}{a} \qquad \text{Eq. 5.17}$$

$$J = \frac{Q(S^{in} - S)}{aV} \approx \frac{QS^{in}}{aV} = SL \qquad \text{Eq. 5.18}$$

where

S^{in}, S = substrate concentrations in the influent and effluent ($M_s\ L^{-3}$)

V =reactor volume (L^3)

a = biomass-carrier specific surface area ($L^2\ L^{-3}$)

VL = QS_i/V ($M_s L^{-3} T^{-1}$)

SL = QS_i/aV ($M_s L^{-2} T^{-1}$)

$EBCT$ = V/Q (T)

Combining Eqs. 5.13 and 5.15 to 5.18 yields the final form of the design equation:

$$S_{NO2-} \approx f''(J_{NO3-}) \approx f''(SL_{NO3-}) \approx f''(VL_{NO3-}, a) \approx f''(EBCT, S^{in}, a) \quad \text{Eq. 5.19}$$

To achieve the same effluent NO_2^- concentration, the *VL* and *EBCT* may vary significantly, but the *SL* must be relatively constant. This is obvious since the function involving *SL* has only *SL*, while the functions with *VL* or *EBCT* also must contain *a*. (The equation with *EBCT* also contains S^{in}). Therefore, *SL* is the primary design criterion that has and should have a relatively narrow range, while *EBCT* and *VL* can vary widely, depending on the *a* value (and also the influent concentration for *EBCT*). Since reactor size and capital cost are directly related to the *EBCT* and *VL*, they are important as secondary design parameters.

The discussion above is strictly true for a CMBR. Examples of CMBR used for denitrification are the membrane bioreactor, rotating biological contactor, and moving-bed reactors. Packed-bed reactors using high-porosity carrier (*e.g.*, plastic carrier with a pore size of a few millimeters to a few centimeters) and having a small bed-depth can be approximated as CMBRs. If the bed is deep, the bed can be approximated as CMBRs in series (Rittmann and McCarty, 2001). For each CMBR, its *SL* is the prime design criterion for its performance; thus, *SL*

should still be the prime design criterion for the whole reactor. However, *SL* should not be used to design packed-bed reactor having low-porosity carriers (*e.g.*, sand and GAC), since the pores are so small that plugging and flow channeling can occur, which leads to ineffective use of carrier surface, especially the surface close to the reactor outlet.

2. Review of Design Parameters in Previous Studies

I summarized the critical operation and performance data from previous studies in Table 5.3, including reactor type, electron donor and dose, temperature, pH, *EBCT*, *VL*, *SL*, influent NO_3^-, NO_2^-, and DO concentrations, and effluent NO_3^-, NO_2^-, and COD concentrations. In five of ten cases, the authors of the original papers did not report *SL*, and we computed it from other operating data. All of these data correspond to having an effluent NO_2^--N concentration close to the MCL (1 mg N/L). While the reported *EBCT* and *VL* vary significantly from study to study -- *EBCT* from 0.2 to 17 hours and *VL* from 0.3 to 22 kg N/m^3-d -- the *SL* values are relatively stable among the different studies: 1.3 to 10.0 g N/m^2-d.

Table 5.3 Comparison of EBCT, VL, and SL from past studies

reactor	electron donor (COD:N)	temperature (^oC) &pH	EBCT (hour)	VL (kg N/m^3-d)	SL (g N/m^2-d)	influent DO, NO_3^-, & NO_2^- (mg/L)	effluent NO_3^-, NO_2^-, & COD(mg/L)	reference
packed bed	ethanol (4:1)	pH: 7.5-7.8	0.5	2.4	5.5	DO: 0; NO_3^--N: 50; NO_2^--N: 0	NO_3^--N: 0.9; NO_2^--N: 0.7; COD: 34	Dahab and Kalagiri, 1996
packed bed	ethanol (4:1)	T: 20 pH: 7.0	0.5	2.4	5.5	DO: 0; NO_3^--N: 50; NO_2^--N: 0	NO_3^--N: 2.4; NO_2^--N: 0.8; COD: 18	Woodbury and Dahab, 2001
packed bed	corn syrup (5.3:1)	T: 13-18 pH: 7.2	1.1	0.44	10.0	DO: 3.3; NO_3^--N: 20; NO_2^--N: 0	NO_3^--N: 5.0; NO_2^--N: 1.7; COD: 20	Silverstein and Carlson, 1999
packed bed	ethanol (4.3:1)	T: 15-20 pH: 7.0-7.5	1.2	1.4	1.4	DO: 0; NO_3^--N: 68; NO_2^--N: 0	NO_3^--N + NO_2^--N: < 3; COD: 10	Moreno et al., 2005
packed bed	acetate (5.5:1)	T: 20	5.1	0.21	1.3	DO: saturated; NO_3^--N: 45; NO_2^--N: 0	NO_3^--N: 5.0; NO_2^--N: 0.5; COD: 60	Vrtovšek and Roš, 2006
moving bed	acetate (13:1)	T: 20 pH: >7	0.9	1.6	4.6	NO_3^--N: 60; NO_2^--N: 0	NO_3^--N: 4.7; NO_2^--N: 0.25; COD: 400	Welander and Mattiasson, 2003
moving bed	acetate (4:1)	T: 17 pH: 7.8	17	1.3	6.2	NO_3^--N: 800; NO_2^--N: 0;	NO_3^--N:~ 0; NO_2^--N: ~ 0	Welander et al., 1998
moving	acetate (4:1)[a]	T: 7-10	0.43	0.8	2.5	DO: 9.3; NO_3^--N:	NO_3^--N: 2.0; NO_2^--	Rusten et

Table 5.3 Comparison of EBCT, VL, and SL from past studies

reactor	electron donor (COD:N)	temperature (^oC) &pH	EBCT (hour)	VL (kg N/m^3-d)	SL (g N/m^2-d)	influent DO, NO_3^-, & NO_2^- (mg/L)	effluent NO_3^-, NO_2^-, & COD(mg/L)	reference
bed membrane bioreactor	methanol (3:1)	pH: 7.2	0.2	22	6.1	13; NO_2^--N: 0.5	N: 0.9; COD: 50	al., 1995
rotating biological contactor	acetate (4.6:1)	T: 20 ±2 pH: 7.0	8.8	0.3	4.8	DO: 0; NO_3^--N: 200; NO_2^--N: 0	NO_3^--N: 5.7; NO_2^--N: 0.02; COD: 70	Ergas and Rheinheimer, 2004
						DO: 9.2; NO_3^--N: 100; NO_2^--N: 0	NO_3^--N: 4.0; NO_2^--N: 0.9; COD: 16	Mohseni-Bandpi et al., 1999

Note a. The C:N ratio is related to the total equivalent concentration of NO_3^--N by converting influent NO_2^--N and DO to equivalent amounts of NO_3^--N.

3. Design Parameters in the Pilot-Scale PBHR

As documented in Chapter 3, the loading limits obtained from increases to the flow-rate (6.0-7.9 g N/m^2-d) and the nitrate concentration (6.3-10.0 g N/m^2-d) were consistent despite different changes to the *EBCT* and *VL*. Furthermore, the loading limits obtained from this study are in the range of the *SL* values computed from literature reports with a wide range of process types (1.3-10 g N/m^2-d, Table 5.3). This consistency confirms that *SL* is the primary design parameter for heterotrophic denitrification, since it controls the effluent NO_3^- and NO_2^- concentrations despite wide ranges in *EBCT* and *VL*.

To assess the impact of the ethanol supply rate on the effluent water quality, Table 5.4 compares the water quality of the effluents from the two load-increase tests that had approximately the same *SL*: the test increasing the flow rate (*SL* of 6.0 g N/m^2-d) and the test increasing the nitrate concentration (*SL* of 6.3 g N/m^2-d). The former is an example of case 2 (Theoretical Base): stoichiometric ethanol addition, dual substrate (N and COD) limitation, and simultaneously low concentrations of NO_3^-, NO_2^-, and COD in the effluent. The latter exemplifies case 1: ethanol addition over the stoichiometric requirement, NO_3^- and NO_2^- limitation, low effluent NO_3^- and NO_2^- concentrations, and high

effluent COD concentration. The comparison underscores why case 2 should be the desirable design condition.

Table 5.4 Effect of the ethanol supply rate

test	*SL* (g N/m^2-d)	ethanol supply rate: stoichiometric requirement	effluent NO_3^- (mg N/L)	effluent NO_2^- (mg N/L)	effluent COD (mg/L)	effluent DOC (mg C/L)
flow-rate increase	6.0	1:1	0.1	0.6	5	1.8
nitrate-concentration increase	6.3	1.25:1	0.1	0.1	19	5

4. Conclusions

Nitrate carrier-surface loading (*SL*), instead of empty bed contact time (*EBCT*) or nitrate volumetric loading (*VL*), is the primary design criterion for heterotrophic denitrification reactors. The maximum *SLs* at which the effluent NO_2^- concentration was around the Maximum Contaminant Level ranged from 1.3 to 10 g N/m^2-d based on literature reports. Our experiments using two means to control the *SL* gave a maximum *SL* of approximately 6 g N/m^2-d, despite wide differences in *EBDT* and *VL*.

Chapter 6

A pH-CONTROL MODEL FOR HETEROTROPHIC AND H_2-BASED AUTOTROPHIC DENITRIFICATION

The main goal of this chapter is to construct a model to predict pH change in denitrification reactors. Relevant background information was presented in pages 10-11 in Chapter 1. This chapter (Chapter 6) develops the model, evaluates the model using the pH, alkalinity, and LSI data from the pilot-scale denitrification plant, evaluates the necessity of pH-control in denitrificaiton reactors, and proposes the preferred pH-control methods for the autotophic and heterotriphic denitrification reactors. This work was published in Tang et al. (2011b). I led the effort in developing and evaluating the model and discussing the model results. Chen Zhou mainly contributed to the model development. Bruce E. Rittmann and Michal Ziv-El mainly contributed to discussing the model results, and they reviewed and revised the manuscript.

1. Model Development

The alkalinity and pH increase in heterotrophic and H_2-based autotrophic denitrification because nitrite reduction consumes protons (H^+). Proton consumption is illustrated in Eqs. 6.1-6.4 (stoichiometry based on Rittmann and McCarty (2001)), in which ethanol (CH_3CH_2OH) or hydrogen gas (H_2) is the heterotrophic or autotrophic electron donors, respectively, and biomass is indicated by $C_5H_7O_2N$. A typical biomass retention time of 15 days (Rittmann and McCarty, 2001) was used to develop the stoichiometry for these equations.

Heterotrophic Denitrification:

$$NO_3^- + 0.263CH_3CH_2OH + 0.0445H^+ = 0.954NO_2^- + 0.0445C_5H_7O_2N + 0.655H_2O + 0.303\mathbf{CO_2} \quad \text{Eq. 6.1}$$

$$NO_2^- + 0.425CH_3CH_2OH + \mathbf{H^+} = 0.455N_2 + 0.0912C_5H_7O_2N + 1.457H_2O + 0.393\mathbf{CO_2} \quad \text{Eq. 6.2}$$

Autotrophic Denitrification:

$$NO_3^- + 1.13H_2 + 0.01H^+ + 0.05\mathbf{CO_2} = 0.99NO_2^- + 0.01C_5H_7O_2N + 1.1H_2O \quad \text{Eq. 6.3}$$

$$NO_2^- + 0.122\mathbf{CO_2} + \mathbf{H^+} + 1.78H_2 = 0.488N_2 + 0.0244C_5H_7O_2N + 2.19H_2O \quad \text{Eq. 6.4}$$

In both reactors, nitrite reduction is the predominant source of alkalinity, consuming 1 H^+ equivalent per N equivalent of NO_2^- (highlighted by **boldface** in Eqs. 6.2 and 6.4). Another factor that affects pH is the net production of CO_2 in heterotrophic reactors (highlighted by **boldface** in Eqs. 6.1 and 6.2) and net consumption of CO_2 in autotrophic reactors (highlighted by **boldface** in Eqs. 6.3 and 6.4). CO_2 is a weak acid, and its addition partially suppresses the pH rise from proton consumption, as well as increases the concentration of total inorganic carbon species.

Dissolved oxygen almost always is present in water to be treated by denitrification. While respiration of O_2 does not consume significant protons, oxygen respiration can affect the pH by CO_2 addition in a heterotrophic reactor (highlighted by **boldface** in Eq. 6.5) and CO_2 consumption in an autotrophic reactor (highlighted by **boldface** in Eq. 6.6).

Heterotrophic O_2 respiration:

$$O_2 + 0.613CH_3CH_2OH + 0.120NO_3^- + 0.120H^+ = 0.120C_5H_7O_2N + 0.667\mathbf{CO_2} + 1.48H_2O \quad \text{Eq. 6.5}$$

Autotrophic O_2 respiration:

$$O_2 + 2.39H_2 + 0.0282NO_3^- + 0.141\mathbf{CO_2} + 0.0282H^+ = 0.0282C_5H_7O_2N + 2.31H_2O \quad \text{Eq. 6.6}$$

The feed water's alkalinity buffers pH changes and affects pH in the reactor. For natural water, the carbonate reaction dominates the alkalinity due to the common occurrence and dissolution of carbonate minerals and the presence of carbon dioxide in the atmosphere (Snoeyink and Jenkins, 1980). Addition of certain chemicals to the influent or into the reactor can also affect pH. For example, HCl can be added to the influent to lower the alkalinity and pH, while CO_2 can be sparged inside the reactor to add a weak acid and increase the buffering capacity of the water.

When coupled with an alkalinity mass balance (via the proton condition) in the influent and effluent, the factors mentioned above can be used to predict the effluent pH, alkalinity, and LSI. This constitutes the pH-control model, whose development is described next in a stepwise manner.

First, the following six assumptions are made:

1) Phosphate species are not considered as a buffer due to two factors. First, the concentration of total phosphorus in most natural groundwater is very low due to its precipitation with calcium (Snoeyink and Jenkins, 1980). Second, phosphate added as a nutrient and dosed at the stoichiometric requirement for P uptake in biomass synthesis provides negligible phosphate buffering in the reactor,

compared to carbonate buffering.

2) Other natural buffering species (*e.g.*, ammonium) also are neglected, because they are trivial compared to the carbonate species (Snoeyink and Jenkins, 1980).

3) Calcium carbonate is the most common mineral precipitate and the only solid species considered; the Langlier Saturation Index (LSI) is used as an indication of precipitation potential of $CaCO_3$ (Snoeyink and Jenkins, 1980). Calcium phosphate species are neglected, since the phosphate concentration is low. $Mg(OH)_2$ also is neglected, because it is super-saturated only at pH values that are too high to be relevant for biological treatment.

4) The reactor is a closed reactor, which means that CO_2 does not exchange between the reactor and the atmosphere.

5) Activity coefficients are ignored, since most source water for drinking water treatment has a low salinity. This assumption would need to be removed if denitrification were being carried out with high-salinity water, such as regeneration brine from ion exchange (Van Ginkel et al., 2008).

6) The model assesses the conditions in the bulk liquid based on reactions occurring in the biofilm, which assumes that the pH inside the biofilm does not differ greatly from that in the bulk liquid. Therefore, the model could be

expanded to consider the pH gradient in the biofilm and generate more accurate results.

Second, the alkalinity concentrations in the influent and effluent of the reactor are tabulated by coupling the proton condition, the total concentration of inorganic carbonate species (C_T), and the hydrogen-ion concentration ($[Alk] = f(C_T, [H^+])$). The alkalinity equations (Eqs. 6.7 and 6.8) are identical to the proton conditions with H_2O and H_2CO_3 as the reference levels (VanBriesen and Rittmann, 1999).

Alkalinity in the influent of the reactor:

$$\begin{aligned}[Alk]_{in} &= 2[CO_3^{2-}]_{in} + [HCO_3^-]_{in} + [OH^-]_{in} - [H^+] \\ &= 2[C_{T,in}]\frac{1}{1+[H^+]_{in}/K_2 + [H^+]_{in}^{\ 2}/K_1K_2} + [C_{T,in}]\frac{1}{1+[H^+]_{in}/K_1 + K_2/[H^+]_{in}} \\ &+ \frac{10^{-14}}{[H^+]_{in}} - [H^+]_{in}\end{aligned} \quad \text{Eq. 6.7}$$

Alkalinity in the effluent of the reactor:

$$\begin{aligned}[Alk]_{out} &= 2[CO_3^{2-}]_{out} + [HCO_3^-]_{out} + [OH^-]_{out} - [H^+]_{out} \\ &= 2[C_{T,out}]\frac{1}{1+[H^+]_{out}/K_2 + [H^+]_{out}^{\ 2}/K_1K_2} + [C_{T,out}]\frac{1}{1+[H^+]_{out}/K_1 + K_2/[H^+]_{out}} \\ &+ \frac{10^{-14}}{[H^+]_{out}} - [H^+]_{out}\end{aligned} \quad \text{Eq. 6.8}$$

in which

K_1, K_2 = acid-dissociation constants of H_2CO_3 and HCO_3^- ($K_1 = 10^{-10.3}$, $K_2 = 10^{-6.3}$ @ 25 ^{0}C)

$C_{T,in}, C_{T,out}$ = total concentration of inorganic carbon species in the influent and effluent (mole/L).

$[Alk]_{in}, [Alk]_{out}$ = alkalinity in the influent and effluent (mole/L)

Eq. 6.7 can be used to obtain $C_{T,in}$, since $[Alk]_{in}$ and $[H^+]_{in}$ can be measured. In order to solve Eq. 6.8 for the effluent pH ($[H^+]_{out}$), $[Alk]_{out}$ and $C_{T,out}$ are calculated using Eqs. 6.9 - 6.10:

$$C_{T,out} = C_{T,in} + C_{T,\Delta} \qquad \text{Eq. 6.9}$$

$$[Alk]_{out} = [Alk]_{in} + [Alk]_{\Delta} \qquad \text{Eq. 6.10}$$

in which

$C_{T,\Delta}$ = the change of total concentration of inorganic carbon species due to denitrification (Eqs. 6.1-6.4), oxygen respiration (Eqs. 6.5-6.6), precipitation, and external CO_2 addition.

$$C_{T,\Delta} = ([NO_3^-]_{in} - [NO_3^-]_{out}) \times 0.303 + ([NO_3^-]_{in} - [NO_3^-]_{out} + [NO_2^-]_{in} - [NO_2^-]_{out}) \times 0.393 + ([O_2]_{in} - [O_2]_{out}) \times 0.667 + ([Ca^{2+}]_{out} - [Ca^{2+}]_{in}) + [CO_2] \text{ (heterotrophic)} \qquad \text{Eq. 6.11}$$

$$C_{T,\Delta} = ([NO_3^-]_{out} - [NO_3^-]_{in}) \times 0.05 + ([NO_3^-]_{out} - [NO_3^-]_{in} + [NO_2^-]_{out} - [NO_2^-]_{in}) \times 0.122 + ([O_2]_{out} - [O_2]_{in}) \times 0.141 + ([Ca^{2+}]_{out} - [Ca^{2+}]_{in}) + [CO_2] \text{ (autotrophic)} \quad \text{Eq. 6.12}$$

$[Alk]_\Delta$ = change of alkalinity due to denitrification (Eqs. 6.1-6.4), oxygen respiration (Eqs. 6.5-6.6), precipitation, and external acid addition (*e.g.*, HCl and H_3PO_4).

$$[Alk]_\Delta = ([NO_3^-]_{out} - [NO_3^-]_{in}) \times 0.0445 + ([NO_3^-]_{in} - [NO_3^-]_{out} + [NO_2^-]_{in} - [NO_2^-]_{out}) \times 1 + ([O_2]_{out} - [O_2]_{in}) \times 0.120 + 2([Ca^{2+}]_{out} - [Ca^{2+}]_{in}) - [Acid] \text{ (heterotrophic)} \quad \text{Eq. 6.13}$$

$$[Alk]_\Delta = ([NO_3^-]_{in} - [NO_3^-]_{out}) \times 0.01 + ([NO_3^-]_{in} - [NO_3^-]_{out} + [NO_2^-]_{in} - [NO_2^-]_{out}) \times 1 + ([O_2]_{in} - [O_2]_{out}) \times 0.0282 + 2([Ca^{2+}]_{out} - [Ca^{2+}]_{in}) - [Acid] \text{ (autotrophic)} \quad \text{Eq. 6.14}$$

The concentration of external CO_2 addition can be obtained using the CO_2 flow rate, or it can be computed from the set pH, as shown below. After substituting Eqs. 6.7 and 6.9-6.14, the only unknown variable in Eq. 6.8 is $[H^+]_{out}$. Thus, the model can solve for $[H^+]_{out}$ and, from that, the pH in the effluent. After that, the effluent alkalinity can be calculated with Eq. 6.8, and the Langlier Saturation Index (LSI) can be computed with Eq. 6.15 (Ziv-El and Rittmann, 2009a; Snoeyink and Jenkins, 1980).

$$LSI = pH - (pK_2 - pK_{so} + p[Ca^{2+}]_{out} + p[HCO_3^-]_{out} - \log \gamma_{Ca^{2+}} - \log \gamma_{HCO_3^-}) \quad \text{Eq. 6.15}$$

where

K_{so} = solubility constant of $CaCO_{3(s)}$ ($10^{-8.3}$ @ 25^0C)

$\gamma_{Ca^{2+}}$ = activity coefficient of Ca^{2+}

$\gamma_{HCO_3^-}$ = activity coefficient of HCO_3^-

2. Model Evaluation Using the Data from the Pilot-Scale HPBR

The model was evaluated using data from the pilot-scale HPBR. The model inputs for the heterotrophic reactor are listed in Table 6.1. As described in the next paragraph, the model was able to predict the effluent values of pH, alkalinity, and LSI with minimal error.

Table 6.2 presents a comparison for the heterotrophic reactor of the measured effluent pH, alkalinity, and LSI with the model-predicted values. The model outputs of the pH and alkalinity had an error of less than 1% for all cases, and the LSI deviated by less than 0.1 LSI units. It should be noted that, when the influent nitrate concentration was spiked to elevated levels (19.6 mg-N/L and 32.1 mg-N/L) in the heterotrophic pilot reactor, calcium precipitation occurred; this was observed as a deficit in effluent soluble calcium concentration compared to

the influent (Table 6.2). Measures to control the pH were not taken then, since these tests were short term (20 days) and the predicted pH (7.3-8.7) was within the optimum range for denitrification. The implications for long-term operation are discussed in "Necessity of pH Control".

Table 6.1 Experimentally measured model inputs for the heterotrophic reactor

	influent nitrate = 11.8 mg-N/L			influent nitrate = 19.6 mg-N/L			influent nitrate = 32.1 mg-N/L		
	influent	stage-1	Stage-2	influent	stage-1	stage-2	influent	stage-1	stage -2
DO (mg/L)	4.5 ± 1.0	0	0	4.5 ± 1.0	1.0	0	4.5 ± 1.0	0	0
NO_3^- (mg-N/L)	11.8 ± 0.4	0.34 ± 0.2	< 0.01	19.6	5.9 ± 1.0	< 0.01	32.1	13.1 ± 0.8	0.1
NO_2^- (mg-N/L)	< 0.01	0.60 ± 0.3	< 0.01	< 0.01	2.3 ± 0.5	< 0.01	< 0.01	2.9 ± 0.2	2.5
Ca^{2+} (mg/L)	67.1 ± 0.2	67.1 ± 0.2	67.0 ± 0.3	65.6 ± 0.1	65.6 ± 0.1	63.6 ± 0.2	65.7 ± 0.3	65.7 ± 0.2	63.6 ± 0.1
PO_4^{3-} (mg-P/L)	1.5	< 0.01	< 0.01	2	< 0.01	< 0.01	3	< 0.01	< 0.01
pH	7.6 ± 0.1			7.6 ± 0.2			7.6 ± 0.1		
alkalinity (mg/L as $CaCO_3$)	84 ± 4			84 ± 2			84 ± 3		

Table 6.2 Comparison of the measured and model-predicted pH, alkalinity, and LSI for the heterotrophic reactor

		influent nitrate = 11.8 mg-N/L		influent nitrate = 19.6 mg-N/L		influent nitrate = 32.1 mg-N/L	
		stage-1	stage-2	stage-1	stage-2	stage-1	stage-2
pH	measured	7.7 ± 0.1	7.8 ± 0.1	7.4 ± 0.1	8.2 ± 0.0	7.4 ± 0.1	8.3 ± 0.1
	model-predicted	7.7	7.8	7.4	8.3	7.5	8.4
	difference (%)	0%	0%	0%	1%	1%	1%
alkalinity (mg/L as $CaCO_3$)	measured	116 ± 3	120 ± 7	114 ± 4	142 ± 2	127 ± 5	168 ± 5
	model-predicted	116	119	115	139	127	164
	difference (%)	0%	-0.8%	0.9%	-2%	0%	-2%
LSI	measured	-0.03	0.08	-0.34	0.54	-0.30	0.70
	model-predicted	-0.07	0.09	-0.29	0.64	-0.22	0.78
	difference	-0.04	0.01	0.05	0.10	0.08	0.08

3. Model Evaluation Using the Data from the Pilot-Scale MBfR

The model was also evaluated using data from the pilot-scale MBfR. The model inputs for the autotrophic reactor are listed in Table 6.3. As described in the next paragraph, the model was able to predict the effluent values of pH, alkalinity, and LSI with minimal error.

Table 6.4 presents a comparison of the measured and model-predicted values for the autotrophic reactor. This reactor required a modification to the model, since the pH in the pilot reactor had a fixed pH of 7.0; this pH was achieved by adding CO_2 with an automated feedback loop. In this case, CO_2 dosage (*i.e.*, $[CO_2]$ in Eqs. 6.11 and 6.12) was the unknown, and the effluent pH was a model input. The alkalinity in the effluent was obtained using Eqs. 6.10 and 6.14 and the LSI with Eq. 6.15. The deviations between measured and model-predicted values were small for the MBfR: less than 2% for the alkalinity, with the LSI within 0.01 LSI units.

Table 6.3 Experimentally measured model inputs for the autotrophic reactor

	influent nitrate = 11.8 mg-N/L			influent nitrate = 19.6 mg-N/L			influent nitrate = 32.1 mg-N/L		
	influent[a]	stage-1	stage-2	influent[a]	stage-1	stage-2	influent[a]	stage-1	stage-2
DO (mg/L)	4.5 ± 1.0	0	0		1.0	0		0	0
NO_3^- (mg-N/L)	11.8 ± 0.4	< 0.01	< 0.01		0.7 ± 0.3	< 0.01		10.4	0.1
NO_2^- (mg-N/L)	< 0.01	< 0.01	< 0.01		1.7 ± 0.5	< 0.01		7.3	2.5
Ca^{2+} (mg/L)	67.1 ± 0.2	67.1 ± 0.2	67.0 ± 0.3		65.7 ± 0.1	65.5 ± 0.2		65.6 ± 0.2	65.7 ± 0.1
PO_4^{3-} (mg-P/L)	0.15	< 0.01	< 0.01	0.48	< 0.01	< 0.01	0.76	< 0.01	< 0.01
pH	7.6 ± 0.1	7.0	7.0		7.0	7.0		7.0	7.0
alkalinity (mg/L as $CaCO_3$)	84 ± 4			84 ± 2			84 ± 3		

Note：a. The influent quality was the same as in Table 6.1.

Table 6.4 Comparison of the measured and model-predicted alkalinity and LSI for the autotrophic reactor

		influent nitrate = 11.8 mg-N/L		influent nitrate = 19.6 mg-N/L		influlent nitrate = 32.1 mg-N/L	
		stage-1	stage-2	stage-1	stage-2	stage-1	stage-2
alkalinity (mg/L as $CaCO_3$)	measured	124 ± 3	124 ± 4	140 ± 4	155 ± 3	135 ± 4	185 ± 2
	model-predicted	125	125	143	152	132	186
	difference (%)	0.08%	0.08%	2%	-2%	-0.2%	0.05%
LSI	measured	-0.70	-0.70	-0.65	-0.61	-0.66	0.53
	model-predicted	-0.69	-0.69	-0.64	-0.61	-0.67	0.52
	difference	0.01	0.01	0.01	0	-0.01	-0.01

4. Necessity of pH Control

In order to highlight the need to control the influent pH, Figs. 6.1 (heterotrophic reactor) and 6.2 (autotrophic reactor) present the model simulations of the effluent pH, alkalinity, and LSI with and without controlling the influent pH. The measured influent values also are displayed.

To simulate scenarios where the pH was not controlled, we assumed no acid addition ($[CO_2] = 0$ and [Acid] = 0) and no precipitation ($[Ca^{2+}]_{out} = [Ca^{2+}]_{in}$) when solving Eqs. 6.11-6.14. The latter is a simplification that yields the maximum effluent precipitation risk displayed as the LSI. For the autotrophic reactor, the pH in the actual pilot reactor was controlled, and the modifications to the model are described in the previous section. For the heterotrophic reactor, to simulate the scenario where the pH was controlled, the concentration of acid required in the influent ([Acid] in Eqs. 6.13 and 6.14) was obtained using a trial-and-error method for the input acid until the predicted LSI equaled 0 and the pH in the effluent was less than 9. The same method could have been used for the autotrophic reactor, but by varying $[CO_2]$ in Eqs. 6.11 and 6.12 instead of the input acid. In practice, an LSI above 0.5 leads to noticeably increased scaling (Camerata et al., 2008); thus, LSI = 0 was used here in order to incorporate a

safety factor. A pH of 9 was selected, since this is the upper limit for high-rate denitrification, as discussed in the Introduction.

4.1 Heterotrophic reactor

Looking at the influent nitrate concentration of 11.8 mg N/L, the pH remains within the optimal range in the influent and both stages, the LSI is negative in stage-1 and just above zero in stage-2; thus, pH adjustment was not required in the heterotrophic reactor when the influent nitrate concentration was 11.8 mg N/L. In this case, the potential to increase in pH by proton consumption during denitrification was mostly balanced by production of CO_2 by denitrification and O_2 respiration. The following calculations quantify the impact of the different factors affecting alkalinity and pH changes. Proton consumption through denitrification is calculated using Eqs. 6.1, 6.2, and 6.5: 8.4×10^{-4} mol/L. External proton addition from phosphoric acid is obtained from Table 6.1: 1.5×10^{-4} mole/L. Thus, the alkalinity increased by 6.9×10^{-4} mol/L = 35 mg/L as $CaCO_3$ (Fig. 6.1). CO_2 production through denitrification and O_2 respiration is calculated using Eqs. 6.1, 6.2, and 6.5: 6.6×10^{-4} mol/L. The CO_2 production was slightly lower than the alkalinity increase, resulting in only a slight pH increase.

When nitrate was spiked to 19.6 and 32.1 mg-N/L, the scenario of "without HCl addition" shows a pH of around 7.5 in stage-1, with the LSI remaining negative in stage-1. However, the effluent pH increases to over 8.5, making the LSI greater than 1 in stage-2 and indicating a serious precipitation risk that would necessitate pH control for long-term operation. The experimental results for the short-term experiments showed $CaCO_3$ precipitation (Table 6.1).

The following calculations quantify how the alkalinity and pH in stage-1 significantly differed from those in stage-2. Taking the scenario of 19.6 mg-N/L for example, alkalinity increased in stage-1 by 6.1×10^{-4} mol/L = 31 mg/L as $CaCO_3$ (Fig. 6.1). CO_2 was produced in stage-1 at 7.1×10^{-4} mol/L through denitrification and O_2 respiration. The CO_2 production was higher than the alkalinity increase on an equivalent basis, resulting in a slight decrease of pH (Fig. 6.1) in stage-1. In stage-2, compared to the influent, the alkalinity increase (1.2×10^{-3} mol/L = 60 mg/L as $CaCO_3$ (Fig. 6.1)) was much higher than the CO_2 production (1.0×10^{-3} mol/L), leading to the large increase in pH.

Fig. 6.1 also presents a scenario in which acid addition is administered to the influent so that the LSI is negative or zero in both stages. The influent pH is 6.5, as the alkalinity drops to ~60 mg/L as $CaCO_3$ when enough HCl is added to compensate for alkalinity addition in both stages of the reactor. Since the pH and

LSI are within the optimal range in stage-1 without HCl addition, the pH adjustment could be implemented between stage-1 and stage-2, which has an advantage that the pH in the influent (and the inlet of stage-1) would not drop below 7.0, the lower limit of the optimal range for denitrification.

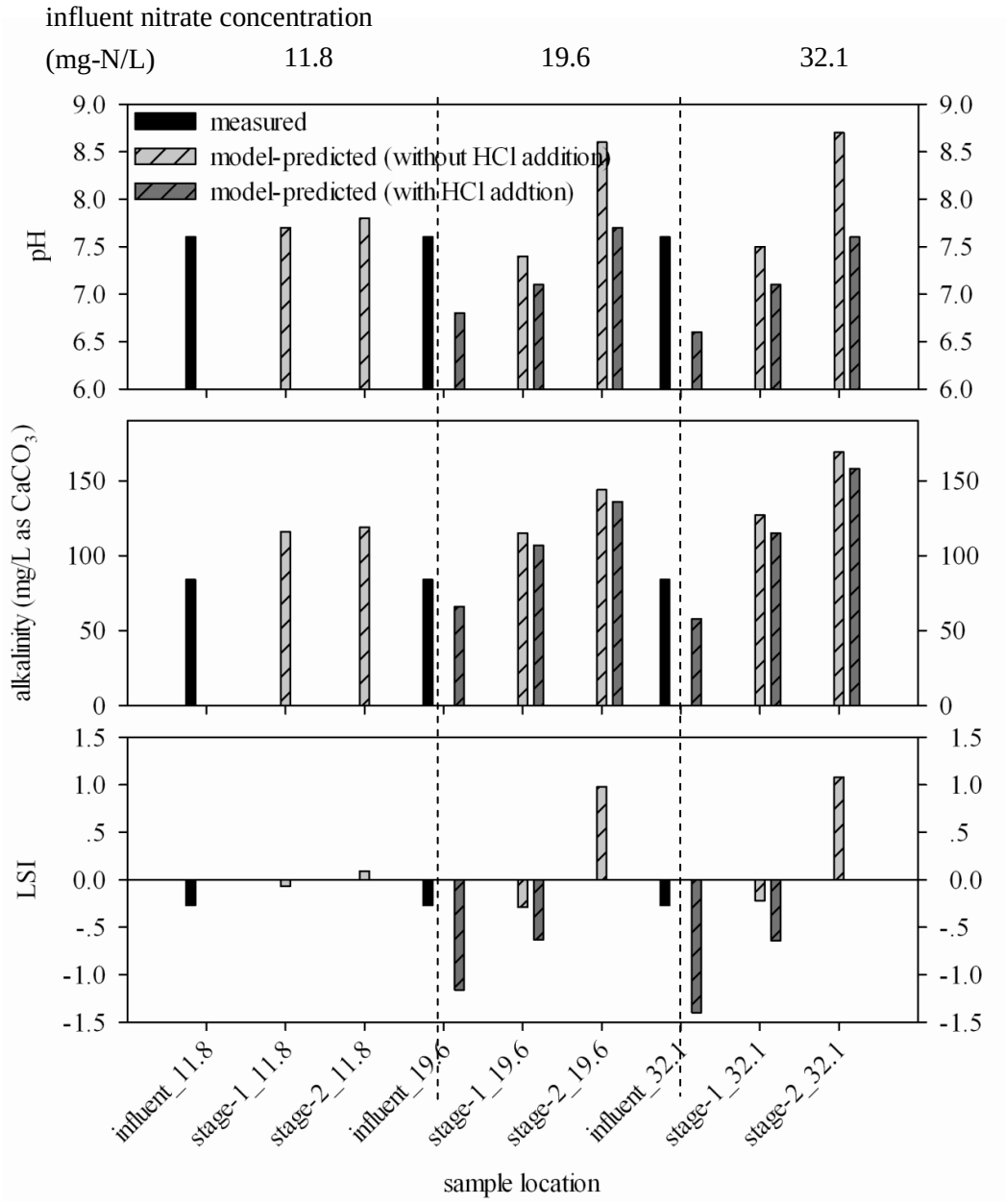

Fig. 6.1 Measured and model-predicted pH, alkalinity, and LSI in the heterotrophic reactor for three influent nitrate concentrations. Two scenarios are considered, with and without HCl addition. To control LSI = 0 in stage-2, HCl should be added at 1.7×10^{-4} and 2.3×10^{-4} mole/L when the nitrate concentration at the influent is 19.6 and 32.1 mg-N/L, respectively.

4.2 Autotrophic reactors

Fig. 6.2 presents similar analyses for the autotrophic reactor. Distinct from the relatively mild pH increase in heterotrophic reactors without acid addition, the pH would increase to greater than 10 and the LSI to greater than 2 in both stages and for all three influent nitrate concentrations if CO_2 were not added inside the reactor. This means that the autotrophic denitrification reactor has greater risks of severe pH and precipitation problems than does the heterotrophic reactor.

The scenario of 11.8 mg-N/L without pH control was analyzed to quantify how the pH and LSI differ significantly in the two denitrification reactors, even though the alkalinity increase was about the same. In stage-2 of the autotrophic reactor, proton consumption was calculated using Eqs. 6.3, 6.4, and 6.6: 8.4×10^{-4} mol/L. External proton addition from phosphoric acid was obtained from Table 6.1: 1.5×10^{-5} mole/L. Thus, the alkalinity increased by 8.2×10^{-4} mol/L = 41 mg/L as $CaCO_3$ (Fig. 6.2), which is close to that in the heterotrophic reactor (31 mg/L as $CaCO_3$). CO_2 consumption was calculated using Eqs. 6.3, 6.4, and 6.6: 1.7×10^{-4} mol/L, which contrasts to CO_2 production in the heterotrophic reactor (6.6×10^{-4} mol/L). The combined effect of alkalinity

increase and CO_2 consumption in the autotrophic reactor led to the much larger increases in pH and, thus, LSI.

In the pH-control scenario, the added CO_2 offsets the protons consumed by increasing the total concentration of carbonate species, but without changing the alkalinity. The "with CO_2" in Fig. 6.2 indicates that precipitation can be prevented entirely by sparging CO_2 to keep a pH set point at 7, and the experimental results confirm the prediction (Table 6.3).

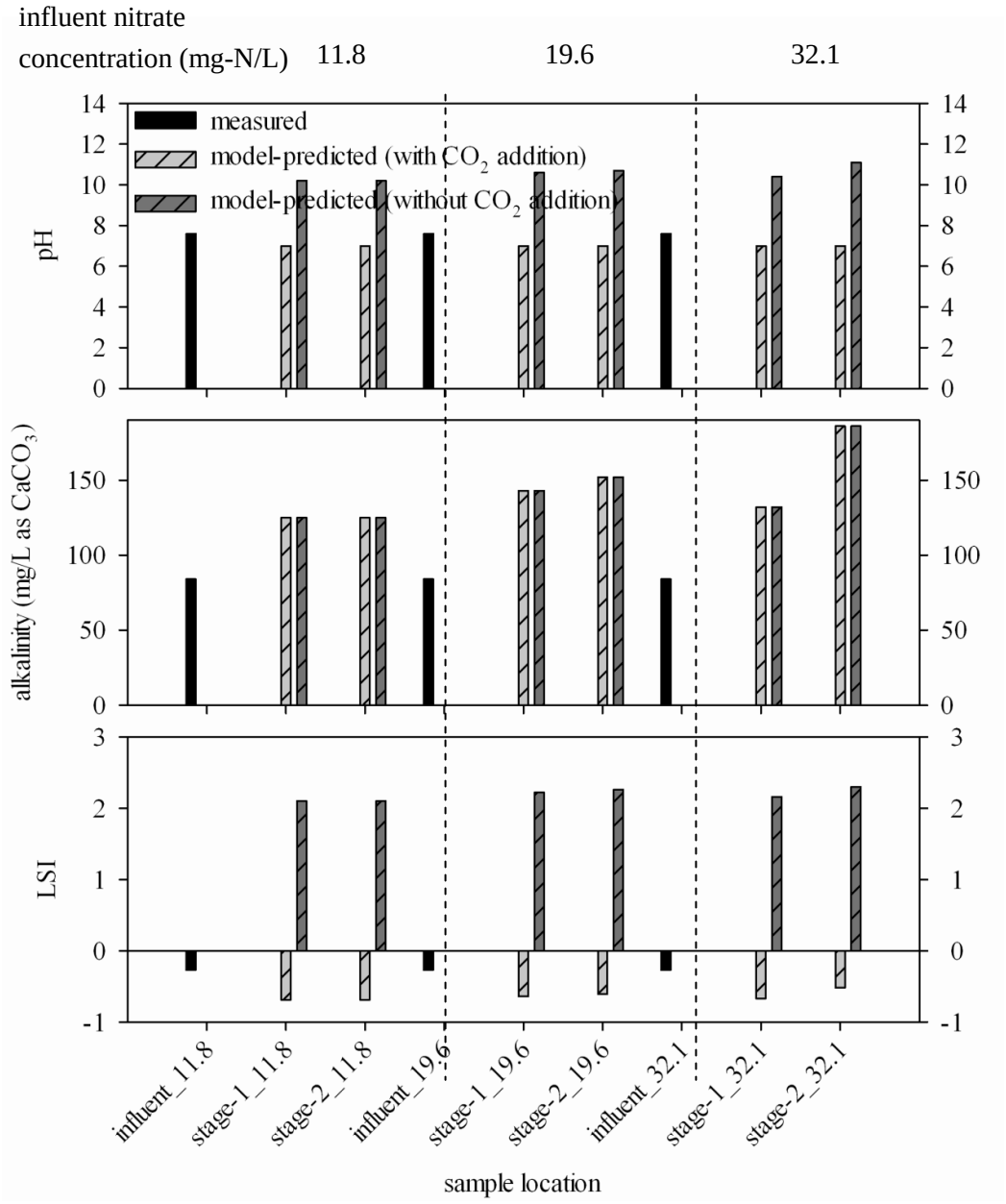

Fig. 6.2 Measured and model-predicted pH, alkalinity, and LSI in the autotrophic reactor for three influent nitrate concentrations. Two scenarios were considered, with and without CO_2 addition.

5. Preferred pH-Control Method

Though both methods -- CO_2 addition and HCl addition -- can be used for pH control in heterotrophic and autotrophic reactors, CO_2 addition is the preferred method for autotrophic reactor, since it has an additional advantage of providing the inorganic carbon source and increasing the total concentration of the carbonate buffering reactor. HCl addition is the preferred method for the heterotrophic reactor, since oxidation of organic matter already is increasing the concentration of the carbonate buffering system. Adding more CO_2 by sparging could cause the water to become over-saturated with CO_2, which would lead to CO_2 escape after the water leaves the denitrification reactor and a subsequent positive LSI.

The scenario of 32.1 mg-N/L can be used to illustrate the better pH-control method for autotrophic versus heterotrophic denitrification. With all nitrate completely reduced to N_2 in the H_2-based autotrophic reactor, CO_2 consumption due to denitrification and oxygen respiration was 4.1×10^{-4} mol/L. The total inorganic carbon concentration in the influent was calculated using the influent pH and alkalinity: 1.8×10^{-3} mole/L. Therefore, around 23% of the total inorganic carbon in the influent was consumed due to denitrification and oxygen respiration; this number would increase if the influent alkalinity were lower or the

influent nitrate concentration were higher. Should more than 100% of the influent inorganic carbon be consumed, CO_2 sparging would be the only feasible method.

In a heterotrophic reactor, when all nitrate was completely reduced to N_2, CO_2 production due to denitrification and oxygen respiration was 1.7×10^{-3} mol/L, which is close to the total carbon concentration in the influent. If external CO_2 were added to make the LSI 0, it should be added at 4.5×10^{-4} mole/L according to the model. When this CO_2 super-saturated water leaves the reactor and is open the atmosphere, 3.5×10^{-4} mole/L CO_2 (78% of the externally added CO_2) would escape, the pH would increase to 8.9, and the LSI would increase to 1.3; this follows calculation of carbonate species concentrations in open and closed systems (Snoeyink and Jenkins, 1980). In order to avoid the super-saturation condition in the effluent, HCl addition is a preferred pH-control method for heterotrophic reactors.

6. Conclusions

This chapter presents a model to predict the pH, alkalinity, and LSI in the effluent of H_2-based autotrophic denitrification and heterotrophic reactors. If the model outputs a pH value outside the optimal range for the denitrifiers or a high LSI value indicating serious precipitation potential, operators should take

measures to control the pH. The pH can be controlled using either of two methods: One is to add acid (*e.g.*, HCl) to balance excessive base production from denitrification; the other is to add acid CO_2 into the reactor to hold the pH to an set point using an automated pH feedback loop. The model can be used to estimate the required acid additions for both scenarios.

The model was evaluated using data from two pilot denitrification reactors: a two-stage heterotrophic reactor using ethanol as the electron donor and a two-stage H_2-based autotrophic reactor. The model-predicted pH, alkalinity, and LSI matched well with the experimental data in all cases tested. For the heterotrophic reactor, no acid addition was required for the long-term operation with an input NO_3^- concentration of 11.8 mg N/L, since the LSI remained negative. For short-term experiments with higher influent NO_3^- concentrations, the LSI was positive, and $CaCO_3$ precipitated. For the autotrophic reactor, precipitation would have been severe at all input NO_3^- concentrations, but precipitation was prevented by sparging CO_2 directly into the reactor.

The model showed that the autotrophic reactor was more sensitive to pH increases, even though denitrification directly increased alkalinity about the same amount for heterotrophic and H_2-based autotrophic processes. Since CO_2 is consumed in the autotrophic process and produced in the heterotrophic process,

pH and LSI increase more in the H_2-based autotrophic process than in the heterotrophic process, meaning that the autotrophic process is more susceptible to an increase in pH and to $CaCO_3$ precipitation. The actual impact on pH depends on the natural alkalinity (buffering) and the use of pH-control measures.

Acid *(e.g., HCl)* addition is the preferred pH-control method for heterotrophic processes, but CO_2 addition is the preferred method for H_2-based autotrophic processes.

Chapter 7

H_2-PERMEATION COEFFICIENTS OF THE FIBERS USED IN H_2-BASED MEMBRANE BIOFILM REACTORS

The main goal of this chapter is to test the H_2-permeation coefficients of three fibers commonly used in the MBfR. Relevant background information was presented in pages 16-18 in Chapter 1. This chapter (Chapter 7) develops and uses steady-state H_2-permeation tests and a mathematical model to determine the H_2-permeation coefficients of three fibers (composite, polyester, and polypropylene) commonly used in the MBfR. The H_2-permeation coefficients were then used as model inputs for the three multispecies biofilm models (Chapters 8, 9, and 10) and also used to correlate fiber type to contaminant-removal flux in previous MBfR experiments. Since existing contaminant-removal data for the polyester and polypropylene fibers were not adequate, special experiments were conducted to investigate the effect of H_2 pressure on contaminant removal in the MBfR with the polyester and polypropylene fibers.

This work was submitted to the *Journal of Membrane Science* and is currently in revision (Tang et al., 2012e). Chen Zhou and I collaboratively developed the mathemactical model and conducted the H_2-permeation tests. I

also correlated the fiber type to the contaminant-removal flux in previous MBfR experiments and prepared the manuscript. Aura Ontiveros-Valencia and Junghun Shin mainly conducted special contaminant-removal tests. Bruce E. Rittmann and Steven Van Ginkel mainly contributed to discussing the results, and they reviewed and revised the manuscript.

1. Materials and Methods

1.1 H_2-permeation experiments

Fig. 7.1 is schematic of the experimental set up for the steady-state H_2-permeation experiments. Deionized water was pumped through a serum bottle (total volume of 1.4×10^{-4} m^3) at a flow rate in the range of 2.0×10^{-3} to 4.5×10^{-3} m^3/d. The fibers in the serum bottle were pressurized with a H_2 pressure of 1.34 to 2.7 atm. H_2 diffused through the fiber wall and into the water, where it partitioned into headspace. Volumes of the water and headspace in the serum bottle depended on the steady-state pressure in the headspace. A magnetic stirring bar provided mixing to ensure that the liquid was completely mixed and that partitioning to the gas phase was rapid. The headspace gas was sampled regularly and assayed for its H_2 partial pressure. Steady state was achieved when

the H_2 partial pressure was stable for at least 3 days (> 40 hydraulic retention times).

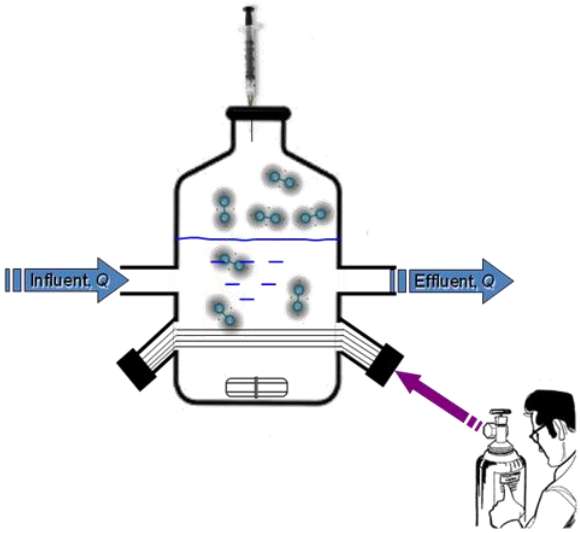

Fig. 7.1 Schematic of the set up for the H_2-permeation experiments

The H_2 pressure (P_{H2}) was measured using a gas chromatograph (GC 2010, Shimadzu) equipped with a thermal conductivity detector and a packed column (ShinCarbon ST 100/120 mesh, Restek Corporation). N_2 was the carrier gas fed at a constant pressure of 5.4 atm and a constant flow rate of 0.014 m^3/d, and the temperature conditions for injection, column, and detector were 120, 145, and 150 ℃, respectively. Analytical grade H_2 was used for standard calibration curves and for the experiments.

1.2 Mathematical model to determine the H_2-permeation coefficient

Fig. 7.2 illustrates the mathematical model using a representative fiber in a serum bottle. Fig. 7.3 plots a typical H_2-concentration profile in the permeation test. Based on Fig. 7.2, the H_2 mass balance at steady state in the serum bottle is

$$QC_{\text{inf}} - QC_{eff} = -J_m A_m = -J_{lf} A_{lf} \qquad \text{Eq. 7.1}$$

in which

$$J_m = D_m \frac{dC}{dz} = \frac{D_m}{z_m}\left(\frac{P_0}{RT} k_m - \frac{P_{m-lf}}{RT} k_m\right) \qquad \text{Eq. 7.2}$$

$$= \frac{D_m k_m}{RTz_m}(P_0 - P_{m-lf}) = \frac{K_m}{RTz_m}(P_0 - P_{m-lf})$$

$$J_{lf} = \frac{D_{lf}}{z_{lf}}\left(\frac{P_{m-lf}}{H} - \frac{P_{hs}}{H}\right) \qquad \text{Eq. 7.3}$$

$$A_m = \pi d_m L_m n_m \qquad \text{Eq. 7.4}$$

$$A_{lf} = \pi d_{lf} L_m n_m = \pi\left(d_m + z_{lf}\right) L_m n_m \qquad \text{Eq. 7.5}$$

$$z_{lf} = 2.1\times10^{-4} e^{-6.8\times10^{-3} u} \text{ (Chen and Huang, 1996)} \qquad \text{Eq. 7.6}$$

$$u = \frac{Q}{rh} \qquad \text{Eq. 7.7}$$

where

Q	= water flow rate	m^3/d
C_{inf}, C_{eff}	= H_2 concentrations in the influent and effluent	g/m^3
J_{lf}	= H_2 flux through the liquid film	g/m^2-d

A_m, A_{lf}	= total surface area of the membrane and liquid film	m^2
P_0, $P_{m\text{-}lf}$, P_{hs}	= H_2 pressure in the fiber lumen, at the interface of membrane and liquid film, and in the headspace	atm
D_{lf}	= H_2-diffusion coefficient in water	4.4×10^{-4} m^2/d (Macpherson and Unwin, 1997)
H	= Henry's Law constant of H_2	1.28 m^3-atm/mole (Crittenden et al., 2005)
d_m	= fiber outer diameter	m
L_m	= fiber length	m
n_m	= number of fibers	
d_{lf}	= liquid film outer diameter	m
z_{lf}	= liquid film thickness	m
u	= average flow shear velocity	m/d
r	= radius of the serum bottle	0.05 m
h	= water deeps in the serum bottle	0.04 - 0.08 m
Q	= water flow rate	m^3/d

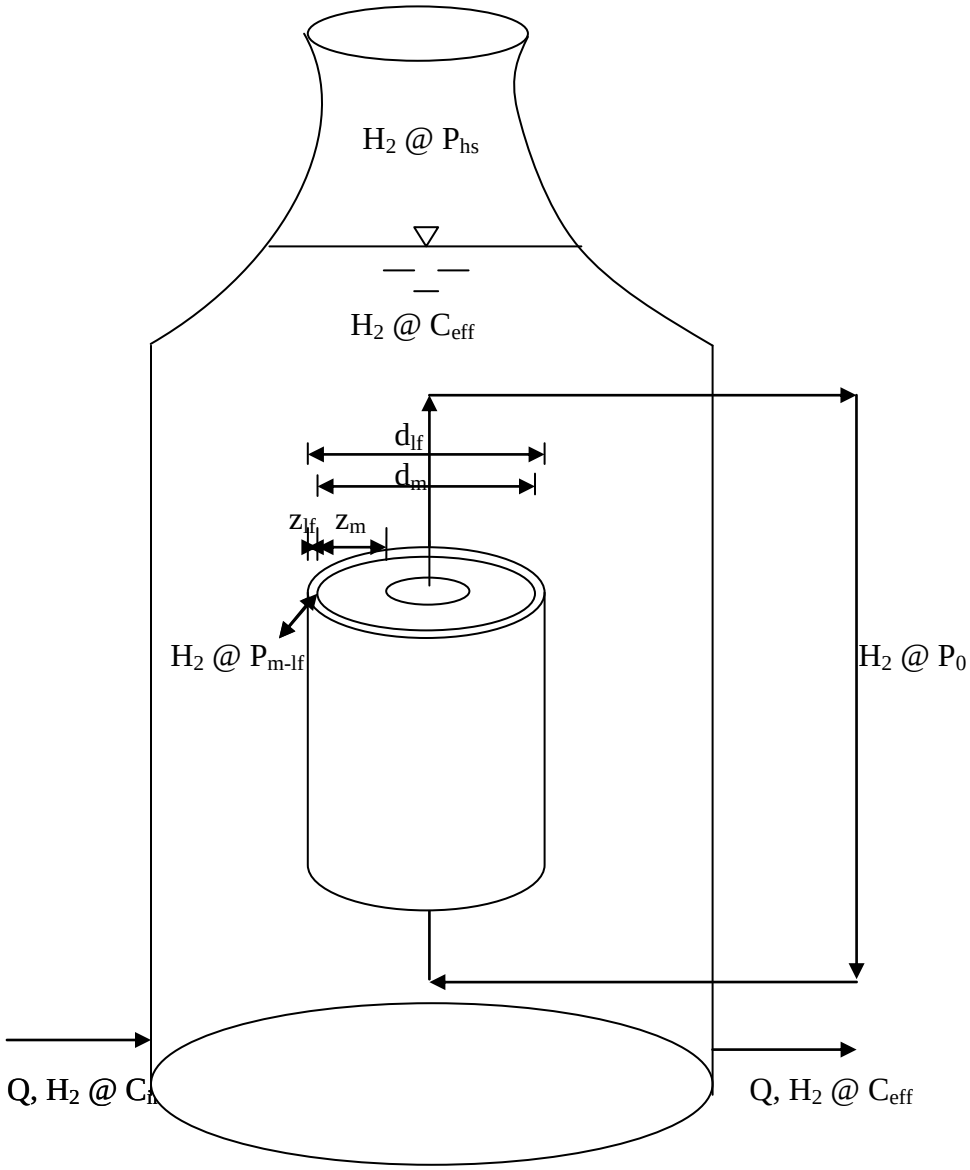

Fig. 7.2 Schematic diagram of the H_2 permeation tests

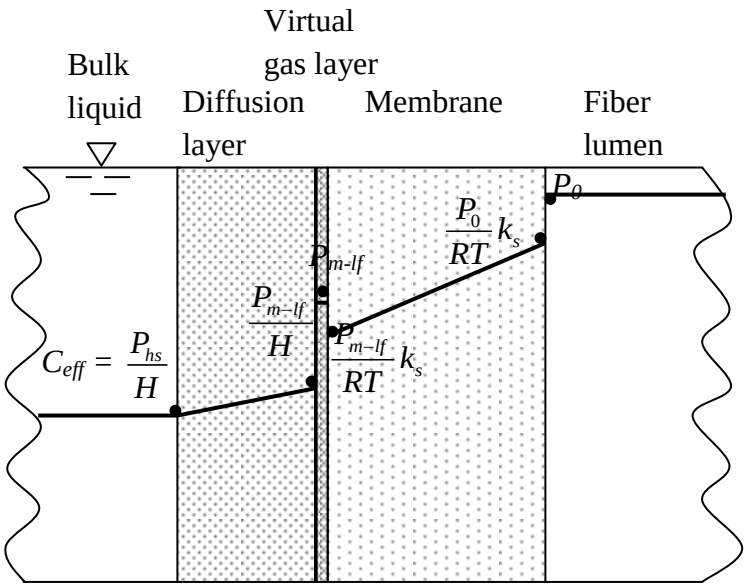

Fig. 7.3 A typical H_2-concentration profile in the permeation test. A virtual gas layer with a negligible thickness is added to correlate the H_2 concentrations in the membrane and diffusion layer. The symbols are defined in Chapters 1 and 7.

Substitution of Eqs. 7.2 - 7.5 into Eq. 7.1 leads to

$$P_{m-lf} = \frac{\alpha P_0 + \beta P_{hs}}{\alpha + \beta} \qquad \text{Eq. 7.8}$$

in which, $$\alpha = \frac{K_m}{z_m RT}, \beta = \frac{d_m + z_{lf}}{d_m} \frac{D_{lf}}{z_{lf} H}$$

Substitution of Eq. 7.8 into Eq. 7.1 ($QC_{\text{inf}} - QC_{eff} = -J_m A_m$) yields

$$P_{hs} = \frac{\alpha\beta H}{\alpha + \beta} \cdot \frac{(P_0 - P_{hs})\pi d_m L_m n_m}{Q} \qquad \text{Eq. 7.9}$$

Since we measured P_{hs}, the only unknown in Eq. 7.9 is K_m, which is part of α. Therefore, we determined K_m directly from P_{hs} using Eq. 7.9.

1.3 Fiber characteristics

We tested three fibers that have been utilized in bench and pilot testing of the MBfR (Lee and Rittmann, 2000; Chung et al., 2006; Ahn et al., 2009; Ziv-El and Rittmann, 2009a; Van Ginkel et al, 2008, 2011a,b,c): composite, polyester, and polypropylene. The wall of the composite fiber (Mitsubishi-Rayon Co.) has three layers. The outer and inner layers are hydrophobic, microporous (pore size: 0.1-0.15 μm), and made of polyethylene. Between the two layers is a 1-micron-thick layer of non-porous polyurethane. The non-porous layer allows the creation of a high driving force for gas permeation without bubble formation. The walls of the polyester and polypropylene fibers (Teijin Fibers, Ltd.) are single-layer and

non-porous. Characteristics of the three fibers are summarized in Table 7.1, and the experimental parameters for the experiments for each fiber are summarized in Table 7.2.

Table 7.1 Characteristics of three bubbleless gas-transfer fibers

Parameter	Composite fiber[a]	Polyester fiber[b]	Polypropylene fiber[b]	Units
Fiber outer diameter	280	200	200	μm
Cross-sectional area	61,544	31,400	31,400	μm^2
Fiber wall thickness	50	67	55	μm

[a]Model MHF 200TL Mitsubishi Rayon Co., Ltd., Tokyo, Japan.
[b]Products of Teijin Fibers Ltd., Osaka, Japan.

Table 7.2 Experimental parameters for the H_2-permeation tests

Parameter	Composite	Polyester	Polypropylene	Units
T	298	298	298	K
P_0	1.34	2.70	2.70	atm
Q	4.5×10^{-3}	2.0×10^{-3}	2.7×10^{-3}	m^3/d
z_m	5.0×10^{-5}	6.7×10^{-5}	5.5×10^{-5}	m
d_m	2.8×10^{-4}	2.0×10^{-4}	2.8×10^{-4}	m
L_m	0.07	0.07	0.07	m
n_m	36	72	72	

1.4 Comparison to existing results from MBfR experiments

In order to correlate the theoretical maximum H_2 fluxes for the different fibers at different H_2 pressures with actual H_2 fluxes observed in H_2-based MBfR experiments (tabulated in Table 7.3), we first calculated the theoretical maximum

H_2 fluxes using Eq. 7.2 by letting $P_{m\text{-}lf} = 0$. Then, we calculated the actual H_2 fluxes ($J_{H2} = J_{NO3} \times 3.03 \times 2/14 + J_{O2} \times 2.39 \times 2/32 + J_{SO4} \times 4.21 \times 2/96 + J_{SeO4} \times 3.38 \times 2/79 + J_{ClO4} \times 5.48 \times 2/99.5$) using the experimentally determined fluxes of oxidized compounds and the stoichiometric coefficients from Eqs. 7.10 - 7.14, which we obtained using the stoichiometric method established in Rittmann and McCarty (2001).

$$NO_3^- + 3.03H_2 + 0.23\ CO_2 + H^+ = 0.48N_2 + 0.046C_5H_7O_2N + 3.37H_2O \quad \text{Eq. 7.10}$$

$$O_2 + 2.39H_2 + 0.028NO_3^- + 0.14CO_2 + 0.028H^+ = 0.028C_5H_7O_2N + 2.31H_2O \quad \text{Eq. 7.11}$$

$$SO_4^{2-} + 4.21H_2 + 0.015NO_3^- + 0.075CO_2 + 1.52H^+ = 0.5H_2S + 0.5\ HS^- + 4.17\ H_2O + 0.015C_5H_7O_2N \quad \text{Eq. 7.12}$$

$$SeO_4^{2-} + 3.38H_2 + 0.027NO_3^- + 0.13CO_2 + 2.03H^+ = Se + 4.3H_2O + 0.027C_5H_7O_2N \quad \text{Eq. 7.13}$$

$$ClO_4^- + 5.48H_2 + 0.11H^+ + 0.11NO_3^- + 0.53CO_2 = Cl^- + 5.15\ H_2O + 0.11C_5H_7O_2N \quad \text{Eq. 7.14}$$

The actual H_2 fluxes are summarized in Table 7.3, which contains eleven data sets from seven independent studies with the composite fibers, three

data sets from one study with the polypropylene fibers, and one data set from a study using the polyester fibers. To provide more data sets for the polypropylene and polyester fibers, I helped Heping Zhao and Aura Ontiveros to do special experiments to generate H_2 fluxes using seven different H_2 pressures for both types of fibers. Materials and methods for the special experiments are summarized in the next section.

Table 7.3 Summary of actual H_2 fluxes in experiments with the H_2-based MBfR

Units	H_2 pressure atm	H_2 flux (J_{H2}) g H_2/m^2-d	NO_3 flux (J_{NO3}) g N/m^2-d	O_2 flux (J_{O2}) g O_2/m^2-d	SO_4^{2-} flux (J_{SO4}) g SO_4^{2-}/m^2-d	SeO_4^{2-} flux (J_{SeO4}) g Se/m^2-d	ClO_4^- flux (J_{ClO4}) g ClO_4^-/m^2-d	References
Composite	1.17	0.59	0.16	1.09	3.95	0.13	0.00	Chung et al., 2006
Composite	1.17	0.67	1.20	1.02	0.00	0.00	0.00	Ziv-El and Rittmann, 2009a
Composite	1.17	0.97	0.16	1.05	8.42	0.03	0.00	Chung et al., 2006
Composite	1.27	0.79	0.15	1.04	6.34	0.13	0.00	Chung et al., 2006
Composite	1.30	0.33	0.74	0.08	0.00	0.00	0.00	Ahn et al., 2009
Composite	1.31	0.44	0.80	0.64	0.00	0.00	0.00	Lee and Rittmann, 2000
Composite	1.42	0.55	1.00	0.80	0.00	0.00	0.00	Lee and Rittmann, 2000
Composite	1.44	0.95	1.70	1.45	0.00	0.00	0.00	Ziv-El and Rittmann, 2009a
Composite	2	0.17	0.38	0.01	0.00	0.00	0.00	Van Ginkel et al., 2008
Composite	2	0.57	1.3	0.02	0.00	0.00	0.00	Van Ginkel et al., 2011a
Composite	2	2.75	6.2	0.45	0.00	0.00	0.00	Van Ginkel et al., 2011b
polypropylene	1.24	0.19	0.14	0.87	0.00	0.00	0.00	this study
polypropylene	1.34	0.25	0.28	0.87	0.00	0.00	0.00	this study
polypropylene	1.68	0.24	0.26	0.87	0.00	0.00	0.00	this study
polypropylene	2.02	0.38	0.58	0.87	0.00	0.00	0.00	this study
polypropylene	2.19	0.34	0.60	0.51	0.00	0.00	0.04	Zhao et al. 2011
polypropylene	2.19	0.42	0.72	0.51	0.00	0.00	0.31	Zhao et al. 2011
polypropylene	2.19	0.45	0.84	0.51	0.00	0.00	0.12	Zhao et al. 2011
polypropylene	2.43	0.44	0.71	0.87	0.00	0.00	0.00	this study
polypropylene	2.70	0.50	0.85	0.87	0.00	0.00	0.00	this study

Table 7.3 Summary of actual H_2 fluxes in experiments with the H_2-based MBfR

Units	H_2 pressure atm	H_2 flux (J_{H2}) g H_2/m^2-d	NO_3 flux (J_{NO3}) g N/m^2-d	O_2 flux (J_{O2}) g O_2/m^2-d	SO_4^{2-} flux (J_{SO4}) g SO_4^{2-}/m^2-d	SeO_4^{2-} flux (J_{SeO4}) g Se/m^2-d	ClO_4^- flux (J_{ClO4}) g ClO_4^-/m^2-d	References
polypropylene	3.04	0.64	1.17	0.87	0.00	0.00	0.00	this study
polyester	2.50	0.14	0.31	0.05	0.00	0.00	0.00	this study
polyester	2.63	0.14	0.31	0.05	0.00	0.00	0.00	this study
polyester	2.77	0.14	0.32	0.05	0.00	0.00	0.00	this study
polyester	2.90	0.17	0.38	0.05	0.00	0.00	0.00	this study
polyester	3.0	0.31	0.6	0.09	0.00	0.4	0.00	Van Ginkel et al., 2011c
polyester	3.04	0.18	0.39	0.05	0.00	0.00	0.00	this study
polyester	3.18	0.19	0.41	0.05	0.00	0.00	0.00	this study
polyester	3.31	0.18	0.40	0.05	0.00	0.00	0.00	this study

1.5 Special polypropylene-fiber and polyester-fiber tests

The setup of the MBfRs was similar to that in Chung et al. (2006). The MBfR with polypropylene fibers had a working volume of 6.0×10^{-5} m^3 and contained 59 fibers that were 0.25-m long. The total fiber surface area was 0.0092 m^2. The MBfR was fed at a flow rate of 1.0×10^{-3} m^3/d with a synthetic groundwater that was similar to Chung et al. (2006) except that the influent nitrate concentration was 10 g N/m^3 and sulfate concentration was 42.5 g/m^3. We fixed all operating conditions except for stepwise increasing the H_2 pressure from 3.5 to 5, 10, 15, 20, 25, and 30 psig (1.24 to 1.34, 1.68, 2.02, 2.43, 2.70, and 3.04 atm). Note that all pressures in this paper with the units of atm represent absolute pressures. The H_2 pressure was stepped up once a steady state reduction of NO_3^- was achieved.

The MBfR with polyester fibers had a working volume of 6.0×10^{-5} m^3 and contained 120 fibers that were 0.28 m long. The total fiber surface area was 0.021 m^2. The MBfR was fed at a flow rate of 1.44×10^{-4} m^3/d with a groundwater. The groundwater contained NO_3^- at 65 g/m^3 as N, no NO_2^-, SO_4^{2-} at 3,740 g/m^3, alkalinity at 180 g/m^3 as $CaCO_3$, and hardness at 2,300 g/m^3 as $CaCO_3$. To prevent $CaCO_3$ precipitation, HCl was added to decrease alkalinity in the groundwater to 64 g $CaCO_3/m^3$. All operating conditions were fixed except for

the H_2 pressure, which we increased stepwise from 22 to 24, 26, 28, 30, 32, and 34 psig (2.50 to 2.63, 2.77, 2.90, 3.04, 3.18, and 3.31 atm).

Influents and effluents were sampled every day and assayed for NO_3^-, NO_2^-, and SO_4^{2-} using U.S.EPA method 300.1 (U.S.EPA, 1999). Dissolved oxygen was assumed to be at a saturated concentration in the influent (~8 g/m^3), since the feeding solution was open to the air, and we assumed that dissolved oxygen was zero in the effluent; these assumptions have been validated in previous MBfR studies (Nerenberg and Rittmann, 2004; Ziv-El and Rittmann, 2009a). The flux of an oxidized compound was calculated as $v(S_{in} - S_{out})/A$, where v = the flow rate (m^3/d), S_{in}, S_{out} = the average influent and effluent concentrations during a steady state (g/m^3), and A = the surface area of fibers (m^2). NO_2^- was ignored in calculation, since its concentration in the effluent was close to zero throughout the tests.

2. Results and Discussion

2.1 H_2-permeation coefficient

H_2 pressures in the headspace of the serum bottles are plotted in Fig. 7.4. The composite-fiber test reached steady state in the shortest time (~20 hours) and ended up with the highest headspace H_2 pressure (0.46 ± 0.00 atm). The test with the polyester fiber reached steady state in the longest time (~600 hours) and ended up with the lowest H_2 pressure (0.15 ± 0.01 atm).

Substitution of the average headspace H_2 pressures and the experimental parameters in Table 7.2 into Eq. 7.9 led to K_m values of 1.6×10^{-6}, 1.3×10^{-7}, and 4.6×10^{-8} m^2/d for the composite, polypropylene, and polyester fibers, respectively. Assuming $P_{m\text{-}lf} = 0$ in Eq. 7.2, a H_2 pressure (P_0) of 2.7 atm (25 psig) gives maximum H_2 fluxes of 7.0, 0.52, and 0.15 g H_2/m^2-d respectively, for the composite, polypropylene, and polyester fibers. At the same H_2 pressure, the ratios of the maximum H_2 fluxes are: composite: polypropylene: polyester fibers = 46: 3.5: 1.

Since the flow shear velocity (u) varied by position within the serum bottle, the empirical equation that I used to estimate the diffusion layer thickness (z_{lf}) may present some error. Therefore, I evaluated the sensitivity of z_{lf} to u and the sensitivity of the permeation coefficient (K_m) to z_{lf}. I summarize the

sensitivity analysis results for the polypropylene fiber in Table 7.4 as an example. A ten-fold change of u resulted in a change of z_{lf} of no more than 10%. z_{lf} was weakly sensitive to u, since the flow rate in the experiment (1.8 m/d) was very low, which made the diffusion layer thickness close to its maximum value (2.1×10^{-4} m) according to Eq. 7.6 ($z_{lf} = 2.1\times10^{-4} e^{-6.8\times10^{-3}u}$). A ten-fold change of z_{lf} resulted in a change of K_m of no more than 16%. Thus, K_m was weakly sensitive to z_{lf}, because the limiting step of H_2 diffusion is within the membrane instead of the liquid diffusion layer. Taking the two results together, variability in u within the serum bottle had minimal impact on the estimate of K_m.

Table 7.4 Sensitivity analysis for the polypropylene fiber

	Variable	Dependent	Sensitivity
z_{lf} to u	0.1 u	$z_{lf} = 2.10 \times 10^{-4}$ m	1.5%
	u = 1.8 m/d	$z_{lf} = 2.07 \times 10^{-4}$ m	
	10 u	$z_{lf} = 1.86 \times 10^{-4}$ m	10%
K_m to z_{lf}	0.1 z_{lf}	$K_m = 1.31 \times 10^{-7}$ m^2/d	2%
	$z_{lf} = 2.07 \times 10^{-4}$ m	$K_m = 1.34 \times 10^{-7}$ m^2/d	
	10 z_{lf}	$K_m = 1.55 \times 10^{-7}$ m^2/d	16%

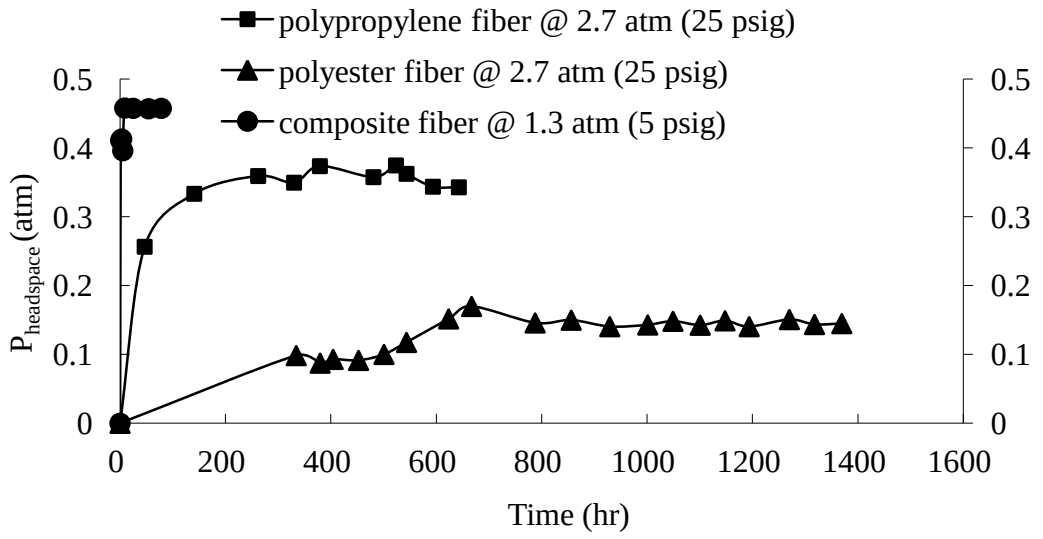

Fig. 7.4 Headspace H_2 pressures during the H_2-permeation experiments. Steady state P_{hs} was achieved at 20, 300, and 600hr for the composite, polypropylene, and polyester fibers, respectively.

2.2 Comparison between theoretical maximum H_2 fluxes and actual H_2 fluxes

Fig. 7.5 compares the theoretical maximum H_2 fluxes with calculated H_2 fluxes from MBfR experiments at various H_2 pressures. Consistent with the H_2-permeation coefficients we obtained, MBfRs with composite fibers were operated at the lowest H_2 pressures (2-15 psig, 1.1-2.0 atm), with polypropylene fiber at medium H_2 pressures (4-30 psig, 1.3-3.0 atm) and polyester fiber at the highest H_2 pressures (22-35 psig, 1.5-3.4 atm). Likewise, the MBfRs with composite fibers was operated at the high loadings (0.17-2.75 g H_2/m^2-d), with the MBfRs using polypropylene fibers and polyester fibers at correspondingly lower loadings (0.19-0.64 g H_2/m^2-d and 0.14-0.31 g H_2/m^2-d, respectively). Thus, the difference in H_2 pressures and contaminant loadings among different fibers originated from the ability of the fiber to deliver H_2 to the biofilm.

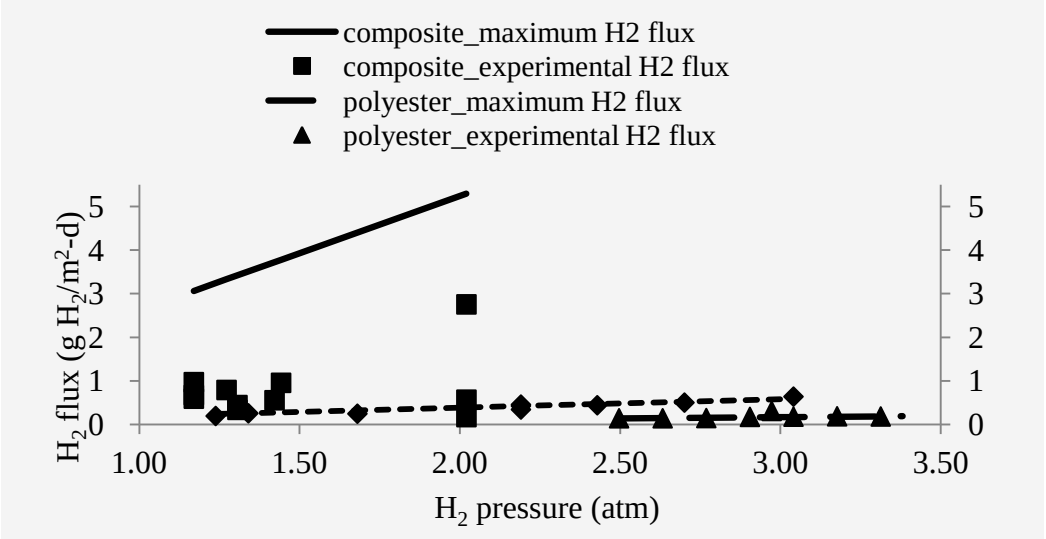

Fig. 7.5 Comparison of theoretical maximum H_2 fluxes and actual H_2 fluxes in MBfR experiments. To coordinate with this figure, the studies in Table 7.3 are arranged in ascending order of H_2 pressures for each fiber type.

Fig. 7.5 can be used to design a H_2-based MBfR. According to stoichiometry, contaminant removal fluxes determine the H_2 flux, and Fig. 7.5 relates the H_2 flux to a fiber type and a H_2 pressure. Therefore, a particular fiber type and H_2 pressure can be specified for a specific contaminant loading rate.

2.3 Limitation by H_2 delivery and membrane fouling

According to Fig. 7.5, the polypropylene and polyester fibers were operated close to their maximum H_2-delivery capacities; this is consistent with experimental observation that H_2 was limiting in these studies (Van Ginkel et al., 2011c; Zhao et al., 2011; this study): a change of H_2 pressure caused an almost

proportional change in the contaminant flux or an increase of contaminant loading did not lead to increase of contaminant flux.

Based on Fig. 7.5, the composite fiber was not operated close to its maximum H_2-delivery capacity. This reflects, in part, that the composite fibers have 13- to 46-fold higher H_2-delivery capacity than the single-wall fibers. However, other experimental evidence indicates that H_2 was limiting for some studies with the composite membrane (Chung et al., 2006; Van Ginkel et al., 2008, 2011a,b; Ahn et al., 2009; Ziv-El and Rittmann, 2009a; Lee and Rittmann, 2000, 2003): A change in H_2 pressure brought about an almost proportional change in the contaminant flux.

The explanation for H_2 limitation with the composite fiber is precipitation of mineral solids on and in the membrane. Precipitate fouling can increase mass-transport resistance associated with the fiber and lower the H_2 delivery rate. Whereas precipitate-associated fouling was not observed in the experiments with the polypropylene and polyester fibers, four of the seven composite-fiber studies (Van Ginkel et al., 2008, 2011a; Ziv-El and Rittmann, 2009a; 2009b; Lee and Rittmann, 2000; 2003) reported evidence of precipitation. Adham et al. (2004) observed $CaCO_3$ precipitation, and mild acid cleaning restored H_2 delivery. Van Ginkel et al. (2011a) also observed significant increases

in H_2 fluxes after acid cleanings. Ziv-El and Rittmann (2009b) observed $CaCO_3$ precipitate in the MBfR and then added HCl to lower the pH, which prevented further precipitation and loss of H_2 delivery. Lee and Rittmann (2003) observed a large amount of calcium-phosphate precipitate when using a phosphate buffer to control the pH. They found that higher pH was associated with more precipitates and lower nitrate removal efficiency.

Precipitation was important in experiments with the composite fibers because they allowed higher NO_3^- surface loadings, which led to higher production rates of proton consumption inside the biofilm during denitrification (Tang et al., 2011b). Furthermore, the effect of precipitates may be more severe with the composite fibers if the precipitates plug the small pores (pore size: 0.1-0.15 μm) in the outer layer of the composite fibers. In an MBfR-denitrification study that used X-ray diffraction to analyze precipitation, Rezania et al. (2006) observed the deposition of $CaCO_3$ and $\beta Ca_3(PO_4)_2$ inside the microporous membranes, and this counteracted the permeation advantage of the microporous outer layer. The single-wall polyester and polypropylene fibers do not have micropores that can be plugged.

2.4 Summary comparison of the fiber types

Compared to the single-wall polyester and polypropylene fibers, the composite fiber has an advantage of higher contaminant surface loading due to its higher H_2-permeation kinetics. Disadvantages of the composite fiber are its higher cost (associated with the three-layer structure) and the potential for pore plugging by precipitates. Fortunately, precipitation can be prevented by proper pH control (Tang et al., 2011b; Van Ginkel et al. 2011a).

Comparing the single-wall fibers, the polypropylene fiber's H_2 permeation coefficient is 3.5 fold larger than for the polyester fiber, and this gives a commensurately higher H_2 flux and contaminant loading. Thus, the polypropylene fiber is better, as long as precipitate fouling is managed through pH control.

3 Conclusions

Steady-state H_2-permeation tests established the H_2-permeation coefficients of three fibers commonly used in the H_2-based MBfR: 1.6×10^{-6}, 1.3×10^{-7}, and 4.6×10^{-8} m^2/d for composite, polypropylene, and polyester fibers, respectively. Based on the H_2-permeation coefficients, the ratio of the maximum H_2 flux is composite: polypropylene: polyester fibers = 46: 3.5: 1. Actual H_2 fluxes from MBfR experiments showed that the polyester and polypropylene

fibers were operated at their maximum H_2-delivery capacity, but the composite fibers operated well below the theoretical maximum. In some cases, the H_2 fluxes for the composite fibers were relatively low due to fiber fouling by mineral precipitates. Precipitation occurred in experiments with the composite fiber due to the higher NO_3^- loadings and plugging of the micropores of its outer layer.

Chapter 8

A MULTISPECIES BIOFILM MODEL FOR SIMULTANEOUS REDUCTION OF NITRATE AND PERCHLORATE

The main goal of this chapter is to develop a multispecies biofilm model that represents how the three important operating conditions (nitrate loading, perchlorate loading, and H_2 pressure) affect nitrate and perchlorate reduction and biomass distribution in the steady-state biofilm of an MBfR via four mechanisms. Relevant background information was presented in pages 11-14 in Chapter 1. This chapter (Chapter 8) develops the model, numerically solves the model using a novel three-step approach, optimizes model parameters by fitting data from bench-scale experiments, compares experimental biomass data to simulated biomass data, and quantifies the effect of operating conditions on nitrate and perchlorate reduction and biomass distribution.

This work was published in Tang et al. (2012b,c). I took the lead in developing and solving the model, optimizing parameters, and interpreting the results. Heping Zhao mainly conducted the bench-scale experiments used for parameter optimization, Andrew Marcus mainly contributed to developing the

model, and Bruce E. Rittmann and Rosa Krajmalnik-Brown mainly contributed to interpreting the results, along with reviewing and revising the manuscript.

1 Model Development

1.1 Model overview

The one-dimension model includes dual-substrate Monod kinetics for a steady-state biofilm having five solid and five dissolved components. The solid components are autotrophic denitrifying bacteria (DB), autotrophic perchlorate-reducing bacteria (PRB), heterotrophic bacteria (HB), inert biomass (IB), and extracellular polymeric substances (EPS). The dissolved components are nitrate, perchlorate, hydrogen (H_2), substrate-utilization-associated products (UAP), and biomass-associated products (BAP).

Fig. 8.1 shows the relationship among different model components. The relationships are based on the unified model of active biomass, inert biomass, and soluble microbial products, but adapted to the MBfR setting with denitrification and perchlorate reduction (Laspidou and Rittmann, 2002a, 2002b, 2004a, 2004b; Merkey, 2008; Ni et al., 2011). H_2, an inorganic electron donor and the sole energy source to the system, is oxidized by autotrophic DB that reduce nitrate and by autotrophic PRB that reduce perchlorate and nitrate. The

bacteria carry out these oxidation/reduction reactions to gain energy to allow synthesis of new biomass. At the same time, these reactions produce UAP and EPS. Thus, the electrons from H_2 are routed three ways: biomass synthesis (the fraction of electrons used for biomass synthesis is denoted k_1), UAP formation (k_2), EPS formation (k_3); mass balance requires that $k_1 + k_2 + k_3 = 1$. The electrons used for biomass synthesis are further divided into two parts: f_s° and f_e° (where $f_s^\circ + f_e^\circ = 1$). f_s° represents the portion converted to biomass, and f_e° represents the portion transferred to the electron acceptor to generate energy to produce biomass. f_s° equals the true yield (Y) when Y has the units of mg COD/mg COD. DB and PRB compete directly for H_2, and, within the PRB, perchlorate and nitrate can compete for H_2 and for common enzymes.

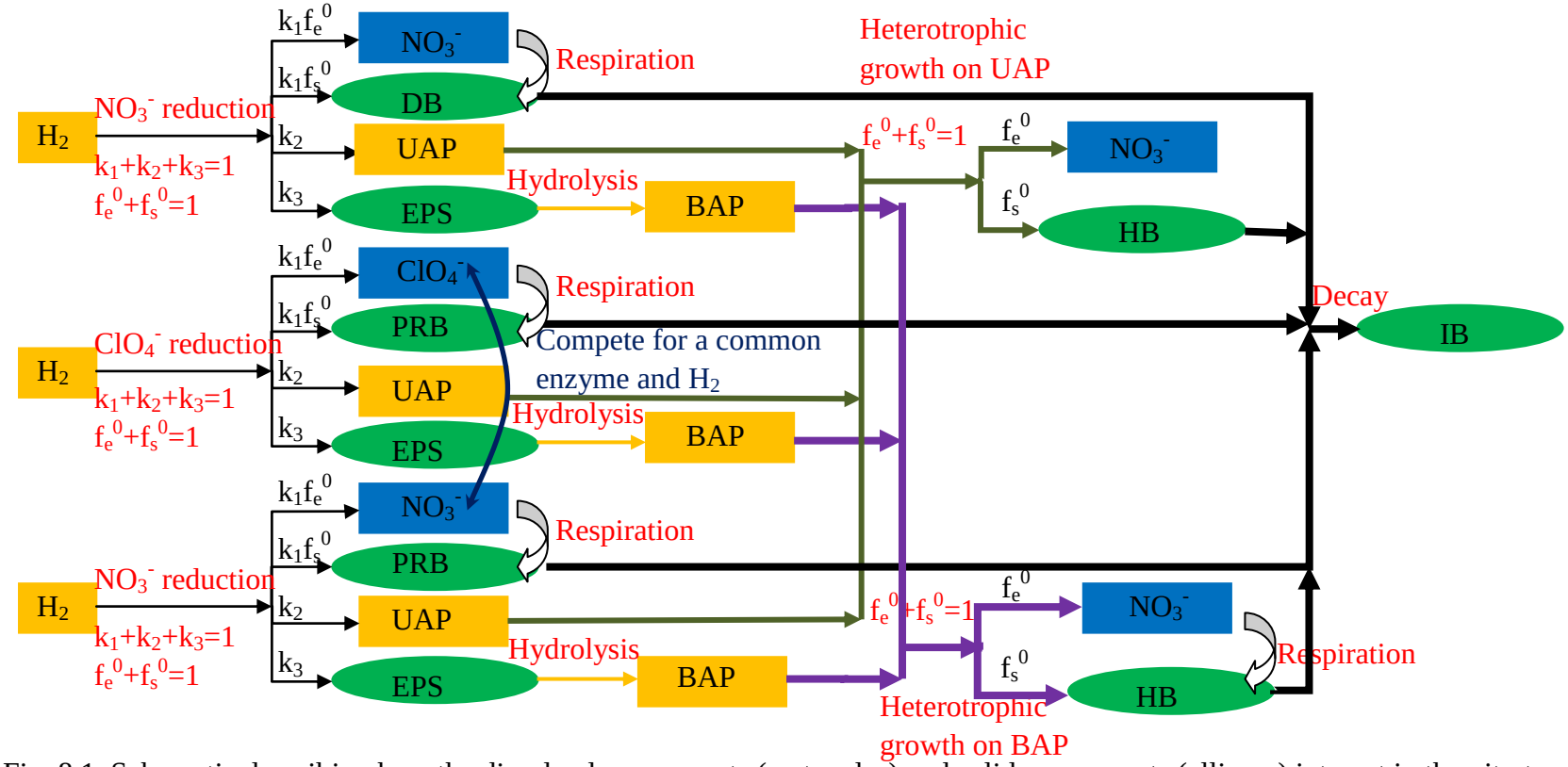

Fig. 8.1 Schematic describing how the dissolved components (rectangles) and solid components (ellipses) interact in the nitrate and perchlorate model. DB: autotrophic denitrifying bacteria; PRB: autotrophic perchlorate-reducing bacteria; HB: heterotrophic bacteria; IB: inert biomass; EPS: extracellular polymeric substances; UAP: substrate-utilization-associated products; BAP: biomass-associated products.

Hydrolysis converts EPS to BAP. HB can oxidize BAP and UAP as organic electron donors with nitrate as their electron acceptor. DB, PRB, and HB comprise the active biomass, and they are subject to inactivation and endogenous respiration. The inactivation processes produce inert, or nonbiodegradable, biomass (IB). Endogenous respiration oxidizes some of the active biomass and reduces the electron acceptors as a means to gain energy for cell maintenance.

1.2 Assumptions and simplifications

The model makes the following simplifying assumptions:

a) Suspended solids are negligible and ignored.

b) If present in the influent, dissolved O_2 is converted to equivalent NO_3^- according to electron equivalence (*i.e.*, 1 mg O_2/L is equivalent to 0.35 mg NO_3^--N/L): Most bacteria that respire NO_3^- also respire O_2 (Murray et al., 1990; Rittmann and McCarty, 2001).

c) The rate of biofilm detachment is a second-order function of the biofilm thickness; this is widely used in biofilm models (Wanner and Gujer, 1986; Stewart, 1992; Eberl et al., 2006; Merkey, 2008).

d) The biofilm is treated as a continuum: Components are described by averaging quantities such as concentrations and volume fractions instead of

characteristics of individual molecules and bacteria. The biofilm contains the five solid components in Fig. 8.1 in a distribution that has all or several types present at the same distance from the substratum and with the distribution changing with location in the biofilm. The void spaces between the solid components are interconnected and occupied by liquid that contains the dissolved components, and its volume fraction is constant across the biofilm depth. Active biomass consumes dissolved components in the liquid phase. (Laspidou and Rittmann, 2002a, 2002b, 2004a, 2004b).

e) PRB use nitrate and perchlorate as electron acceptors (Giblin and Frankenberger, 2001; Okeke et al., 2001; Nerenberg et al., 2002; Xu et al., 2004).

f) Competition for the same resources in PRB is expressed by competitive-inhibition coefficients in the acceptor part of dual-substrate Monod kinetics (Rittmann and McCarty, 2001). The inhibition coefficients equal the half-maximum-rate concentrations, a common practice for competitive inhibition (Garant and Lynd, 1998; Yu et al., 2005).

g) HB use only nitrate as their electron acceptor. Perchlorate use by HB is neglected because the nitrate loading is usually at orders of magnitude higher than the perchlorate loading (Gu et al., 2007; Choi and Silverstein, 2008).

Neglecting perchlorate use by HB can significantly simplify the numerical solution, while not significantly affecting the objective of the model.

h) HB produce no UAP and EPS, because the HB grow by oxidizing UAP and BAP produced by autotrophic DB and PRB. While heterotrophic metabolism may produce new UAP and EPS, their production must be small compared to the original production (de Silva and Rittmann, 2000; Laspidou and Rittmann, 2002a, 2002b).

i) A resistance approach using Fick's first law describes the flux of H_2 through the membrane (Shanahan and Semmens, 2004; Merkey, 2008).

j) Nutrients such as carbon and nitrogen source are not limiting. The energy required for biomass synthesis using carbon and nitrogen sources are considered in the true yields. For example, the H_2-oxidizing autotrophs have lower true yields than the heterotrophs due to the energy cost to fix inorganic C.

k) The system is well buffered so that extreme pH is avoided.

1.3 Mathematical equations

The mathematical equations are based on the multispecies biofilm models of Wanner and Gujer, Rittmann and Manem, and Laspidou and Rittmann,

but adapted to address the unique feature of nitrate and perchlorate reduction in the H_2-based MBfR (Wanner and Gujer, 1985, 1986; Rittmann and Manem, 1992; Laspidou and Rittmann, 2002a, 2002b, 2004a, 2004b). Table 8.1 summarizes growth and utilization rate terms (μ_{oi} and r_{oi}); Table 8.2 summarizes symbols in these equations and rate terms for model inputs; and Table 8.3 summarizes for model outputs. For dissolved components, subscripts 1 to 5 refer to nitrate, perchlorate, hydrogen, UAP, and BAP, respectively. For solid components, 1 to 5 refer to DB, PRB, IB, HB, and EPS, respectively. The finite difference method divides the biofilm into N elements: [0], [1],……, [N]. [0] represents the liquid/biofilm interface, and [N] represents the biofilm/membrane interface. For consistency, chemical oxygen demand (COD) is used as the mass unit for all components, since it represents electron equivalents. When used for electron acceptors, the unit COD refers to the electron-accepting capacity, expressed as negative COD.

Table 8.1 Process, component, and rate matrix in the nitrate and perchlorate model

Process (j)		Coefficient of component i in process j (η_{ij})									Conversion rate (R_j)
		Solid component					Dissolved component				
		DB	PRB	IB	HB	EPS	NO_3^-	ClO_4^-	H_2	UAP	BAP	
DB	growth	k_1				$\frac{k_5}{Y_1}$	$\frac{(Y_1-1)k_1}{Y_1}$		$-\frac{1}{Y_1}$	$\frac{k_4}{Y_1}$		$\mu_1 f_1 X_f \frac{S_{f1}}{K_1+S_{f1}} \frac{S_{f3}}{K_{31}+S_{f3}}$
	endogenous respiration	-1					-1					$p_1 f_1 X_f \frac{S_{f1}}{K_1+S_{f1}}$
	inactivation	-1		$(1-f_d)$								$b_1 f_1 X_f$
PRB	growth on ClO_4^-		k_2			$\frac{k_5}{Y_2}$		$\frac{(Y_2-1)k_2}{Y_2}$	$-\frac{1}{Y_2}$	$\frac{k_4}{Y_2}$		$\mu_2 f_2 X_f \frac{S_{f2}}{K_{22}(1+\frac{S_{f1}}{K_{21i}})+S_{f2}} \frac{S_{f3}}{K_{32}+S_{f3}}$
	growth on NO_3^-		k_3			$\frac{k_5}{Y_1}$	$\frac{(Y_1-1)k_3}{Y_1}$		$-\frac{1}{Y_1}$	$\frac{k_4}{Y_1}$		$\mu_1 f_2 X_f \frac{S_{f1}}{K_{21}(1+\frac{S_{f2}}{K_{22i}})+S_{f1}} \frac{S_{f3}}{K_{31}+S_{f3}}$
	endogenous respiration on ClO_4^-		-1					-1				$p_{22} f_2 X_f \frac{S_{f2}}{K_{22}(1+\frac{S_{f1}}{K_{21i}})+S_{f2}}$
	endogenous respiration on NO_3^-		-1				-1					$p_{21} f_2 X_f \frac{S_{f1}}{K_{21}(1+\frac{S_{f2}}{K_{22i}})+S_{f1}}$

Table 8.1 Process, component, and rate matrix in the nitrate and perchlorate model

Process (j)		Coefficient of component i in process j (η_{ij})									Conversion rate (R_j)
		Solid component					Dissolved component				
		DB	PRB	IB	HB	EPS	NO_3^-	ClO_4^-	H_2	UAP	BAP	
	inactivation	-1	$(1-f_d)$									$b_2 f_2 X_f$
HB	growth on UAP				1		$-\frac{(1-Y_4)}{Y_4}$			$-\frac{1}{Y_4}$		$\mu_4 f_4 X_f \frac{S_{f4}}{K_4+S_{f4}} \frac{S_{f1}}{K_1+S_{f1}}$
	growth on BAP				1		$-\frac{(1-Y_5)}{Y_5}$				$-\frac{1}{Y_5}$	$\mu_4 f_4 X_f \frac{S_{f5}}{K_5+S_{f5}} \frac{S_{f1}}{K_1+S_{f1}}$
	endogenous respiration				-1		-1					$p_4 f_4 X_f \frac{S_{f1}}{K_1+S_{f1}}$
	inactivation			$(1-f_d)$	-1							$b_4 f_4 X_f$
EPS	hydrolysis					-1					1	$k_{hyd} f_5 X_f$
summed conversion rate of component i		summed specific growth rate: $\mu_{oi} = \frac{\sum_j (\eta_{ij} R_j)}{f_i X_f}$					summed utilization rate: $r_{oi} = \sum_j (\eta_{ij} R_j)$					

Table 8.2 Inputs for the nitrate and perchlorate model[a]

Symbols	Description	Units	Values
K_1	Half-maximum-rate concentration for nitrate	mg-COD/cm^3	5.7×10^{-4} (optimized)
K_{21}	Half-maximum-rate concentration for nitrate (PRB)	mg-COD/cm^3	5.7×10^{-4} (optimized)
K_{22}	Half-maximum-rate concentration for perchlorate	mg-COD/cm^3	5.0×10^{-4} (optimized)
K_{31}	Half-maximum-rate concentration for H_2 in denitrification	mg-COD/cm^3	1.6×10^{-5} (Kurt et al., 1987)
K_{32}	Half-maximum-rate concentration for H_2 in perchlorate reduction	mg-COD/cm^3	1.6×10^{-5} (Kurt et al., 1987)
K_4	Half-maximum-rate concentration for UAP	mg-COD/cm^3	5.0×10^{-3} (Wanner and Gujer, 1986)
K_5	Half-maximum-rate concentration for BAP	mg-COD/cm^3	5.0×10^{-3} (Wanner and Gujer, 1986)
K_{1i}	Inhibition coefficient of nitrate on perchlorate	mg-COD/cm^3	5.7×10^{-4} (optimized)
K_{2i}	Inhibition coefficient of perchlorate on nitrate	mg-COD/cm^3	5.0×10^{-4} (optimized)
Y_1	Yield in denitrification	mg-COD/mg-COD	0.2 (Rittmann and McCarty,2001)
Y_2	Yield in perchlorate reduction	mg-COD/mg-COD	0.27 (Rittmann and McCarty,2001)
Y_4	Yield of HB growing on UAP	mg-COD/mg-COD	0.6 (Rittmann and McCarty,2001)
Y_5	Yield of HB growing on BAP	mg-COD/mg-COD	0.6 (Rittmann and McCarty,2001)
μ_1	Maximum specific growth rate in denitrification	d^{-1}	1.0 (Rittmann and McCarty,2001)
μ_2	Maximum specific growth rate in perchlorate	d^{-1}	1.5 (Rittmann and

Table 8.2 Inputs for the nitrate and perchlorate model[a]

Symbols	Description	Units	Values
	reduction		McCarty,2001)
μ_4	Maximum specific growth rate of HB	d^{-1}	13.2 (Rittmann and McCarty,2001)
k_1	Coefficient for electrons used for biomass production		0.77 (Rittmann and McCarty,2001)
k_2	Coefficient for electrons going to UAP		0.05 (Rittmann and McCarty,2001)
k_3	Coefficient for electrons going to EPS		0.18 (Rittmann and McCarty,2001)
b_1	Inactivation coefficient for DB	d^{-1}	0.05 (Wanner and Gujer, 1986)
b_2	Inactivation coefficient for PRB	d^{-1}	0.1 (Rittmann and McCarty,2001)
b_4	Inactivation coefficient for HB	d^{-1}	0.1 (Wanner and Gujer, 1986)
k_d	Biofilm detachment coefficient	$cm^{-1}d^{-1}$	36 (Trulear and Characklis; 1982)
p_1	Endogenous respiration rate for DB	d^{-1}	0.05 (Wanner and Gujer, 1986)
p_{21}	Endogenous respiration rate for PRB (nitrate as the electron acceptor)	d^{-1}	0.05 Wanner and Gujer, 1986
p_{22}	Endogenous respiration rate for PRB (perchlorate as the electron acceptor)	d^{-1}	0.075 (Rittmann and McCarty,2001)
p_4	Endogenous respiration rate for HB	d^{-1}	0.2 (Rittmann and McCarty,2001)
D_1	Nitrate diffusion coefficient within the diffusion layer	cm^2/d	1.2 (Williamson and McCarty,1976)
D_2	Perchlorate diffusion coefficient within the diffusion layer	cm^2/d	1.6 (Tuwiner, 1962)

Table 8.2 Inputs for the nitrate and perchlorate model[a]

Symbols	Description	Units	Values
D_3	H_2 diffusion coefficient within the diffusion layer	cm^2/d	4.4 (Macpherson and Unwin, 1997)
D_4	UAP diffusion coefficient within the diffusion layer	cm^2/d	1 (Merkey, 2008)
D_5	BAP diffusion coefficient within the diffusion layer	cm^2/d	0.6[b] (Merkey, 2008)
D_{f1}	Nitrate diffusion coefficient within the biofilm	cm^2/d	0.96 (Williamson and McCarty,1976)
D_{f2}	Perchlorate diffusion coefficient within the biofilm	cm^2/d	1.3 (Tuwiner, 1962)
D_{f3}	H_2 diffusion coefficient within the biofilm	cm^2/d	3.5 (Macpherson and Unwin, 1997)
D_{f4}	UAP diffusion coefficient within the biofilm	cm^2/d	0.8 (Merkey, 2008)
D_{f5}	BAP diffusion coefficient within the biofilm	cm^2/d	0.5[b] (Merkey, 2008)
k_{hyd}	Hydrolysis rate of EPS	d^{-1}	0.22 (Rittmann and McCarty, 2001)
f_d	Fraction of biomass that is biodegradable		0.8 (Rittmann and McCarty, 2001)
X_f	Biomass density	$mg\text{-}COD/cm^3$	79.3 (Rittmann and McCarty, 2001)
L_d	Thickness of effective diffusion layer	cm	0.01 (Rittmann and McCarty, 2001)
k_H	dimensionless Henry's Law constant of H_2		0.01907 (Sander, 1999)
L_m	Thickness of membrane	cm	0.0055 [c]
A	Total membrane surface area	cm^2	54.9 [c]
Q	Flow rate	cm^3/d	350 [c]

Table 8.2 Inputs for the nitrate and perchlorate model[a]

Symbols	Description	Units	Values
K_m	Hydrogen permeation coefficient within the membrane	cm^2/d	0.0013 [c]
S_0	Oxygen concentration in the influent	$mg\text{-}COD/cm^3$	0.008 [c]
S_1	Nitrate concentration in the influent	$mg\text{-}COD/cm^3$	0 - 0.064 [c]
S_2	Perchlorate concentration in the influent	$mg\text{-}COD/cm^3$	0.00054 - 0.0061 [c]
S_{g3}	H_2 concentration in the bulk gas	$mg\text{-}COD/cm^3$	1.44 [c]

Notes:

a. Conversion factors: 1 mg NO_3^--N: 2.857 mg COD; 1 mg cell: 1.982 mg COD; 1 mg ClO_4^{2-}: 0.643 mg COD; 1 mg H_2: 8 mg COD.
b. Since BAP molecules are larger than UAP, the diffusion coefficients of BAP are assumed to be 60% of those of UAP.
c. All the system-specific data are from the bench-scale experiment used to optimize parameters (Zhao et al., 2011).

Table 8.3 Outputs for the nitrate and perchlorate model

Symbols	Description	Units
J_1	nitrate flux into the biofilm	mg-COD/cm^2-d
J_2	perchlorate flux into the biofilm	mg-COD/cm^2-d
J_{3m}	H_2 flux into the biofilm	mg-COD/cm^2-d
J_3	H_2 flux out of the biofilm	mg-COD/cm^2-d
J_4	UAP flux out of the biofilm	mg-COD/cm^2-d
J_5	BAP flux out of the biofilm	mg-COD/cm^2-d
L_f	thickness of biofilm	cm
f_1	fraction of DB	--
f_2	fraction of PRB	--
f_3	fraction of IB	--
f_4	fraction of HB	--
f_5	fraction of EPS	--
S_{f1}	nitrate concentration in the biofilm	mg-COD/cm^3
S_{f2}	perchlorate concentration in the biofilm	mg-COD/cm^3
S_{f3}	H_2 concentration in the biofilm	mg-COD/cm^3
S_{f4}	UAP concentration in the biofilm	mg-COD/cm^3
S_{f5}	BAP concentration in the biofilm	mg-COD/cm^3
S_{b1}	nitrate concentration in the effluent	mg-COD /cm^3
S_{b2}	perchlorate concentration in the effluent	mg-COD /cm^3
S_{b3}	H_2 concentration in the effluent	mg-COD /cm^3
S_{b4}	UAP concentration in the effluent	mg-COD /cm^3
S_{b5}	BAP concentration in the effluent	mg-COD /cm^3

1.3.1 Dissolved components

1.3.1.1 Governing equation

For dissolved components, Fick's first law describes diffusion, and dual-limitation Monod kinetics describes utilization (Rittmann and McCarty, 1980; Bae and Rittmann, 1996). Because these rates are very fast compared to solid-component growth or decay, a steady-state mass balance is accurate for dissolved components at any point in the biofilm (Eberl et al., 2006):

$$D_{fi}\frac{d^2S_{fi}}{dz^2} - r_{oi} = 0 \qquad (i = 1,2,3,4,5) \qquad \text{Eq. 8.1}$$

1.3.1.2 Boundary equations

Eq. 8.1 has two boundary conditions: one at the attachment surface (membrane side) and the other at the biofilm surface (liquid side). At the attachment surface, the fluxes of components 1 (nitrate), 2 (perchlorate), 4 (UAP), and 5 (BAP) are zero.

$$\left.\frac{dS_{fi}}{dz}\right|_{z=L_f} = 0 \qquad (i = 1,2,4,5) \qquad \text{Eq. 8.2}$$

Dissolved-component 3 (H_2) has a consistent-flux boundary condition at the attachment surface: The H_2 flux through the membrane must equal the flux into the biofilm at the biofilm-membrane interface (Eq. 8.3). Using the resistance

approach, Fick's first law describes the flux of H_2 through the membrane (Shanahan and Semmens, 2004; Merkey, 2008).

$$\frac{D_m}{L_m}\left(S_{g3}k_s - \frac{S_{f3}[N]}{k_H}k_s\right) = D_{f3}\left.\frac{dS_{f3}}{dz}\right|_{z=L_f} = J_{m3} \qquad \text{Eq. 8.3}$$

The physical meaning of Eq. 8.3 is illustrated in Fig. 8.2, a typical H_2-concentration profile in the MBfR. A virtual gas layer, whose thickness is negligible, is used to correlate the H_2 concentrations in the membrane and the biofilm, since an equilibrium coefficient between the membrane and the biofilm is not available. The product of the H_2-diffusion coefficient within the membrane (D_m) and the H_2 solubility within the membrane (k_s) in Eq 8.3 is the H_2-permeation coefficient within the membrane (symbol K_m); it is a characteristic of a fiber and can be experimentally determined (Chapter 7).

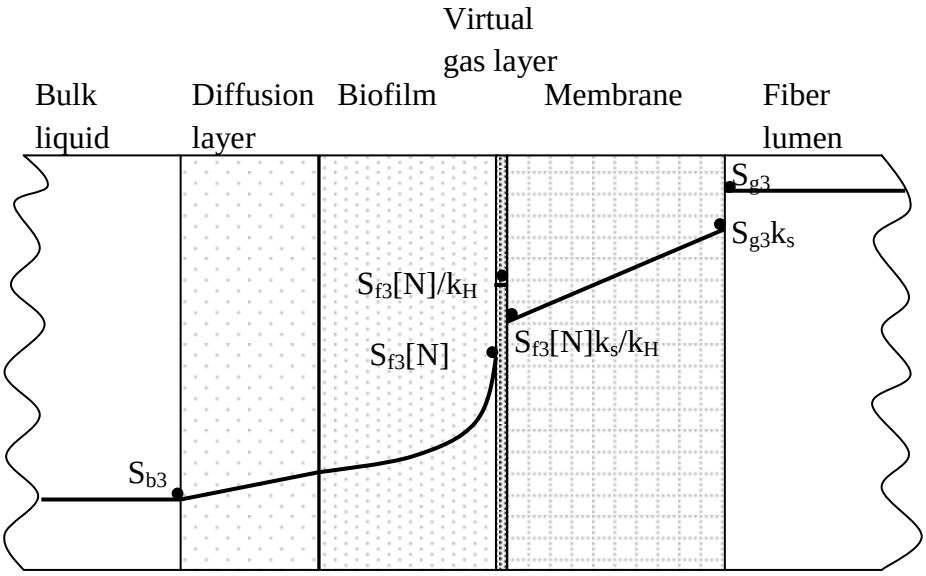

Fig. 8.2 A typical H_2-concentration profile in the MBfR. A virtual gas layer with a negligible thickness is added to correlate the H_2 concentrations in the membrane and biofilm. S_{b3}: H_2 concentration in the bulk liquid; $S_{f3}[N]$: H_2 concentration at the biofilm surface (interface of biofilm and membrane); k_H: Henry's law constant for H_2; k_s: solubility coefficient of H_2 in membrane; and S_{g3}: H_2 concentration in the fiber lumen.

All dissolved components at the biofilm's outer surface are subject to a consistent-flux boundary condition: A dissolved-component flux through the diffusion layer equals the flux of this dissolved component in or out of the biofilm (Eq. 8.4). The transport of dissolved components through the diffusion layer and into or out of the biofilm is described with the resistance approach using Fick's first law (Rittmann and McCarty, 2001).

$$\frac{D_i}{L_i}(S_{bi} - S_{fi}[0]) = D_{fi}\left.\frac{dS_{fi}}{dz}\right|_{z=0} \qquad (i = 1,2,3,4,5) \qquad \text{Eq. 8.4}$$

S_b in Eq. 8.4 is obtained using Eq. 8.5, which comes from combining mass conservation in the reactor (Eq. 8.6) and Fick's first law for the diffusion layer (Eq. 8.7).

$$S_{bi} = \frac{S_i \frac{Q}{A} + S_{fi}[0]\frac{D_i}{L_i}}{(\frac{D_i}{L_i} + \frac{Q}{A})} \qquad (i = 1,2,3,4,5) \qquad \text{Eq. 8.5}$$

$$J_i A = (S_i - S_{bi})Q \qquad (i = 1,2,3,4,5) \qquad \text{Eq. 8.6}$$

$$J_i = \frac{D_i}{L_i}(S_{bi} - S_{fi}[0]) \qquad (i = 1,2) \qquad \text{Eq. 8.7}$$

Substituting Eq. 8.5 into 8.4 provides the final form of the boundary condition at the biofilm surface (Eq. 8.8).

$$\frac{S_i - S_{fi}[0]}{\frac{A}{Q} + \frac{L_i}{D_i}} = D_{fi}\left.\frac{dS_{fi}}{dz}\right|_{z=0} = J_i \qquad (i = 1,2,3,4,5) \qquad \text{Eq. 8.8}$$

1.3.2 Solid components

1.3.2.1 Governing equation

A steady-state mass balance for solid-component i can be written for a differential volume element A'dz of the biofilm, (Rittmann and Manem, 1992)

$$A'dz\mu_{oi(z)}X_f f_{i(z)} = A'J_{Xi(z+dz)} - A'J_{Xi(z)} \qquad (i = 1,2,3,4,5) \qquad \text{Eq. 8.9}$$

In Eq. 8.9, A' is the biofilm volume element's lateral area for mass transport (L^2), and $J_{x(z)}$ and $J_{x(z+dz)}$ are the flux of solid-component i through area A' at the points z and (z + dz) in the biofilm. The sum of the volume fraction of every solid-component must equal 1.

$$\sum_{i=1}^{i=5} f_i = 1 \qquad \text{Eq. 8.10}$$

Eq. 8.9 divided by $A' dz X_f$ yields

$$\mu_{oi(z)} f_{i(z)} = \frac{1}{X_f} \frac{J_{Xi(z+dz)} - J_{X\,i(z)}}{dz} \qquad (i = 1,2,3,4,5) \qquad \text{Eq. 8.11}$$

which for dz approaching 0 leads to

$$\mu_{oi(z)} f_{i(z)} = \frac{1}{X_f} \frac{\partial J_{X\,i(z)}}{\partial z} \qquad (i = 1,2,3,4,5) \qquad \text{Eq. 8.12}$$

The biomass flux can be expressed by the velocity u at which the biomass moves with respect to the support medium multiplied by the concentration $X_f f_i$ of the solid component.

$$J_{X\,i(z)} = u_{(z)} X_f\, f_{i(z)} \qquad (i = 1,2,3,4,5) \qquad \text{Eq. 8.13}$$

Using Eq. 8.13, Eq. 8.12 can be rewritten as:

$$\mu_{oi(z)} f_{i(z)} = \frac{1}{X_f} \frac{\partial (u_{(z)} X_f\, f_{i(z)})}{\partial z} = \frac{\partial (u_{(z)} f_{i(z)})}{\partial z}$$
$$\overset{\text{chain rule}}{=} f_{i(z)} \frac{\partial u_{(z)}}{\partial z} + u_{(z)} \frac{\partial f_{i(z)}}{\partial z} \qquad (i = 1,2,3,4,5) \qquad \text{Eq. 8.14}$$

The average observed specific growth rate of all solid components at a location z in the biofilm is defined as

$$\overline{\mu_{o(z)}} = \sum_{i=1}^{i=5} (\mu_{oi(z)} f_{i(z)}) \qquad \text{Eq. 8.15}$$

which can be converted to

$$\begin{aligned}
\overline{\mu_{o(z)}} &= \sum_{i=1}^{i=5} (\mu_{oi(z)} f_{i(z)}) \\
&= \sum_{i=1}^{i=5} \left(\frac{1}{X_f} \frac{\partial J_{X\,i(z)}}{\partial z}\right) \text{ (}\textit{obtained from}\text{ Eq. 8.12)} \\
&= \frac{1}{X_f} \frac{\partial \sum_{i=1}^{i=5} (J_{X\,i(z)})}{\partial z} \\
&= \frac{1}{X_f} \frac{\partial \sum_{i=1}^{i=5} (u_{(z)} X_f f_{i(z)})}{\partial z} \text{ (}\textit{obtained from}\text{ Eq. 8.13)} \\
&= \frac{\partial \sum_{i=1}^{i=5} (u_{(z)} f_{i(z)})}{\partial z} = \frac{\partial (u_{(z)} \times \sum_{i=1}^{i=5} f_{i(z)})}{\partial z} \\
&= \frac{\partial u_{(z)}}{\partial z} \text{ (}\textit{obtained from equation}\text{ 10)} \qquad (i = 1,2,3,4,5)
\end{aligned} \qquad \text{Eq. 8.16}$$

Substituting Eq. 8.16 into Eq. 8.14 gives

$$\mu_{oi(z)} f_{i(z)} = f_{i(z)} \frac{\partial u_{(z)}}{\partial z} + u_{(z)} \frac{\partial f_{i(z)}}{\partial z} = f_{i(z)} \overline{\mu_{o(z)}} + u_{(z)} \frac{\partial f_{i(z)}}{\partial z}$$

or

$$(\mu_{oi(z)} - \overline{\mu_{o(z)}}) f_{i(z)} - u_{(z)} \frac{\partial f_{i(z)}}{\partial z} = 0 \qquad \text{Eq. 8.17}$$

or

$$\frac{\partial f_{i(z)}}{\partial z} = \frac{(\mu_{oi(z)} - \overline{\mu_{o(z)}}) f_{i(z)}}{u_{(z)}} \qquad (i = 1,2,3,4,5)$$

The physical meaning of Eq. 8.17 is that the fraction variation of a solid component at the position z ($\frac{\partial f_{i(z)}}{\partial z}$) is in direct proportion to the difference between the specific growth rate of this solid component and the average specific growth rate of all solid components at the position z ($(\mu_{oi(z)} - \overline{\mu_{o(z)}})$) and the fraction of this solid component at the position z ($f_{i(z)}$), but it is in inverse proportion to the velocity at which the biomass moves in respect to the support media ($u_{(z)}$).

The $u_{(z)}$ term in Eq. 8.17 can be calculated using Eq. 8.13

$$u_{(z)} = \frac{J_{X\,i(z)}}{X_f f_{i(z)}} = \frac{f_{i(z)} \int_{L_f}^{z} (\textit{net growth rate of all species}) dz}{X_f f_{i(z)}}$$
$$= \frac{\int_{L_f}^{z} (\textit{net growth rate of all species}) dz}{X_f} \qquad \text{Eq. 8.18}$$
$$= \frac{\int_{L_f}^{z} (\sum_{i=1}^{i=5} \mu_{oi} f_i X_f) dz}{X_f} = \int_{L_f}^{z} (\sum_{i=1}^{i=5} \mu_{oi} f_i) dz$$

Substitution of Eqs. 8.15 and 8.18 into Eq. 8.17 provides the final form of the mass balance for solid component i,

$$(\int_{L_f}^{z} (\sum_{i=1}^{i=5} \mu_{oi} f_i) dz) \frac{\partial f_{i(z)}}{\partial z} = (\mu_{oi(z)} - \sum_{i=1}^{i=5} (\mu_{oi(z)} f_{i(z)})) f_{i(z)} \qquad (i = 1,2,3,4,5) \quad \text{Eq. 8.19}$$

1.3.2.2 Boundary equations

The boundary condition of Eq. 8.19 is no flux for any solid species into the attachment surface,

$$\left.\frac{\partial f_i}{\partial z}\right|_{z=L_f} = 0 \qquad (i = 1,2,3,4,5) \qquad \text{Eq. 8.20}$$

Substitution of Eq. 8.20 into Eq. 8.19 provides the final form of the membrane-side boundary condition for Eq. 8.19,

$$(\mu_{oi(z)}\Big|_{z=L_f} - \sum_{i=1}^{i=5}(\mu_{oi(z)}\, f_{i(z)})\Big|_{z=L_f})\, f_{i(z)}\Big|_{z=L_f} = 0 \qquad (i = 1,2,3,4,5) \qquad \text{Eq. 8.21}$$

The physical meaning of Eq. 8.21 is that all existing solid components have the same net specific growth rate at the attachment surface.

For a steady-state biofilm, the mass of solid components detached from the biofilm's outer surface equals the net production of all solid components throughout the biofilm:

$$b_{\text{det}} AX_f = u_{(z)} AX_f \qquad \text{Eq. 8.22}$$

When this situation is true, the biofilm attains a constant surface accumulation, and this translates into a constant thickness if the biomass density does not change.

The specific detachment rate is given by a second-order function of biofilm thickness (Wanner and Gujer, 1986; Stewart, 1992; Eberl, 2006; Merkey, 2008):

$$b_{\text{det}} = k_d L_f^{\,2} \qquad \text{Eq. 8.23}$$

Divided by AX_f, Eq. 8.22 transforms to:

$$b_{\text{det}} = u_{(z)} \qquad \text{Eq. 8.24}$$

The physical meaning of Eq. 8.24 is that, at the biofilm surface, the detachment rate equals the velocity at which the biomass moves with respect to the support media. In other words, the biofilm surface remains stationary, because advecting surface biomass balances the biomass removed from the surface by detachment.

Substituting Eqs. 8.18 and 8.23 into Eq 8.24 provides the final steady-state equation, which is also the liquid-side boundary condition for Eq. 8.19.

$$k_d L_f^{\,2} = \int_{L_f}^{0} \left(\sum_{i=1}^{i=5} \mu_{oi} f_i\right) dz \qquad \text{Eq. 8.25}$$

In summary, the dissolved-component mass-balance Eq. 8.1, which is associated with boundary-condition Eqs. 8.2, 8.3, and 8.8, governs dissolved components. The solid-component mass-balance Eq. 8.19, which is associated with boundary-condition Eqs. 8.20 and 8.25, governs solid components. Eqs. 8.3, 8.5, and 8.8 calculate model outputs, including effluent concentrations and fluxes of dissolved components.

1.3.3 Causality of promotion and inhibition

The model mathematically captures the four mechanisms responsible for promoting and inhibiting effects:

1) Eq. 8.3 captures how competition for H_2 leads to inhibition between DB and PRB and between nitrate and perchlorate reduction by PRB (Mechanism 1); this is represented using the membrane-side boundary condition in which the H_2 flux through the membrane equals the H_2 flux into the biofilm. The H_2 flux has a maximum that is determined by membrane type and H_2 pressure in the fiber lumen.
2) In Table 8.1, the PRB growth term shows how nitrate promotes PRB growth, because PRB also can use nitrate as an electron acceptor (Mechanism 2).
3) In Table 8.1, competitive-nhibition coefficients for nitrate and perchlorate show how competition for the same resources in PRB for reduction of nitrate and perchlorate leads to inhibition effects between nitrate and perchlorate (Mechanism 3).
4) Eq. 8.10 captures how competition for space in a biofilm leads to inhibition of DB, PRB, or both: the biomass conservation equation in which the sum of volume fraction of every solid component must equal 1 (Mechanism 4). Competition for space exists among the five solid components and the volume fraction of a solid component depends on its relative growth rate compared to

the growth rates of other solid components. The specific growth rates depend on substrate concentrations and kinetics parameters (e.g., specific maximum growth rates and half-maximum-rate concentrations). Though PRB can use two electron acceptors and have the same kinetics for denitrification as DB, the net synthesis rate of PRB is not always higher than the net synthesis rate of DB, because, 1) nitrate and perchlorate competitively inhibit the reduction kinetics of each other within PRB; and 2) PRB have slightly higher inactivation and endogenous respiration rates, since they can respire two electron acceptors.

The four mechanisms are considered because they correlate the major operating conditions (nitrate loading, perchlorate loading, and H_2 pressure) to nitrate and perchlorate removal. The mechanisms act in concert. Mechanism 1 (competition for H_2) controls the maximum H_2 available and the distribution of H_2 between nitrate and perchlorate reduction. The distribution of H_2 depends on the distribution of biomass in the biofilm, which is controlled by Mechanism 4 (competition for space). Mechanism 4 is directly affected by Mechanisms 2 (PRB use two acceptors) and 3 (competition for the same resources within PRB).

2. Numerical Solution

The mathematical model is solved in three steps, implemented using Microsoft Visual C++ 6.0 (Microsoft Corporation). The first step uses a guessed biofilm thickness (L_f) to solve together for dissolved-component Eqs. 8.1, 8.2, 8.3, and 8.8 and solid-component Eqs. 8.19, 8.20, and 8.25: This gives the biofilm profiles for all dissolved and solid components. Since the dissolved-component and solid-component equations are partial differential equations and/or integral equations, these equations are approximated using a Finite Difference Method. More specifically, N elements, each having a thickness of $dz = L_f/N$, are used to define the biofilm domain. Based on these elements, 9N + 9 functions generated approximates the partial differential equations and/or integral equations involving 9N + 9 unknowns: $S_{fi}[0] - S_{fi}[N]$ (i = 1, 2, 3, 4, 5) and $f_i[0] - f_i[N]$ (i = 1, 2, 4, 5). Because most the 9N + 9 equations are nonlinear, they are numerically solved using a Newton-Raphson Method (Chapra and Canale, 2002). Then, $f_3[0] - f_3[N]$ is obtained using $\sum_{i=1}^{i=5} f_i = 1$. $S_{fi}[0] - S_{fi}[N]$ (i = 1,2,3,4,5) and $f_i[0] - f_i[N]$ (i = 1,2,3,4,5) obtained in this step are pseudo-steady-state solutions based on an assumed biofilm thickness.

The second step is to calculate the biofilm thickness. Since pseudo-steady-state solutions of $S_{fi}[0] - S_{fi}[N]$ (i = 1,2,3,4,5) and $f_i[0] - f_i[N]$ (i = 1,2,3,4,5)

are available from step 1, a new biofilm thickness (L_f') is calculated using Eq. 8.25: $L_f' = \frac{\int_{L_f}^{0} (\sum_{i=1}^{i=5} \mu_{oi} f_i) dz}{k_d L_f} = \frac{\int_{L_f}^{0} (\sum_{i=1}^{i=5} \mu_{oi} f_i)}{k_d N}$. This thickness usually is different from the one guessed in step one (L_f). Then, another new thickness is calculated as $L_f'' = L_f + \frac{L_f' - L_f}{2}$, and this thickness is closer to the solution, compared with L_f and L_f' . Then, L_f'' is used in step 1 to recalculate $S_{fi}[0] - S_{fi}[N]$ (i = 1,2,3,4,5) and $f_i[0] - f_i[N]$ (i = 1,2,3,4,5). This process repeated until $L_f'' = L_f$, which is the steady-state-biofilm thickness.

In the third step, Eqs. 8.3, 8.5, and 8.8 are used to calculate the effluent concentrations and fluxes.

This three-step approach differs from the traditional way of solving multispecies biofilm models, because it solves the model directly for steady state. Multispecies biofilm models are inherently stiff, since they include certain variables (solid components) that respond orders of magnitude slower to changes of operating conditions than other variables (dissolved components) (Gujer and Wanner, 1989; Eberl et al., 2006). The traditional way to treat the challenge of high stiffness is to calculate the profiles of the dissolved components by a steady-state model and model the biofilm itself as dynamic. A steady-state solution is achieved when biofilm also reaches a steady-state condition. This concept has

been applied in almost all complicated biofilm models, and an excellent example is the simulation program AQUASIM (Gujer and Wanner, 1989; Reichert, 1998; Eberl et al., 2006). In my approach, I treat the dissolved and solid components in the same way and directly solve them for steady state.

My three-step approach converges quickly, since, after each iteration, the biofilm thickness approaches its steady-state value by approximately halving the difference between its value in this iteration and its steady-state value. The iteration number depends on the initial guess and is typically less than 10. Thus, this approach saves substantial computational time compared to the traditional method, a major benefit when many steady states should be modeled. Section 4 provides a good example when it models the performance for nitrate loadings ranging from 0 to 1.6 g N/m^2-d, perchlorate loadings ranging from 0 to 0.65 g ClO_4^-/m^2-d, and H_2 pressures ranging from 1.4 to 3.0 atm. Furthermore, the three-step approach converges effectively for different operating conditions, because it takes advantage of two factors that reduce the stiffness. First, the number of unknowns in the mathematical model is reduced to only include L_f, $S_{fi}[0] - S_{fi}[N]$ ($i = 1, 2, 3, 4, 5$), and $f_i[0] - f_i[N]$ ($i = 1, 2, 4, 5$). Other model outputs, including the effluent dissolved-component concentrations and fluxes, are calculated after solving the model. This is possible because all the boundary-condition equations are set up for this purpose. Second, L_f, an important characteristic of the biofilm,

is known in each iteration; this significantly reduces the stiffness, since L_f frequently appears in the model functions.

3. Parameter Optimization

Model inputs, which are summarized in Table 8.2, fall into five categories:

1) System-specific parameters, such as flow rate and nitrate and perchlorate concentrations in the influent.

2) Physical constants, such as diffusion coefficients and Henry's law constant for H_2.

3) Biological parameters that are constrained in a narrow range by the cell's stoichiometry and energetics, such as biomass yields, maximum specific growth rates, and endogenous respiration rates. Rittmann and McCarty (2001) presented thermodynamic and kinetic methods to estimate these parameters; I also evaluated them using experimentally measured values when available. I used maximum specific growth rates (μ_{max}) with perchlorate and nitrate reduction of 1.5 and 1.0 d^{-1}, respectively. I computed them using the thermodynamic and kinetic methods in Rittmann and McCarty (2001). Growth-rate ranges of the literature support my computations: Nerenberg et al. (2006) summarized the μ_{max} for perchlorate of

0.8-2.4 d^{-1}, and Ghafaria et al. (2010) summarized the μ_{max} with nitrate of 0.8-1.1 d^{-1}.

4) Biological parameters that are not constrained by the cell's stoichiometry and energetics, but have consistent reported values, such as the half-maximum-rate concentration of H_2.

5) Biological parameters that are not constrained by the cell's stoichiometry and energetics, and the literature does not report consistent values: e.g., the half-maximum-rate concentrations of nitrate and perchlorate and the inhibition coefficients of nitrate and perchlorate (the half-maximum-rate concentration of nitrate or perchlorate equals its inhibition coefficient according to assumption f). The previously reported half-maximum-rate concentrations of nitrate ($K_1 = K_{21}$, Table 8.2) vary from 0.035 to 0.5 mg N/L^3 (Kurt et al., 1987; Smith et al., 1994; Buttiglieri et al., 2005; Rezania et al. 2005; Nerenberg and Rittmann, 2006). The reported half-maximum-rate concentrations for perchlorate (K_{22}, Table 8.2) vary from 0.16 to 31 mg ClO_4^-/L^3 (Logan et al., 2001; Waller et al., 2004; Nerenberg and Rittmann, 2006). The values of these two parameters are optimized by best-fitting data from a bench-scale experiment with six combinations of influent nitrate and perchlorate concentrations (Zhao et al., 2011).

The six steady-state experiments had the same H_2 pressure (2.2 atm), but the influent nitrate and perchlorate concentrations varied from 2.8 - 25 mg

NO_3-N/L and 0.85 - 9.5 mg ClO_4^-/L, respectively (Zhao et al., 2011). A steady state was reached when the effluent nitrate and perchlorate concentrations were stable in the effluent for at least three consecutive days. The six steady states can be classified into 2 groups. Group 1 -- including steady states 1 to 3 -- had a steady influent perchlorate concentration of ~ 0.9 mg ClO_4^-/L, and the influent nitrate concentration increased from 2.8 to 14 mg N/L. Group 2 -- steady states 4 to 6 – had a stable influent perchlorate concentration of ~9 mg ClO_4^-/L, and the influent nitrate concentration increased from 2.8 to 25 mg N/L.

Optimized K_{21} (= K_1) and K_{22} are defined as the combination of K_{21} and K_{22} that best fit the six steady-state data sets from Zhao et al. (2011). Best fitting occurs when the objective function $\sum_{k=1}^{k=6}[(\frac{J^k_{1,experiment}-J^k_{1,model}}{J^k_{1,experiment}})^2+(\frac{J^k_{2,experiment}-J^k_{2,model}}{J^k_{2,experiment}})^2]$ reaches a minimum; this is a relative least-squares criterion (Sáez and Rittmann, 1992). J_1^k and J_2^k represent the nitrate and perchlorate fluxes in the steady state k. During the modeling process, I varied K_{21} and K_{22} in their reported range, but fixed all other parameters (Table 8.2) except the influent nitrate and perchlorate concentrations.

Fig. 8.3 compares the experimental and model-simulated fluxes of nitrate and perchlorate with the optimized parameters. Fig. 8.4 compares the effluent concentrations of nitrate and perchlorate. Experimental and model results

fit best when the half-maximum-rate concentration of nitrate ($K_1 = K_{21}$) equals 0.2 mg N/L and the half-maximum-rate concentration of perchlorate (K_{22}) equals 0.8 mg ClO_4^-/cm^3. These parameters are approximately in the middle of their reported ranges mentioned in above.

To assess the sensitivity of these parameters, Figs. 8.3 and 8.4 also plot model simulated data with the parameters at 0.5 and 2 times of the optimized values. The nitrate data are less sensitive to changes of the three parameters than are the perchlorate data, because PRB and DB can reduce nitrate; thus, changes in their distribution do not affect nitrate removal much. Perchlorate data in steady state 6 are most sensitive because all four mechanisms act most intensively in this steady state. Doubling K_{22} or halving K_1 reduces the competitiveness of PRB against DB, decreasing the ClO_4^- flux from 0.12 to 0 g ClO_4^-/m^2-d and increasing the NO_3^- flux from 0.84 to 0.86 g N/m^2-d. In contrast, halving K_{22} or doubling K_1 improves the competitiveness of PRB against DB, increasing the ClO_4^- flux from 0.12 to 0.32 g ClO_4^-/m^2-d and decreasing the NO_3^- flux from 0.84 to 0.78 g N/m^2-d. The values of K_1 and K_{22} depend on the microorganisms selected in the microbial community.

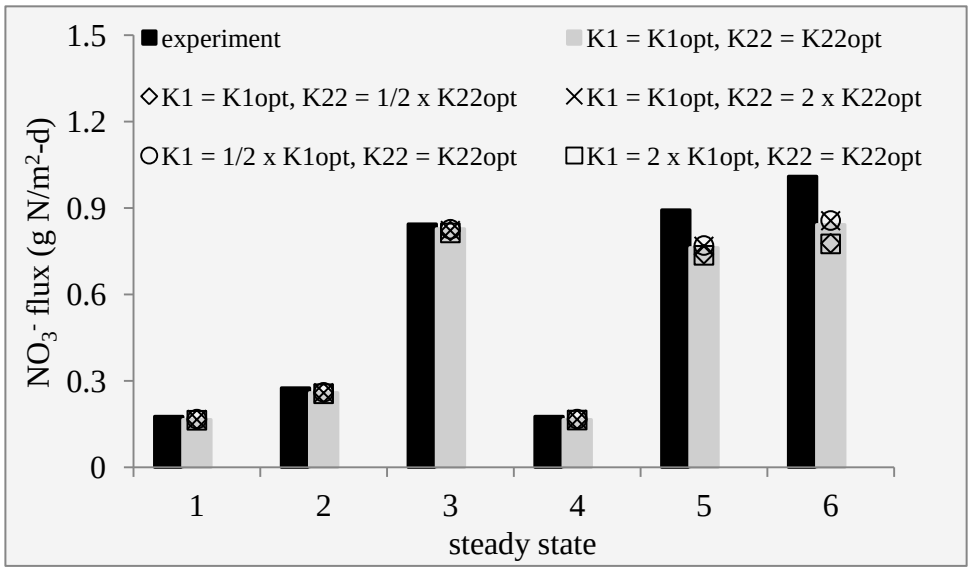

a.

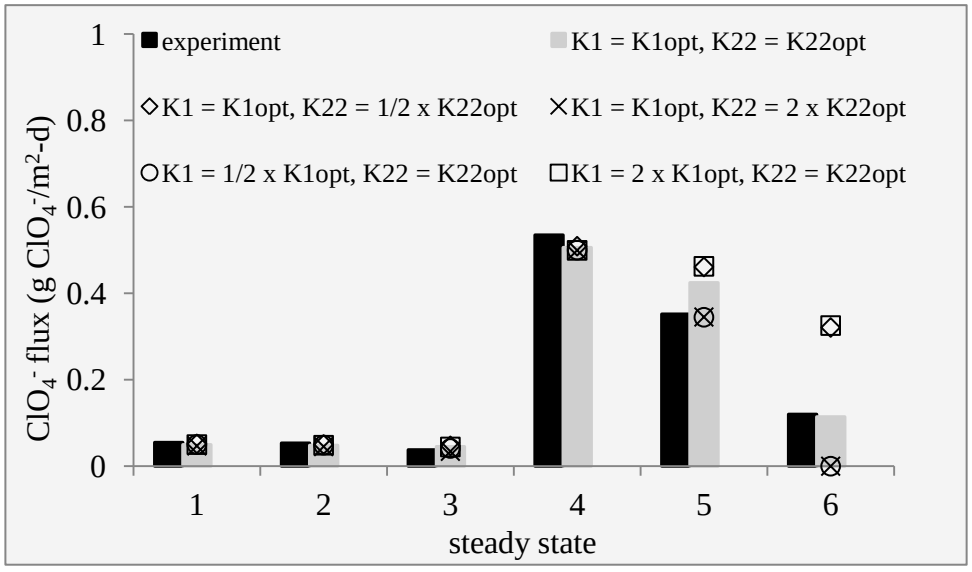

b.

Fig. 8.3 Comparison of fluxes of nitrate and perchlorate from the experiments and from the model with optimized parameters ($K_1 = K_{21} = 0.2$ mg N/L and $K_{22} = 0.8$ mg ClO_4^-/L), and with the three parameters at a half or two times of the optimized values.

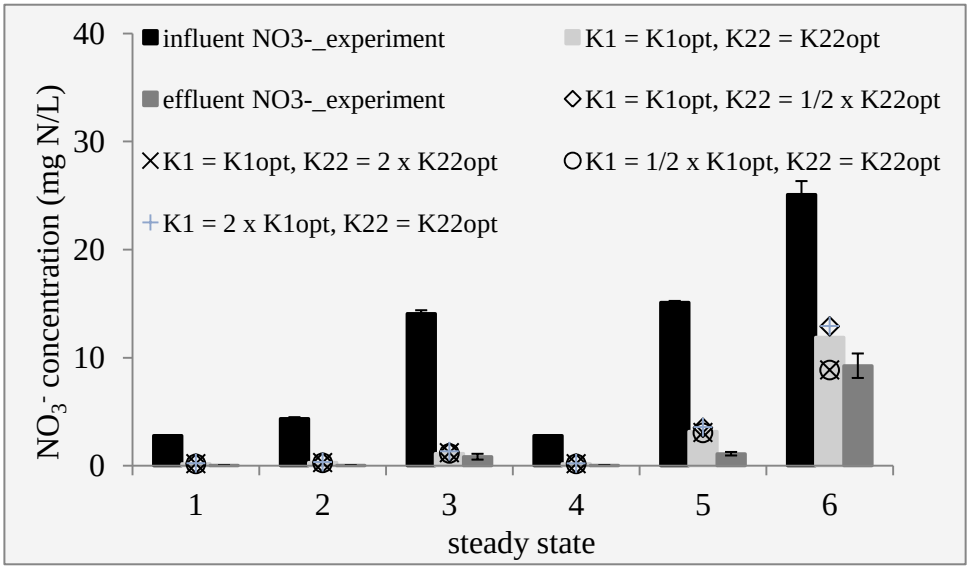

a.

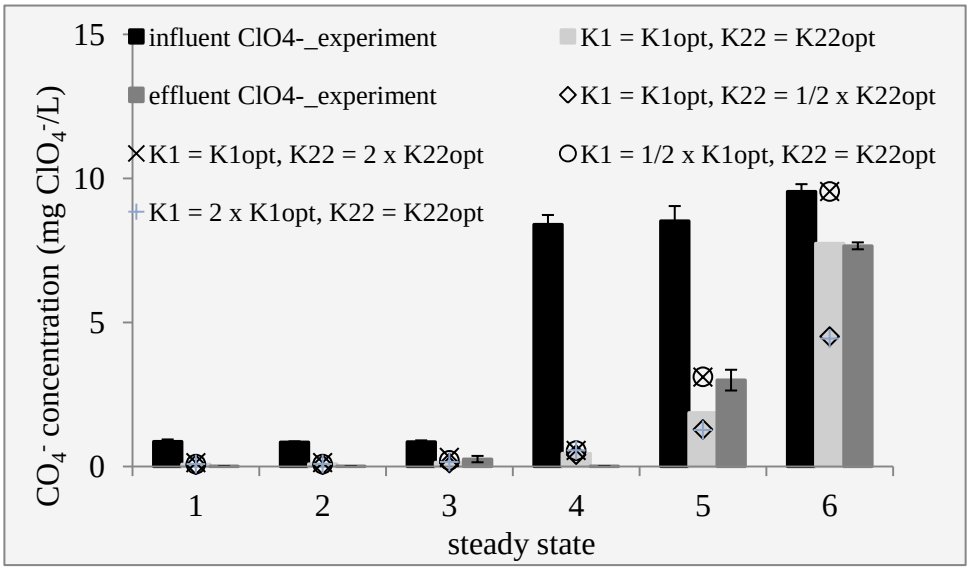

b.

Fig. 8.4 Comparison of effluent nitrate and perchlorate concentrations from the experiment and from the model with optimized parameters ($K_1 = K_{21} = 0.2$ mg N/L and K_{22} equals 0.8 mg ClO_4^-/L), and with the three parameters at a half or two times of the optimized values.

4. Modeling Results and Discussion

4.1 Effect of nitrate loading, perchlorate loading, and H_2 pressure on perchlorate and nitrate removals

Fig. 8.5 plots the predicted effluent perchlorate concentrations for operating conditions including perchlorate loading ranging from 0 to 0.65 g ClO_4^- /m^2-d (*i.e.*, influent perchlorate concentrations ranging from 0 to 10 mg ClO_4^-/L), nitrate loading ranging from 0 to 1.6 g N/m^2-d (*i.e.*, influent nitrate concentrations ranging from 0 to 25 mg N/L), and the three H_2 pressures of 1.4, 2.2, or 3.0 atm. H_2 pressure and perchlorate loading have clear impacts on effluent perchlorate concentrations: Higher H_2 pressure or lower perchlorate loading leads to lower effluent perchlorate concentration. The effect of nitrate loading on effluent perchlorate concentration is not as straightforward, since nitrate affects perchlorate removal through promotion mechanism 2 (PRB use two acceptors) and inhibition mechanisms 1 (competition for H_2), 3 (competition for the same resources within PRB), and 4 (competition for space). Thus, I use the middle panel of Fig. 8.5 to aid in interpreting how nitrate loading affects effluent perchlorate concentration. The sloping dashed-line on the middle left panel of Fig. 8.5 delineates the H_2-limiting area.

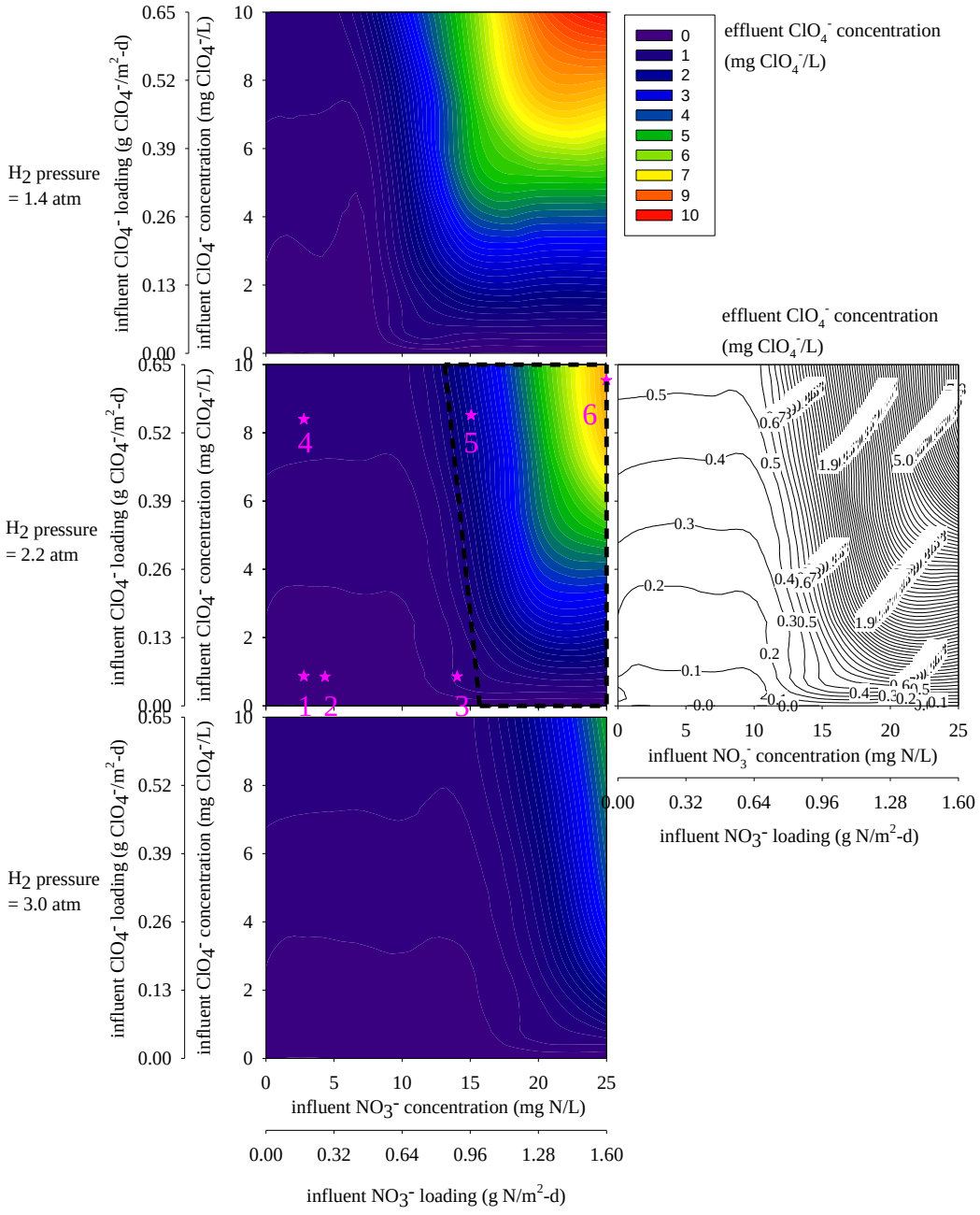

Fig. 8.5 Effluent perchlorate concentration contours at different H_2 pressures and nitrate and perchlorate loadings. Top: H_2 pressure @ 1.4 atm; Middle left: H_2 pressure @ 2.2 atm; Middle right: H_2 pressure @ 2.2 atm, with contours labeled; Bottom: H_2 pressure @ 3.0 atm. Stars with numbers identify the locations of the six steady states in the bench-scale tests. The dashed line surrounds the area representing H_2-limitation for 2.2 atm.

The net effect of influent nitrate loading on perchlorate removal can be categorized into four situations that are summarized in Table 8.4. As Fig. 8.5 (middle right) illustrates, increasing nitrate loading for < 0.1 g N/m^2-d slightly increases perchlorate removal, especially when the influent perchlorate loading is low; this is situation 1. This trend in situation 1 occurs because the promotion effect in mechanism 2 is dominant. In situation 2, perchlorate removal plateaus at nitrate loading between 0.1 and 0.6 g N/m^2-d due to a trade-off situation in which the promotion effect due to mechanism 2 balances out the inhibition effect due to mechanisms 3 and 4. As nitrate loading increases in the range of 0.6-1.0 g N/m^2-d, perchlorate removal steadily decreases in situation 3, since the inhibition from mechanisms 3 and 4 outweighs the promotion effect in mechanism 2. Finally, nitrate loading > 1.0 g N/m^2-d results in poor perchlorate removal in situation 4, since mechanism 1 becomes active, further strengthening the inhibition effect.

Table 8.4 The mechanistic effects of nitrate loading on PRB and perchlorate removal

Nitrate-Loading Situation	Promotion Mechanism	Inhibition Mechanisms			Net Effect
	2 Using NO_3^- and ClO_4^- as electron acceptors	3 Competition for a common enzyme	1 Competition for H_2	4 Competition for space	
1 <0.1 g N/m^2-d	+	+	No	+	promotion
2 0.1-0.6 g N/m^2-d	++	++	No	++	no effect
3 0.6-1.0 g N/m^2-d	+++	+++	No	+++	inhibition
4 >1.0 g N/m^2-d	++++	++++	Yes	++++	strong inhibition

Notes: +: very weak effect; ++: weak effect; +++: strong effect; ++++: very strong effect. The effects are qualitative.

As shown in Fig. 8.5 by stars and numbers, steady states 1 to 4 among the six steady states tested experimentally fall into situation 2 (no effect), state 5 falls into situation 3 (inhibition), and state 6 falls into situation 4 (strong inhibition).

The "four-situation" pattern can be used to rationalize the seemingly contradictory experimental observations by previous researchers. Researchers

who reported no inhibition of nitrate on perchlorate reduction include Coppola and McDonald (2000) and Giblin et al. (2000). While unreported, the nitrate surface loadings in their experiments had to have been low, since influent nitrate concentrations were low (0.2-6 mg N/L) and nitrate was completely removed; these experiments probably fall into situations 1 (promotion) or 2 (no effect). Nerenberg et al. (2002) and Choi and Silverstein (2008) report significant inhibition of nitrate on perchlorate reduction. Nerenberg et al. (2002) showed that an increase in nitrate loading from 0 to 1.2 g N/m^2-d decreased perchlorate removal from 57% to 30%; this probably falls into situations 3 (inhibition) or 4 (strong inhibition). While Choi and Silverstein (2008) did not report the nitrate surface loadings, they showed the reduction rate of perchlorate decreased by 30% in the presence of 28 mg/L of nitrate when the electron donor was not limiting (probably situation 3 (inhibition)) and decreased by 70% when the electron donor was limiting (probably situation 4 (strong inhibition)).

Simulation results for how the operating conditions affect nitrate removal for conditions matching those in Fig. 8.5 are presented in Fig. 8.6. As expected, higher H_2 pressure or lower influent nitrate loading leads to lower effluent nitrate concentration. However, influent perchlorate loading generally does not affect nitrate removal for two reasons. When H_2 is non-limiting, higher influent perchlorate loading favors PRB growth and decreases the fraction of DB,

but does not decrease nitrate removal, since PRB also can reduce nitrate. When H_2 becomes limiting, effluent nitrate and perchlorate concentrations are high, which leads to a strong inhibition effect to PRB by mechanisms 2, 3, and 4; thus PRB decline and DB become dominant, but this does not significantly affect nitrate reduction. The trend here agrees with Nerenberg et al. (2002), where perchlorate loading at 0-5 g ClO_4^-/m^2-d showed no effect on removal of nitrate at 5 mg N/L.

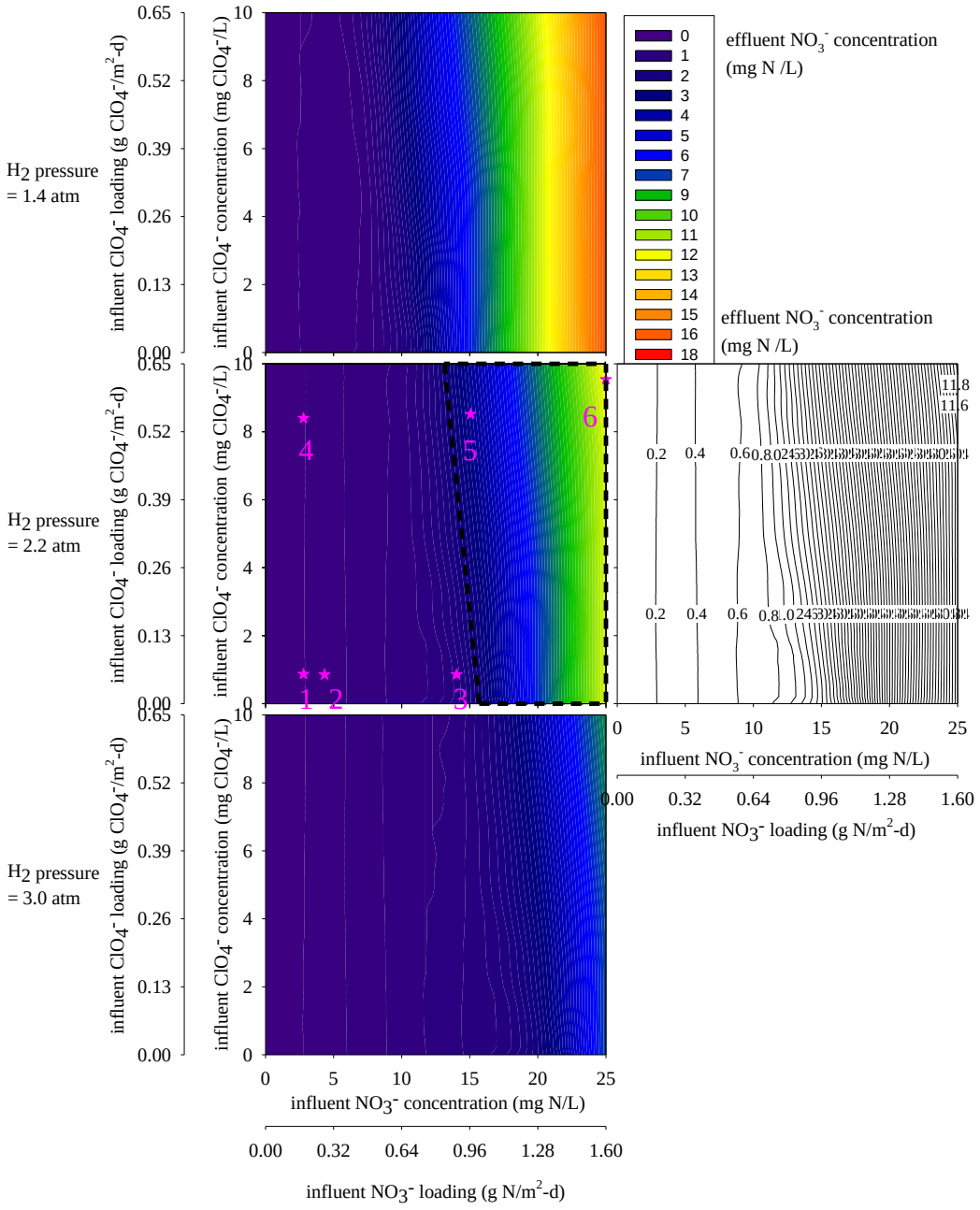

Fig. 8.6 Effluent nitrate concentration contours at different H_2 pressures and nitrate and perchlorate loadings. Top: H_2 pressure @ 1.4 atm; Middle left: H_2 pressure @ 2.2 atm; Middle right: H_2 pressure @ 2.2 atm, with contours labeled; Bottom: H_2 pressure @ 3.0 atm. Stars with numbers identify the locations of the six steady states in the bench-scale tests. The dashed line surrounds the area representing H_2-limitation at 2.2 atm.

4.2 Distribution of solid components

For steady states 1, 3, 4, 5 and 6, Zhao et al. (2011) conducted molecular assays to characterize composition of the MBfR biofilms. Here, I first simulate the distribution of solid components for these scenarios and discuss how the operating conditions relate to the biomass distribution. Then, I compare the simulated distributions to experimental results.

Figs. 8.7 and 8.8 show simulated solid-component distributions in the biofilm for experimental steady states 1 to 6. Fig. 8.7 contains the three types of active biomass: DB, PRB, and HB. Fig. 8.8 contains IB and EPS.

Important trends in Figs. 8.7 and 8.8 include:

1) As the nitrate loading increases (from steady state 1 to 3 or from steady state 4 to 6) or the perchlorate loading increases (from group 1 to 2), the biofilm thickness increases, but the increase from steady state 5 to 6 is not significant due to H_2 limitation.
2) Within group 1 or 2, an increase in the nitrate loading (Fig. 8.4a) correlates to increases in nitrate flux (Fig. 8.3a) and fraction of denitrifiers (Fig. 8.7), but to decreases in perchlorate flux (Fig. 8.3b) and PRB (Fig. 8.7). The extent to which the nitrate loading affects perchlorate flux and PRB growth/fraction resembles how the nitrate loading affects effluent perchlorate concentration discussed above, *i.e.*, the "four-situation pattern." The 3 steady states in group

1 fall into situation 2 (no effect); therefore, the perchlorate flux and PRB fraction decreases only slightly as the nitrate loading increases. In group 2, the perchlorate flux and PRB fraction decrease from steady state 4 to 5 and more significantly to steady state 6, since steady state 4 falls into situation 2 (no effect), steady state 5 falls into situation 3 (inhibition), and steady state 6 falls into situation 4 (strong inhibition).

3) The perchlorate-loading increase from group 1 to 2 (Fig. 8.4b) correlates to an increase in perchlorate flux (Fig. 8.3b) and PRB fraction (Fig. 8.7), but a decrease of DB fraction (Fig. 8.7). However the perchlorate-loading increase (Fig. 8.4b) has no effect on nitrate flux (Fig. 8.3a), similar to the lack of impact of the perchlorate loading on effluent nitrate concentration (Fig. 8.6).

4) H_2 limitation in steady states 5 and 6 causes redistribution of fluxes of nitrate and perchlorate and of DB and PRB in the biofilm. The fluxes of nitrate and perchlorate are 2.2 and 0.27 g COD/m^2-d (respectively) in steady state 5 and 2.4 and 0.07 g COD/m^2-d (respectively) in steady state 6 (Fig. 8.3). The average fractions of DB and PRB across the biofilm are 0.08 and 0.37 (respectively) in steady state 5 and 0.37 and 0.08 (respectively) in steady state 6 (Fig. 8.7).

5) The fractions of DB, PRB, and EPS are higher in the membrane side than in the liquid side of the biofilm, whereas the HB mainly accumulate near the

liquid side. This distribution feature is associated with the soluble-component profiles in the biofilms. As an example, Fig. 8.9 shows the profiles of the five soluble components in steady state 5. H_2 concentration is high on the membrane side, but essentially zero on the liquid side; thus H_2 is much more rate limiting on the membrane side. This determines the DB and PRB profiles. Since EPS are produced by DB and PRB, they follow the distribution trends of DB and PRB. HB are opposite to DB, PRB, and EPS because HB are able to out-compete DB, PRB, and EPS only when H_2 is depleted on the liquid side.

6) The fraction of IB is higher in steady states 1, 2, and 4 than in steady states 3, 5, and 6. This is due to higher concentration of electron acceptors (nitrate + perchlorate) in steady states 3, 5 and 6, and the trend can be understood from two perspectives. First, the specific growth rate of IB is constant (based on biomass decay), while the specific growth rates of other solid components increases when the concentration of electron acceptors (nitrate + perchlorate) increases; thus, IB are less competitive for space in steady states 3, 5, and 6. Second, a higher concentration of electron acceptors results in a greater biofilm thickness, which makes the detachment rate higher. Detachment is a selective force that washes out slower growers, such as IB, but enriches faster growers, such as denitrifiers and EPS (Rittmann and Manem, 1992).

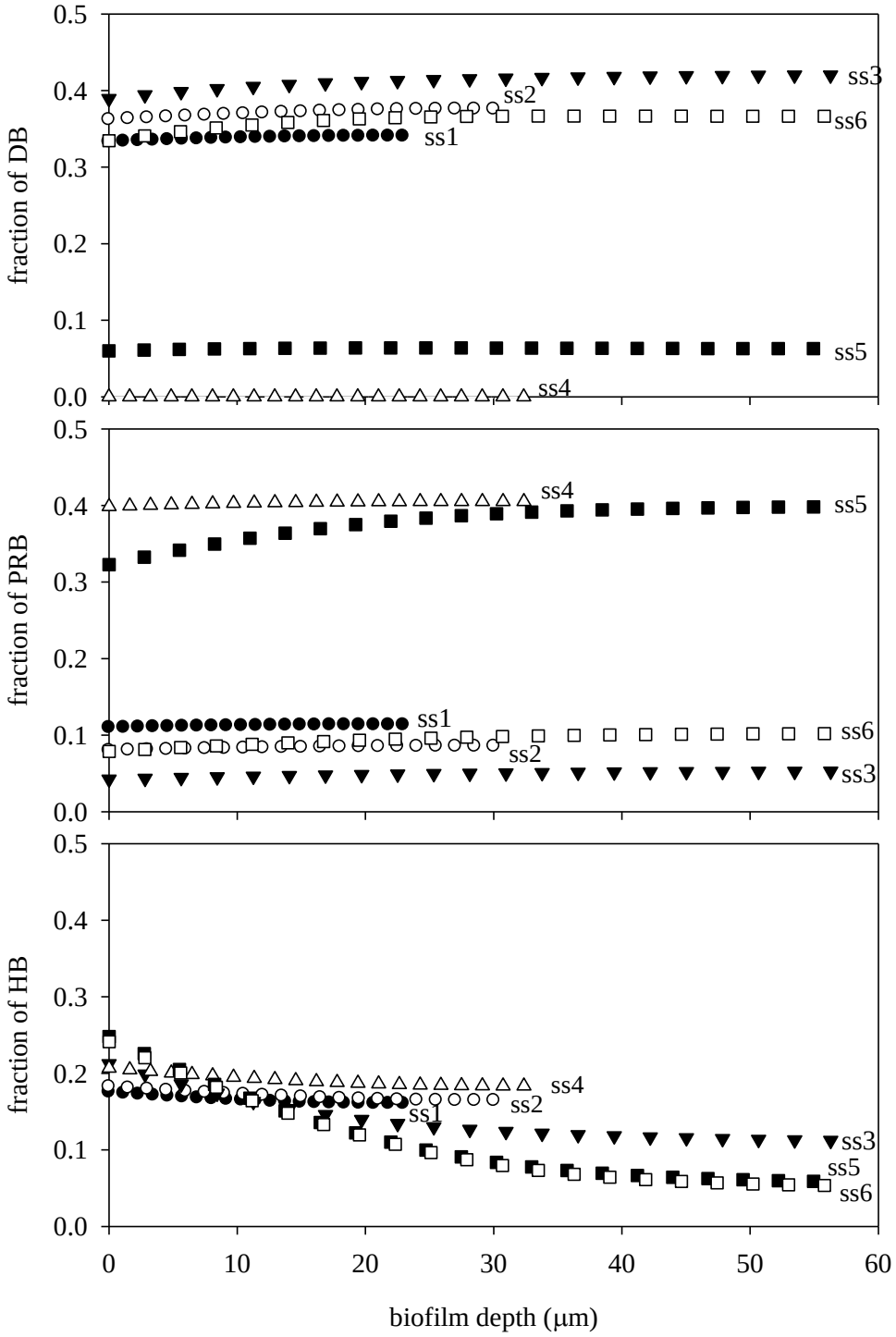

Fig. 8.7 Simulated profiles of active biomass (top to bottom: DB, PRB, and HB) in the biofilm in the six steady states. The membrane substratum is to the right, and the thickness of the biofilm is shown by the extent of the symbols to the right.

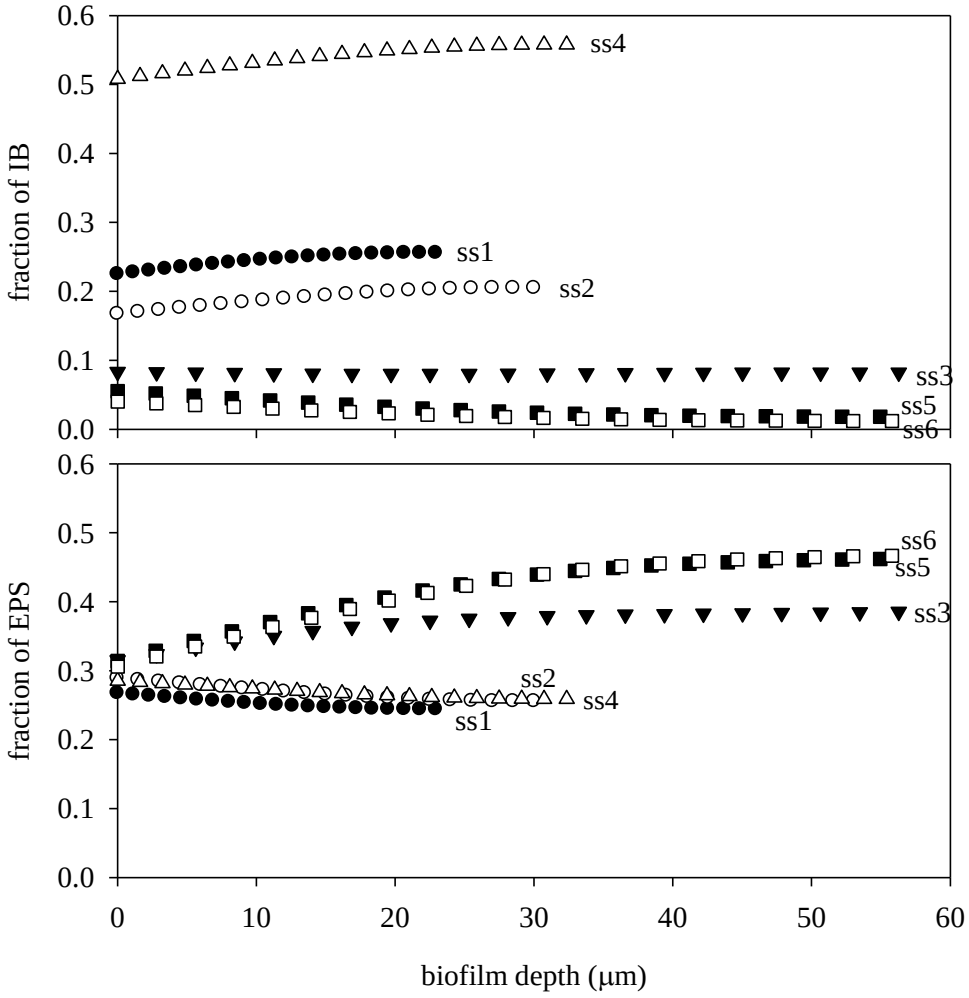

Fig. 8.8 Simulated profiles of IB (top) and EPS (bottom) in the biofilm in the six steady states. The membrane substratum is to the right, and the thickness of the biofilm is shown by the extent of the symbols to the right.

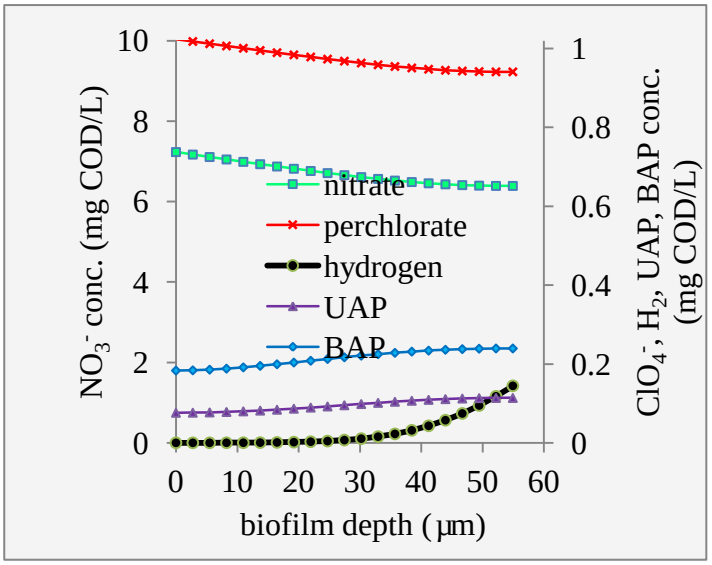

Fig. 8.9 Example substrate profiles (steady state 5). The liquid is to the left, and the membrane is to the right. The thickness of the biofilm is shown by the extent of the symbols to the right.

4.3 Comparison of biofilm thicknesses from the experiments and model

Table 8.5 compares the biofilm thicknesses in the six steady states in the experiments and in the model. Because the biofilm thickness was not uniform on a fiber, I measured the thicknesses at different sections of a fiber and reported a thickness range for each steady state. I used scanning confocal laser microscopy to measure the biofilm thickness, following all procedures in Lee et al. (2009). I compare the median thickness for each steady state to the model-simulated thickness. The trends of biofilm thicknesses across the six steady states are consistent for the experiments and the model: steady states $1 < 2 < 4 < 3 \approx 5 \approx 6$.

The median biofilm thicknesses ranged from 14 to 43 μm across the six steady states, while the model-simulated thicknesses were 23 to 58 μm.

Table 8.5 Comparison of biofilm thicknesses from the experiments and model

Steady State	Experiment		Model (μm)
	Range (μm)	Median (μm)	
1	10 - 18	14	23
2	15 - 28	22	30
3	30 - 55	43	58
4	13 - 40	27	33
5	38 - 47	43	56
6	28 - 52	40	57

4.4 Comparison of microbial ecology in experiment and model results

Zhao et al. (2011) conducted qPCR analyses that targeted 16S rDNA for total bacteria, perchlorate reductase (*pcrA*) for PBR, and nitrite reductases (*nirS & nirK*) for DB for steady states 1, 3, 4, 5 and 6. They then used the number of gene copies to estimate cell numbers of total bacteria, PRB, and DB (units: cell number/m^2 of fiber). The cell numbers in the model (also in units of cell number/m^2 of fiber) are estimated as $\frac{(L_f \times \frac{1m}{10^6 \mu m} \times m^2\text{-}fiber) \times X_f / m_{cell}}{m^2\text{-}fiber} \times \xi$, in which, L_f (μm) is the biofilm thickness, X_f (4×10^4 g VSS/m^3) is the biofilm density and is from Part 1, m_{cell} (2×10^{-13} g VSS/cell) is the unit cell weight and is from Madigan and Martinko (2006), and ξ is the fraction of relevant bacteria. For calculating total bacteria, ξ equals the sum of fractions of DB, PRB, and HB.

The trends of estimated cell numbers across the five steady states are compared to the trends from the model in Table 8.6. Except for steady state 3, the trends match for total cells: $1 < 4 < 5 < 6$. The PRB cell numbers follow exactly the same trends for experiments and model: $5 > 4 > 6 > 3 > 1$. However, the DB cell numbers do not match as well, and the most significant discrepancies occur in steady states 4 and 5, in which DB in the experiment are close to the highest, while DB in the model are the lowest. Because steady state 4 had the lowest nitrate concentration in the influent, it ought not have one of the highest DB fractions at steady state. There are three possible explanations for why the experimental results gave significant DB in steady state 4. First, some DB that contained *nirS* or *nirK* might also have contained nitrate reductases that can reduce nitrate and perchlorate (Hochstein and Tomlinson, 1988; Shanmugam et al., 1992; Kengen et al., 1999). In other words, these bacteria actually were PRB, even though they did not have *pcrA*, and they could maintain themselves by perchlorate reduction when nitrate was absent. Second, when the influent nitrate concentration decreased significantly from steady state 3 to 4, some DB persisted until samples were taken for steady state 4. Based on the first order rates of biomass decay and detachment, about 7% of DB in steady state 3 still should have remained in the biofilm at the time of sampling for steady state 4. This calculation is based on an inactivation rate of 0.05 d^{-1}, an endogenous respiration

rate of 0.03 d^{-1}, a detachment rate of 0.12 d^{-1}, and a time period of 13 days (Zhao et al., 2011). This possibility comes from the fact that we moved to the next stage when the substrate concentrations reached a steady state, but the biofilm might have not achieved complete steady state. Third, as DB accumulated in steady state 3 decayed by endogenous respiration and to inert biomass, some DNA was released and persisted in the biofilm until the time of sampling for steady state 4. The qPCR measurements reflect DNA in the biofilm, whether in active and non-active biomass, while the model accounts for the active biomass only.

Table 8.6 Comparison[a] of simulated biomass data and qPCR data

Steady state	Total bacteria (cell/m^2-fiber)		PRB (cell/m^2-fiber)		DB (cell/m^2-fiber)	
	Experiment	Model	Experiment	Model	Experiment	Model
1	3.3×10^{10}	2.8×10^{12}	4.9×10^{9}	5.0×10^{11}	1.5×10^{10}	1.6×10^{12}
3	1.5×10^{11}	6.6×10^{12}	8.9×10^{9}	6.0×10^{11}	7.1×10^{10}	4.6×10^{12}
4	2.3×10^{12}	4.0×10^{12}	1.2×10^{11}	2.6×10^{12}	6.1×10^{11}	0
5	3.7×10^{12}	6.0×10^{12}	1.5×10^{11}	4.4×10^{12}	7.2×10^{11}	8.0×10^{11}
6	8.5×10^{12}	6.4×10^{12}	8.0×10^{10}	1.0×10^{12}	6.4×10^{11}	4.2×10^{12}

Notes:
a. The comparison aims at trends across the five steady states.

4.5 Practical values

Knowing this “four-situation” pattern has practical value. It is common that the effluent perchlorate concentration limits the reactor loading (i.e., inflow

rate), since its MCL is much lower than the MCL of nitrate. Under the condition that the effluent perchlorate concentration must be lower than its MCL, the flow rate should be as close to the higher-loading extreme of situation 2 as possible, since nitrate has no effect on the effluent perchlorate concentration during situation 2. However, the flow rate should not increase to situations 3 and 4, since the effluent perchlorate is very sensitive to loading (i.e., inflow rate). This paper presents model results for operating conditions varying within wide ranges; these results can be used to assist design of the MBfR for simultaneous reduction of nitrate and perchloate. Some of the results (e.g., the "four-situation" pattern) are qualitatively transferable to other biofilm reactors, since the four mechanisms occur similarly whenever nitrate and perchlorate are to be reduced simultaneously. The major difference would that H_2 is delivered into the biofilm from the fiber side in an MBfR, while the electron donor (organic or H_2) is delivered from the liquid side in a conventional reactor.

5 Conclusions

A multispecies biofilm model was developed for simultaneous reduction of nitrate and perchlorate in the H_2-based membrane biofilm reactor. The one-dimension model includes dual-substrate Monod kinetics for a steady-state biofilm with five solid and five dissolved components. The solid

components are autotrophic denitrifying bacteria (DB), autotrophic perchlorate-reducing bacteria (PRB), heterotrophic bacteria (HB), inert biomass (IB), and extracellular polymeric substances (EPS). The dissolved components are nitrate, perchlorate, hydrogen (H_2), substrate-utilization-associated products (UAP), and biomass-associated products (BAP). The model explicitly considers four mechanisms involved in how three important operating conditions (H_2 pressure, nitrate loading, and perchlorate loading) affect nitrate and perchlorate removals: 1) competition for H_2, 2) promotion of PRB growth due to having two electron acceptors (nitrate and perchlorate), 3) competition between nitrate and perchlorate reduction for the same enzyme in the PRB, and 4) competition for space in the biofilm. Two other special features are having H_2 delivered from the membrane substratum and solving directly for steady state using a novel three-step approach: finite-differences for approximating partial differential and/or integral equations, Newton-Raphson for solving non-linear equations, and an iterative scheme to obtain the steady-state biofilm thickness.

The half-maximum-rate concentrations and inhibition coefficients of nitrate and perchlorate are optimized by fitting data from experiments with different combinations of influent nitrate and perchlorate concentrations. The optimized half-maximum-rate concentration of nitrate and inhibition coefficient of nitrate to perchlorate are 5.7×10^{-4} mg/cm^3, and the optimized half-maximum-

rate concentration of perchlorate and the inhibition coefficient of perchlorate to nitrate are 5.7×10^{-4} mg/cm^3. These values are approximately in the middle of their ranges in literature.

The model with optimized parameters is used to quantitatively and systematically explain how three important operating conditions (nitrate loading, perchlorate loading, and H_2 pressure) affect nitrate and perchlorate reduction and biomass distribution in the biofilms. The effects of influent nitrate loading on perchlorate removal can be categorized into four situations. For the H_2 pressure used in the experiments, nitrate loading of < 0.1 g N/m^2-d slightly promotes perchlorate removal, because the promotion effect in mechanism 2 (PRB use two acceptors) is dominant. A nitrate loading of 0.1-0.6 g N/m^2-d has no effect on perchlorate removal due to the fact that the promotion effect in mechanism 2 balances out the inhibition effect in mechanisms 3 (competition for the same resources within PRB) and 4 (competition for space). A nitrate loading of 0.6-1.0 g N/m^2-d inhibits perchlorate removal, since the inhibition effect from mechanisms 3 and 4 outweighs the promotion effect in mechanism 2. A nitrate loading of > 1.0 g N/m^2-d strongly inhibits perchlorate removal, since mechanism 1 (competition for H_2) becomes active. The effects of nitrate loading on accumulation of perchlorate-reducing bacteria resemble the effects on perchlorate

removal. However, perchlorate loading has minimal impact on nitrate removal, since both DB and PRB can reduce nitrate.

The simulated biomass distributions in the biofilm are compared to the qPCR data. While the data for the total bacteria and perchlorate-reducing bacteria are consistent, the data for the denitrifying bacteria are not due to difference between the model and experiment in defining the denitrifying bacteria.

Chapter 9

A MULTISPECIES BIOFILM MODEL FOR SIMULTANEOUS REDUCTION OF NITRATE AND SULFATE

The main goal of this chapter is to modify the nitrate and perchloate model in Chapter 8 into a nitate and sulfate model and use it to study how operating conditions affect the onset of sulfate reduction in a denitrifying MBfR. Relevant background information was presented in pages 14-15 in Chapter 1. This chapter (Chapter 9) presents the model adaption, parameter optimization using data from bench-scale experiments, and the effect of operating conditions on the onset of sulfate reduction.

I am preparing a manuscript for this work (Tang et al., 2012d). I took the lead in the model adaption, parameter optimization, and results interpretation. Aura Ontiveros-Valencia and Liang Feng mainly conducted the bench-scale experiments used for parameter optimization, Chen Zhou mainly contributed to the model adaption, and Bruce E. Rittmann and Rosa Krajmalnik-Brown mainly contributed to the results interpretation, along with reviewing and revising the manuscript.

1. Materials and Methods

1.1 Model adaption

The nitrate and sulfate model is adapted from the nitrate and perchlorate model in Chapter 8. The basic mathematical equations that comprise the two models are the same. These equations include the dissolved-component mass-balance Eq. 8.1 and its boundary-condition Eqs. 8.2, 8.3, and 8.8, and the solid-component mass-balance Eq. 8.19 and its boundary-condition Eqs. 8.20 and 8.25. The numerical solution for the two models is also the same. However, the two models differ in model components and their interactions, model assumptions and simplifications, and substrate-utilization and biomass-growth terms and kinetic parameters in equations. The differences are addressed in this section.

1.1.1 Model components and their interactions

This model has five solid components: autotrophic denitrifying bacteria (DB), autotrophic sulfate-reducing bacteria (SRB), heterotrophic bacteria (HB), inert biomass (IB), and extracellular polymeric substances (EPS). The model has five dissolved components: nitrate (NO_3^-), sulfate (SO_4^{2-}), hydrogen (H_2), substrate-utilization-associated products (UAP), and biomass-associated products (BAP). The components in the nitrate and sulfate model are the same as those in

the nitrate and perchlorate model, except that perchlorate is changed to sulfate and PRB are changed to SRB.

Fig. 9.1 describes how the different components in the model are related. The relationships in the nitrate and sulfate model are similar to those in the nitrate and perchlorate model. The differences come from two dissolved components and two solid components in each model. In the nitrate and perchlorate model, PRB can use nitrate and perchlorate as their electron acceptors, and nitrate and perchlorate competitively inhibit each other, since the two electron acceptors are reduced by the same enzyme in PRB. However, in the nitrate and sulfate model, DB only use nitrate and SRB only use sulfate; thus, competitive inhibition due to using the same enzyme is not relevant.

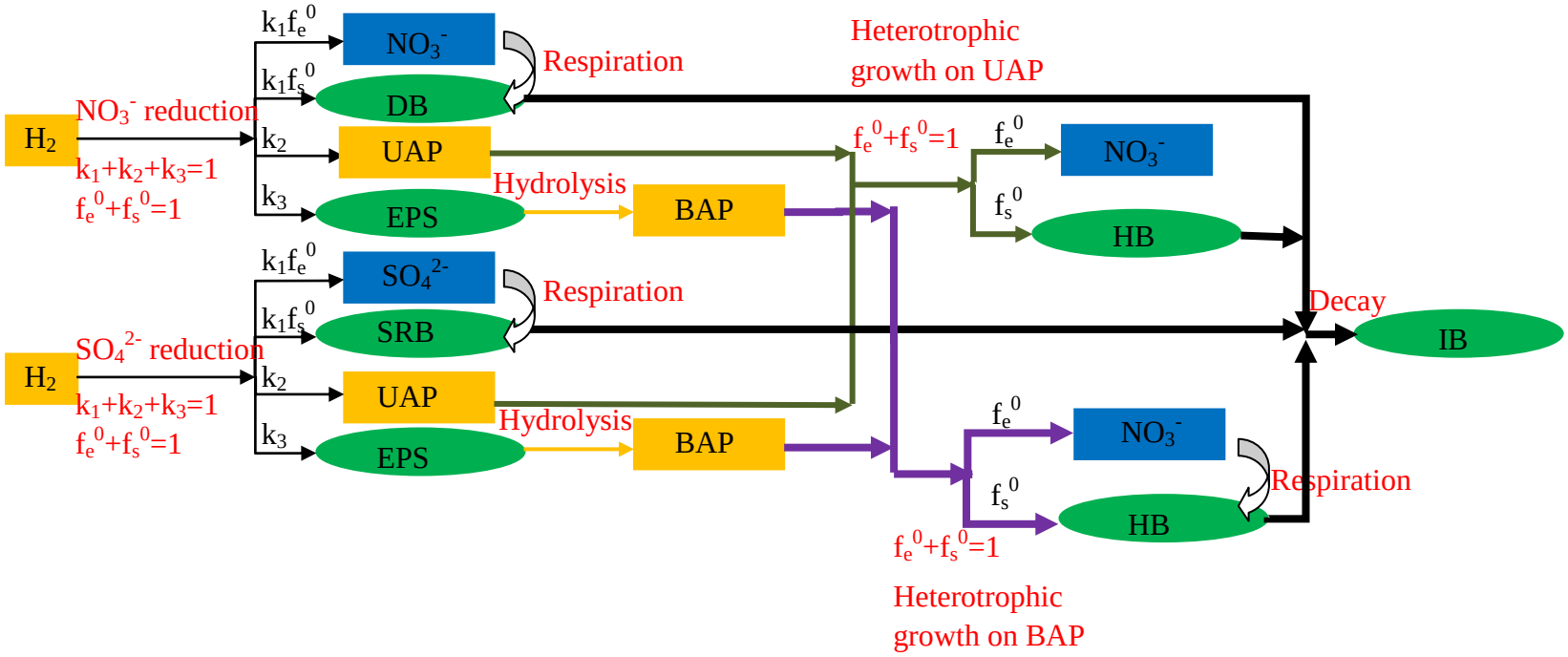

Fig. 9.1 Schematic describing how the dissolved components (rectangles) and solid components (ellipses) interact. DB: autotrophic denitrifying bacteria; SRB: autotrophic sulfate-reducing bacteria; HB: heterotrophic bacteria; IB: inert biomass; EPS: extracellular polymeric substances; UAP: substrate-utilization-associated products; BAP: biomass-associated products. Other symbols are defined in Table 9.2.

1.1.2 Model assumptions and simplifications

The assumptions and simplifications a), b), c), d), h), i), j), and k) in the nitrate and perchlorate model also apply in the nitrate and sulfate model, but one more assumption should be added here: HB, which use SMP as their electron donor, use only nitrate as their electron acceptor. This assumption is based on two facts: a) nitrate is a thermodynamically preferred electron acceptor compared to sulfate, and b) most SRB are not capable of using the complex organic matter in SMP (Barton, 1995).

1.1.3 Substrate-utilization and biomass-growth terms and kinetic parameters

Table 9.1 mathematically represents the processes considered in the model and how the five solid and five dissolved components interact with each other in these processes. Symbols in Table 9.1 are described in Table 9.2 for model inputs and Table 9.3 for model outputs. The inputs in the nitrate and sulfate model are the same as those in the nitrate and perchlorate model except for system-specific parameters and kinetics parameters unique to sulfate reduction.

Table 9.1 Process, component, and rate matrix in the nitrate and sulfate model

process (j)		coefficient of component i in process j (η_{ij})									conversion rate (R_j)
		solid component					dissolved component				
		DB	SRB	IB	HB	EPS	NO_3^-	SO_4^{2-}	H_2	UAP	BAP	
nitrate reduction	growth	k_1				$\frac{k_5}{Y_1}$	$-\frac{(1-Y_1)k_1}{Y_1}$		$-\frac{1}{Y_1}$	$\frac{k_4}{Y_1}$		$\mu_1 f_1 X_f \frac{S_{f1}}{K_1+S_{f1}} \frac{S_{f3}}{K_{31}+S_{f3}}$
	endogenous respiration	-1					-1					$p_1 f_1 X_f \frac{S_{f1}}{K_1+S_{f1}}$
	inactivation	-1		$(1-f_d)$								$b_1 f_1 X_f$
sulfate reduction	growth		k_1			$\frac{k_5}{Y_2}$		$-\frac{(1-Y_2)k_1}{Y_2}$	$-\frac{1}{Y_2}$	$\frac{k_4}{Y_2}$		$\mu_2 f_2 X_f \frac{S_{f2}}{K_2+S_{f2}} \frac{S_{f3}}{K_{32}+S_{f3}}$
	endogenous respiration		-1					-1				$p_2 f_2 X_f \frac{S_{f2}}{K_2+S_{f2}}$
	inactivation		-1	$(1-f_d)$								$b_2 f_2 X_f$
SMP utilization	growth on UAP				1		$-\frac{(1-Y_4)}{Y_4}$			$-\frac{1}{Y_4}$		$\mu_4 f_4 X_f \frac{S_{f4}}{K_4+S_{f4}} \frac{S_{f1}}{K_1+S_{f1}}$
	growth on BAP				1		$-\frac{(1-Y_5)}{Y_5}$				$-\frac{1}{Y_5}$	$\mu_4 f_4 X_f \frac{S_{f5}}{K_5+S_{f5}} \frac{S_{f1}}{K_1+S_{f1}}$
	endogenous respiration				-1		-1					$p_4 f_4 X_f \frac{S_{f1}}{K_1+S_{f1}}$
	inactivation			$(1-f_d)$	-1							$b_4 f_4 X_f$

Table 9.1 Process, component, and rate matrix in the nitrate and sulfate model

process (j)	coefficient of component i in process j (η_{ij})		conversion rate (R_j)
	solid component	dissolved component	
	DB SRB IB HB EPS	NO_3^- SO_4^{2-} H_2 UAP BAP	
EPS hydrolysis	-1	1	$k_{hyd} f_5 X_f$
observed conversion rate of component i	observed specific growth rate: $\mu_{oi} = \frac{\sum_j (\eta_{ij} R_j)}{f_i X_f}$	observed utilization rate: $r_{oi} = \sum_j (\eta_{ij} R_j)$	

Table 9.2 Inputs for the nitrate and sulfate model[a]

Symbols	Description	Units	Values
K_1	Half-maximum-rate concentration for nitrate	mg-COD/cm^3	6.0×10^{-4} (optimized)
K_2	Half-maximum-rate concentration for sulfate	mg-COD/cm^3	1.0×10^{-3} (optimized)
K_{31}	Half-maximum-rate concentration for H_2 in denitrification	mg-COD/cm^3	1.6×10^{-5} (Kurt et al., 1987)
K_{32}	Half-maximum-rate concentration for H_2 in sulfate reduction	mg-COD/cm^3	2.2×10^{-5} (Noguera et al., 1998)
K_4	Half-maximum-rate concentration for UAP	mg-COD/cm^3	5.0×10^{-3} (Wanner and Gujer, 1986)
K_5	Half-maximum-rate concentration for BAP	mg-COD/cm^3	5.0×10^{-3} (Wanner and Gujer, 1986)
Y_1	Yield in denitrification	mg-COD/mg-COD	0.2 (Rittmann and McCarty,2001)
Y_2	Yield in sulfate reduction	mg-COD/mg-COD	0.05 (Rittmann and McCarty,2001)
Y_4	Yield of HB growing on UAP	mg-COD/mg-COD	0.6 (Rittmann and McCarty,2001)
Y_5	Yield of HB growing on BAP	mg-COD/mg-COD	0.6 (Rittmann and McCarty,2001)
μ_1	Maximum specific growth rate of DB	d^{-1}	1.0 (Rittmann and McCarty,2001)
μ_2	Maximum specific growth rate of SRB	d^{-1}	0.3 (Rittmann and McCarty,2001)
μ_4	Maximum specific growth rate of HB	d^{-1}	13.2 (Rittmann and McCarty,2001)
k_1	Coefficient for electrons used for biomass production		0.77 (Rittmann and McCarty,2001)
k_2	Coefficient for electrons going to UAP		0.05 (Rittmann and McCarty,2001)
k_3	Coefficient for electrons going to EPS		0.18 (Rittmann and McCarty,2001)
b_1	Inactivation coefficient for DB	d^{-1}	0.05 (Wanner and Gujer, 1986)

Table 9.2 Inputs for the nitrate and sulfate model[a]

Symbols	Description	Units	Values
b_2	Inactivation coefficient for SRB	d^{-1}	0.01 (Rittmann and McCarty,2001)
b_4	Inactivation coefficient for HB	d^{-1}	0.1 (Wanner and Gujer, 1986)
k_d	Biofilm detachment coefficient	$cm^{-1}d^{-1}$	36 (Trulear and Characklis; 1982)
p_1	Endogenous respiration rate for DB	d^{-1}	0.05 (Wanner and Gujer, 1986)
p_2	Endogenous respiration rate for SRB	d^{-1}	0.01 (Rittmann and McCarty, 2001)
p_4	Endogenous respiration rate for HB	d^{-1}	0.2 (Rittmann and McCarty,2001)
D_1	Nitrate diffusion coefficient within the diffusion layer	cm^2/d	1.2 (Williamson and McCarty,1976)
D_2	Sulfate diffusion coefficient within the diffusion layer	cm^2/d	0.71 (Nielsen, 1987)
D_3	H_2 diffusion coefficient within the diffusion layer	cm^2/d	4.4 (Macpherson and Unwin, 1997)
D_4	UAP diffusion coefficient within the diffusion layer	cm^2/d	1 (Merkey, 2008)
D_5	BAP diffusion coefficient within the diffusion layer	cm^2/d	0.6[b] (Merkey, 2008)
D_{f1}	Nitrate diffusion coefficient within the biofilm	cm^2/d	0.96 (Williamson and McCarty,1976)
D_{f2}	Sulfate diffusion coefficient within the biofilm	cm^2/d	0.57 (Nielsen, 1987)
D_{f3}	H_2 diffusion coefficient within the biofilm	cm^2/d	3.5 (Macpherson and Unwin, 1997)
D_{f4}	UAP diffusion coefficient within the biofilm	cm^2/d	0.8 (Merkey, 2008)
D_{f5}	BAP diffusion coefficient within the biofilm	cm^2/d	0.5[b] (Merkey, 2008)
k_{hyd}	Hydrolysis rate of EPS	d^{-1}	0.22 (Rittmann and McCarty, 2001)
f_d	Fraction of biomass that is biodegradable		0.8 (Rittmann and McCarty, 2001)
X_f	Biomass density	$mg\text{-}COD/cm^3$	79.3 (Rittmann and McCarty,

Table 9.2 Inputs for the nitrate and sulfate model[a]

Symbols	Description	Units	Values
			2001)
L_d	Thickness of effective diffusion layer	cm	0.01 (Rittmann and McCarty, 2001)
k_H	dimensionless Henry's Law constant of H_2		0.01907 (Sander, 1999)
L_m	Thickness of membrane	cm	0.0055 [c]
A	Total membrane surface area	cm^2	92.4 [c]
Q	Flow rate	cm^3/d	860 [c]
K_m	Hydrogen permeation coefficient within the membrane	cm^2/d	0.0013 [c]
S_0	Oxygen concentration in the influent	mg-COD/cm^3	0.008 [c]
S_1	Nitrate concentration in the influent	mg-COD/cm^3	0.0286 [c]
S_2	Sulfate concentration in the influent	mg-COD/cm^3	0.0307 [c]
S_{g3}[d]	H_2 concentration in the bulk gas	mg-COD/cm^3	1.24-3.72 [c]

Notes:

a. Conversion factors: 1 mg NO_3^--N: 2.86 mg COD; 1 mg cell: 1.98 mg COD; 1 mg SO_4^{2-}: 0.67 mg COD; 1 mg H_2: 8 mg COD.
b. Since BAP molecules are larger than UAP, the diffusion coefficients of BAP are assumed to be 60% of those of UAP.
c. All the system-specific data are from the bench-scale experiment used to optimize parameters (Ontiveros-Valencia et al., 2011).
d. For consistency, H_2 concentration in COD, instead of H_2 pressure, is used. H_2 concentration is calculated using the ideal gas law: $S_{g3} = S_3 \div 0.082 \div 298 \times 2 \times 8$ (mg COD/cm^3), where, S_3 is the hydrogen pressure in the fibers, 0.082 L-atm/K-mol is the gas constant, 298 K is the temperature, 2×8 g COD/mole H_2 is the conversion factor from H_2 mass to COD.

Table 9.3 Outputs for the nitrate and sulfate model

Symbols	Description	Units
J_1	nitrate flux into the biofilm	mg-COD/cm^2-d
J_2	sulfate flux into the biofilm	mg-COD/cm^2-d
J_{3m}	H_2 flux into the biofilm	mg-COD/cm^2-d
J_3	H_2 flux out of the biofilm	mg-COD/cm^2-d
J_4	UAP flux out of the biofilm	mg-COD/cm^2-d
J_5	BAP flux out of the biofilm	mg-COD/cm^2-d
L_f	thickness of biofilm	cm
f_1	fraction of DB	--
f_2	fraction of SRB	--
f_3	fraction of IB	--
f_4	fraction of HB	--
f_5	fraction of EPS	--
S_{f1}	nitrate concentration in the biofilm	mg-COD/cm^3
S_{f2}	sulfate concentration in the biofilm	mg-COD/cm^3
S_{f3}	H_2 concentration in the biofilm	mg-COD/cm^3
S_{f4}	UAP concentration in the biofilm	mg-COD/cm^3
S_{f5}	BAP concentration in the biofilm	mg-COD/cm^3
S_{b1}	nitrate concentration in the effluent	mg-COD /cm^3
S_{b2}	sulfate concentration in the effluent	mg-COD /cm^3
S_{b3}	H_2 concentration in the effluent	mg-COD /cm^3
S_{b4}	UAP concentration in the effluent	mg-COD /cm^3
S_{b5}	BAP concentration in the effluent	mg-COD /cm^3

1.2 A Bench-scale experiment for parameter optimization

A bench-scale MBfR was operated to provide data for parameter optimization. The methods and results of this test are presented in Ontiveros-Valencia et al. (2011). Here, I summarize the overall experimental setting. The concentrations of NO_3^- (10 mg N/L) and SO_4^{2-} (46 mg/L) in the influent were similar in terms of electron equivalence (~3.6×10^{-3} mole /L), or negative COD (~30 mg COD/L). All the operating parameters were held constant throughout the experiment except that the H_2 pressure was increased stepwise each time a steady state was reached: 1.24 -> 1.34 -> 1.68 -> 2.02 -> 2.43 -> 2.70 -> 3.04 -> 3.40 -> 3.72 atm (3.5 -> 5 -> 10 -> 15 -> 21 -> 25 -> 30 -> 35 -> 40 psig).

1.3 A method for parameter optimization

The half-maximum-rate concentrations of nitrate (K_1) and sulfate (K_2) should be optimized, since they are not consistent in literature. I optimized parameters by best fitting the nine steady-state data sets from the bench-scale experiment (Ontiveros Valencia et al., 2011). Best fitting was achieved when the objective function $\sum_{k=1}^{k=6}[(\frac{S_{1,experiment}^k - S_{1,model}^k}{S_{1,experiment}^k})^2 + (\frac{S_{2,experiment}^k - S_{2,model}^k}{S_{2,experiment}^k})^2]$ reached a minimum; this is a relative least-squares criterion (Sáez and Rittmann, 1992). S_1^k and S_2^k represent the effluent nitrate and sulfate concentrations in the steady state

k. During the modeling process, I varied K_1 and K_2 in their reported range, but fixed all other parameters (Table 9.2) except the H_2 pressure, which was the experimental variable.

2. Results and Discussion

In this section, I first optimize the half-maximum-rate concentrations of nitrate and sulfate by best-fitting nitrate and sulfate data from the bench-scale experiment with different H_2 pressures. Then, using the optimized parameters, I simulate the effluent H_2, UAP, and BAP concentrations and biomass distributions and compare them to experimental data to evaluate this model. Finally, using the optimized parameters, I modeled the effluent nitrate and sulfate concentrations at different influent nitrate and sulfate concentrations and different flow rates and use the results to investigate how these operating conditions affect the onset of sulfate reduction.

2.1 Parameter optimization

Fig. 9.2 compares the experimental and model-simulated effluent concentrations of nitrate and sulfate with the optimized parameters. Experimental and model results fit best when the half-maximum-rate concentration of nitrate (K_1) equals 0.2 mg N/L and the half-maximum-rate concentration of sulfate (K_2)

equals 1.6 mg SO_4^{2-}/L. These parameters are approximately in the middle of their reported ranges (Table 9.2: K_1 = 0.04 - 0.5 mg N/L; K_2 = 0.16 - 31 mg SO_4^{2-}/L).

The experimental and model data match well overall, although a discrepancy of nitrate concentration appears when the hydrogen pressures are > 3.0 atm (> 30 psig): Effluent nitrate in the model was 1.5 mg N/L, while the effluent nitrate in the experiment was 0.1 mg N/L. The experimental and model results agree that denitrification began at the lowest H_2 pressure and continually increased until reaching its maximum near 3 atm. Sulfate reduction was suppressed until the H_2 pressure was about 3 atm, when denitrification was almost complete. Thus, sulfate reduction could compete well for H_2 and space in the biofilm only when denitrification has removed almost all nitrate.

For H_2 pressure > 3 atm, the modeled nitrate concentration did not approach zero, as it did with the experimental results. To investigate if the model nitrate plateau is due to H_2 or space competition from SRB, I ran the model without SRB. The effluent NO_3^- still was high (1.4 mg N/L) at a high H_2 pressure of 3.6 atm (38 psig). Therefore, competition was not the cause.

The low experimental NO_3^- concentration for high H_2 pressures probably is caused by a factor not included in the model: suspended biomass. When the H_2 pressure was higher than 3.0 atm (30 psig), the H_2 in the reactor (> 2 μg/L or > 0.2 × half-maximum-rate concentration of H_2) combined with UAP

and BAP (> 0.3 mg COD/L or 0.06 × half-maximum-rate concentration of COD) can support significant growth of suspended biomass that could consume nitrate and reduce its concentration in the bulk liquid. The hydraulic detention time of the MBfR, 1.5 h, was not great enough to completely wash out suspended biomass. The concentrations of H_2, UAP, and BAP are discussed more below.

To assess the sensitivity of these parameters, Fig. 9.2 also plots model-simulated data with the parameters (K_1 and K_2) at two extremes of their reported ranges in literature. Most model results are not sensitive to changes of the two parameters, although a larger K_1 or K_2 increases the effluent sulfate concentrations. While a larger K_2 increases the effluent sulfate concentrations by directly decreasing the sulfate reduction rates, a larger K_1 decreases the growth rates of DB, which results in a smaller biofilm thickness, which provides less space for SRB growth.

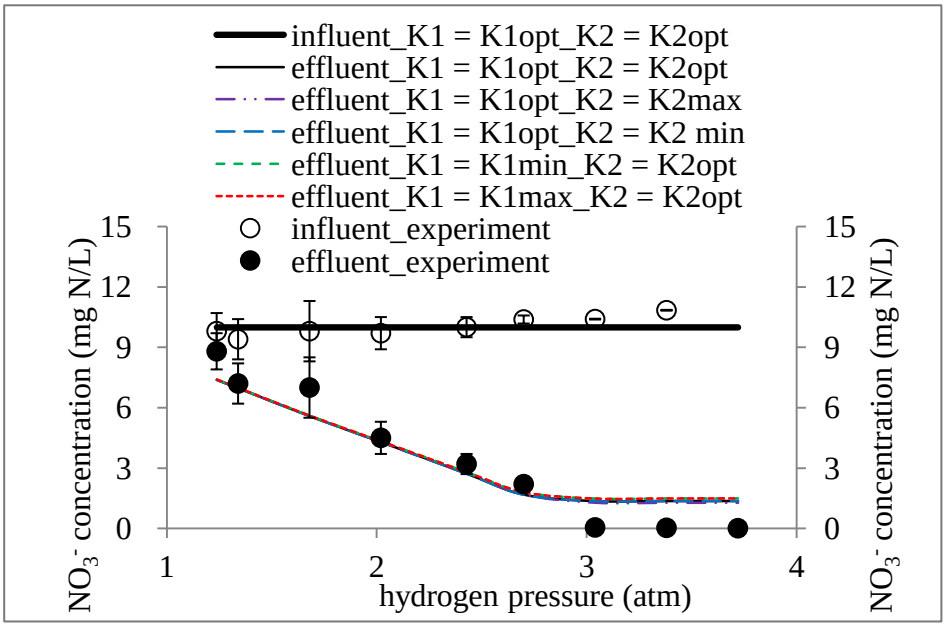

a.

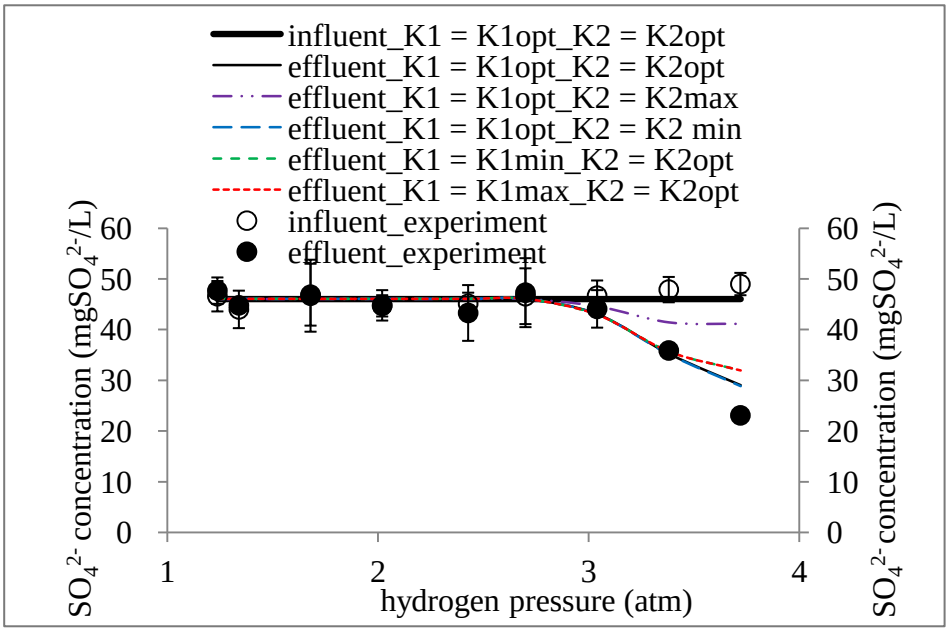

b.

Fig. 9.2 Comparison of effluent nitrate and sulfate concentrations from the experiment and from the model with optimized parameters (K_1 = 0.2 mg N/L and K_2 equals 1.6 mg SO_4^{2-}/L), and with the two parameters at the two extremes of their reported ranges in literature (K_1 = 0.04 - 0.5 mg N/L; K_2 = 0.16 - 31 mg SO_4^{2-}/L).

2.2 Concentrations of H_2, UAP, and BAP in the effluent

Fig. 9.3 plots the model-predicted concentrations of H_2, UAP, and BAP in the effluent for the H_2 pressure ranging from 1.24 to 3.72 atm (3.5 - 40 psig). The effluent H_2 concentration increases when the H_2 pressure increases, but, in all cases, the H_2 concentrations are low, < 7 μg/L. This is consistent with previous bench-scale and pilot-scale MBfR tests in which H_2 were limiting: *e.g.*, the effluent H_2 concentrations were < 70 μg/L in Lee and Rittmann (2000), < 9 μg/L in Ziv-El and Rittmann (2009b), and < 16 μg/L in Meyer et al. (2010).

The UAP and BAP concentrations in the effluent are relatively stable for all H_2 pressures, except for showing a slight increase when sulfate starts to be reduced. The slight increase is due to more UAP and BAP production from SRB. The sum of UAP and BAP concentrations (~ 0.1 + ~ 0.2 = ~ 0.3 mg COD/L) represents the effluent COD concentration. Assuming that UAP and BAP have the same chemical composition as biomass ($C_5H_7O_2N$: 3.74 g COD/g C), the increase of DOC is ~ 0.1 mg C/L. This is in the range of DOC increase reported in Ziv-El and Rittmann (2009b) (< the detection limit of 0.1 mg C/L), Lee and Rittmann (2002) (0.5 mg C/L), and Meyer et al. (2010) (0.2 mg C/L).

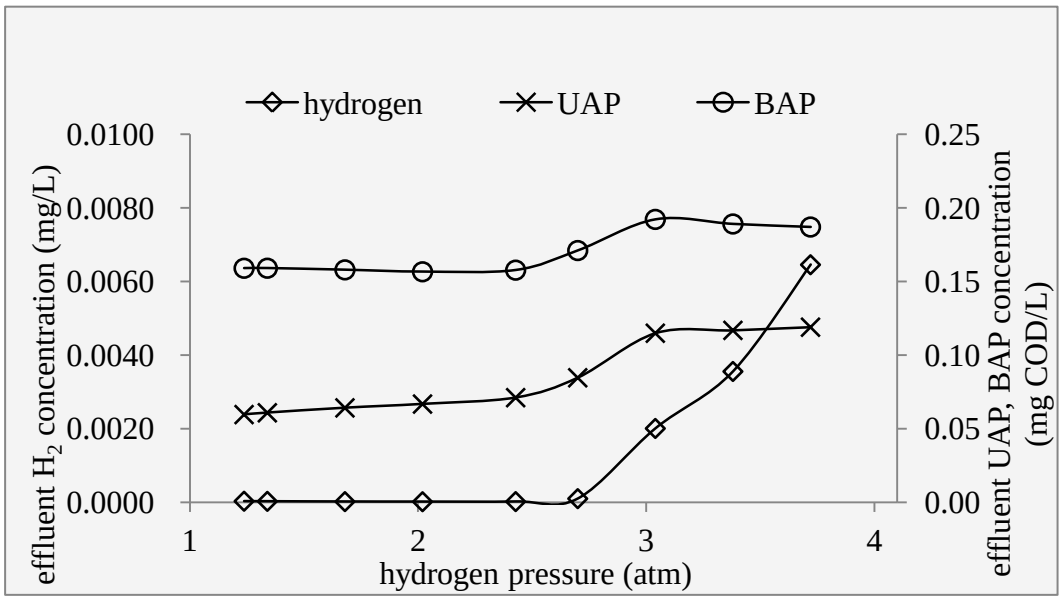

Fig. 9.3 Predicted concentrations of H_2, UAP, and BAP in the effluent

2.3 Distributions of solid components and profiles of dissolved components in the biofilm

Fig 9.4 plots distributions of the five solid components in the biofilms at three H_2 pressures: 2.0, 3.0, and 3.7 atm (15, 30, and 40 psig). Fig. 9.5 plots profiles of the five dissolved components at the three H_2 pressures. The three H_2 pressures correspond to around 50% nitrate reduction, the start of sulfate reduction, and 50% sulfate reduction, respectively.

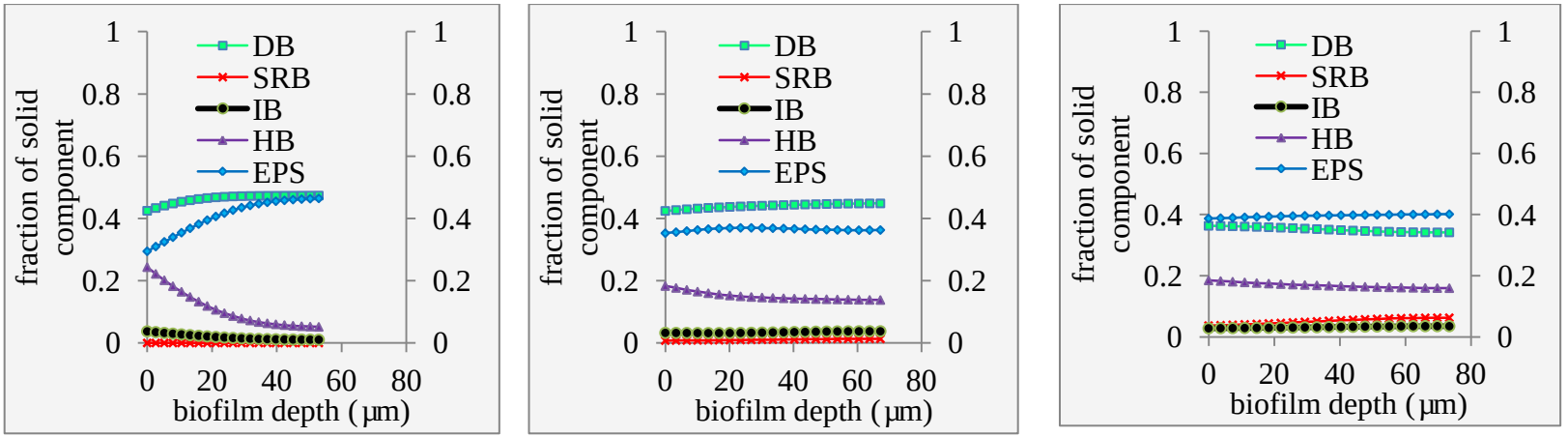

a. b. c.

Fig. 9.4 Distributions of solid components in the biofilm. Liquid is on the left and fiber is on the right. The biofilm thickness can be seen by looking at the rightmost extent of a line. a. H_2 pressure = 2.0 atm (15 psig); b. H_2 pressure = 3.0 atm (30 psig); c. H_2 pressure = 3.7 atm (40 psig).

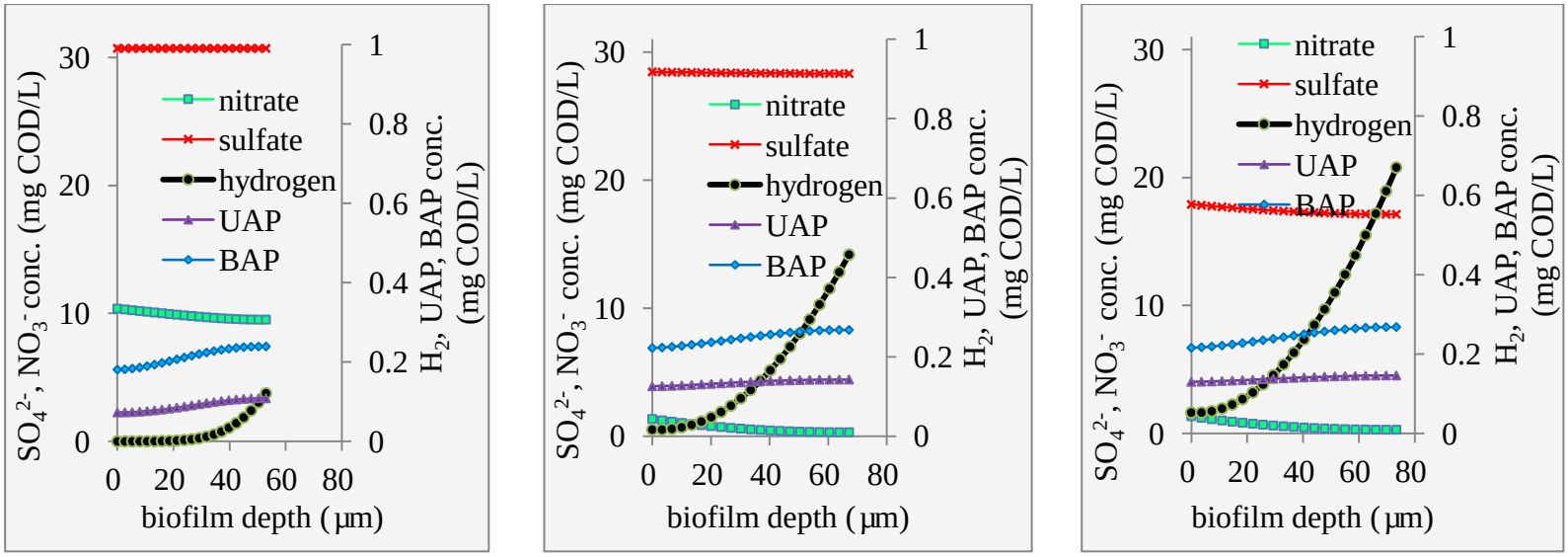

a. b. c.

Fig. 9.5 Profiles of dissolved components in the biofilm. Liquid is on the left and fiber is on the right. The biofilm thickness can be seen by looking at the rightmost extent of a line. a. H_2 pressure = 2.0 atm (15 psig); b. H_2 pressure = 3.0 atm (30 psig); c. H_2 pressure = 3.7 atm (40 psig).

As the H_2 pressure increases for the three runs, the fraction of DB decreases and the fraction of SRB increases. SRB are essentially zero for the lowest H_2 pressure, but increase to an average of about 5% for the highest pressure. Also, SRB have a higher fraction near the membrane surface once they are established, since a location near the source of H_2 is favorable. When SRB are not present, DB occupy up to 50% of the biofilm, and they also have a higher density near the membrane surface. In this model situation, onset of sulfate reduction occurs at a H_2 pressure of ~3.0 atm (30 psig) and an effluent nitrate concentration of ~1.5 mg N/L. As the H_2 pressure continues increasing, the flux of nitrate only slightly increases, but the flux of sulfate significantly increases (Fig. 9.2). This results in increase of the biofilm thickness and the fraction of SRB, as well as a slight decrease of the fraction of DB.

These changes can be explained mechanically. The H_2 pressure increase directly results in lower nitrate concentrations in the effluent (Fig. 9.2) and in the biofilm (Fig. 9.5), which lead to lower growth rates of DB. Once the growth rates of DB is low enough to equal the growth rate of SRB at the fiber surface, which is the coexistence boundary condition of the mathematical model, SRB start to grow in the biofilm. This explanation is consistent with the previous experimental observations that sulfate reduction only occurred when nitrate were almost completely removed (Ziv-El and Rittmann, 2009a; Tang et al., 2010).

EPS also have a higher density near the membrane surface, because they are produced by DB and SRB in proportion to H_2 consumption. IB and HB have higher fractions on the liquid side, since they can compete better with DB, SRB, and EPS on the liquid side, where H_2 is more limited for growth of DB, SRB, and EPS (Fig. 9.5). As H_2 pressure decreases, this competition advantage is enhanced, and IB and HB move towards the liquid side to gain this advantage.

To compare the cell numbers in the model and in the experiment, I first estimate the cell numbers in the model (units: cell number/m^2 of fiber) as

$$\frac{(L_f \times \frac{1m}{10^6 \mu m} \times m^2\text{-}fiber) \times X_f / m_{cell}}{m^2\text{-}fiber} \times \xi$$

, in which, L_f (μm) is the biofilm thickness, X_f (4×10^4 g VSS/m^3) is the biofilm density in Table 9.2, m_{cell} (2×10^{-13} g VSS/cell) is the unit cell weight and is from Madigan and Martinko (2006), and ξ is the fraction of relevant bacteria. For calculating total bacteria, ξ equals the sum of fractions of DB, SRB, and HB.

The cell numbers in the experiment are cited from Ontiveros Valencia et al. (2011), who conducted qPCR analyses that targeted 16S rDNA for total bacteria, sulfate reductase (*dsr*) for SRB, and nitrite reductases (*nirS & nirK*) for DB for H_2 pressures at 2.0 atm (15 psig), 3.0 atm (30 psig), and 3.7 atm (40 psig). They then used the number of gene copies per cell to estimate cell numbers of total bacteria, SRB, and DB (units: cell number/m^2 of fiber).

The estimated cell numbers from the experiment are compared to the estimated cell numbers from the model in Table 9.4. The trends in model and experiment match well. First, the numbers of total cells, SRB, and DB increase as the H_2 pressure increases. Second, the increase of SRB from 3.0 atm (corresponding to the start of sulfate reduction) to 3.7 atm (corresponding to around 50% sulfate reduction) is 5.0 times in the experiment and 6.4 times in the model, the increase of DB from 3.0 to 3.7 atm is 1.6 times in the experiment and 1.03 times in the model, the increase of total bacteria from 3.0 to 3.7 atm is 2.4 times in the experiment and 1.2 times in the model. Third, the percentage of SRB increased two-fold from 3.0 to 3.7 atm in the experiment and five-fold in the model, and the percentage of DB decreases by 32% from 3.0 to 3.7 atm in the experiment and by 13% in the model.

Table 9.4 Comparison[a] of simulated biomass data in the nitrate and sulfate model and qPCR data

H_2 pressure	Total bacteria (cell/m^2-fiber)		SRB (cell/m^2-fiber)		DB (cell/m^2-fiber)	
	Experiment	Model	Experiment	Model	Experiment	Model
2.0 atm	1.2×10^{13}	5.4×10^{12}	2.7×10^{11}	0	1.4×10^{12}	4.4×10^{12}
3.0 atm	1.3×10^{14}	8.0×10^{12}	1.7×10^{12}	1.4×10^{11}	2.9×10^{13}	5.8×10^{12}
3.7 atm	3.1×10^{14}	9.6×10^{12}	8.4×10^{12}	9.0×10^{11}	4.6×10^{13}	6.0×10^{12}

Notes:

a. The comparison aims at trends across the three steady states.

2.4 The effect of influent nitrate and sulfate concentrations on onset of sulfate reduction

Using the optimized parameters, I modeled the effluent nitrate and sulfate concentrations of the MBfR used for parameter optimization at a fixed H_2 pressure of 3.0 atm (30 psig), a fixed flow rate of 0.86 L/d (HRT = 1.5 h), and influent nitrate and sulfate concentrations ranging from 0 to 17.5 mg N/L and 0 to 75 mg SO_4^{2-}/L. The results are plotted in Fig. 9.6. The pink line on the sulfate panel of Fig. 9.6 notes the onset of sulfate reduction: On the right of this line, the effluent sulfate concentration equals the influent sulfate concentration, and on the left of this line, the effluent sulfate concentration is smaller than the influent sulfate concentration.

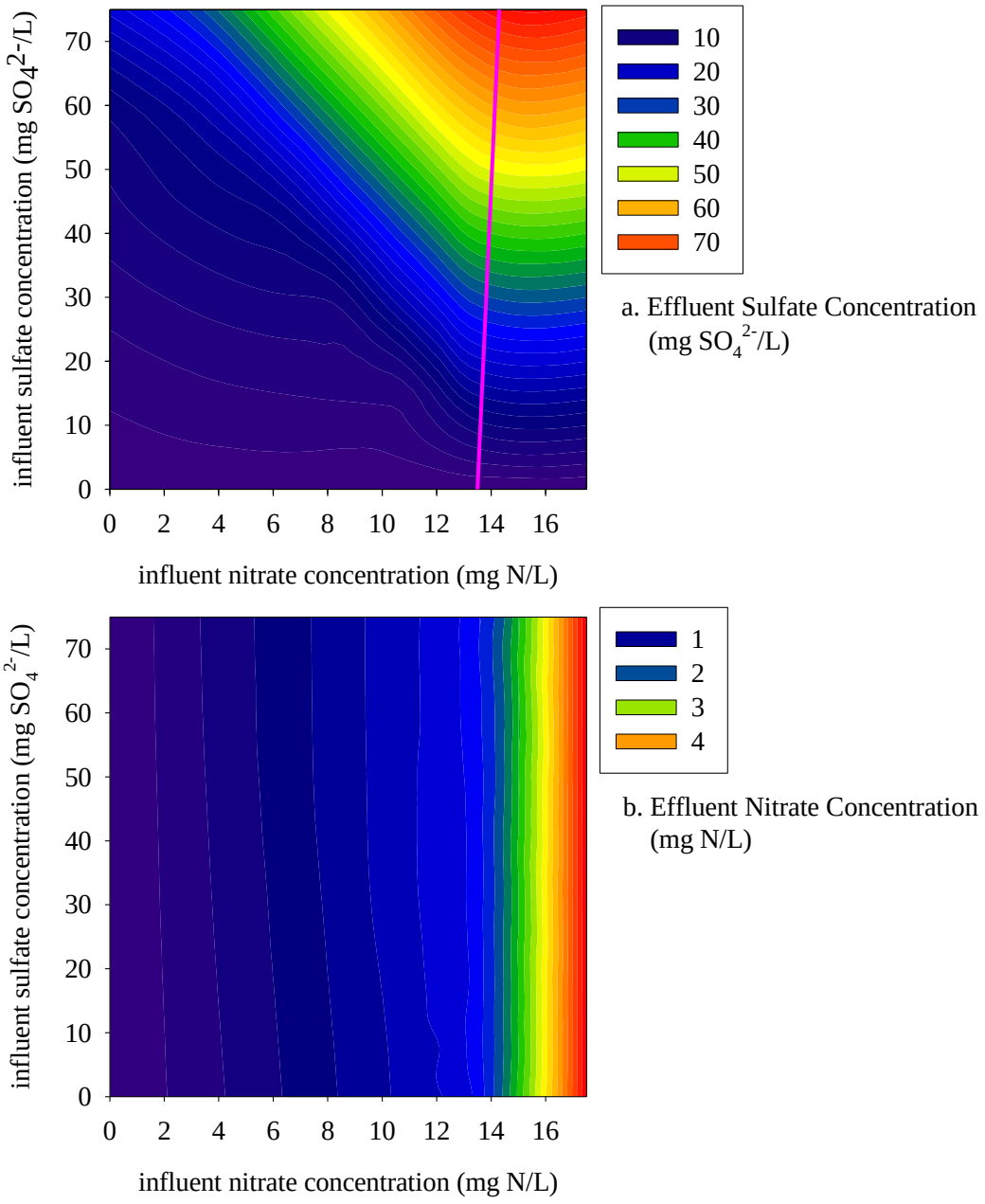

Fig. 9.6 Effluent concentration contours of nitrate and sulfate at different influent nitrate and sulfate concentrations. a. sulfate; b. nitrate. The pink line on the sulfate panel notes the onset of sulfate reduction.

The pink line slopes slightly right, indicating that the onset of sulfate reduction is strongly determined by the influent nitrate concentration, but only slightly affected by the influent sulfate reduction. This can be mechanically explained using the mathematical model. As discussed above, the onset of sulfate reduction corresponds to the boundary condition where the growth rates of SRB and DB are equal at the fiber surface. The growth rate of SRB is not sensitive to the influent sulfate concentration, since the sulfate concentration at the fiber surface is typically much higher than the half-maximum-rate concentration of sulfate (1.6 mg SO_4^{2-}/L) due to two reasons: 1) The effluent sulfate concentration is very close to the influent sulfate concentration when sulfate starts to be reduced; and 2) The sulfate concentration profile is flat (Fig. 9.5b), i.e., the sulfate concentrations at the fiber surface and in the liquid (the effluent) are close, because of a very small fraction of SRB. However, the growth rate of DB at the fiber surface is very sensitive to the influent nitrate concentration, since the nitrate concentration at the fiber surface is typically close to the half-maximum-rate concentration of nitrate (0.2 mg N/L) for two reasons: 1) The effluent nitrate concentration is much lower than the influent nitrate concentration; 2) The nitrate concentration profile in the biofilm non-linear declines in the biofilm (Fig. 9.5b); then, the nitrate concentration at the fiber surface is much lower than its concentration in the liquid (the effluent), because of a large fraction of DB.

The highest nitrate concentration at the fiber surface to allow sulfate reduction can be estimated using the boundary condition that the growth rates of SRB and DB are equal at the fiber surface:

$$k_1\mu_1 \frac{S_{f1}}{K_1 + S_{f1}} \frac{S_{f3}}{K_{31} + S_{f3}} - p_1 \frac{S_{f1}}{K_1 + S_{f1}} - b_1$$
$$= k_1\mu_2 \frac{S_{f2}}{K_2 + S_{f2}} \frac{S_{f3}}{K_{32} + S_{f3}} - p_2 \frac{S_{f2}}{K_2 + S_{f2}} - b_2$$

in which, S_{f1} is unknown, S_{f2} is assumed to equal the influent sulfate concentration, S_{f3} is assumed to be in equilibrium with the H_2 pressure in the fiber lumen, and the other parameters are kinetics parameters and can be found in Table 9.2. Thus, S_{f1} can be estimated by solving this equation, e.g., it is S_{f1} = 0.1 mg N/L if the influent sulfate concentration is 46 mg SO_4^{2-}/L, and the H_2 pressure is 3 atm.

Nitrate reduction is not affected by the influent sulfate concentration. When sulfate is not reduced, the effect of sulfate is not relevant. When sulfate is reduced, it has little effect on nitrate reduction, since the nitrate concentrations are already very low when sulfate reduction occurs.

2.5 The effect of flow rate on onset of sulfate reduction

Using the optimized parameters, I also modeled the effluent nitrate and sulfate concentrations of the MBfR used for parameter optimization at a fixed H_2 pressure of 3.0 atm (30 psig), a fixed influent nitrate concentration of 12.8 mg N/L, a fixed influent sulfate concentration of 46 mg SO_4^{2-}/L, and flow rates ranging from 0 to 2 L/d (HRT > 0.7 h). The results are plotted in Fig. 9.7. Onset of sulfate reduction occurs at a flow rate of ~1.0 L/d for these condidtions. While a flow rate of < 1.0 L/d results in sulfate reduction, a flow rate of > 1.0 L/d leads to a higher effluent nitrate reduction. Therefore, 1.0 L/d is the optimum operating flow rate to achieve good nitrate reduction without sulfate reduction.

The approach here can be used for MBfR design in practice. The influent nitrate and sulfate concentrations are system-specific, the H_2 pressure is usually the maximum bubbleless H_2 pressure provided by the fiber manufacturer, and the configuration of an MBfR module is also provided by the MBfR manufacture (e.g., total fiber surface area, H_2 permeation coefficients of the fibers). This information can be input into the model to generate a figure similar to Fig. 9.7. The optimum flow rate can then be determined using this figure. Finally, the number of modules required can be determined by dividing the total flow rate by the optimum flow rate of one MBfR module.

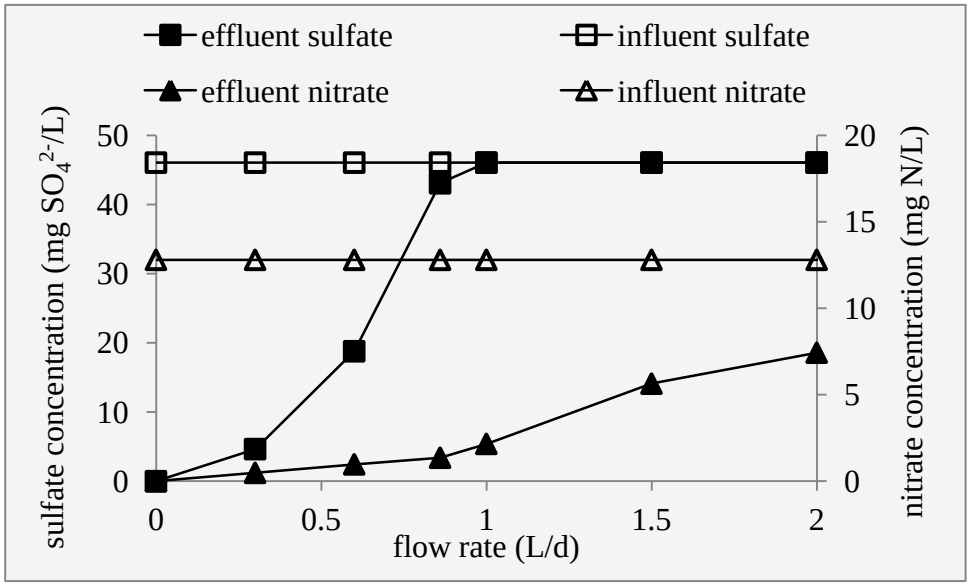

Fig. 9.7 Effluent nitrate and sulfate concentrations at different flow rates.

2.6 A design example

I provide an example of using this model to design a H_2-based MBfR for treating a groundwater for human consumption. The groundwater has a dissolved oxygen concentration (S_0) of 4.0 mg O_2/L, a nitrate concentration (S_1) of 30 mg N/L, and a sulfate concentration (S_2) of 100 mg SO_4^{2-}/L. The flow (Q) is 1.0×10^3 m^3/d.

First, I choose a commercially available MBfR module that has a volume (V) of 250 L and contains polypropylene fibers with a total surface area (A) of 320 m^2, a H_2-permeation coefficient (P_m) of 0.0013 cm^2/d, a fiber wall thickness (L_m) of 55 μm, and a miximum bubbleless H_2 pressure (S_3) of 3.4 atm (Meyer et al., 2010).

Second, I use the model to generate Fig. 9.8: Effluent nitrate and sulfate concentrations at flow rates of 1 to 22 m^3/d in a module. Four of the eight system-specific parameters (L_m, A, q, P_m, S_0, S_1, S_2, S_{g3}) of the model, including q, S_0, S_1, and S_{g3} are specially treated. First, considering a safety factor of 0.7, I use an operating H_2 pressure of 2.4 atm (= 3.4×0.7 atm), convert the operating H_2 pressure to H_2 concentration in the fibe lumen using the equation in Table 9.2. (S_{g3} = 1.58 mg COD/cm^3), and directly input S_{g3} into the model. Second, according to model assumptions and simplifications, 4 mg O_2/L (S_0) and 30 mg NO_3^--N/L (S_1) are equivalent to 31.4 mg NO_3^--N/L in the model: O_2 is converted to NO_3^- according to electron equivalence (1 mg O_2/L is equivalent to 0.35 mg NO_3^--N/L). Third, the flow rate q in a module is varied from 1 to 22 m^3/d to make effluent nitrate and sulfate concentrations vary enough for use in the third step.

Third, according to Fig. 9.8, the flow rate in a module should be between 10 and 15 m^3/d to achieve no sulfate reduction and effluent NO_3^- concentration below its maximum contaminant level of 10 mg N/L. The medium flow rate of 12.5 m^3/d is the optimum flow rate, since the effluent water quality is good even if the flow rate changes up to about ±25%.

Finally, the required number of modules is calculated as (1.0×10^3 m^3/d) /(12.5 m^3/d) = 80. Assuming each compartment contains 40 (= 5×8) modules

(typical for full-scale MBfRs (Meyer et al. 2010)), the total number of compartments is 80/40 = 2.

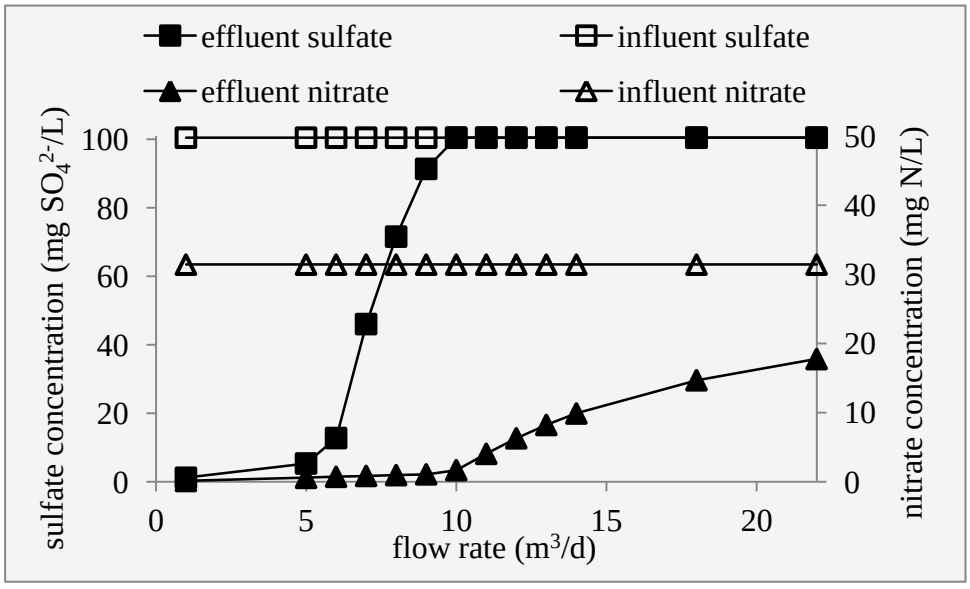

Fig. 9.8 Effluent nitrate and sulfate concentrations at flow rates of 1 to 22 m^3/d in a module.

3.0 Conclusions

I produced a multispecies biofilm model for simultaneous reduction of nitrate and sulfate in the H_2-based membrane biofilm reactor (MBfR) by adapting my multispecies biofilm model for simultaneous reduction of nitrate and perchlorate. As required, I modified model components and their relationships, model assumptions and simplifications, substrate-utilization and biomass-growth kinetics, and model parameters.

Two parameters, the half-maximum-rate concentrations of nitrate and sulfate, are not consistent in literature; thus I optimized them by best-fitting the nitrate and sulfate data from a bench-scale experiment with H_2 pressures ranging from 1.2 to 3.7 atm. The optimized parameters, 0.2 mg N/L and 1.6 mg SO_4^{2-}/L, are in the middle of their reported ranges: 0.04 - 0.5 mg N/L and 0.16 - 31 mg SO_4^{2-}/L.

To evaluate the model, I compared the effluent H_2, UAP (substrate-utilization-associated products), and BAP (biomass-associated products) concentrations to data in experiments, and I compared biomass distributions to qPCR data in the bench-scale experiment for parameter optimization. Model outputs and experimental results matched in terms of all major trends. For example, as the H_2 pressure increases, the numbers of total cells, SRB, and DB increase, the percentage of SRB increases, but the percentage of DB decreases.

Using the optimized parameters, I predicted effluent nitrate and sulfate concentrations over a wide range of operating conditions, including H_2 pressure, influent nitrate and sulfate concentrations, and flow rate. The influent sulfate concentration has little effect on the onset of sulfate reduction. Instead, sulfate reduction occurs when the H_2 pressure is high enough, the influent nitrate concentration is low enough, or the flow rate is low enough. In general, the onset of sulfate reduction occurs when the nitrate concentration at the fiber surface is

low enough to allow the growth rates of DB and SRB equal at the fiber surface. For example, the maximum nitrate concentration at the fiber surface is 0.1 mg N/L to allow coexistence of SRB in the biofilm when the influent sulfate concentration is 46 mg SO_4^{2-}/L, and the H_2 pressure is 3.0 atm. Since the model can predict the H_2-pressure and nitrate loading conditions corresponding to the onset of sulfate reduction, it can be used as a tool to design MBfR and to quantitatively obtain the desired reductions of nitrate and sulfate in an MBfR.

Chapter 10

A MULTISPECIES BIOFILM MODEL FOR SIMULTANEOUS REDUCTION OF NITRATE AND TCE

The main goal of this chapter is to modify the nitrate and perchloate model in Chapter 8 into a nitate and TCE model and use it to investigate how operating conditions affect TCE reduction and accumulation of TCE reduction intermediates in a denitrifying MBfR. Relevant background information was presented in pages 15-16 in Chapter 1. This chapter (Chapter 10) presents the first-step extention of the nitrate and perchlorate model and the preliminary modeling results.

1. Materials and Methods

1.1 Model adaption

The nitrate and TCE model is a first-step extention of the nitrate and perchlorate model in Chapter 8. The basic mathematical equations that comprise the two models are the same. These equations include the dissolved-component mass-balance Eq. 8.1 and its boundary-condition Eqs. 8.2, 8.3, and 8.8, and the solid-component mass-balance Eq. 8.19 and its boundary-condition Eqs. 8.20 and 8.25. The numerical solution for the two models is also the same. However, the

two models differ in model components and their interactions, model assumptions and simplifications, and substrate-utilization and biomass-growth terms and kinetic parameters in equations. The differences are addressed in this section.

1.1.1 Model components and their interactions

This model has five solid components: autotrophic denitrifying bacteria (ADB), *Dehalococcoides* (DH), heterotrophic denitrifying bacteria (HDB), inert biomass (IB), and extracellular polymeric substances (EPS). The model has eight dissolved components: nitrate (NO_3^-), TCE, hydrogen (H_2), substrate-utilization-associated products (UAP), biomass-associated products (BAP), DCE, VC, and ethene. The components in the nitrate and TCE model are the same as those in the nitrate and perchlorate model, except that PRB are changed to DH, perchlorate is changed to TCE, and DCE, VC, and ethene are added. The component ethene is treated specially in the mathematical model: Its concentration in the effluent is directly obtained by subtracting the effluent TCE, DCE, and VC concentrations (mole/L) from the influent TCE concentration (mole/L) after the mathematical model is numerically solved. This mass-balance approach is based on the fact that the carbon in TCE is not incorporated into biomass, because DH use acetate as their carbon source (Tang et al., 2009; Ziv-El et al., 2012).

Fig. 10.1 describes how the different components in the model are related. Many relationships in the nitrate and TCE model are similar to those in the nitrate and perchlorate model, and the differences are discussed here. In the nitrate and perchlorate model, PRB can use nitrate and perchlorate as their electron acceptors, and nitrate and perchlorate competitively inhibit each other, since the two electron acceptors are reduced by the same enzyme in PRB. In the nitrate and TCE model, DH use TCE, DCE, and VC as their electron acceptors, and TCE inhibits DCE and VC reductions, DCE inhibits only VC reduction, and VC does not inhibit any reductions.

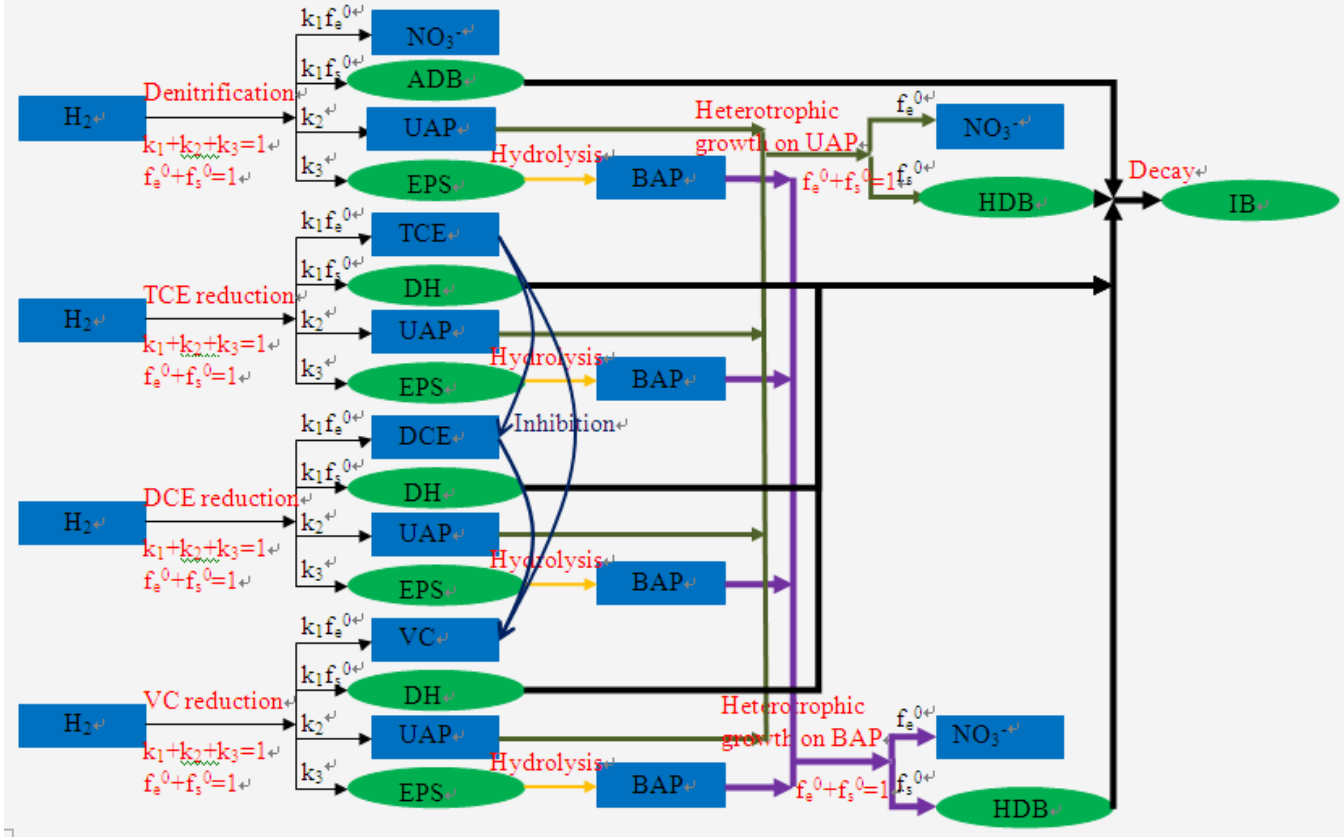

Fig. 10.1 Schematic describing how the dissolved components (rectangles) and solid components (ellipses) interact in the nitrate and TCE model. TCE is sequentially reduced to DCE, VC, and ethane. ADB: autotrophic denitrifying bacteria; DH: *Dehalococcoides*; HDB: heterotrophic denitrifying bacteria; IB: inert biomass; EPS: extracellular polymeric substances; UAP: substrate-utilization-associated products; BAP: biomass-associated products.

1.1.2 Model assumptions and simplifications

The assumptions and simplifications a), b), c), d), h), i), j), and k) in the nitrate and perchlorate model also apply in the nitrate and TCE model, but five more assumptions should be added here:

1) Inhibition among chlorinated ethenes is expressed by inhibition coefficients in the acceptor part of dual-substrate Monod kinetics (Rittmann and McCarty, 2001). The inhibition coefficients equal the half-maximum-rate concentrations (Garant and Lynd, 1998; Yu et al., 2005).
2) Endogenous respiration is neglected for all bacteria to simply the numerical solution; however, all bacteria are inactivated to inert biomass (IB).
3) Bacteria that can reduce TCE to DCE or VC, but cannot reduce it to ethene are neglected.
4) Homoacetogenesis and methanogenesis are not included in the model.
5) Nutrients are not limiting for all bacteria. For example, DH have sufficient vitamin B12 and acetate (as its carbon source) either from the influent, decay of biomass, or the activity of homoacetogens.

1.1.3 Substrate-utilization and biomass-growth terms and kinetic parameters in equations

Table 10.1 mathematically describes the processes considered in the model and how the five solid and eight dissolved components interact with each other in these processes. Symbols in Table 10.1 are described in Table 10.2 for model inputs and Table 10.3 for model outputs. The inputs in the nitrate and TCE

model are the same as those in the nitrate and perchlorate model, except for system-specific parameters and kinetics parameters unique to TCE, DCE, and VC reduction. The reactor configuration is the same as that used in Chung et al. (2008). The reactor used composite fiber that has a total membrane surface area (A) of 72.6 cm^2, a membrane wall thickness (L_m) of 0.005 cm, and a H_2-permeation coefficient of 0.016 cm^2/d. The operating conditions -- influent nitrate concentration (S_1), influent TCE concentration (S_2), H_2 pressure (S_3), and flow rate (Q) -- are varied one by one in wide ranges to investigate how they affect TCE reduction and intermediates accumulation in the MBfR. The standard condition is the same as the operating condition used in Chuang et al. (2008) and includes S_1 = 14.3 mg COD/L, S_2 = 0.37 mg COD/L, S_3 = 1.17 atm, and Q = 1 mL/min. As in Chapters 8 and 9, COD can be positive COD for electron donors and negative COD for electron acceptors (e.g., nitrate, TCE, DCE, and VC). Chambon et al. (2009) summarized the TCE, DCE, and VC reduction kinetics data available in the literature, and they varied over wide ranges. I use the median values of these kinetics data summarized by Chambon et al. (2009).

Table 10.1 Process, component, and rate matrix in the nitrate and TCE model

Process (j)		Coefficient of component i in process j (η_{ij})												Conversion rate (R_j)
		Solid component					Dissolved component[a]							
		ADB	DH	IB	HDB	EPS	NO_3^-	TCE	DCE	VC	H_2	UAP	BAP	
ADB	growth	k_1				$\frac{k_5}{Y_1}$	$\frac{(Y_1-1)k_1}{Y_1}$				$-\frac{1}{Y_1}$	$\frac{k_4}{Y_1}$		R_1[b]
	inactivation	-1		$(1-f_d)$										$b_1 f_1 X_f$
DH	growth on TCE		k_1			$\frac{k_5}{Y_2}$		$\frac{(Y_2-1)k_1}{Y_2}$	$\frac{2(1-Y_2)k_1}{3Y_2}$		$-\frac{1}{Y_2}$	$\frac{k_4}{Y_2}$		R_2[b]
	growth on DCE		k_1			$\frac{k_5}{Y_6}$			$\frac{(Y_6-1)k_1}{Y_6}$	$\frac{(1-Y_6)k_1}{2Y_6}$	$-\frac{1}{Y_6}$	$\frac{k_4}{Y_6}$		R_6[b]
	growth on VC		k_1			$\frac{k_5}{Y_7}$				$\frac{(Y_7-1)k_1}{Y_7}$	$-\frac{1}{Y_7}$	$\frac{k_4}{Y_7}$		R_7[b]
	inactivation		-1	$(1-f_d)$										$b_2 f_2 X_f$
HDB	growth on UAP				1		$-\frac{(1-Y_4)}{Y_4}$					$-\frac{1}{Y_4}$		R_4[b]
	growth on BAP				1		$-\frac{(1-Y_5)}{Y_5}$						$-\frac{1}{Y_5}$	R_5[b]
	inactivation			$(1-f_d)$	-1									$b_4 f_4 X_f$
EPS	hydrolysis					-1							1	$k_{hyd} f_5 X_f$

summed conversion rate of component i	summed specific growth rate: $\mu_{oi} = \frac{\sum_j (\eta_{ij} R_j)}{f_i X_f}$	summed utilization rate: $r_{oi} = \sum_j (\eta_{ij} R_j)$	

Notes:

a. The eighth dissolved component (ethene) is computed by mass balance from TCE, DCE, and VC concentrations.

b. $R_1 = \mu_1 f_1 X_f \frac{S_{f1}}{K_1 + S_{f1}} \frac{S_{f3}}{K_{31} + S_{f3}}$; $R_2 = \mu_2 f_2 X_f \frac{S_{f2}}{K_2 + S_{f2}} \frac{S_{f3}}{K_{32} + S_{f3}}$; $R_4 = \mu_4 f_4 X_f \frac{S_{f4}}{K_4 + S_{f4}} \frac{S_{f1}}{K_1 + S_{f1}}$; $R_5 = \mu_4 f_4 X_f \frac{S_{f5}}{K_5 + S_{f5}} \frac{S_{f1}}{K_1 + S_{f1}}$

$R_6 = \mu_6 f_2 X_f \frac{S_{f6}}{K_6(1 + \frac{S_{f2}}{K_{26i}}) + S_{f6}} \frac{S_{f3}}{K_{36} + S_{f3}}$; $R_7 = \mu_7 f_2 X_f \frac{S_{f7}}{K_7(1 + \frac{S_{f2}}{K_{27i}} + \frac{S_{f6}}{K_{67i}}) + S_{f7}} \frac{S_{f3}}{K_{37} + S_{f3}}$

Table 10.2 Inputs for the nitrate and TCE model[a]

Symbols	Description	Units	Values
K_1	Half-maximum-rate concentration for nitrate	mg-COD/cm^3	5.7×10^{-4} (Chapter 8)
K_2	Half-maximum-rate concentration for TCE	mg-COD/cm^3	1.4×10^{-4} (Chambon et al., 2009)
K_{31}	Half-maximum-rate concentration for H_2 in denitrification	mg-COD/cm^3	1.6×10^{-5} (Kurt et al., 1987)
K_{32}	Half-maximum-rate concentration for H_2 in TCE reduction	mg-COD/cm^3	8.0×10^{-6} (Chambon et al., 2009)
K_{36}	Half-maximum-rate concentration for H_2 in DCE reduction	mg-COD/cm^3	8.0×10^{-6} (Chambon et al., 2009)
K_{37}	Half-maximum-rate concentration for H_2 in VC reduction	mg-COD/cm^3	8.0×10^{-6} (Chambon et al., 2009)
K_4	Half-maximum-rate concentration for UAP	mg-COD/cm^3	5.0×10^{-3} (Wanner and Gujer, 1986)
K_5	Half-maximum-rate concentration for BAP	mg-COD/cm^3	5.0×10^{-3} (Wanner and Gujer, 1986)
K_6	Half-maximum-rate concentration for DCE	mg-COD/cm^3	1.1×10^{-4} (Chambon et al., 2009)
K_7	Half-maximum-rate concentration for VC	mg-COD/cm^3	2.0×10^{-3} (Chambon et al., 2009)
K_{26i}	Inhibition coefficient of TCE on DCE reduction	mg-COD/cm^3	1.4×10^{-4} (Chambon et al., 2009)
K_{27i}	Inhibition coefficient of TCE on VC reduction	mg-COD/cm^3	1.4×10^{-4} (Chambon et al., 2009)
K_{67i}	Inhibition coefficient of DCE on VC reduction	mg-COD/cm^3	1.1×10^{-4} (Chambon et al., 2009)
Y_1	Yield of ADB growing on H_2	mg-COD/mg-COD	0.2 (Rittmann and McCarty,2001)

Table 10.2 Inputs for the nitrate and TCE model[a]

Symbols	Description	Units	Values
Y_2	Yield of DH growing on TCE	mg-COD/mg-COD	0.06 (Chambon et al., 2009)
Y_4	Yield of HDB growing on UAP	mg-COD/mg-COD	0.6 (Rittmann and McCarty,2001)
Y_5	Yield of HDB growing on BAP	mg-COD/mg-COD	0.6 (Rittmann and McCarty,2001)
Y_6	Yield of DH growing on DCE	mg-COD/mg-COD	0.09 (Chambon et al., 2009)
Y_7	Yield of DH growing on VC	mg-COD/mg-COD	0.13 (Chambon et al., 2009)
μ_1	Maximum specific growth rate of ADB	d^{-1}	1.0 (Rittmann and McCarty,2001)
μ_2	Maximum specific growth rate of DH in TCE reduction	d^{-1}	0.49 (Chambon et al., 2009)
μ_4	Maximum specific growth rate of HDB	d^{-1}	13.2 (Rittmann and McCarty,2001)
μ_6	Maximum specific growth rate of DH in DCE reduction	d^{-1}	0.43 (Chambon et al., 2009)
μ_7	Maximum specific growth rate of DH in VC reduction	d^{-1}	0.28 (Chambon et al., 2009)
k_1	Coefficient for electrons used for biomass production		0.77 (Rittmann and McCarty,2001)
k_2	Coefficient for electrons going to UAP		0.05 (Rittmann and McCarty,2001)
k_3	Coefficient for electrons going to EPS		0.18 (Rittmann and McCarty,2001)
b_1	Inactivation coefficient for ADB	d^{-1}	0.05 (Wanner and Gujer, 1986)
b_2	Inactivation coefficient for DH	d^{-1}	0.03 (Chambon et al., 2009)
b_4	Inactivation coefficient for HDB	d^{-1}	0.1 (Wanner and Gujer, 1986)
k_d	Biofilm detachment coefficient	$cm^{-1}d^{-1}$	36 (Trulear and Characklis; 1982)

Table 10.2 Inputs for the nitrate and TCE model[a]

Symbols	Description	Units	Values
D_1	Nitrate diffusion coefficient within the diffusion layer	cm^2/d	1.2 (Williamson and McCarty,1976)
D_2	TCE diffusion coefficient within the diffusion layer	cm^2/d	0.54 (Stewart, 1998)
D_3	H_2 diffusion coefficient within the diffusion layer	cm^2/d	4.4 (Macpherson and Unwin, 1997)
D_4	UAP diffusion coefficient within the diffusion layer	cm^2/d	1 (Merkey, 2008)
D_5	BAP diffusion coefficient within the diffusion layer	cm^2/d	0.6[b] (Merkey, 2008)
D_6	DCE diffusion coefficient within the diffusion layer	cm^2/d	0.61 (Stewart, 1998)
D_7	VC diffusion coefficient within the diffusion layer	cm^2/d	0.71 (Stewart, 1998)
D_{f1}	Nitrate diffusion coefficient within the biofilm	cm^2/d	0.96 (Williamson and McCarty,1976)
D_{f2}	TCE diffusion coefficient within the biofilm	cm^2/d	0.16 (Tuwiner, 1962)
D_{f3}	H_2 diffusion coefficient within the biofilm	cm^2/d	3.5 (Macpherson and Unwin, 1997)
D_{f4}	UAP diffusion coefficient within the biofilm	cm^2/d	0.8 (Merkey, 2008)
D_{f5}	BAP diffusion coefficient within the biofilm	cm^2/d	0.5[b] (Merkey, 2008)
D_{f6}	DCE diffusion coefficient within the biofilm	cm^2/d	0.18 (Stewart, 1998)
D_{f7}	VC diffusion coefficient within the biofilm	cm^2/d	0.20 (Stewart, 1998)
k_{hyd}	Hydrolysis rate of EPS	d^{-1}	0.22 (Rittmann and McCarty, 2001)
f_d	Fraction of biomass that is biodegradable		0.8 (Rittmann and McCarty, 2001)
X_f	Biomass density	$mg\text{-}COD/cm^3$	79.3 (Rittmann and McCarty, 2001)
L_d	Thickness of effective diffusion layer	cm	0.01 (Rittmann and McCarty, 2001)

Table 10.2 Inputs for the nitrate and TCE model[a]

Symbols	Description	Units	Values
k_H	Dimensionless Henry's Law constant of H_2		0.01907 (Sander, 1999)
L_m	Thickness of membrane	cm	0.005[c]
A	Total membrane surface area	cm^2	72[c]
Q	Flow rate	cm^3/d	1440[c]
K_m	Hydrogen permeation coefficient within the membrane	cm^2/d	0.016[c]
S_1	Nitrate concentration in the influent	mg-COD/cm^3	0.0143[c]
S_2	TCE concentration in the influent	mg-COD/cm^3	0.00037[c]
S_{g3}[d]	H_2 concentration in the bulk gas	mg-COD/cm^3	0.77[c]

Notes:

a. Conversion factors: 1 mg NO_3^--N: 2.857 mg COD; 1 mg cell: 1.982 mg COD; 1 mg TCE: 0.37 mg COD; 1 mg DCE: 0.33 mg COD; 1 mg VC: 0.27 mg COD 1 mg H_2: 8 mg COD.

b. Since BAP molecules are larger than UAP, the diffusion coefficients of BAP are assumed to be 60% of those of UAP.

c. The same as in Chung et al. (2008).

d. For consistency, H_2 concentration in COD, instead of H_2 pressure, is used. H_2 concentration is calculated using the ideal gas law: $S_{g3} = S_3 \div 0.082 \div 298 \times 2 \times 8$ (mg COD/cm^3), where, S_3 is the hydrogen pressure in the fibers, 0.082 L-atm/K-mol is the gas constant, 298 K is the temperature, 2×8 g COD/mole H_2 is the conversion factor from H_2 mass to COD.

Table 10.3 Outputs for the nitrate and TCE model

Symbols	Description	Units
J_1	nitrate flux into the biofilm	mg-COD/cm^2-d
J_2	TCE flux into the biofilm	mg-COD/cm^2-d
J_{3m}	H_2 flux into the biofilm	mg-COD/cm^2-d
J_3	H_2 flux out of the biofilm	mg-COD/cm^2-d
J_4	UAP flux out of the biofilm	mg-COD/cm^2-d
J_5	BAP flux out of the biofilm	mg-COD/cm^2-d
J_6	DCE flux out of the biofilm	mg-COD/cm^2-d
J_7	VC flux out of the biofilm	mg-COD/cm^2-d
L_f	thickness of biofilm	cm
f_1	fraction of ADB	--
f_2	fraction of DH	--
f_3	fraction of IB	--
f_4	fraction of HDB	--
f_5	fraction of EPS	--
S_{f1}	nitrate concentration in the biofilm	mg-COD/cm^3
S_{f2}	TCE concentration in the biofilm	mg-COD/cm^3
S_{f3}	H_2 concentration in the biofilm	mg-COD/cm^3
S_{f4}	UAP concentration in the biofilm	mg-COD/cm^3
S_{f5}	BAP concentration in the biofilm	mg-COD/cm^3
S_{f2}	DCE concentration in the biofilm	mg-COD/cm^3
S_{f2}	VC concentration in the biofilm	mg-COD/cm^3
S_{b1}	nitrate concentration in the effluent	mg-COD /cm^3
S_{b2}	TCE concentration in the effluent	mg-COD /cm^3
S_{b3}	H_2 concentration in the effluent	mg-COD /cm^3
S_{b4}	UAP concentration in the effluent	mg-COD /cm^3
S_{b5}	BAP concentration in the effluent	mg-COD /cm^3
S_{b6}	DCE concentration in the effluent	mg-COD /cm^3
S_{b7}	VC concentration in the effluent	mg-COD /cm^3
S_{b8}	Ethene concentration in the effluent	mg-COD /cm^3

1.2 Coexistence of ADB and DH

The coexistence condition for ADB and DH is a key to understanding space competition between ADB and DH in the biofilm. According to the mathematical model, the growth rates of ADB and DH should be equal at the fiber surface to allow them to coexist in the biofilm:

$$k_1\mu_1 \frac{S_{f1}}{K_1+S_{f1}} \frac{S_{f3}}{K_{31}+S_{f3}} - b_1$$

$$= k_1\mu_2 f_2 X_f \frac{S_{f2}}{K_2+S_{f2}} \frac{S_{f3}}{K_{32}+S_{f3}} + k_1\mu_6 f_2 X_f \frac{S_{f6}}{K_6(1+\frac{S_{f2}}{K_{26i}})+S_{f6}} \frac{S_{f3}}{K_{36}+S_{f3}}$$

$$+k_1\mu_7 f_2 X_f \frac{S_{f7}}{K_7(1+\frac{S_{f2}}{K_{27i}}+\frac{S_{f6}}{K_{67i}})+S_{f7}} \frac{S_{f3}}{K_{37}+S_{f3}} - b_2$$

In general, DH are slower growers compared with ADB, because 1) the maximum growth rates of DH (μ_2, μ_6, and μ_7) are smaller than the maximum growth rate of ADB (μ_1), and 2) due to inhibition among chlorinated ethenes, the apparent half-maximum-rate concentrations of DCE and VC ($K_6(1+\frac{S_{f2}}{K_{26i}})$ and $K_7(1+\frac{S_{f2}}{K_{27i}}+\frac{S_{f6}}{K_{67i}})$) are typically higher than the half maximum-rate concentration of nitrate (K_1).

To satisy the coexistence equation, the reactor should have at least one of the following two conditions: 1) a relatively small S_{f1}, and 2) relatively higher S_{f2}, S_{f6}, and/or S_{f7}. The two conditions are associated with the four operating conditions: Condition 1) could be the result of a low influent nitratate concentration, a high H_2 pressure, or a low flow rate; condition 2) normally is the

result of a high influent TCE concentratraon. Therefore, a lower influent nitrate concentration, a higher H_2 pressure, a lower flow rate, or a higher influent TCE concentration favors DH growth. Condition 1) coincides with the scenarios of no H_2 limitation for a groundwater that has a high nitrate to TCE ratio, which is common.

1.3 Analysis of H_2 limitation

H_2 limitation occurs when the H_2 supply is less than the H_2 requirement for full reduction of all acceptors. I identify the conditions giving H_2-limitation by calculating when the stoichiometric H_2 requirement (expressed as the H_2 flux needed to fully reduce NO_3^- and TCE) exceeds the maximum H_2 delivery flux:

$$\frac{(S_1\ (mg\ COD/L)\times 1.25 + S_2\ (mg\ COD/L)\times 1.1)Q}{A} > J_{\max}\ (mg\ COD/cm^2 - d)$$

in which S_1 and S_2 are the influent nitrate and TCE concentrations, respectively. Q is the flow rate, and A is the total fiber surface area, 72 cm^2 (Table 10.2). Stoichiometric coefficients are obtained using the yield coefficients of ADB and DH in Table 10.2: $1.25 = 1/(1-Y_1)$; $1.1 = 1/(1-(Y_2+Y_6+Y_7)/3)$. The theoretical maximum H_2 flux (J_{max}) for the fiber type and H_2 pressure is obtained using Eq. 7.2: J_{max} is proportional to the H_2 pressure (S_3). Thus, the four operating conditions -- S_1, S_2, S_3, and Q -- are the four unknowns in this inequality. Once three of them are known, the fourth one can be computed. Table 10.4 summarizes the solution of this inequality when three of the four unknowns are the standard operating conditions.

Table 10.4 Operating conditions corresponding to H_2 competition

Situations	S_1 (mg COD/L)	S_2 (mg COD/L)	S_3 (atm)	Q (L/d)
S_1 is variable	> 98	0.37	1.17	1.44
S_2 is variable	14.3	> 95	1.17	1.44
S_3 is variable	14.3	0.37	< 0.18	1.44
Q is variable	14.3	0.37	1.17	> 9.6

2. Results and Discussion

2.1 Simulation of a bench-scale experiment

The bench-scale experiment in Chung et al. (2008) was simulated using this model. The simulated results are compared to the experimental results in Table 10.5. The model simulated the trends well: almost complete removal of nitrate, incomplete reduction of TCE, and almost no accumulation of DCE and VC. However, the simulated effluent concentrations are slightly, but systematically higher than the experimental concentrations. One possible explanation is that H_2 was over-supplied in the experiment (supported by discussion in sections 2.2 - 2.5), leading to growth of suspended biomass that can further reduce the concentrations of nitrate, TCE, DCE, and VC.

Table 10.5 Comparison of experimental and simulated results for a bench-scale experiment

Parameters (mg COD/L)	Experimental results	Simulated results
Influent NO_3^- concentration	14.3	14.3
Influent TCE concentration	0.37	0.37
Effluent NO_3^- concentration	< 0.3	2.7
Effluent TCE concentration	0.07 ±0.02	0.17
Effluent DCE concentration	< 0.002	0.03
Effluent VC concentration	< 0.001	0.05

2.2 The effect of influent nitrate concentration on TCE reduction and intermediates accumulation

Fig. 10.2 plots the effluent TCE, DCE, VC, and NO_3^- concentrations at influent NO_3^- concentrations ranging from 1 to 70 g COD/L. The reactor performance depends on the influent nitrate concentration and can be categorized into two situations, which are separated by a vertical line in Fig 10.2. Distributions of solid components and profiles of dissolved components in the biofilms at the three loadings that delimit the two situations are plotted in Figs. 10.3 and 10.4, respecitively. I use these two figures to help explain how the nitrate loading affects reactor performance for NO_3^- and TCE reductions. I also use them as examples of distributions of solid components and profiles of dissolved components. Similar figures are not shown in sections 2.3-2.5, since the patterns are similar.

In the first situation, occurring when the influent nitrate concentration increases from 1 to 68 mg COD/L, the effluent nitrate, TCE, and DCE concentrations increase, but the effluent VC concentration decreases due to less conversion of DCE to VC. The reduction of chlorinated ethenes is slightly

suppressed in this situation. For the lowest NO_3^- loading (1 mg COD/L), Fig. 10.3a shows that DH are about 7% of the total biomass, and this drops to close to 0% for 68 mg COD/L, as DH are outcompeted by ADB. The exact fractionof DH at 68 mg/L is $4 \times 10^{-4} - 8 \times 10^{-4}$, depending on location in the biofilm. In the second situation, as the influent nitrate concentration increases from 68 to 70 g COD/L, the effluent nitrate concentration continues to increase, the effluent TCE concentration rapidly increases until reaching the influent TCE concentration, and the effluent DCE and VC concentrations rapidly decrease to zero. The reduction of chlorinated ethenes is strongly suppressed in this situation due to strong competition from denitrifiers for space in the biofilm (the fraction of DH decreases from 4×10^{-4} - 8×10^{-4} in Fig. 10.3b to 8×10^{-5} - 2×10^{-4} in Fig. 10.3c). The fraction of DH is orders of magnitude smaller than the fraction of ADB (~45% in Figs. 10.3b and 10.3c), because the influent nitrate concentration is orders of magnitude higher than the influent TCE concentration, allowing ADB to force DH out of the biofilm.

H_2 is not limiting in the two situations, because the maximum influent nitrate concentrations (70 mg COD/L) is < 98 mg COD/L (Table 10.4). This is confirmed by the significant H_2 concentrations in Fig. 10.4.

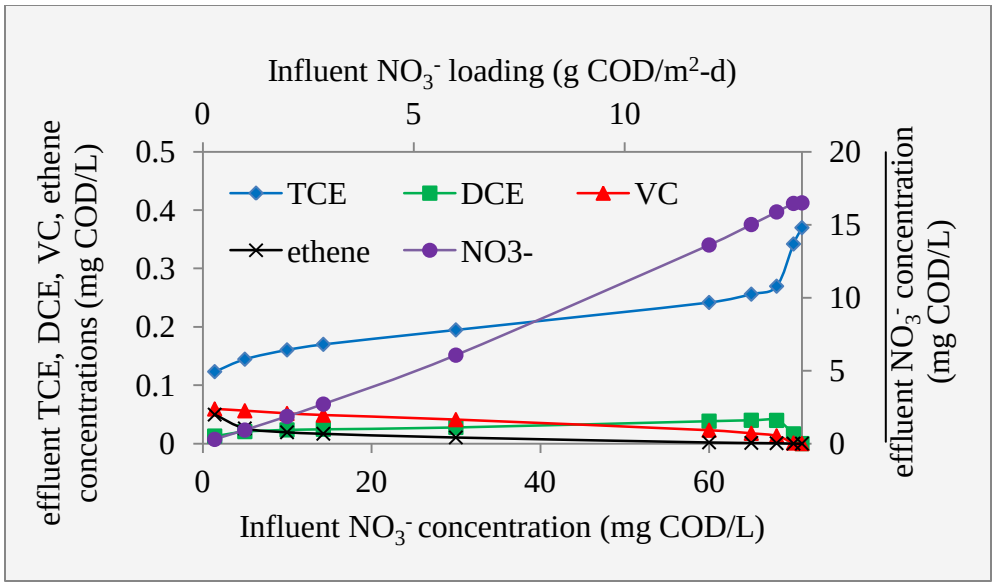

Fig. 10.2. The effluent TCE, DCE, VC, ethene, and NO_3^- concentrations at influent nitrate concentrations ranging from 1 to 70 g COD/m^2-d. The influent TCE concentration is 0.37 mg COD/L, the H_2 pressure is 1.17 atm, and the flow rate is 1.0 mL/min. The vertical line separates the figure into two situations.

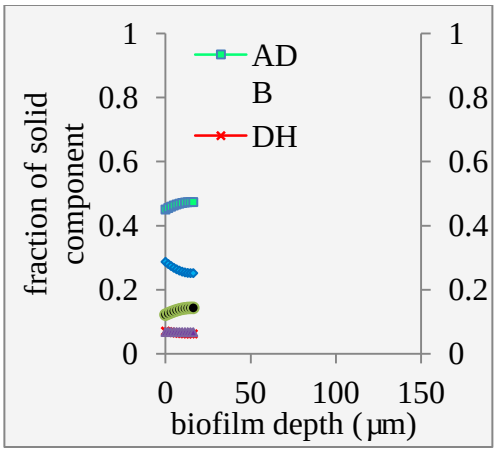

a. NO_3^-: 1 mg COD/L

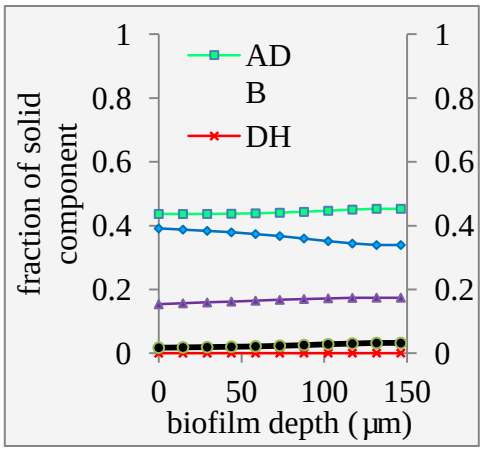

b. NO_3^-: 68 mg COD/L

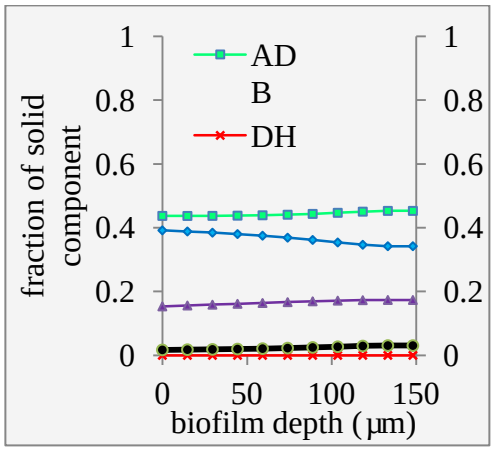

c. NO_3^-: 70 mg COD/L

Fig. 10.3. Biomass distributions at three influent nitrate concentrations that delimit the two situations. Liquid is on the left and fiber is on the right. The biofilm thickness can be seen by looking at the rightmost extent of a line. a. 1 mg COD/L; b. 68 mg COD/L; c. 70 mg COD/L .

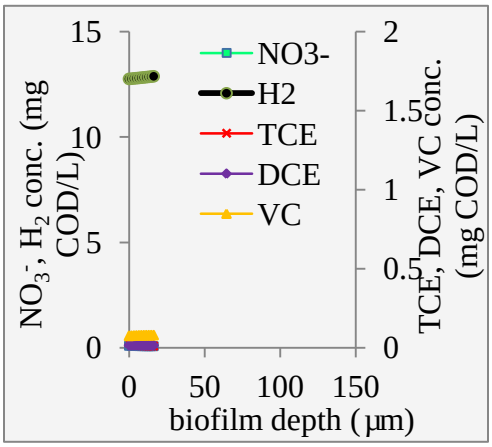

a. NO_3^-: 1 mg COD/L

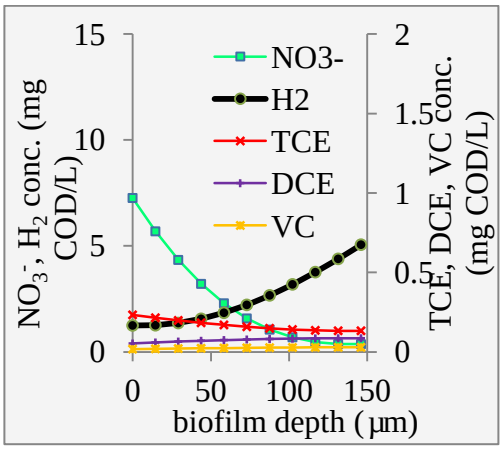

b. NO_3^-:68 mg COD/L

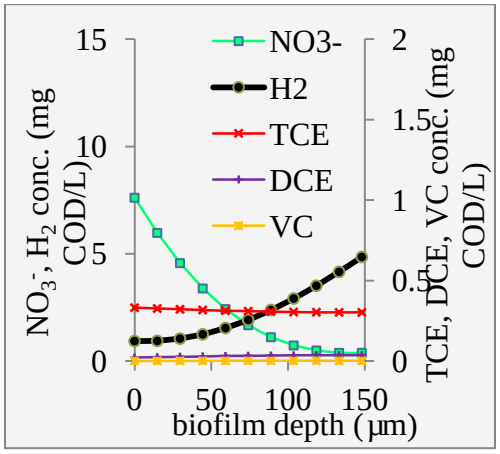

c. NO_3^-: 70 mg COD/L

Fig. 10.4. Profiles of dissolved components at three influent nitrate concentrations that delimit the two situations. Liquid is on the left and fiber is on the right. The biofilm thickness can be seen by looking at the rightmost extent of a line. a. 1 mg COD/L; b. 68 mg COD/L; c. 70 mg COD/L.

2.3 The effect of H_2 pressure on TCE reduction and intermediates accumulation

Fig. 10.5 plots the effluent TCE, DCE, VC, and NO_3^- concentrations at H_2 pressures ranging from 0.18 to 1.17 atm. A vertical line in Fig. 10.5 seperates the reactor performance into two situations.

In the first situation, the H_2 pressure increases from 0.18 to 0.22 atm. TCE reduction starts at 0.18 atm, coinciding with the ending point of H_2 competition (Table 10.4). The TCE concentration in the effluent decreases significantly as the H_2 pressure increases. The effluent DCE concentration increases first because of increasing conversion of TCE to DCE and then decreases due to more H_2 available. The effluent VC concentration keeps increasing due to increasing reduction of DCE to VC. Ethene concentration increases from 0 until reaching the maximum of 0.02 mg COD/L. The fraction of DH also inceases from zero until reaching the maximum (0.004 - 0.009, depending on location in the biofilm).

In the second situation, the H_2 pressure is larger than 0.22 atm. The reactor performance does not change as the H_2 pressure increases, because H_2 is over supplied and is not a limiting factor at all. All acceptors are removed to the maximum amount allowed by the NO_3^- and TCE loadings, and the biofilm composition is stable with the DH fraction at 0.004 - 0009.

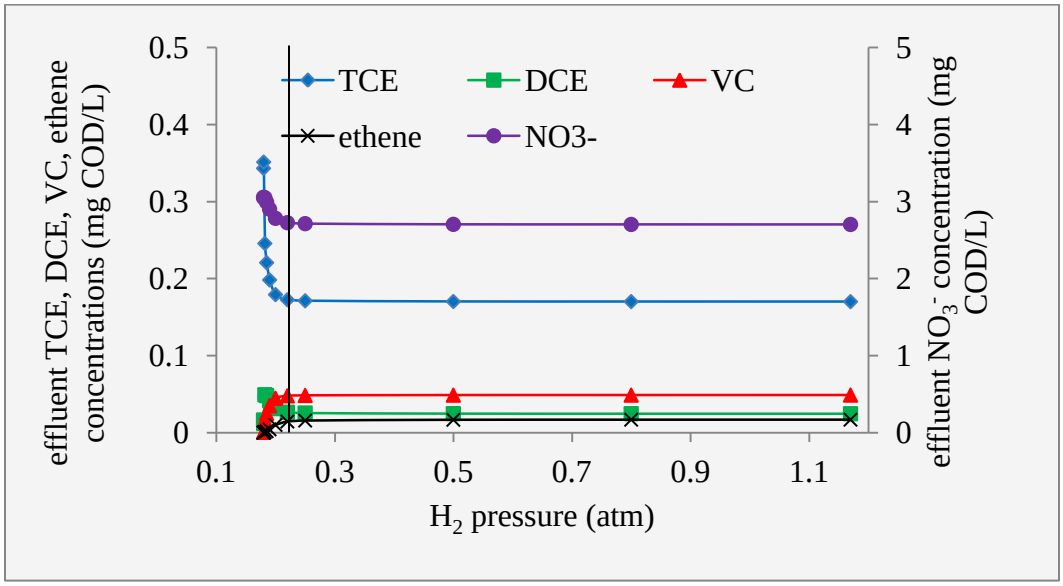

Fig. 10.5. The effluent TCE, DCE, VC, ethene, and NO_3^- concentrations at H_2 pressures ranging from 0.18 to 1.17 atm. The influent TCE concentration is 0.37 mg COD/L, the influent nitrate concentration is 14.3 mg COD/L, and the flow rate is 1.0 mL/min. The vertical line separates the figure into two situations.

2.4 The effect of flow rate on TCE reduction and intermediates accumulation

Fig. 10.6 plots the effluent TCE, DCE, VC, and NO_3^- concentrations at flow rates ranging from 0.003 to 14 mL/min. As distinguished from the previous scenarios, the loadings of nitrate and TCE go up together in this scenario. A vertical line in Fig. 10.7 separates the reactor performance into two situations.

In the first situation, the flow rate increases from 0.003 to 0.03 mL/min. The effluent nitrate, TCE, DCE, and VC concentrations keep increasing as the flow rate increases. The effluent ethene concentration and the fraction of DH decrease rapidly. These trends are attributed to space competition between ADB and DH in the biofilm. In the second situation, the flow rate is higher than 0.03 mL/min. The effluent TCE and nitrate concentrations continue increasing, but the effluent DCE, VC, and ethene concentrations decrease due to less conversion of TCE to DCE, DCE to VC, and VC to ethene. Competition for space intensifies in this situation. Once the flow rate is higher than 9.6 L/min, a flow rate corresponding to onset of H_2 limitation, TCE reduction is negligible.

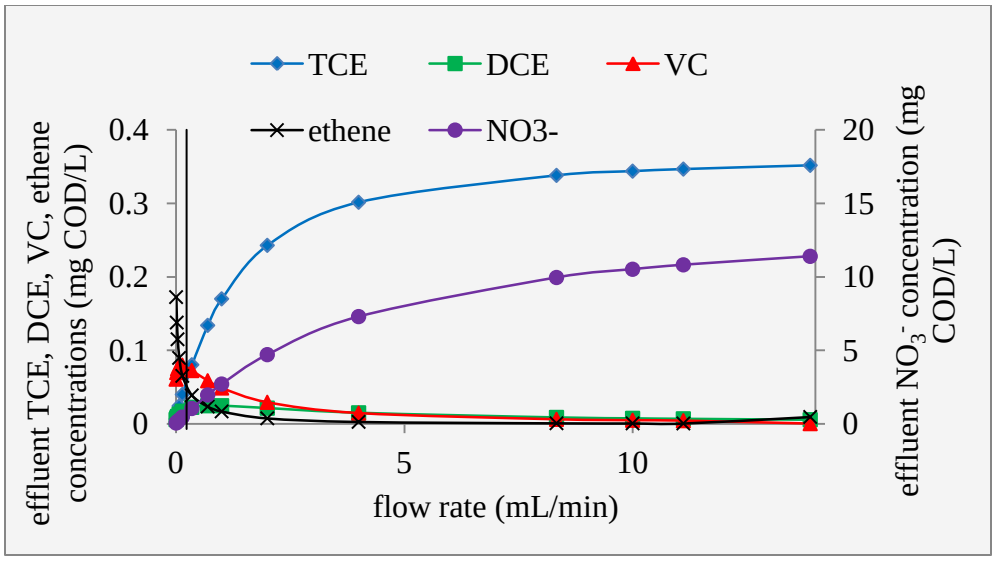

Fig. 10.6. The effluent TCE, DCE, VC, ethene, and NO_3^- concentrations at flow rates ranging from 0.003 to 14 mL /min. The influent nitrate concentration is 14.3 mg COD/L, the influent TCE concentration is 0.37 mg COD/L, and the H_2 pressure is 1.17 atm. The vertical line separates the figure into two situations.

2.5 The effect of TCE loading on TCE reduction and intermediates accumulation

Fig. 10.7 plots the effluent TCE, DCE, VC, and NO_3^- concentrations at influent TCE concentrations ranging from 0.07 to 200 mg COD/L. TCE is not reduced when its influent concentration is below 0.07 mg COD/L (190 μg TCE/L), because it is below the minimum concentration to meet the coexistence boundary condition. Therefore, TCE reduction will not occur in a completely mixed MBfR for a groundwater that contains TCE at < 190 μg/L and nitrate at > 5 mg N/L at this flow rate (1 mL/min). To reduce TCE in such a groundwater (i.e., TCE: < 190 μg/L; nitrate: > 5 mg N/L), the operator can either reduce the flow rate (section 2.4) or operate the reactor in series to remove most nitrate in the lead reactor; both measures can reduce the effluent nitrate concentration, thus allowing DH to grow in the biofilm.

Above the coexistence criterion, how the reactor performance depends on the influent TCE concentration can be categorized into two situations, which are separated by a vertical line in Fig 10.7.

In the first situation, the influent TCE concentration increases from 0.07 to 100 mg COD/L. The effluent nitrate, TCE, DCE,VC, and ethene concentrations keep increasing as the influent TCE concentration increases. The fraction of DH also increases. 100 mg COD/L is the turning point to the second situation, and it corresponds to the starting point of H_2 competition (Table 10.4).

In the second situation, the effluent TCE concentration continues increasing, but the increase becomes linear because the TCE flux into the biofilm reaches its maximum because of H_2 limitation. The effluent DCE concentration

slightly increases due to stronger inhibition of TCE on DCE reduction, the effluent VC concentration slightly decreases because of less conversion of DCE to VC, and the effluent ethene concentration also decreases due to stronger inhibition of TCE on VC reduction. The increased influent TCE concentration strengthens the inhibition effects among the chlorinated ethenes, which slightly decreases the electrons used for reduction of chlorinated ethenes and increases the electrons used for nitrate reduction, leading to the decreased effluent nitrate concentration in Fig. 10.7. The redistribution of electrons leads to a slight decrease of DH and a slight increase of ADB.

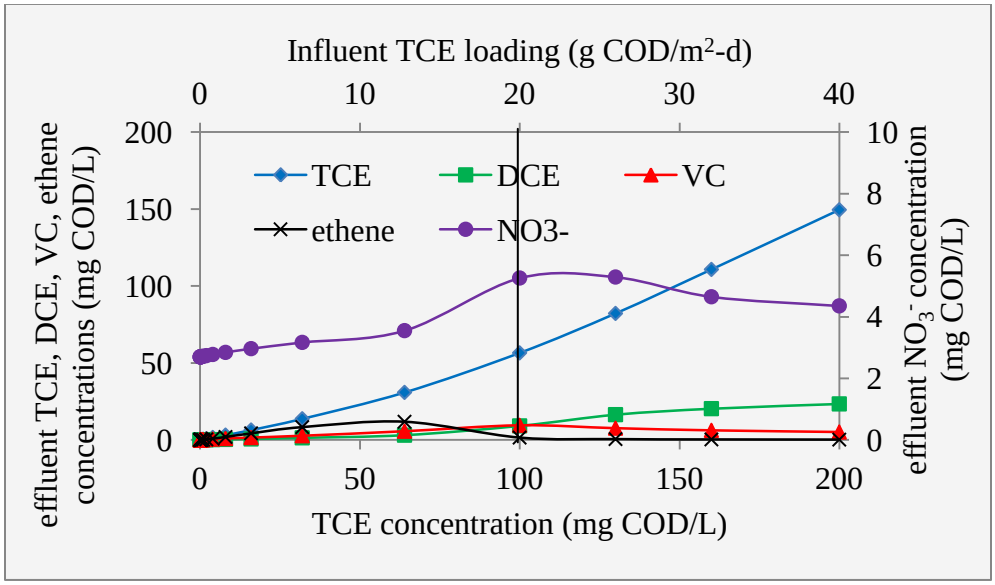

Fig. 10.7. The effluent TCE, DCE, VC, ethene, and NO_3^- concentrations at influent TCE concentrations ranging from 0.07 to 200 mg COD/L. The influent nitrate concentration is 14.3 mg COD/L, the H_2 pressure is 1.17 atm, and the flow rate is 1.0 mL/min. The vertical line separates the figure into two situations.

2.6 Practical values of the modeling results

The modeling results lead to a few key recommendations for practice:

1) For a groundwater with TCE < 100 mg COD/L, increasing the influent concentrations of TCE, nitrate, or both will increase the effluent nitrate, TCE, DCE, and VC concentrations.
2) TCE reduction cannot occur in a completely mixed MBfR for a groundwater with a high nitrate to TCE ratio at a certain flow rate, because ADB force DH out of the biofilm. To reduce TCE, the operator should reduce the flow rate or operate the reactor in stages.
3) For a groundwater that has a high nitrate to TCE ratio, TCE reduction occurs only when the H_2 pressure is high enough to exclude H_2 competition between ADB and DH, and the effluent nitrate and TCE concentrations decrease as the H_2 pressure increases beyond that point. The DCE and VC peaks occur at a H_2 pressure slightly larger than the pressure that corresponds to the onset of TCE reduction. Thus, H_2 should be over supplied to achieve simultaneous low concentrations of nitrate, TCE, DCE, and VC. The optimum H_2 pressure can be determined using this model. A good example may be the bench-scale experiment of Chung et al. (2008), who over supplied H_2 and achieved simultaneous low concentrations of effluent TCE, DCE, and VC.
4) While high effluent TCE concentrations occur at high flow rates, high effluent DCE and VC concentrations occur at low flow rates,

but not the minimal flow rate. The flow rate that corresponds to the DCE and VC peaks is neither too high to cause minimal TCE reduction nor too low to cause almost complete removal of all chlorinated compounds. Thus, theorectically, a minimal flow rate or a medium flow rate (i.e., a flow rate that is slightly higher than the flow rate that corresponds to the DCE and VC peaks) can be used to achieve simultaneous low concentrations of TCE, DCE, and VC. In practice, a medium flow rate is usually economically feasible. This flow rate can be determined using this model. For example, the bench-scale experiment in Chung et al. (2008) was operated at a medium flow rate of 1.0 mL/min, gave ~80 % removal of TCE, and had almost no intermediates accumulation. While a high flow rate of > 9.6 mL/min would end up with minimum TCE reduction, a low flow rate of 0.03 mL/min would lead to accumulation of DCE and VC in the effluent.

2.7 Model insights and limitations

As a first-step extention of the nitrate and perchlorate model, the nitrate and TCE model produces results that provide important insights about how the operating conditions affect TCE reduction and DCE and VC accumulation in an MBfR that also carries out denitrification. For example, DH cannot coexist with ADB in an MBfR that treats groundwater having a commonly found high nitrate to TCE ratio when the MBfR is operated under H_2 limitation.

Despite its ability to provide profound insights, the first-stage model has three limitations that need ultimately to be overcome by future research.

First, I used median values as model inputs for the TCE, DCE, and VC reduction kinetics, as summarized by Chambon et al. (2009). Although the modeling results represent well the general trends of reactor performance, biological kinetics parameters are likely to vary from reactor to reactor, depending on the micborial community. To use the model to quantitatively study the performance of a specific reactor, these biological parameters should be optimized using experimental data specific to that reactor or at least to the microbial communities inhabiting MBfR biofilms. Gathering these kinds of reactor-specific information is a major experimental effort that can be guided by the first-step model.

Second and as I pointed out when I simulated the bench-scale experiment of Chung et al. (2008), the effluent nitrate, TCE, DCE, and VC concentrations are slightly, but systematically higher than the experimental data, probably due to that suspended bacteria are not considered in the model. Thus, to better represent reactor performance, suspended bacteria should be added to the biofilm model. This should improve the simulation in circumstances where H_2 is over supplied and the hydraulic retention time is long, thus promoting the accumulation of significant suspended biomass. The model with no suspended biomass may be adequate with MBfRs that are more typicallyy biofilm-dominated, and the expanded model can define condition in which suspended biomass is or is not important.

Third, I neglect homoacetogenesis and methanogenesis, which can occur with some operating conditions, e.g., when H_2 is over supplied, the the hydraulic retention time is large, the bicarbonate concentration is a few orders of magnitude higher than the TCE and nitrate concentrations, or combinations (Ziv-El et al., 2012). Homoacetogens and methanogens can compete with DH for the same electron donor (H_2) and space in the biofilm, and both reactions tend to raise the pH outside the optimal range for DH (Ziv-El et al., 2012). All of these effects tend to suppress DH and reductive dechlorination of TCE. However, homoacetogens can produce acetate, the carbon source for DH. Thus, a small amount of homoactogenesis can be a benefit for DH. To comprehensively understand TCE reductive dechlorination in an MBfR, these two processes ultimately should be added to the nitrate and TCE model.

3. Conclusions

I produced a multispecies biofilm model for simultaneous reduction of nitrate and TCE in the H_2-based membrane biofilm reactor (MBfR) by adapting my multispecies biofilm model for simultaneous reduction of nitrate and perchlorate. As appropriate, I modified model components and their relationships, model assumptions and simplifications, substrate-utilization and biomass-growth kinetics, and model parameters.

I used representative values (median values from literature) for the biological TCE, DCE, and VC reduction parameters to simulate a bench-scale experiment that has one steady state (Chung et al., 2008). The simulated results

and experimental results agree well in trends: complete nitrate reduction, incomplete TCE reduction, and insignificant accumulation of DCE and VC.

I also used the same representative values (median values from literature) to predict effluent TCE, DCE, VC, and ethene concentrations over a wide range of operating conditions, including influent nitrate and TCE concentrations, H_2 pressure, and flow rate. To understand the mechanisms that affect reactor performance, I quantified conditions for coexistence of ADB and HB and H_2 limitation. While H_2 limitation usually coincides with ADB forcing out DH in a biofilm for a groundwater that has a high nitrate to TCE ratio, DH can coexist with ADB under H_2 limitation if the ratio of nitrate to TCE is low. Since H_2 limitation tends not to occur with a lower influent nitrate concentration, a lower flow rate, or a higher H_2 pressure, these operating conditions favor the growth of DH. Also, a higher influent TCE concentration favors the growth of DH.

Many groundwaters have high nitrate-to-TCE ratios. For such groundwaters, the effluent nitrate, TCE, DCE, and VC concentrations increase as the influent nitrate or TCE concentration increases. The effluent nitrate and TCE concentrations decrease as the H_2 pressure increases or the flow rate decreases. The DCE and VC peaks occur at a low flow rate or a H_2 pressure slightly higher than the H_2 pressure that corresponds to the onset of H_2 limitation. Therefore, simultaneous low concentrations of effluent nitrate, TCE, DCE, and VC occur at a low influent nitrate concentration, a low influent TCE concentration, a high H_2

pressure, or a medium flow rate. The optimal operating conditions can be quantified using the nitrate and TCE model.

To quantitatively study a specific MBfR for simultaneous reduction of nitrate and TCE, the biological reduction kinetics parameters should be optimized using kinetics experiments specific to the reactor. Also, to accurately represent reactor performance at operating conditions spanning over wide ranges, suspended bacteria should be considered, and homoacetogenesis and methanogenesis should be included.

Chapter 11
CONCLUSIONS AND RECOMMENDATIONS

1. Conclusions

This dissertation advances understanding of the reduction of three oxidized contaminants -- nitrate (NO_3^-), perchlorate (ClO_4^-), and trichloroethene (TCE) -- by two biofilm processes: the H_2-based membrane biofilm reactors (MBfR) and packed-bed heterotrophic reactors (PBHR).

I demonstrated and compared nitrate removal in groundwater using a pilot-scale MBfR and a pilot-scale PBHR. The maximum nitrate loadings to achieve effluent nitrate and nitrite concentrations below the maximum contamination levels (MCLs) were around 6 g N/m^2-d for the MBfR and the PBHR. The concentrations of dissolved organic carbon (DOC), biodegradable organic dissolved carbon (BDOC), heterotrophic place count (HPC), and turbidity were higher in the PBHR effluent than in the MBfR effluent. However, post-treatment that included an ozone-contact tank and a post-filter brought them to the same level; the finished water met drinking water standards except for HPC, which would require further disinfection.

I theoretically and experimentally demonstrated that the nitrate carrier-surface loading (*SL*), instead of empty bed contact time (*EBCT*) or nitrate volumetric loading (*VL*), is the primary design criterion for heterotrophic denitrification reactors. The maximum *SLs* at which the effluent NO_2^- concentration was around the Maximum Contaminant Level (MCL) ranged from 1.3 to 10 g N/m^2-d based on literature reports. The pilot-scale PBHR used two

means to control the *SL* and gave a maximum *SL* of approximately 6 g N/m^2-d, despite wide differences in *EBDT* and *VL*.

I constructed a model to predict the pH, alkalinity, and LSI in the effluent of H_2-based autotrophic denitrification and heterotrophic reactors. If the model outputs a pH value outside the optimal range for the denitrifiers or a high LSI value indicating serious precipitation potential, operators should take measures to control the pH. The pH can be controlled using either of two methods: One is to add acid (*e.g.*, HCl) to balance excessive base production from denitrification; the other is to add acid CO_2 into the reactor to hold the pH to a set point using an automated pH feedback loop. The model can be used to estimate the required acid additions for both scenarios.

I evaluated hte model using data from the two pilot-scale denitrification reactors. The model-predicted pH, alkalinity, and LSI matched well with the experimental data in all cases tested. The model showed that the autotrophic reactor is more sensitive to pH increases, that acid *(e.g., HCl)* addition is the preferred pH-control method for heterotrophic processes, and CO_2 addition is the preferred method for H_2-based autotrophic processes.

I developed and used steady-state H_2-permeation tests and a mathematical model to determine the H_2-permeation coefficients of three fibers commonly used in the H_2-based MBfR: 1.6×10^{-6}, 1.3×10^{-7}, and 4.6×10^{-8} m^2/d for composite, polypropylene, and polyester fibers, respectively. I used these H_2-permeation coefficients to correlate the performance of oxidized contaminants

removal to fiber types in previous MBfR tests. They also became important model inputs for the following three multispecies biofilm models.

I developed a multispecies biofilm model for simultaneous reduction of nitrate and perchlorate in the H_2-based membrane biofilm reactor. The model explicitly considers four mechanisms involved in how three important operating conditions (H_2 pressure, nitrate loading, and perchlorate loading) affect nitrate and perchlorate removals: 1) competition for H_2, 2) promotion of perchlorate-reducing bacteria (PRB) growth due to having two electron acceptors (nitrate and perchlorate), 3) competition for the same resources in the PRB, and 4) competition for space in the biofilm.

The model was solved directly for steady state using a novel three-step approach: finite-difference for approximating partial differential and/or integral equations, Newton-Raphson for solving non-linear equations, and an iterative scheme to obtain the steady-state biofilm thickness.

The half-maximum-rate concentrations and inhibition coefficients of nitrate and perchlorate were optimized by fitting data from experiments with different combinations of influent nitrate and perchlorate concentrations. The optimized half-maximum-rate concentration of nitrate and inhibition coefficient of nitrate to perchlorate are 5.7×10^{-4} mg/cm^3, and the optimized half-maximum-rate concentration of perchlorate and the inhibition coefficient of perchlorate to nitrate are 5.7×10^{-4} mg/cm^3. These values are approximately in the middle of their ranges in the literature.

I used the model with optimized parameters to quantitatively and systematically explain how three important operating conditions (nitrate loading, perchlorate loading, and H_2 pressure) affect nitrate and perchlorate reduction and biomass distribution in the biofilms. The effects of influent nitrate loading on perchlorate removal can be categorized into four situations. For the H_2 pressure used in the experiments for parameter optimization, nitrate loading of < 0.1 g N/m^2-d slightly promotes perchlorate removal, because the promotion effect in mechanism 2 (PRB use two acceptors) is dominant. A nitrate loading of 0.1-0.6 g N/m^2-d has no effect on perchlorate removal due to the fact that the promotion effect in mechanism 2 balances out the inhibition effect in mechanisms 3 (competition for the same enzyme) and 4 (competition for space). A nitrate loading of 0.6-1.0 g N/m^2-d inhibits perchlorate removal, since the inhibition effect from mechanisms 3 and 4 outweighs the promotion effect in mechanism 2. A nitrate loading of > 1.0 g N/m^2-d strongly inhibits perchlorate removal, since mechanism 1 (competition for H_2) becomes active. I also compared the simulated biomass distributions in the biofilm to qPCR data from the experiment used for parameter optimization. The trends matched well. In particular, the PRB cell numbers follow exactly the same trends for experiments and model: steady state 5 > 4 > 6 > 3 > 1. .

I produced a multispecies biofilm for simultaneous reduction of nitrate and sulfate in the MBfR by adapting the nitrate and perchlorate model above. The key change is that the sulfate-reducing bacteria cannot use nitrate. Thus, two mechanisms in the nitrate and perchlorate model are not relevant in the nitrate and

sulfate model: the mechanism that nitrate promotes the growth of PRB and the mechanism that nitrate and perchlorate compete for the same resources within PRB. I optimized the half-maximum-rate concentrations of nitrate and sulfate by best-fitting the nitrate and sulfate data from a bench-scale experiment with H_2 pressures ranging from 1.2 to 3.7 atm. The optimized parameters, 0.2 mg N/L and 1.6 mg SO_4^{2-}/L, are in the middle of their reported ranges.

To evaluate the model, I compared the effluent H_2, UAP (substrate-utilization-associated products), and BAP (biomass-associated products) concentrations to data in experiments. The simulated effluent H_2, UAP, and BAP concentrations are in the range of the previous experimental results. I also compared the simulated biomass distributions to qPCR data in the bench-scale experiment for parameter optimization. Model outputs and experimental results matched in terms of all major trends. In particular, the numbers of total cells, SRB, and DB increase as the H_2 pressure increases, the increase of SRB from 3.0 atm (corresponding to the start of sulfate reduction) to 3.7 atm (corresponding to around 50% sulfate reduction) is ~ 5.0 times.

Using the optimized parameters, I predicted effluent nitrate and sulfate concentrations over a wide range of operating conditions, including H_2 pressure, influent nitrate and sulfate concentrations, and flow rate. The influent sulfate concentration has little effect on the onset of sulfate reduction. Sulfate reduction occurs when the H_2 pressure is high enough, the influent nitrate concentration is low enough, or the flow rate is low enough. In general, the onset of sulfate reduction occurs when the nitrate concentration at the fiber surface is low enough

to allow the growth rates of DB and SRB equal at the fiber surface. For example, the maximum nitrate concentration at the fiber surface is 0.1 mg N/L to allow coexistence of SRB in the biofilm when the influent sulfate concentration is 46 mg SO_4^{2-}/L, and the H_2 pressure is 3.0 atm. Since the model can predict the H_2-pressure and nitrate loading conditions corresponding to the onset of sulfate reduction, it can be used as a tool to design MBfR and to quantitatively obtain the desired reductions of nitrate and sulfate in an MBfR.

I also produced a multispecies biofilm model for simultaneous reduction of nitrate and TCE in the H_2-based membrane biofilm reactor (MBfR) by adapting the nitrate and perchlorate model above. Critical changes for the nitrate and TCE model are that intermediates -- DCE and VC -- accumulate during TCE reduction and the chlorinated ethenes inhibit the reduction of their daughter products.

I used representative values (median values from literature) for the biological TCE, DCE, and VC reduction parameters to simulate a bench-scale experiment that has one steady state. The simulated results and experimental results agree well in trends: complete nitrate reduction, incomplete TCE reduction, and insignificant accumulation of DCE and VC.

I also used the same representative values (median values from literature) to predict effluent TCE, DCE, VC, and ethene concentrations over a wide range of operating conditions, including influent nitrate and TCE concentrations, H_2 pressure, and flow rate. Simultaneous low concentrations of effluent nitrate, TCE, DCE, and VC occur at a low influent nitrate concentration,

a low influent TCE concentration, a high H_2 pressure, or a medium flow rate for a groundwater that has a high nitrate-to-TCE ratio, which is common. The optimal operating conditions can be quanitified using the model.

To understand the mechanisms that affect reactor performance, I quantified conditions for coexistence of ADB and HB and H_2 limitation. While H_2 limitation usually coincides with ADB forcing out DH in a biofilm for a groundwater that has a high nitrate-to-TCE ratio, DH can coexist with ADB under H_2 limitation if the ratio of nitrate to TCE is low. Since H_2 limitation tends not to occur with a lower influent nitrate concentration, a lower flow rate, or a higher H_2 pressure, these operating conditions favor the growth of DH. Also, a higher influent TCE concentration favors the growth of DH.

2. Recommendations for Future Research

1) To quantitatively study a specific MBfR for simultaneous reduction of nitrate and TCE, the biological reduction kinetics parameters should be optimized using kinetics experiments specific to the MBfR. The kinetics experiments could be batch tests that are commonly used or a series of steady-state tests similar to those I used for the nitrate and perchlorate model and the nitrate and suflate model.

2) To fully understand microbial interactions in a biofilm reducing TCE and nitrate, homoacetogenesis and methanogenesis should be included in the model. One interaction is that homoacetogens produce acetate, a carbon source

for *Dehalococcoides* and an electron donor for heterotrophic denitrifying bacteria. It can also be used as the electron donor and acceptor for methanogens.

3) To accurately represent reactor performance at operating conditions spanning over wide ranges, suspended bacteria should be considered in these biofilm models.

4) To represent spatial 2-dimension heterogeneity in the biofilm, the 1-dimension models should be expanded to 2-dimension models: one dimension perpendicular and the other dimension parallel to the substratum.

5) To comprehensively compare the experimental biomass data to simulated biomass data, fluorescence *in situ* hybridization (FISH) analysis should be conducted to show spatial distribution of biomass in the biofilm.

6) To accurately measure the biofilm thickness, biofilm samples should be measured "fresh." Sample should not be frozen, because melting ice breaks the biofilm, which can result in loss of biofilm, distortion of the physical shape, and killing of some bacteria. Likewise, long storage in the refrigerator (e.g., 4 ℃) can lead to biomass decay and loss of ecological and physical structure.

REFERENCES

Adham, S.; Gillogly, T.; Lehman, G.; Rittmann, B.E.; Nerenberg, R. 2004 *Membrane Biofilm Reactor Process for Nitrate and Perchlorate Removal*. Denver, CO: AwwaRF and AWWA.

Ahn, C.H.; Oh, H.; Ki, D.; Van Ginkel, S.W.; Rittmann, B.E.; Park, J. 2009 Bacterial biofilm-community selection during autohydrogenotrophic reduction of nitrate and perchlorate in ion-exchange brine. *Journal of Applied Microbiology and Biotechnology*, 81, 1169-1177.

Amirtharajah, A. 1993 Optimum backwashing of filters with air scour: a review. *Water Science & Technology*, 27(10), 195-211.

Bae, W.; Rittmann, B.E. 1996 A structured model of dual-limitation kinetics. *Biotechnology and bioengineering*, 49(6), 683-689.

Baeseman, J.L.; Smith, R.L.; Silverstein, J. 2006 Denitrification potential in stream sediments impacted by acid mine drainage: effects of pH, various electron donors, and iron. *Microbial Ecology*, 51, 232-241.

Barton, L.L. 1995 Sulfate-reducing bacteria. In *Biotechnology Handbooks*. Edited by T. Atkinson and R.F. Sherwood. New York: Plenum Press.

Bradley, P.M. 2000 Microbial degradation of chloroethenes in groundwater systems. *Journal of Hydrology*, 8,104-111.

Brown, J.C.; Snoeyink, V.L.; Raskin, L.; and Lin, R. 2003 The sensitivity of fixed-bed biological perchlorate removal to changes in operating conditions and water quality characteristics. *Water Research*, 37, 206-214.

Brown, J.C.; Anderson, R.D.; Min, J.H.; Boulos, L.; Prasifka, D.; Juby, G.J.G. 2005 Fixed bed biological treatment of perchlorate-contaminated drinking water. *Journal American Water Works Association*, 97(9), 70-81.

Brown, J.C.; Raskin, L.; Morgenroth, E. 2009 *Direct Fixed-Bed Biological Perchlorate Destruction Demonstration. Report No. 0544*. Arlington, Virginia: Environmental Security Technology Certification Program Office (DOD).

Buttiglieri, G.; Malpei, F.; Daverio, E.; Melchiori, M.; Nieman, H.; Ligthart, J. 2005 Denitrification of drinking water sources by advanced biological treatment using a membrane bioreactor. *Desalination*, 178, 211-218.

Camerata, J.; Pearce, E.; Greer, P.; White, J.; Silva Bueno, M.A. 2008 Active sludge: professional development course. http://www.tlch20.com/courses/ActivatedSludge.pdf

Chambon, J.C.C.; Damgaard, I.; Christiansen, C.M.; Lemming, G.; Broholm, M.M.; Binning, P.J.; Bjerg, P.L. 2009 *Model Assessment of Reductive Dechlorination as a Remediation Technology for Contaminant Sources in Fractured Clay: Modeling Tool Delrapport II*. Environmental Project (ISBN: 978-87-92548-08-5), Copenhagen: Danish Environmental Protection Agency.

Chapra, S.C.; Canale, R.C. 2002 *Numerical Methods for Engineers With Software and Programming Applications, 4th Edition*. New York: McGraw-Hill Companies, Inc.

Chaudhuri, S.K.; O'Connor, S.M.; Gustavson, R.L.; Achenbach, L.A.; Coates, J.D. 2002 Environmental factors that control microbial perchlorate reduction. *Applied Environmental Microbiology*, 68(9), 4425-4430.

Chen, G.H.; Huang, J.C. 1996 Determination of diffusion layer thickness on a biofilm. *Journal of Environmental Science and Health Part A*, 31(2), 367-386.

Choi, Y.C.; Li, X.; Raskin, L.; Morgenroth, E. 2007 Effect of backwashing on the removal of perchlorate in fixed bed biofilm reactors, *Water Research*, 41(9), 1949-1959.

Choi, H.; Silverstein, J. 2008 Inhibition of perchlorate reduction by nitrate in a fixed biofilm reactor. *Journal of Hazardous Materials*, 159 (2-3), 440-445.

Christ, J.A.; Abriola, L.M. 2007 Modeling metabolic reductive dechlorination in dense non aqueous phase liquid source-zones, *Advances in Water Resources*, 30, 1547-1561.

Christopher, J.O.; Stone, M.L.; Benson, M.T.; Peterson, E.S. 2003 Testing of polymer membranes for the selective permeability of hydrogen. *Separation Science and Technology*, 38(12-13), 3225-3238.

Chu, M.; Kitanidis, P.K.; McCarty, P.L. 2004 Possible factors controlling the effectiveness of bioenhanced dissolution of non-aqueous phase tetrachloroethene. *Advances in Water Resources*, 27, 601-615.

Chung, J.; Nerenberg, R.; Rittmann, B.E. 2006 Bio-reduction of selenate using a hydrogen-based membrane biofilm reactor. *Environmental Science & Technology*, 40, 1664-1671.

Chung, J.; Krajmalnik-Brown, R.; Rittmann, B.E. 2008 Bioreduction of trichloroethene using a hydrogen-based membrane biofilm reactor. *Environmental Science & Technology*, 42 (2), 477-483.

Coates, J.D.; Michaelidou, U.; Bruce, R.A.; O'Connor, S.M.; Crespi, J.N.; Achenbach, L.A. 1999 Ubiquity and diversity of dissimilatory (per)chlorate-reducing bacteria. *Applied & Environmental Microbiology*, 65(12), 5234-5241.

Coppola, E.N.; McDonald, G.R. 2000 Bio-degradation of ammonium perchlorate, nitrate, hydrolysates and other energenic materials. U.S. patent 6,077,432.

Crittenden, J.C.; Trussell, R.R.; Hand, D.W.; Howe, K.J.; and Tchobanoglous, G. 2005 *Water Treatment: Principles and Design, 2nd Edition*. Hoboken, NJ: John Wiley & Sons, Inc.

Cupples, A.M.; Spormann, A.M; McCarty, P.L. 2004a Vinyl chloride and cis-dichloroethene dechlorination kinetics and microorganism growth under substrate limiting conditions. *Environmental Science & Technology*, 38(4), 1102-1107.

Cupples, A.M.; Spormann, A.M.; McCarty, P.L. 2004b Comparative evaluation of chloroethene dechlorination to ethene by dehalococcoides-like microorganisms. *Environmental Science & Technology*, 38(4), 4768-4774.

Dahab, M.F.; Kalagiri, J. 1996 Nitrate removal from water using cyclically operated fixed-film bio-denitrification reactors. *Water Science and Technology: a Journal of the International Association on Water Pollution Research*, 34(1/2), 331-338.

Debus, O.; Wanner, O. 1992 Degradation of xylene by a biofilm growing on a gas-permeable membrane. *Water Science & Technology*, 26(3-4), 607-616.

Duhamel, M.; Wehr, S.D.; Yu, L.; Rizvi, H.; Seepersad, D.; Dworatzek, S.; Cox, E.E.; Edwards, E.A. 2002 Comparison of anaerobic enrichment cultures maintained on tetrachloroethene, trichloroethene, cis-dichloroethene and vinyl chloride, *Water Research*, 36(17), 4193-4202.

de Silva, D.G.V.; Rittmann, B.E. 2000 Interpreting the response to loading changes in a mixed-culture completely stirred tank reactor. *Water Environment Research*, 72, 554-565.

Eberl, H.J.; Morgenroth, E.; Noguera, D.; Picioreanu, C.; Rittmann, B.E.; van Loosdrecht, M.C.M.; Wanner, O. 2006 *Mathematical Modeling of Biofilms*; IWA Scientific and Technical Report No.18. London: IWA Publishers.

Ergas, S.J.; Rheinheimer, D.E. 2004 Drinking water denitrification using a membrane bioreactor. *Water Research*, 38, 3225-3232.

Escobar, I.C.; Randall, A.A. 2001 Assimilable organic carbon (AOC) and biodegradable dissolved organic carbon (BDOC):: complementary measurements. *Water Research*, 35(18), 4444-4454.

Garant, H.; Lynd, L. 1998 Applicability of competitive and noncompetitive kinetics to the reductive dechlorination of chlorinated ethenes. *Biotechnology and Bioengineering*, 57(6), 751-755.

Gayle, B.P.; Boardman, G.D.; Sherrard, J.H.; Benoit, R.E. 1989 Biological denitrification of water. *Journal of Environmental Engineering*, 115(5), 930-943.

Ghafaria, S.; Hasanb, M.; Aroua, M.K. 2010 A kinetic study of autohydrogenotrophic denitrification at the optimum pH and sodium bicarbonate dose. *Bioresource Technology*, 101 (7), 2236-2242.

Giblin, T.; Frankenberger, W.T. 2001 Perchlorate and nitrate reductase activity in the perchlorate-respiring bacterium perclace. *Research in Microbiology*, 156, 311-315.

Giblin, T.; Herman D.; Deshusses, M.A.; Frankenberger, W.T. 2000 Removal of perchlorate in ground water with a flow-through bioreactor. *Journal of Environmental Quality*, 29, 578-583.

Gros, H.; Schnoor, G.; Rutten, P. 1988 Biological denitrification process with hydrogen-oxidizing bacteria for drinking water treatment. *Water Supply*, 6, 193-198.

Gu, B.; Brown, G.M.; Chiang, C.C. 2007 Treatment of perchlorate-contaminated groundwater using highly selective, regenerable ion-exchange technologies. *Environmental Science & Technology*, 41, 6277-6282.

Gujer, W.; Henze, M; Mino, T; van Loosdrecht, M.C.M. 1999 Activated sludge model No. 3. *Water Science and Technology*, 39, 183-193.

Gujer, W.; Wanner, O. 1989 Modelling mixed population biofilms. In *Biofilms*. Edited by Characklis, W.G.; Marshall, K.C. New York: John Wiley & Sons Inc.

Heilman, W.; Tammela, V.; Meyer, J.A.; Stannett, V.; Szwarc, M. 1956 Permeability of polymer films to hydrogen sulfide gas. *Industrial & Engeneering Chemestry*, 48(4), 821-824.

Hochstein, L.I.; Tomlinson, G.A. 1988 The enzymes associated with denitrification. *Annual Review of Microbiology*, 42, 231-261.

Hozalski, R.M.; Bouwer, E.J. 1998 Deposition and retention of bacteria in backwashed filters. *Journal American Water Works Association*, 90(1), 71-85.

Janda, V.; Rudovsky, J.; Wanner, J.; Marha, K. 1988 In situ denitrification of drinking water. *Water Science and Technology*, 20(3), 215-219.

Kapoor, A.; Viraraghavan, T. 1997 Nitrate removal from drinking water-review. *Journal of Environmental Engineering*, 123(4), 371-380.

Kengen, S.W.M.; Rikken, G.B.; Hagen, W.R.; van Ginkel, C.G.; Stams, A.J.M. 1999 Purification and characterization of (per)-chlorate reductase from the chlorate-respiring strain GR-1. *Journal of Bacteriology*, 181, 6706-6711.

Krajmalnik-Brown, R.; Hölscher, T.; Thomson, I.N.; Saunders, F.M.; Ritalahti, K.M.; Löffler, F.E. 2004 Genetic identification of a putative vinyl chloride reductase in Dehalococcoides sp. strain BAV1. *Applied and Environmental Microbiology*, 70(10), 6347-6351.

Kumar, S.; Sharma, A.; Tripathi, B.; Srivastava, S.; Agrawal, S.; Singh, M.; Awasthi, K.; Vijay, Y.K. 2010 Enhancement of hydrogen gas permeability in electrically aligned MWCNT-PMMA composite membranes. *Micron*, 41, 909-914.

Kumar, A.; Yuan, X.; Ergas, S.; Dewulf, J.; Van Langenhove, H. 2010 Model of a polyethylene microporous hollow-fiber membrane biofilm reactor inoculated with Pseudomonas putida strain To1 1A for gaseous toluene removal. *Bioresource Technology*, 101, 2180-2184.

Kurt, M.; Dunn, I.J. ; Bourne, J.R. 1987 Biological denitrification of drinking water using autotrophic organisms with H_2 in a fluidized-bed biofilm reactor. *Biotechnology and Bioengineering*, 29(4), 493-501.

Lampe, D.G.; Zhang, T.C. 1996. *Evaluation of Sulfur-based Autotrophic Denitrification*. Master's Thesis. University of Nebraska-Lincoln, NE.

Laspidou, C.S.; Rittmann, B.E. 2002a Non-steady-state modeling of extracellular polymeric substrates, soluble microbial products, and active and inert biomass. *Water Research*, 36, 1983-1992.

Laspidou, C.S.; Rittmann, B.E. 2002b A unified theory for extracellular polymeric substrates, soluble microbial products, and active and inert biomass. *Water Research*, 36, 2711-2720.

Laspidou, C.S.; Rittmann, B.E. 2004a Modeling the development of biofilm density including active bacteria, inert biomass, and extracellular polymeric substances. *Water Research*, 38(14-15), 3349-3361.

Laspidou, C.S.; Rittmann, B.E. 2004b Evaluating trends in biofilm density using the UMCCA Model. *Water Research*, 38(14-15), 3362-3372.

Lee, K.C.; Rittmann, B.E. 2000 A novel hollow fiber membrane biofilm reactor for autohydrogenotrophic denitrification of drinking water. *Water Science and Technology*, 14(4-5), 219-226.

Lee, K.C.; Rittmann, B.E. 2002 Applying a novel autohydrogenotrophic hollow-fiber membrane biofilm reactor for denitrification of drinking water. *Water Research*, 36, 2040-2052.

Lee, K.C; Rittmann, B.E. 2003 Effects of pH and precipitation on autohydrogenotrophic denitrification using the hollow-fiber membrane-biofilm reactor. *Water Research*, 37, 1551-1556.

Lee, I.S.; Bae, J.H.; Yang, Y.; McCarty, P.L. 2004 Simulated and experimental evaluation of factors affecting the rate and extent of reductive dechlorination of chloroethenes with glucose. *Journal of Contaminant Hydrology*, 74, 313-331.

Lee, H.S.; César, C.I.; Rittmann, B.E. 2009 Effects of substrate diffusion and anode potential on kinetic parameters for anode-respiring bacteria. *Environmental Science & Technology*, 43(19), 7571-7577.

Logan, B.E. 1998 A review of chlorate and perchlorate-respiring microorganisms. *Bioremediation*, 2(2), 69-79.

Logan, B.E.; Zhang, H.S.; Mulvaney, P.; Milner, M.G.; Head, I.M.; Unz, R.F. 2001 Kinetics of perchlorate- and chlorate-respiring bacteria. *Applied Environmental Microbiology*, 67, 2499-2506.

Macpherson, J.V.; Unwin, P.R. 1997 Determination of the diffusion coefficient of hydrogen in aqueous solution using single and double potential step chronoamperometry at a disk ultramicroelectrode. *Analytical Chemistry*, 69(11), 2063-2069.

Madigan, M.T.; Martinko, J.M. 2006 *Brock Biology of Microorganisms, 11th Edition*. Upper Saddle River, NJ: Pearson Education, Inc.

Matsumoto, S.; Terada, A.; Tsuneda, S. 2007 Modeling of membrane-aerated biofilm: Effects of C/N ratio, biofilm thickness and surface loading of oxygen on feasibility of simultaneous nitrification and denitrification. *Biochemical Engineering Journal*, 37, 98-101.

McCarty, P. L. 1997 Breathing with chlorinated solvents. *Science*, 276, 1521-1522.

Merkey, B.V. 2008 *Biofilm Modeling for Wastewater Treatment: Multiple Species and Multiple Components*. Doctoral Thesis. Northwestern University, Evanston, Illinois.

Meyer, K.J.; Swaim, P.D.; Bellamy, W.D.; Rittmann, B.E.; Tang, Y.; Scott, R. 2010 *Biological and Ion Exchange Nitrate Removal: Performance and Sustainability Evaluation*. Final Project Report. Denver, CO: Water Research Foundation.

Miltner, R.J; Summers, R.S.; Wang, J.Z. 1995 Biofiltration performance: part 2, effect of backwashing. *Journal American Water Works Association*, 87(12), 64-70.

Miltner, R.J. 1996 Comparative evaluation of biological filters. In *Proceedings of Water Quality Technology Conference*. Boston, MA: AWWA.

Mohseni-Bandpi, A.; Elliott, D.J.; Momeny-Mazdeh, A. 1999 Denitrification of groundwater using acetic acid as a carbon source. *Water Science and Technology*, 40(2), 53-59.

Moreno, B.; Gómez, M.A.; Gonzalez-López; Hontoria, E. 2005 Inoculation of a submerged filter for biological denitrification of nitrate polluted groundwater: a comparative study. *Journal of Hazardous Materials*, B117, 141-147.

Murray, R.E.; Parsons, L.L.; Smith, M.S. 1990 Aerobic and anaerobic growth of rifampin-resistant denitrifying bacteria in soil. *Applied Environmental Microbiology*, 56(2), 323-328.

Nerenberg, R.; Rittmann, B.E.; Najm, I. 2002 Perchlorate reduction in a hydrogen-based membrane-biofilm reactor. *Journal American Water Works Association*, 94, 103-114.

Nerenberg, R.; Rittmann, B.E. 2004 Hydrogen-based, hollow-fiber membrane biofilm reactor for reduction of perchlorate and other oxidized contaminants. *Water Science & Technology*, 49(11-12), 223-230.

Nerenberg, R.; Kawagoshi, Y.; Rittmann, B.E. 2006 Kinetics of a hydrogen-oxidizing, perchlorate-reducing bacterium. *Water Research*, 40, 3290-3296.

Ni, B.J.; Rittmann, B.E.; Yu, H.Q. 2011 Soluble microbial products and their implications in mixed culture biotechnology. *Trends in Biotechnology*, 29(9), 454-463.

Nielsen, P.H. 1987 Biofilm dynamics and kinetics during high-rate reduction under anaerobic conditions. *Applied and Environmental Microbiology*, 53(1), 27-32.

Noguera, D.R.; Brusseau, G.A.; Rittmann, B.E.; Stahl, D.A. 1998 A united model describing the role of hydrogen in the growth of *Desulfovibrio Vulgaris* under different environmental conditions. *Biotechnology and Bioengineering*, 59(6), 732-740.

Nogueira, R.; Melo, L.F. 2006 Competition between *Nitrospira spp.* and *Nitrobacter spp.* in nitrite-oxidizing bioreactors. *Biotechnology and Bioengineering*, 95(1), 169-175.

Ogumi, Z.; Takehara, Z.; Yoshizawa, S. 1984 Gas permeation in SPE method. *Journal of The Electrochemical Society*, 131(4), 769-773.

Okeke, B.C.; Giblin, T.; Frankenberger, W.T. 2001. Reduction of perchlorate and nitrate by salt tolerant bacteria. *Environmental Pollution*, 18, 357-363.

Ontiveros-Valencia, A., et al. 2011. Interactions between nitrate and sulfate-reducing bacteria in the hydrogen-based membrane biofilm reactor: the roles of surface loading and electron donor bioavailability, in preparation.

Parthasarathy, A.; Martin, C.R.; Srinivasan, S. 1991 Investigation of the O_2 reduction reaction at the platinum Nafion interface using a solid-state electrochemical-cell. *Journal of The Electrochemical Society*, 138(4), 916-921.

Reichert, P. 1998 AQUASIM 2.0 – Tutorial. Swiss Federal Institute for Environmental Science and Technology (EAWAG) CH - 8600 Dübendorf, Switzerland.

Rezania, B.; Cicek, N.; Oleszkiewicz, J.A. 2005 Kinetics of hydrogen-dependent denitrification under varying pH and temperature conditions. *Biotechnology and Bioengineering*, 92(7), 900-906.

Rezania, R.; Cicek, N.; Oleszkiewicz, J.A. 2006 Quantifying inorganic fouling in a membrane bioreactor treating nitrate-contaminated groundwater using hydrogen as energy source. *Water Science & Technology*, 6(3), 115-121.

Richard, Y. 1989 Operating experiences of full-scale biological and ion-exchange denitrification plants in France. *Water and Environmental Management Journal*, 3(2), 154-167.

Richard, Y.; Leprince, A.; Martin, G. 1980 Denitrification of water for human consumption. *Progress in Water Technology*, 12(6), 173-191.

Rittmann, B.E. 2006 The membrane biofilm reactor: the natural partnership of membranes and biofilm. *Water Science and Technology*, 53(3), 219-226.

Rittmann, B.E. 2007 The membrane biofilm reactor is a versatile platform for water and wastewater treatment. *Journal of Environmental Engineering*, 12 (4), 157-175.

Rittmann, B.E.; Dovantzis, K. 1983 Dual limitation of biofilm kinetics. *Water Research*, 17(12), 1727-1734.

Rittmann, B.E.; Manem, J.A. 1992 Development and experimental evaluation of a steady-state multispecies biofilm model. *Biotechnology and Bioengineering*, 39(9), 914-922.

Rittmann, B.E.; Huck, P.M. 1989 Biological treatment of public water-supplies. In *CRC Critical Reviews in Environmental Control*. Boca Raton, FL: CRC Press.

Rittmann, B.E.; McCarty, P.L. 1980 Model of steady-state-biofilm kinetics. *Biotechnology and Bioengineering*, 22, 2343-2357.

Rittmann, B.E.; McCarty, P.L. 2001 *Environmental Biotechnology: Principles and Applications*. New York: McGraw-Hill Companies, Inc.

Rittmann, B.E.; Snoeyink, V.L. 1984 Achieving biological stable drinking water. *Journal American Water Works Association*, 76(10), 106-114.

Rittmann, B.E.; Tang, T.; Meyer, K.; Bellamy, W.D.; Nerenberg, R. 2011 Biological processes. Chpt. 17 in *Water Treatment Plant Design, fifth ed.*, edited by Randtke, S. Denver, CO.: American Water Works Association.

Rogalla, F.; Ravarini, P.; de Larminat, G.; Couttelle, J. 1990a Large-scale biological nitrate and ammonia removal. *Journal of the Institution of Water and Environmental Management*, 4(4), 319-329.

Rogalla, F. ; de Larminat, G.; Coutelle, J. ; Godart, H. 1990b Experience with nitrate removal methods for drinking water. In *Proc. of the Advanced Reserch Workshop on Nitrate Contamination: Exposure, Consequences, and Control*. Lincoln, NE: NATO (North Atlantic Treaty Organization).

Rusten, B.; Hem, L.J.; ødegaard, H. 1995 Nitrogen removal from dilute wastewater in cold climate using moving-bed biofilm reactors. *Water Environmental Research*, 67(1), 65-74.

Sáez, P.B.; Rittmann, B.E. 1992 Model parameter estimation using least squares. *Water Research*, 26(6), 789-796.

Sander, R. 1999 Compilation of henry's law constants for inorganic and organic species of potential importance in environmental chemistry (version 3). http://www.henrys-law.org.

Sengupta, S.; Ergas, S.J. 2006 *Autotrophic Biological Denitrification with Elemental Sulfur or Hydrogen for Complete Removal of Nitrate-Nitrogen from a Septic System Wastewater*. NOAA/UNH (National Oceanic and Atmospheric Administration/ University of New Hampshire) Cooperative Institute for Coastal and Estuarine Environmental Technology Final Report.

Sethuraman, V.A.; Khan, S.; Jur, J.S.; Haug, A.T.; Weidner, J.W. 2009 Measuring oxygen, carbon monoxide and hydrogen sulfide diffusion coefficient and solubility in Nafion membranes. *Electrochimica Acta*, 54, 6850-6860.

Shanahan, J.W.; Semmens, M.I. 2004 Multipopulation model of membrane-aerated biofilms. *Environmental Science & Technology*, 38(11), 3176-3183.

Shanmugam, K.T.; Stewart, V.; Gunsalus, R.P.; Boxer, D.H.; Cole, J.A.; Chippaux, M.; DeMoss, J.A.; Giordano, G.; Lin, E.C.C.; Rajagopalan, K.V. 1992 Proposed nomenclature for the genes involved in molybdenum metabolism in *Escherichia Coli* and *Salmonella Typhimurium*. *Molecular Microbiology*, 6, 3452-3454.

Silverstein, J.S. ; Carlson, G.L. 1999 *Biological Denitrification of Drinking Water for Rural Communities*. Final Project Report. NRECA (National Rural Electric Cooperative Association) and EPRI (Electric Power Research Institute). WO-2662-84.

Smith, R.L.; Ceazan, M.L.; Brooks, M.H. 1994 Autotrophic, hydrogen-oxidizing, denitrifying bacteria in groundwater, potential agents for bioremediation of nitrate contamination. *Applied and Environmental Microbiology*, 60(6), 1949-1955.

Snoeyink, V.L.; Jenkins, D. 1980 *Water Chemistry*. New York: Wiley, Inc.

Soares, M.I.M. 2000 Biological denitrification of groundwater. *Water, Air and Soil Pollution*, 123(1-4), 183-193.

Srinivasan R.; Sorial, G.A. 2009 Treatment of perchlorate in drinking water: a critical review. *Separation and Purification Technology*, 69(1), 7-21.

Standard Methods for the Examination of Water and Wastewater, 1998 (20th ed.). APHA, AWWA, and WEF, Washington.

Popat, S. C.; Deshusses, M.A. 2011 Kinetics and inhibition of reductive dechlorination of trichloroethene, cis-1,2-dichloroethene and vinyl chloride in a continuously fed anaerobic biofilm reactor. *Enviromental Science & Technology*, 45(4), 1569-1578.

Stewart, P.S. 1998 A review of experimental measurements of effective diffusive permeabilities and effective diffusion coefficients in biofilms. *Biotechnology and Bioengineering*, 59(3), 261-272.

Stewart, P.S. 1992 A model of biofilm detachment. *Biotechnology & Bioengineering*, 41(1), 111-117.

Tang, Y.; Ziv-El, M.; Zhou, C.; Shin, J.H.; Ahn, C.H.; Meyer, K.; Candelaria, D.; Friese, D.; Overstreet, R.; Scott, R.; Rittmann, B.E. 2010 Bioreduction of nitrate in groundwater using a pilot-scale hydrogen-based membrane biofilm reactor. *Frontiers of Environmental Science & Engineering in China*, 4(3), 280-285.

Tang, Y.; Ziv-El, M.; Zhou, C.; Shin, J.H.; Ahn, C.H.; Meyer, K.; McQuarrie, J.; Candelaria, D.; Swaim, P.; Scott, R.; Rittmann, B.E. 2011a Using the carrier-surface loading to design heterotrophic denitrification reactors. *Journal American Water Works Association*, 103(3), 68-78.

Tang, Y.; Zhou, C.; Ziv-El, M.; Rittmann, B.E. 2011b A pH-control model for heterotrophic and hydrogen-based autotrophic denitrification. *Water Research*, 45(1), 232-240.

Tang, Y.; Ziv-El, M.; Meyer, K.; Zhou, C.; Shin, J.H.; Ahn, C.H.; McQuarrie, J.; Candelaria, D.; Swaim, P.; Scott, R.; Rittmann, B.E. 2012a Comparison of heterotrophic and hydrogen-based autotrophic denitrificaiton of drinking water. *Water Science & Technology: Water Supply*, in press.

Tang, Y.; Zhao, H.; Marcus, A.; Krajmalnik-Brown, R.; Rittmann, B.E. 2012b A steady-state biofilm model for simultaneous reduction of nitrate and perchlorate -- Part 1: model development and numerical solution. *Environmental Science & Technology*, in press.

Tang, Y.; Zhao, H.; Marcus, A.; Krajmalnik-Brown, R.; Rittmann, B.E. 2012c A steady-state biofilm model for simultaneous reduction of nitrate and perchlorate -- Part 2: parameter optimization and results and discussion. *Environmental Science & Technology*, in press.

Tang, Y.; Ontiveros-Valencia, A.; Feng, L.; Zhou, C.; Rosa Krajmalnik-Brown; Rittmann, B.E. 2012d. A Multispecies Biofilm Model for Simultaneous Reduction of Nitrate and Sulfate. In preparation.

Tang, Y.; Zhou, C.; van Ginkel, S.; Ontiveros-Valencia, A.; Shin, J.H.; Rittmann, B.E. 2012e Hydrogen-diffusion coefficients of the fibers used in H_2-based membrane biofilm reactors. *Journal of Membrane Science*, in revision.

Tang, Y.J.; Yi, S.; Zhuang, W.Q.; Zinder, S.H.; Keasling, J.D.; Alvarez-Cohen, L. 2009 Investigation of carbon metabolism in "*Dehalococcoides ethenogenes*" Strain 195 by use of isotopomer and transcriptomic analyses. *Journal of Bacteriology*, 191(16), 5224-5231.

Trulear, M.G.; Characklis, W.G. 1982 Dynamics of biofilm processes. *Journal Water Pollution Control Federation*, 54, 1288-1301.

Tuwiner, S.B. 1962 *Diffusion and Membrane Technology, 2nd ed., American Chemical Society, Monograph Series*, New York: Reinhold Pub. Corp.

Urfer, D.; Huck, P.M.; Booth, S.D.J.; Coffey, B.M. 1997 Biological filtration for BOM and particle removal: a critical review. *Journal American Water Works Association*, 89(12), 83-98.

USEPA 1999 Method 300.1: Determination of inorganic ions in drinking water by ion chromotography. Washington, D.C.: USEPA. http://www.caslab.com/EPA-Method-300_1/

USEPA 2002 Perchlorate environmental contamination: toxicological review and risk characterization (2002 external review draft). Washington, D.C.: USEPA.

USEPA 2009 National primary drinking water regulations. Washington, D.C.: USEPA. http://water.epa.gov/drink/contaminants/index.cfm#List

USEPA 2011 Trichloroethylene quickview. Washington, D.C.: USEPA. http://cfpub.epa.gov/ncea/iris/index.cfm?fuseaction=iris.showQuickView&substance_nmbr=0199

VanBriesen, J.M.; Rittmann, B.E. 1999 Modeling speciation effects on biodegradation in mixed metal/chelate systems. *Biodegradation*, 10, 315-330.

van Ginkel, C.G.; Kroon, A.G.M.; Rikken, G.B.; Kengen, S.W.M. 1998 Microbial conversion of perchlorate, chlorate, and chlorite. In *Proceedings of the National Ground Water Association Southwest Focused Ground Water Conference: Discussing the Issue of MTBE and Perchlorate in the Ground Water*. Columbus, OH: National Ground Water Association.

Van Ginkel, S. W.; Ahn, C.H.; Badruzzaman, M.; Roberts, D.J.; Lehman, S.G.; Adham, S.; Rittmann, B.E. 2008 Kinetics of nitrate and perchlorate reduction in ion exchange brine using the membrane biofilm reactor (MBfR). *Water Research*, 42, 197-4205.

Van Ginkel, S.W.; Tang, Y.; Rittmann, B.E. 2011a Impact of precipitation on the treatment of real ion-exchange brine using the H_2-based membrane biofilm reactor. *Water Science & Technology*, 63(7), 1453-1458.

Van Ginkel, S.W.; Kim, B.; Yang, Z.; Sittmann, R.; Sholin, M.; Micelli, J.; Rittmann, B.E. 2011b Effect of NaCl on nitrate removal from ion-exchange spent brine in the membrane biofilm reactor (MBfR). *Water Science & Technology*, submitted.

Van Ginkel, S.W.; Kim, B.; Yang, Z.; Rittmann, B.E. 2011c The removal of selenate to low levels (ppb) from flue gas desulfurization brine using the H_2-based membrane biofilm reactor (MBfR). *Bioresource Technology*, 102 (10), 6360-6364.

Vrtovšek, J.; Roš, M. 2006 Denitrification of groundwater in the biofilm reactor with a specific biomass support material. *Acta Chimica Slovenica*, 53, 396-400.

Waller, A.S.; Cox, E.E.; Edwards, E.A. 2004 Perchlorate-reducing microorganisms isolated from contaminated sites. *Environmental Microbiology*, 6, 517-527.

Wanner, O.; Gujer, W. 1985 Compitition in biofilms. *Water Science and Technology*, 17(2-3), 27-44.

Wanner, O.; Gujer. W. 1986 A multispecies biofilm model. *Biotechnology and Bioengineering*, 28(3), 314-328.

Welander, U.; Mattiasson, B. 2003 Denitrification at low temperatures using a suspended carrier biofilm process. *Water Research*, 37, 2394-2398.

Welander, U.; Henrysson, T.; Welander, T. 1998 Biological nitrogen removal in a pilot scale suspended carrier biofilm process. *Water Research*, 32(5), 1564-1570.

Williamson, K.; McCarty, P.L. 1976 A model of substrate utilization by bacterial films. *Journal Water Pollution Control Federation*, 48(1), 9-24.

Woodbury, B.L.; Dahab, M.F. 2001 Comparison of conventional and two-stage reversible flow, static-bed biodenitrification reactors. *Water Research*, 35(6), 1563-1571.

Woolschlager, J.; Rittmann, B.E.; Piriou, P.; Schwartz, B. 2002 Developing a simple factor to evaluate microbiological stability in distribution systems. In *Proceedings of the Annual Conference*, New Orleans, La: AWWA.

Xu, J.L.; Trimble, J.J.; Steinberg, L.; Logan, B.E. 2004 Chlorate and nitrate reduction pathways are separately induced in the perchlorate-respiring bacterium *Dechlorosoma sp KJ* and the chlorate-respiring bacterium *Pseudomonas sp PDA*. *Water Research*, 38(3), 673-680.

Yu, S.; Semprini, L. 2004 Kinetics and modeling of reductive dechlorination at high PCE and TCE concentrations, *Biotechnology and Bioengineering*, 88(4), 451-464.

Yu, S.; Dolan, M.E.; Semprini, L. 2005 Kinetics and inhibition of reductive dechlorination of chlorinated ethylenes by two different mixed cultures. *Environmental Science & Technology*, 39(1), 195-205.

Zhao, H.P.; Van Ginkel, S.W.; Tang, Y; Kang, D.W.; Rittmann, B.E.; Krajmalnik-Brown, R. 2011 Interactions between perchlorate and nitrate reductions in the biofilm of a hydrogen-based membrane biofilm reactor. *Environmental Science & Technol*onogy, accepted. DOI: 10.1021/es202569b.

Ziv-El, M.; Rittmann, B.E. 2009a Systematic evaluation of nitrate and perchlorate bioreduction kinetics in groundwater using a hydrogen-based membrane biofilm reactor. *Water Research*, 43, 173-181.

Ziv-El, M.; Rittmann, B.E. 2009b Water-quality assessment after treatment in a membrane biofilm reactor. *Journal American Water Works Association*, 101(12), 77-83.

Ziv-El, M.; Sudeep, P.; Katherine, C.; Halden, R.; Krajmalnik-Brown, R.; Rittmann, B.E. 2012 Managing methanogens and homoacetogens to promote reductive dechlorination of trichloroethene with direct delivery of H_2 in a membrane biofilm reactor. *Biotechnology and Bioengineering*, submitted.